A Numerical Evaluation of the Functionality of Coronary Bifurcation Lesions

Catherine Pagiatakis

Department of Mechanical Engineering
McGill University
Montreal, Quebec, Canada

November 2016

A thesis submitted to McGill University in partial fulfillment of the requirements for the degree of Doctor of Philosophy in Mechanical Engineering

ABSTRACT

Cardiovascular disease remains the leading cause of death in the developed world [1-3]. Coronary artery disease, characterized by the thickening and hardening of the vascular wall, and the narrowing of the arterial lumen, constitutes the highest proportion of all cardiovascular-related deaths. In clinic, up to 20 percent of all percutaneous coronary interventions are executed for the treatment of coronary bifurcation lesions (CBLs) [4-6], which are defined as luminal narrowings that are in the vicinity of, and/or include a significant side branch [4, 7]. There is still much uncertainty and debate with regard to the assessment of CBL severity [8] as well as the corresponding optimal interventional technique [7]. In addition, the treatment of CBLs is associated with high rates of peri- and post-procedural clinical events [4, 5, 7, 9-13], which renders them, to this day, a major limitation of interventional cardiology.

Thus far, studies of CBLs have focused on the risk for the initiation and the progression of the disease relative to the disturbed flow hypothesis. There has not been an attempt to study CBLs from the functional perspective where an understanding of the factors that affect the clinical manifestation of the disease is sought, based on standard diagnostic indices. A functional evaluation of CBLs is important because the development of ischemia is more complex than that of isolated lesions due to the presence of haemodynamic interactions. Furthermore, whereas a gold-standard diagnostic index with a well-defined threshold for the onset of ischemia, namely the Fractional Flow Reserve (FFR), has been validated for the decision to revascularize, it is only utilized in less than 10 percent of catheterization labs worldwide [14-16]. As such, cardiologists still rely heavily on an angiographic evaluation, which has been shown to have a poor correlation with haemodynamic impact [17]. Therefore, insight on the functionality of CBLs is important in order to improve the current strategies and thus, reduce the risk associated with their treatment.

Therefore, the main objective of the thesis is to provide insight on the functionality of CBLs. As such, a numerical model of a diseased coronary bifurcation that enables the computation of the gold-standard diagnostic index (FFR), is developed and subsequently

utilized to systematically quantify and compare the effect of various geometric parameters on the corresponding haemodynamic impact. Specifically, the effects of lesion configuration and severity, and the effects of luminal eccentricity and bifurcation angle are investigated. The results showed that clinical manifestation of the disease is a complex factor of both local and global haemodynamic interactions. Specifically, the numerical simulations demonstrated that the number of lesions does not govern the functional severity of a CBL configuration and that the characteristics of the supplying vessel stenosis play an important role in the clinical manifestation of the disease. Within the limitations of the work, the findings have potentially important clinical implications which, with future validation, could help improve the current diagnostic guidelines.

RÉSUMÉ

La maladie cardiovasculaire est l'une des principales causes de mortalité dans les pays développés [1-3]. La majorité des décès sont provoqués par une insuffisance coronarienne, qui consiste à un épaississement et un endurcissement de la paroi vasculaire, ainsi qu'un rétrécissement de la lumière artérielle. Jusqu'à 20 pourcents des interventions coronariennes percutanées (ICP) servent à traiter des lésions de bifurcation coronaires (LBC) [4-6], qui sont sujettes à un rétrécissement de la lumière vasculaire situé dans une branche de bifurcation significative ou bien à proximité de celle-ci [4, 7]. Les incertitudes persistent quant au degré de sévérité des LBC [8] et les traitements qui leurs sont associés [7]. Ces derniers sont reconnus pour être à l'origine de conséquences cliniques néfastes aux niveaux péri- et post-procéduraux [4, 5, 7, 9-13]. Il s'agit donc d'une limitation majeure en cardiologie interventionnelle.

Jusqu'à présent, les études traitant des lésions de bifurcation coronaires se concentraient principalement sur le risque de l'apparition de la maladie, ainsi que de sa progression, prenant en compte la perturbation locale du flux sanguin. Cependant, aucune étude ne porte actuellement sur la fonctionnalité des LBC, alors que cela pourrait amener à une meilleure compréhension des facteurs à l'origine des symptômes cliniques. En effet, une analyse fonctionnelle des LBC serait primordiale puisque le développement de l'ischémie y est plus complexe que celui des lésions isolées dû à la présence des interactions hémodynamiques. Une norme de référence étalon appelée Fraction de Flux de Réserve (FFR, mesure de la réserve coronaire) a été développée à partir du degré de sévérité de l'ischémie pour définir le besoin d'une intervention de revascularisation. Cependant, au niveau mondial, moins de 10 pourcents des laboratoires de cathétérisme cardiaque utilisent cette méthode [14-16] et les cardiologues continuent à se fier à l'angiographie. Or, cette dernière a d'ores et déjà présenté de faibles corrélations avec les états hémodynamiques des patients [17]. C'est pourquoi une compréhension de la fonctionnalité des LBC par rapport à la FFR est importante, et permettrait d'améliorer les diagnostics des patients (avec l'angiographie), réduisant ainsi les risques associés aux traitements.

Pour conclure, l'objectif principal du projet de doctorat vise à mieux comprendre la fonctionnalité des LBC. Un modèle numérique de bifurcation coronaire athérosclérotique, permettant de calculer la FFR, a été développé. Il a ensuite été utilisé pour quantifier et comparer de façon systématique l'effet de divers paramètres géométriques sur l'état hémodynamique. Plus spécifiquement, le degré de sévérité des lésions, leurs configurations, l'excentricité de la lumière et l'angle de bifurcation, ont été étudiés. D'après les simulations numériques, les signes cliniques de la maladie seraient dépendants des interactions hémodynamiques locales et globales. En particulier, les résultats ont démontré que le nombre de lésions présentes n'affecte pas la fonctionnalité d'une configuration de LBC et que les caractéristiques de la lésion principale (dans le vaisseau mère) jouent un rôle central dans l'apparition des symptômes cliniques. Ainsi, malgré les limitations, les résultats ont potentiellement des implications cliniques importantes pouvant aider, après validation, à améliorer le diagnostic des patients.

ACKNOWLEDGEMENTS

Firstly, I would like to acknowledge the advice, guidance and financial support of my supervisors, Prof. Rosaire Mongrain and Dr. Jean-Claude Tardif. Your generous support allowed me to devote my energy into this work, and share it with the scientific community. Prof. Mongrain, your confidence in me gave me the freedom to be independent, which was paramount in shaping me into the researcher I am today. Dr. Tardif, your insight helped give clinical relevance and significance to the research. I would also like to acknowledge the invaluable input of Dr. Philippe L. L'Allier and Prof. Richard Leask.

I would like to thank, from the bottom of my heart, my family, who lived, breathed and sweated my years as a PhD student alongside of me. Your undying support, in all its shapes and forms, and unfading patience are what made this work possible. I would like to express my deepest gratitude to my parents, Spiros and Roula, who have always believed in me and encouraged me to be my best. You are the backbone to my success. I am eternally grateful to my sister, Christina, who has not only been my mentor and my support system over the years, but more importantly my best friend and my other half. Your generosity, compassion and balance are what got me through the ups and downs of my PhD. You are my everything.

I am eternally indebted to my labmate and partner in crime, Jennifer Frattolin, without whom I both physically and emotionally could not have completed this work. Cheers to your steadfast encouragement and our endless hours of discussion, stimulating collaboration and best of all, our waiting games. Finally, I would like to express my most sincere gratitude to my cousins, the Xanthopoulos family, who welcomed me with open arms into their lives, made me laugh until I cried, and helped me find my home away from home.

CONTRIBUTIONS OF AUTHOR

REFEREED JOURNAL PUBLICATIONS

Pagiatakis C, Tardif JC, L'Allier PL, Mongrain R (2016). Effect of stenosis eccentricity on the functionality of coronary bifurcation lesions – a numerical study. *[Submitted to: Medical and Biological Engineering and Computing]*

Pagiatakis C, Tardif JC, L'Allier PL, Mongrain R (2015). A numerical investigation of the functionality of coronary bifurcation lesions with respect to lesion configuration and stenosis severity. *Journal of Biomechanics,* 48(12):3103-3111. DOI: 10.1016/j.jbiomech.2015.07.018

Pagiatakis C, Galaz R, Tardif JC, Mongrain R (2015). A comparison between the principal stress direction and collagen fiber orientation in coronary atherosclerotic plaque fibrous caps. *Medical & Biological Engineering & Computing,* 53(6): 546-555. DOI: 10.1007/s11517-015-1257-z

Frattolin J, Zarandi MM, **Pagiatakis C**, Bertrand OF, Mongrain R (2015). Numerical study of stenotic side branch hemodynamics in true bifurcation lesions. *Computers in Biology and Medicine*. 57:130-138. DOI: 10.1016/j.compbiomed.2014.11.014

Galaz, R., **Pagiatakis, C.,** Gaillard, E., & Mongrain, R. (2013). A parameterized analysis of the mechanical stress for coronary plaque fibrous caps. *Journal of Biomedical Science and Engineering*, 6(12): 38-46. DOI: 10.4236/jbise.2013.612A006

REFEREED CONFERENCE PROCEEDINGS AND ABSTRACTS

Pagiatakis C, Tardif JC, L'Allier PL, Mongrain R. (2016). Bifurcation angle and Fractional Flow Reserve: a multiscale numerical study of coronary bifurcation lesions. *Summer Biomechanics, Bioengineering, and Biotransport Conference 2016 (SB3C2016).* June 29 - July 2, 2016, National Harbor, Maryland, USA.

Pagiatakis C, Tardif JC, L'Allier PL, Mongrain R. (2016). A numerical geometric multiscale evaluation of the localized haemodynamic interactions within coronary bifurcation lesions. *European Congress on Computational Methods in Applied Sciences and Engineering (ECCOMAS).* June 5-10, 2016, Crete, Greece.

Pagiatakis C, Tardif JC, L'Allier PL, Mongrain R. (2015). Stenosis eccentricity has a significant effect on coronary bifurcation lesion functionality. *21st Annual Congress of the European Society of Biomechanics (ESB2015).* July 5-8, 2015, Prague, Czech Republic.

Pagiatakis C, Tardif JC, L'Allier PL, Frattolin J, Mongrain, R. (2015). The number of lesions does not govern the functionality of coronary bifurcation lesions: a study of the effect of relative stenosis severity. *Summer Biomechanics, Bioengineering, and Biotransport Conference 2015 (SB3C2015).* June 17-21, 2015, Snowbird, Utah, USA.

Pagiatakis C, Tardif JC, Mongrain R. (2014). Effect of bifurcation angle on the functional impact of coronary bifurcation lesions. *14th Annual Congress of the Quebec Society of Vascular Sciences.* November 21, 2014, Montreal, Quebec, Canada

Pagiatakis C, Tardif JC, Mongrain R. (2014) Effect of bifurcation angle on the functional impact of coronary bifurcation lesions. *7th World Congress of Biomechanics.* July 6-11, 2014, Boston, Massachusetts, USA.

Pagiatakis C, Mongrain R. (2014). Geometric multiscale modelling for the functional characterization of coronary bifurcation lesions. *11th World Congress on Computational Mechanics (WCCM XI) -5th European Conference on Computational Mechanics (ECCM V) – 6th European Conference on Computational Fluid Dynamics (ECFD VI).* July 20-25, 2014, Barcelona, Spain.

Pitts KL, **Pagiatakis C**, Fenech M. (2011). Comparison of two methods applying cross-correlation for blood microflow velocity profile measurements. *The Canadian Society of Rheology Workshop on Rheology: Current Topics and Trends in Rheology*. June 6-7, 2011, Montreal, Quebec.

TABLE OF CONTENTS

LIST OF FIGURES

LIST OF TABLES

1

INTRODUCTION

Cardiovascular disease remains the leading cause of death globally and in the developed world [1-3]. In 2010, the Global Burden of Diseases, Injuries, and Risk Factors Study estimated that cardiovascular disease was responsible for the highest percentage, approximately 29.6, of all deaths globally. Ischemic heart disease, or in other words, coronary artery disease, constituted the highest proportion, estimated at 45 percent, of all cardiovascular-related deaths [3]. Similar trends were observed in data from 1990. In the 2012 World Health Organization's release of the 10 leading causes of death, coronary artery disease was ranked as the preeminent cause [18]. Consequently, coronary artery disease, including its initiation, progression, diagnosis and treatment remains an important field of study.

In this chapter, the motivation behind the work of the thesis is presented. A brief overview of the clinical background pertaining to coronary artery disease and coronary bifurcation lesions (CBLs), which constitute the main focus of the research, are provided. Moreover, the main shortcomings of the current state of the art with regard to the numerical modelling of coronary bifurcation lesions are outlined. The objectives of the thesis are detailed based on the clinical motivation and the limitations in the literature.

1.1 RATIONALE

1.1.1 Clinical background

The role of the coronary system is to maintain a viable myocardium by delivering oxygenated blood and nutrients to the heart muscle under varying metabolic demands [19]. Coronary artery disease is associated with atherosclerosis and is characterized by the thickening and the hardening of the vascular wall. It commonly manifests itself by the gradual growth of plaques (also referred to as stenoses or lesions), which extend into and ultimately narrow the arterial lumen [20]. Coronary plaques that protrude into the vessel lumen induce a pressure drop which results in a decrease in the blood supplied to the myocardium. When the supply of blood to a myocardial domain decreases to a level where the metabolic requirements (oxygen and/or nutrients) of the heart muscle are not fulfilled, ischemia is induced [21], which manifests itself in the form of angina.

The onset of ischemia, in the context of coronary stenoses, is influenced by various factors including stenosis resistance (which is related to both the morphology of and the flow rate through the stenosis), lesion location, the size and the dynamics of the distal myocardial bed being perfused and the extent of collateral circulation (which provides an alternative route for blood to perfuse an ischemic myocardial domain) [22-25]. Consequently, clinical studies have shown that there is a poor correlation between the angiographic significance (diameter reduction) and the symptomatic manifestation of the disease [17, 26-28] thus, rendering visualization methods inadequate to guide cardiologists in the decision for coronary revascularization [26-28].

The fractional flow reserve (FFR), a dimensionless diagnostic index that quantifies the percent of healthy hyperaemic myocardial blood flow that is preserved when the supplying artery is diseased, is a measure of the haemodynamic (functional) impact of a coronary stenosis and therefore, its likelihood to induce and be responsible for myocardial ischemia [23, 24, 29-31]. Clinical studies have shown that FFR values between 0.75 and 0.8, measured in clinic as the ratio of the distal stenosis pressure to the aortic pressure, correspond to the threshold for the onset of ischemia. By using FFR to assess the functional impact of coronary lesions, interventions can be safely deferred for functionally nonsignificant but angiographically significant lesions [14, 26, 31-33]. Nevertheless,

despite the designation of FFR as the gold-standard clinical diagnostic index for the identification of functionally significant coronary lesions, it is utilized in less than 10 percent of catheterization labs worldwide. As such, cardiologists still rely heavily on an angiographic evaluation.

The scientific community has accepted that the development of atherosclerotic lesions is preferentially localized in vascular sites where the wall shear stress (WSS) is low and oscillatory such as, in regions of curvature, tortuosity and bifurcations [34-38]. In fact, up to 20 percent of all percutaneous coronary interventions (PCIs) involve the treatment of stenoses in the vicinity of a vessel bifurcation. The treatment of said stenoses, referred to as coronary bifurcation lesions (CBLs), is associated with higher rates of peri- and post-procedural clinical events (major cardiac events), target-lesion revascularization, restenosis and thrombosis as compared to non-bifurcation lesions [4, 5, 7, 9-13]. There is still much uncertainty and debate with regard to the optimal interventional technique [7] as well as the assessment of bifurcation lesion severity [8], which renders bifurcation lesions, to this day, a major limitation of interventional cardiology.

1.1.2 Limitations of the current state of the art

To date, only a few studies have used numerical methods to investigate the dynamics of CBLs [39-48]. Moreover, these studies put emphasis on the notion of disease progression rather than physiologic impact and evaluated velocity profiles and WSS distributions in different bifurcation lesion configurations with both idealized and patient-specific coronary geometries [39-44, 47, 48].

The results of the existing studies on coronary bifurcation lesions have demonstrated important haemodynamic differences between the various CBL configurations, which were dependent on both the number and location of stenoses within the flow divider. Certain arrangements were also found to be at higher risk for disease progression. In other studies [45, 46], the ratio of the flow in the side branch to the flow in the proximal main branch was computed at mild and severe constrictions within different CBL arrangements. The results showed that as the severity of the stenoses increased,

the decrease in the corresponding flow ratio was non-uniform between the different configurations.

The results of these works have suggested the intricate relationship between the severity of lesions, the arrangement of plaques within the bifurcation, and the haemodynamics of the corresponding vasculature. They emphasize the inadequacy of anatomy alone to guide and substantiate the decision for clinical intervention. Overall, although indicative of the presence of complicated haemodynamic interactions within CBLs, due to the use of conventional boundary conditions (prescribed inlet healthy flow rates and either zero-pressure outlets or flow-splits between the outlet vessels) for the execution of the CFD simulations, the dynamics of the distal myocardium were inherently disregarded. As such, CBL functionality could not be assessed. While an understanding of the prognostic attributes of this type of disease is important, there is a lack of knowledge regarding the clinical manifestation and severity of CBLs based on clinically-relevant indices. This information is necessary in order to improve diagnostic strategies and thus, reduce the risks associated with their treatment.

Furthermore, the resistance of a stenosis is dependent on the transtenotic flow, which signifies that the application of a predefined healthy flow rate, as was executed in the aforementioned studies, does not allow for the true stenosis resistance to be expressed and therefore, the true effect of the lesions on the perfusion of the myocardium to be elucidated. This idea is amplified when the outlet boundary conditions constitute a prescribed constant flow distribution between the two daughter vessels since the differences in epicardial resistance, as is influenced by the different lesion arrangements, are not taken into account. This shortcoming limits the ability of the studies to provide clinical insight into the dynamics of CBLs since the imposed flow conditions are not representative of the true *in vivo* haemodynamic environment.

In addition, the studies that have been executed to date have not attempted a systematic, thorough and comprehensive investigation of the effect of various geometric and morphological parameters of the stenoses and of the arterial bifurcation, on CBL dynamics and the corresponding haemodynamic interactions. Due to the dependence of

cardiologists on an angiographic evaluation of the severity of coronary lesions, such investigations are essential so as to identify potential independent predictors of a critical haemodynamic environment and thus, improve diagnostic procedures.

1.1.3 Summary

The fractional flow reserve, the gold-standard diagnostic index for the identification of functionally significant coronary lesions, is being utilized in less than 10 percent of catheterization labs worldwide. As such, cardiologists still rely heavily on an angiographic evaluation, which has been shown to have a poor correlation with haemodynamic impact. The treatment of coronary bifurcation lesions is associated with higher rates of peri- and post-procedural clinical events compared to that of isolated lesions. Overall, their haemodynamics and clinical manifestation are still not well understood. To date, to the best of the author's knowledge, there has not been any attempt to evaluate the dynamics of coronary bifurcation lesions from a functional perspective, utilizing clinically-relevant diagnostic indices. Furthermore, there has not been a systematic effort to investigate and identify geometric and morphological parameters of the stenoses and of the arterial geometry that could affect the haemodynamic severity and therefore the clinical manifestation of the disease.

1.2 HYPOTHESIS AND OBJECTIVES

The hypothesis of the research is that haemodynamic interactions, both at the local level and at the global level play a significant role in the functionality of coronary bifurcation lesions and therefore in their clinical manifestation and diagnosis.

The central objective of the thesis is to provide insight into and an understanding of the haemodynamic impact of coronary bifurcation lesions from a clinically-relevant perspective. Such an understanding could help improve diagnostic procedures and therefore reduce the risk associated with their treatment. Thus, the specific objectives of this research are to:

- develop a model of a diseased coronary bifurcation that inherently takes into account both local and global haemodynamic interactions, provides a functional

perspective on its dynamics and allows for the calculation of clinical diagnostic indices.

- investigate the effect of various geometric and morphological parameters of the stenoses and of the arterial bifurcation on the functional impact of coronary bifurcation lesions so as to identify parameters which could be independent predictors of haemodynamic criticality. These parameters include: configuration, stenosis severity, luminal eccentricity and bifurcation angle.

1.3 OUTLINE OF THE THESIS

In Chapter 2, the clinical background associated with the function and dynamics of the cardiovascular system and the development, manifestation and dynamics of coronary artery disease are presented. Chapter 3 provides an overview of cardiovascular computational fluid dynamics and an introduction of geometric multiscale modelling, which is utilized in the thesis to fulfill the objectives of the research. A detailed literature review and the associated limitations regarding coronary bifurcation lesions are also provided in Chapter 3.

In Chapter 4, Chapter 5 and Chapter 6, the development of the geometric multiscale model of the left main coronary artery bifurcation (LMCA), to be utilized in what is to the best of the author's knowledge, the first study of the functionality of coronary bifurcation lesions, is sequentially detailed so as to fulfill the first objective of the thesis. Specifically, Chapter 4 presents the development and numerical implementation of the lumped-parameter model (0D model) of the cardiovascular domains surrounding the 3D model of the LMCA bifurcation (presented in Chapter 5). The implementation of the coupling between the lumped-parameter representation of the cardiovascular system and the 3D model of the LMCA bifurcation is provided in Chapter 6, along with the results of the multiscale CFD simulations of the healthy and of a diseased bifurcation. These initial simulations show the ability of the developed model to provide physiologically-relevant dynamics within the coronary bifurcation lesions.

In the subsequent chapters, the second objective of the thesis is fulfilled. Specifically, studies of the effect of various geometric parameters on the functionality of coronary bifurcation lesions are presented. Chapter 7 investigates the effect of the lesion configuration on the flow-derived and pressure-derived FFR with varying stenosis severity while Chapter 8 studies the effect of relative stenosis severity on the functionality of CBLs. Overall, these two chapters investigate the effect of global haemodynamic parameters on the corresponding clinical manifestation of the disease. In Chapter 9 and Chapter 10, localized haemodynamic effects on CBL functionality are studied. Specifically, the effect of luminal eccentricity on the daughter vessel FFR is presented in Chapter 9, while in Chapter 10, differences in FFR are compared between multilesional configurations with varying bifurcation angle.

Finally, the last chapter summarizes the results of the geometric multiscale CFD simulations presented in the thesis. Emphasis is put on the novel contributions of the research and the main findings and corresponding clinical implications of the results. In addition, the chapter overviews the limitations and corresponding future endeavours associated with the work.

2

CLINICAL BACKGROUND

This chapter presents the clinical background that is pertinent to the thesis. Specifically, the function and dynamics of the cardiovascular system are detailed. Emphasis is put on the coronary arterial system, which constitutes the cardiovascular domain of interest in the thesis. In addition, clinical background regarding the development, manifestation and dynamics of coronary artery disease is presented. Details are provided for coronary bifurcation lesions, which constitute the central focus of the research.

2.1 THE CARDIOVASCULAR SYSTEM

The role of the cardiovascular system is to deliver oxygenated blood, along with other nutrients, to each cell of the body as well as eliminate waste produced by cells. As is displayed in Figure 2.1a, the cardiovascular system is comprised of three main components namely, the heart, the systemic circulation (lower and upper body) and the pulmonic circulation (lungs).

The heart, shown in Figure 2.1b, is a pump comprised of two parallel systems, specifically the high-pressure left heart and the low-pressure right heart. Each compartment is further subdivided into two additional chambers namely, the atrium and

the ventricle. The outlets of the left atrium, left ventricle, right atrium and right ventricle are protected by valves, specifically the mitral, aortic, tricuspid and pulmonary valves respectively, which prevent backflow of blood into the corresponding compartment during specific phases in the cardiac cycle. The heart is the most important element of the cardiovascular system as it is responsible for circulating blood, and therefore oxygen and nutrients to the body.

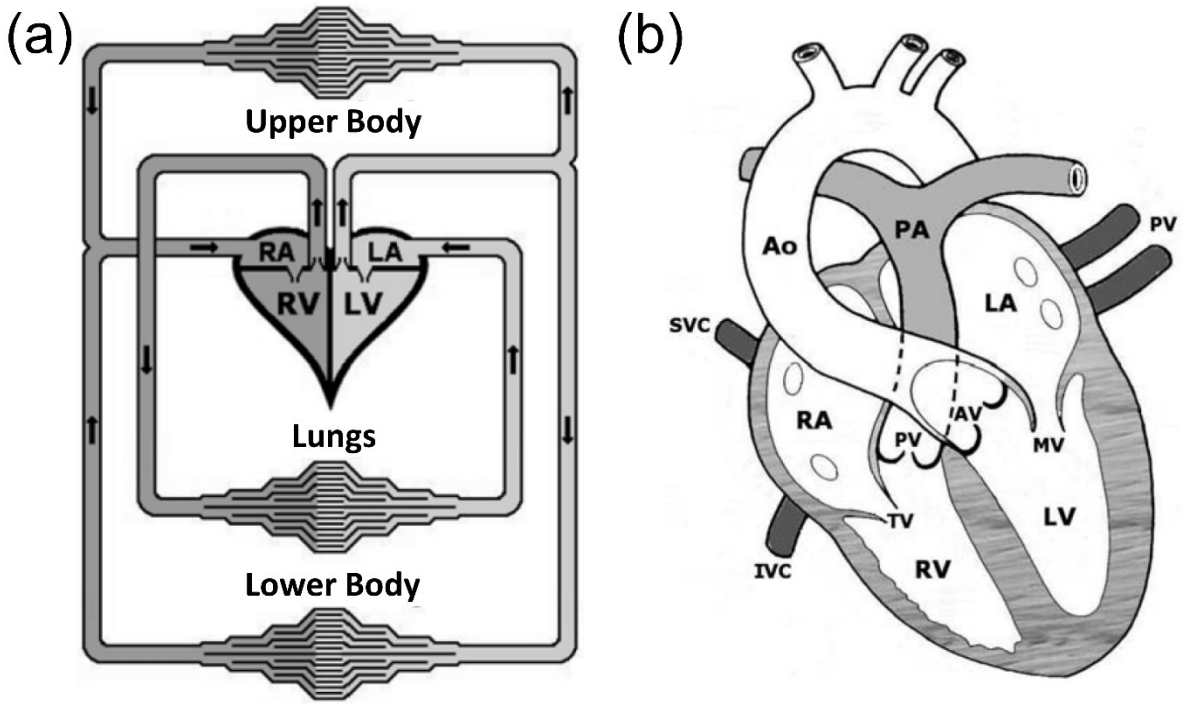

Figure 2.1: Schematic of (a) the circulatory system (with permission from [49]); RA right atrium, RV right ventricle, LA left atrium, LV left ventricle and (b) cardiac anatomy (with permission from [49]): SVC superior vena cava, IVC inferior vena cava, Ao aorta, PA pulmonary artery, PV pulmonary vein, MV mitral valve, AV aortic valve, TV tricuspid valve, PV pulmonary valve.

Figure 2.2 presents a sketch of the main events during the cardiac cycle (adapted from [49]), which can be divided into two distinct phases, specifically, systole and diastole. Systole corresponds to the portion of the cardiac cycle where the ventricles contract and oxygenated blood is delivered to the systemic circulation while deoxygenated blood is delivered to the pulmonic circulation.

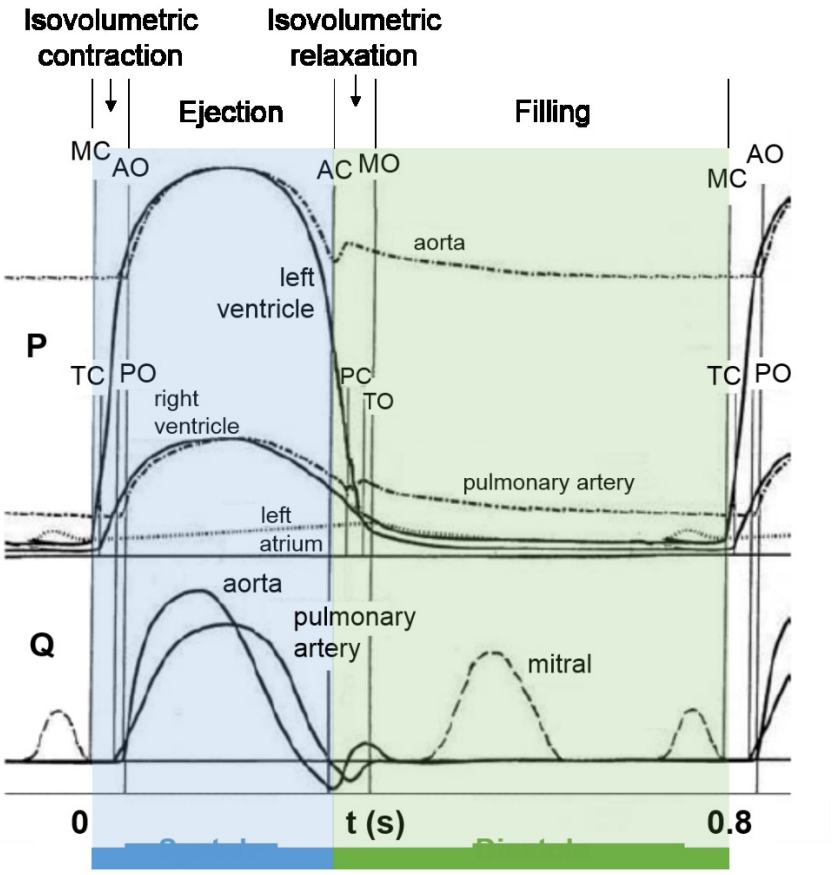

Figure 2.2: Cardiac cycle (adapted with permission from [49]). The blue and green portions denote systole and diastole respectively. P pressure, Q volumetric flow rate; M mitral valve, A aortic valve, T tricuspid valve, P pulmonary, C close, O open.

It begins at the closure of the mitral and tricuspid valves and is followed by the isovolumetric contraction of the ventricles. During this time blood also flows into the left and right atria from the pulmonary veins and the vena cava respectively. Once left ventricular pressure surpasses aortic pressure and right ventricular pressure surpasses the pressure in the pulmonary artery, the aortic and pulmonary valves open, correspondingly. In the systemic circulation, oxygenated blood is ejected to the aortic sinus and the aorta, and is delivered to the rest of the body whereas, in the pulmonic circulation, deoxygenated blood flows into the pulmonary artery and subsequently to the lungs. The ejection of blood into either circulatory system is followed by a decrease in ventricular pressure and ultimately the closure of the corresponding valve (aortic or pulmonary). This valve closure denotes the start of diastole and therefore, the isovolumetric relaxation of the ventricles. When the mitral and tricuspid valves open,

ventricular isovolumetric relaxation ceases and both the left and right ventricles fill with oxygenated and deoxygenated blood from the atria, respectively. Blood flow from the atria to the ventricles occurs both passively due to the pressure differential between the two compartments and actively, due to atrial contraction. The end of ventricular filling corresponds to the end of the cardiac cycle. Figure 2.2 displays the left and right ventricular pressures and the aortic and pulmonary artery flows and pressures during the various phases of the cardiac cycle.

2.2 THE CORONARY ARTERIAL SYSTEM

During the ejection portion of the systolic phase of the cardiac cycle, oxygenated blood flows from the left ventricle to the aortic sinus and aorta and subsequently, to all tissues and organs. The high-pressure portion of the systemic circulation consists of a hierarchy of vessels that originate from the aorta and bifurcate over many generations to arteries, arterioles and capillaries, wherein tissue and organ perfusion occurs. Figure 2.3a provides a general overview of the systemic distribution of blood to the main systems of the body.

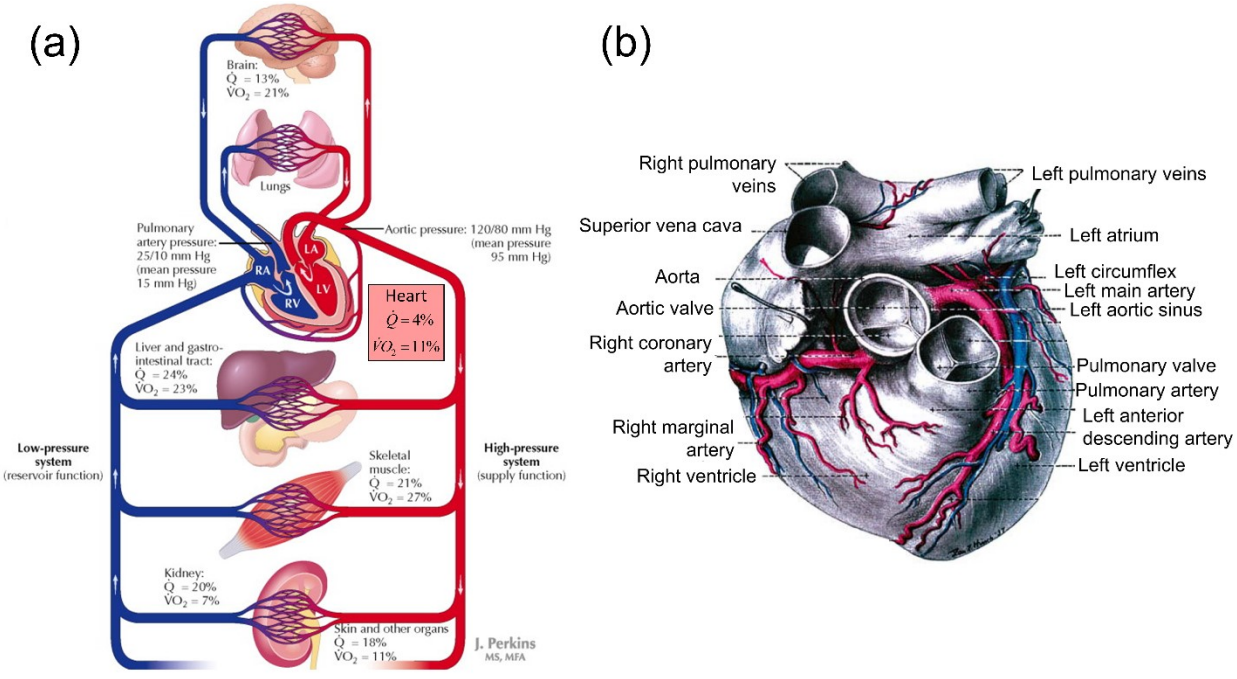

Figure 2.3: Schematic of (a) the cardiac output (adapted from [50]) during resting state and (b) the left and right coronary arterial circulations (adapted with permission from [51]). $\dot{Q}$ is the flow and VO_2 is oxygen consumption.

In Figure 2.3a, one can observe that approximately four percent of the cardiac output, referred to as the coronary circulation, is allocated to the perfusion of the myocardium and therefore the fulfillment of the metabolic needs of the heart muscle. Figure 2.3b presents a schematic of the coronary circulation, for which more detail is provided in the subsequent sections.

2.2.1 Anatomy of the coronary arterial system

The coronary arterial system comprises two hierarchical branching structures of highly tortuous, curved and tapering vessels that originate from the aortic root at the left and right sinuses of Valsalva, encircle the heart at the boundaries of the six myocardial lobes, and embed themselves within the heart tissue. More specifically, the left main and right coronary arteries originate respectively from the left and right sinuses of Valsalva and encircle the left and right sides of the heart at the interface between the atria and the ventricles (Figure 2.4a).

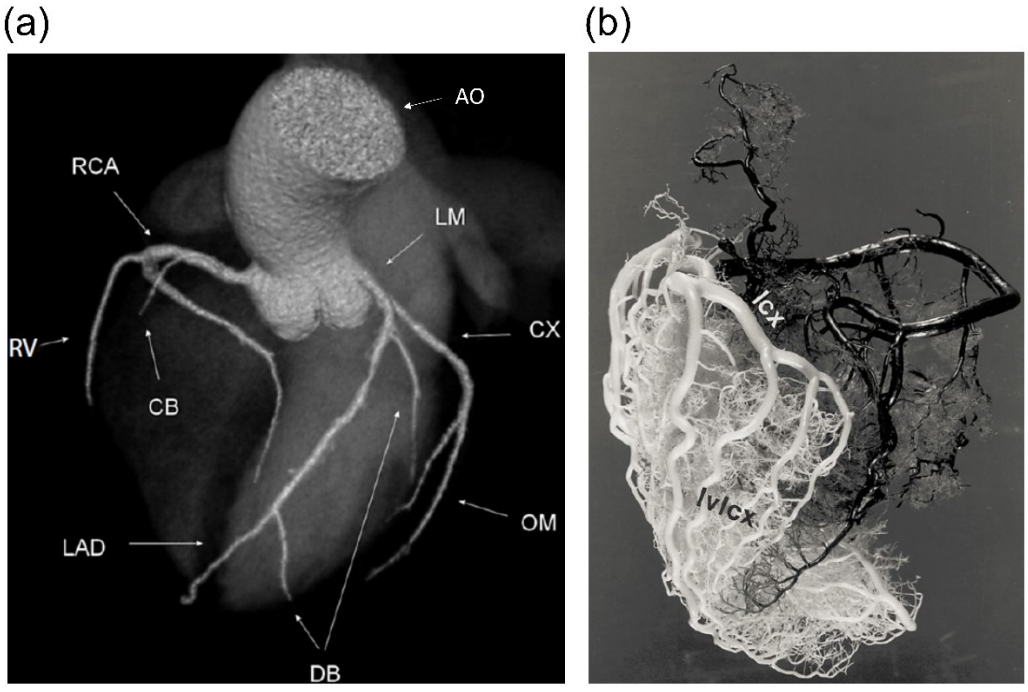

Figure 2.4: (a) Epicardial coronary anatomy as obtained from 3D Computed Tomography (adapted with permission from [52]). AO aorta, LM left main coronary artery, CX left circumflex artery, OM obtuse marginal branch, LAD left anterior descending artery, DB diagonal branch, RCA right coronary artery, RV right ventricular branch, CB conus branch. (b) Cast of the human coronary circulation; the left circulation is displayed in white and the right circulation in black (adapted with permission from [19]).

The left main coronary artery (LMCA) bifurcates into the left anterior descending artery (LAD) and the left circumflex artery (LCX), which supply the interventricular septum and the left atrium and ventricle respectively. The main branches of the LAD are the septal and diagonal branches, while those of the LCX constitute the obtuse marginal branches. The right coronary artery supplies the right atrium and ventricle and eventually gives rise, in the majority of patients, to the posterior descending artery which supplies the interventricular septum and part of the left ventricle [19]. These aforementioned vessels are generally found at the surface of the heart and are referred to as the epicardial coronary arteries. They are considered conducting vessels as they contribute only approximately five percent to the total coronary arterial resistance and are not responsible for myocardial perfusion [53]. In Figure 2.4b, one can observe that the branches of the epicardial arteries bifurcate for many generations from arteries, to arterioles and as far as the capillary level (wherein myocardial perfusion occurs). These vessels, denoted as endocardial arterial conduits, embed themselves into the myocardial tissue for perfusion and constitute the remaining approximate 95 percent of the coronary arterial resistance [53, 54].

2.2.2 Function and dynamics of the coronary arterial system

The coronary system maintains a viable myocardium by delivering oxygenated blood and nutrients to the heart muscle under varying metabolic demands. Similarly to other transport systems in the body and in nature, the coronary tree has a fractal structure associated with an optimal design based on fluid dynamic principles, and therefore ensures the efficient distribution of blood to the myocardium. Vascular morphology and biochemical (vasodilatory/vasoconstrictor) stimuli from neurohormonal and metabolic signals work in conjunction to endothelial contributions to fulfill perfusion requirements [19, 53, 55].

The magnitude of coronary blood flow has been associated with the ratio of oxygen supply to oxygen demand within the myocardium. More specifically, changes in this ratio with respect to the baseline (rest state) initiates a series of biochemical processes that target the myocardial capillary network so as to regulate coronary blood flow and thus, fulfill the metabolic demands of the heart muscle. For example, a decrease in this ratio

results in the release of vasodilators which increase the caliber of the capillaries, decrease their resistance and therefore, increase the corresponding blood flow.

The relationship between the coronary blood flow and perfusion pressure under different metabolic rates is displayed in Figure 2.5a. The effective coronary perfusion pressure is defined as the pressure gradient across the vascular bed. More specifically, in healthy coronary vessels, it is equal to the pressure difference between the diastolic aortic pressure and the left ventricular end-diastolic pressure [56]. In Figure 2.5a, one can observe that for an increased metabolic rate, the coronary blood flow is also increased.

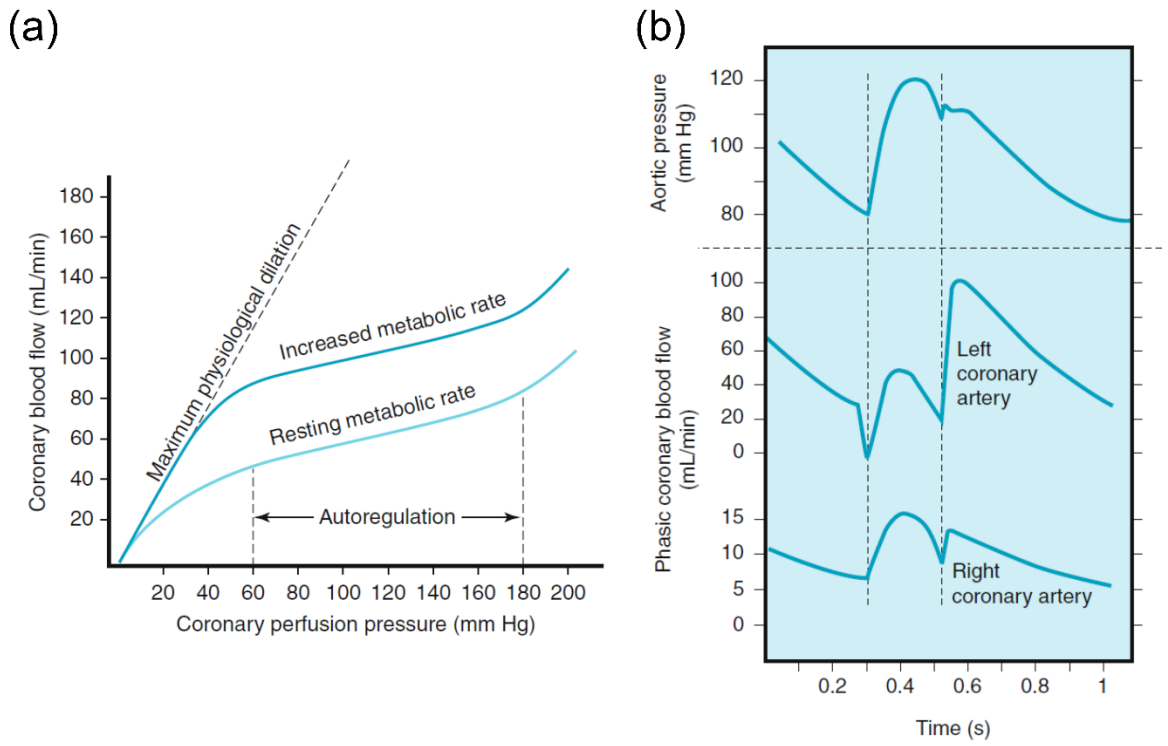

Figure 2.5: Schematics of (a) the autoregulation of coronary blood flow based on perfusion pressure and (b) the physiological, resting aortic pressure and phasic left and right coronary blood flow, in healthy coronary conduits (with permission from [57]).

Furthermore, Figure 2.5 displays other important features of coronary dynamics. Firstly, during maximum physiological dilation, as is represented by the dashed line in the schematic, there exists a linear relationship (assuming laminar flow) between the perfusion pressure and the coronary blood flow which signifies that a change in perfusion pressure corresponds to a direct change in coronary blood flow.

Conversely, the curves for the resting and increased metabolic rate, where the myocardial capillaries are not fully dilated, display a nonlinear relationship between the coronary blood flow and the perfusion pressure. Specifically, over a relatively wide range of perfusion pressures, as is displayed in the figure between 60 and 180mmHg for the resting metabolic rate, the corresponding coronary blood flow does not increase significantly with increasing perfusion pressure. This behaviour denotes the phenomenon of autoregulation, which corresponds to the capacity of the coronary arteries to maintain a relatively constant coronary blood flow with changing coronary perfusion pressure, for constant metabolic demands. The autoregulation phenomenon results from myocardial capillary vasodilation and is important in the development, progression and clinical manifestation of coronary artery disease [57].

Figure 2.5b displays a schematic of the physiological resting aortic pressure, and left and right coronary artery flows. One can observe that the phasic average flow rate within the left and right coronary arteries show markedly different behaviour. More specifically, within the left coronary artery, relative to the aortic pressure curve, the peak flow occurs at the onset of the diastolic phase. In fact, the bulk of the flow within the left coronary circulation occurs over the duration of diastole whereas, in the right coronary circulation, the majority of the flow occurs during ventricular systole. The behaviour displayed within the left coronary circulation is referred to as the phenomenon of predominantly diastolic flow. This phenomenon occurs due to the systolic contraction of the left ventricle which results in the extravascular compression of the endocardial arteries and ultimately, the inhibition of left coronary flow during this portion of the cardiac cycle. When the left ventricle relaxes during diastole and the intramyocardial pressure ceases to act on the endocardial vessels, blood is enabled to flow to the microvessels for perfusion. Conversely, due to the significantly lower pressure associated with the pulmonic circulation and the consequent lesser muscle tone of the right ventricle in comparison to the left ventricle, the endocardial vessels perfusing the right ventricle do not experience significant extravascular compression during systole. Thus, right coronary artery blood flow is not inhibited during this time. Furthermore, one can observe from Figure 2.5b that the magnitude of the coronary flow is greater within the left coronary

circulation than the right coronary circulation. This observation results from the fact that the right heart experiences reduced oxygen consumption due to the smaller myocardial mass, in comparison with the left side [53].

2.3 CORONARY ARTERY DISEASE

2.3.1 Development and manifestation of coronary artery disease

Coronary artery disease is the leading cause of death worldwide, accounting for 13 percent of all deaths [18]. It is associated with atherosclerosis, which constitutes a disease characterized by the accumulation of lipids within the intimal layer of the vasculature and ultimately the thickening and the hardening of the vascular wall. Figure 2.6 displays a schematic of the various stages in the progression of an atherosclerotic plaque.

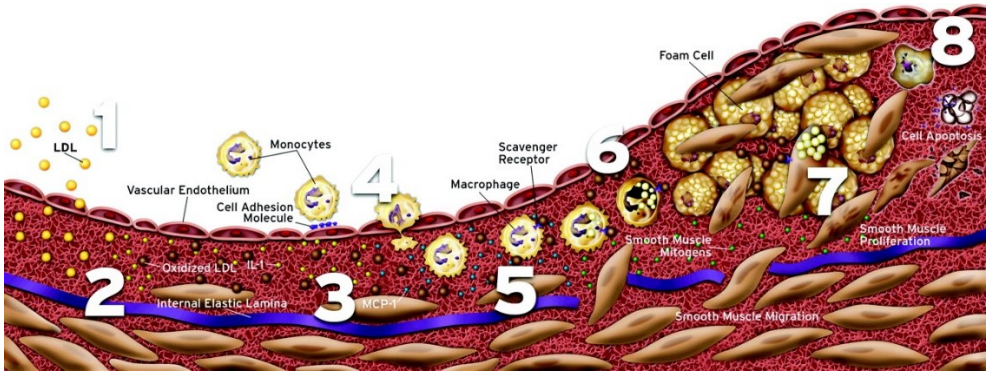

Figure 2.6: Schematic of the initiation and progression of an atherosclerotic plaque (with permission from [58]).

The process is initiated by the permeation of lipids, most commonly low-density lipoprotein, through the endothelial cell layer and their deposition within the intimal layer. The endothelia compose a monolayer of cells which line the lumen of all vasculature and are responsible for maintaining vascular wall homeostasis. The dysfunction of this layer permits this initial transmigration of lipids which subsequently initiates an inflammatory response wherein monocytes also permeate the intimal layer, progressively differentiate into macrophages and form foam cells. The further progression of the plaque is characterized by the recruitment of smooth muscle cells from the medial layer and their subsequent differentiation and conversion to foam cells [59-62].

Mature atherosclerotic plaques are generally composed of a lipid core which is separated from the lumen by a collagen-based fibrous cap. The relative proportion of the two constituents determines the type of lesion, namely stable or unstable plaque. Unstable (vulnerable) plaques, which are not always lumen-occluding, are generally characterized by thin fibrous caps and large and soft lipidic cores. These types of plaques have been associated with higher risk of rupture, which exposes the highly thrombogenic plaque core to the blood and initiates the formation of a lumen-occluding thrombus. The rupture of a vulnerable plaque has been connected to unstable angina pectoris (colloquially referred to as chest pain) and acute myocardial syndromes. Conversely, stable plaques tend to have a higher proportion of fibrotic tissue (smaller lipid cores) and thicker fibrous caps, which allows them to progress to vessel occlusion. This type of plaque has been most commonly associated with stable angina pectoris as a result of chronic myocardial ischemia. Myocardial ischemia denotes the state wherein the myocardial blood supply does not fulfill the metabolic requirements (oxygen and/or nutrients) of the heart muscle [21]. Stable plaques can also ultimately cause total occlusion of the vessel, which results in myocardial infarction [63-71]. Since the focus of the current thesis lies in stable coronary plaques, further use of the terms plaques, lesions and stenoses refers to the stable disease.

The development of atherosclerotic lesions has been accepted to be localized in vascular sites where the local haemodynamics are complex, such as in regions of curvature, tortuosity and vessel bifurcation. More specifically, early observations determined that atherosclerotic plaques were focalized in regions characterized by low and oscillatory shear stress [34-38]. To this date, the association of atherosclerosis with these particular flow characteristics remains the dominant school of thought. Numerical studies are ongoing regarding the determination of factors (such as geometric parameters) and flow conditions that predispose patients to the development and progression of atherosclerosis based on this theory [72-79]. There exists an abundance of literature that demonstrates the role of fluid dynamics in the initiation, development and progression of atherosclerosis in vascular regions characterized by complex geometry.

2.3.2 Isolated lesions

Due to the fact that stable coronary plaques are composed of a high proportion of fibrotic tissue, their progression and intrusion into the vessel lumen is understandable. From a clinical perspective, these types of stenoses are most commonly associated with the development of myocardial ischemia.

2.3.2.a Stenosis resistance

Healthy epicardial coronary arteries induce a negligible pressure drop along their length. Therefore, under healthy conditions, the myocardial blood flow, which is dependent on the perfusion pressure, is driven by aortic pressure. Conversely, coronary plaques induce a pressure drop within the epicardial coronary system which results in a decrease in the effective perfusion pressure and thus, a decrease in the corresponding myocardial blood flow. The total transtenotic pressure gradient results from two energy dispersing sources, namely frictional and inertial losses. The frictional losses stem from viscosity-related energy dispersion at the entrance and along the throat of a lesion whereas, the inertial pressure losses are related to the expansion of the axially-oriented flow jet emerging from the lesion [80, 81]. Consequently, the theoretical translesional pressure drop, $\Delta P_{stenosis}$ [mmHg], can be expressed by the following equation [80]:

$$\Delta P_{stenosis} = V_L Q + I_L Q^2 \,, \tag{2.1}$$

where V_L is the viscous pressure loss coefficient [mmHg·s·ml^{-1}], I_L is the inertial pressure loss coefficient [mmHg·s^2·ml^{-6}] and Q is the volumetric flow rate [ml·s^{-1}]. The viscous pressure loss coefficient, V_L, is calculated by [80]:

$$V_L \cong f \frac{K_v \mu}{D_0 A_0} \,, \tag{2.2}$$

where μ is the blood dynamic viscosity [g·cm^{-1}·s^{-1}], D_0 is the healthy vessel diameter [cm], A_0 is the healthy vessel cross-sectional area [cm^2] and K_v is a dimensionless empirical coefficient based on the morphology of the stenosis. In the above equations, f is a factor that converts [cPa] to [mmHg], and is equal to 1333^{-1} mmHg·cPa^{-1}. The inertial pressure coefficient, I_L, is calculated by [80]:

$$I_L \cong f \frac{K_E \rho}{2A_0^2}\left[\frac{A_0}{A_S} - 1\right]^2 , \quad (2.3)$$

where ρ is the fluid density [g·cm^{-3}], K_E is a dimensionless empirical coefficient based on the morphology of the stenosis and A_S is the area of the stenosis throat [cm^2] [80-83].

From Equation (2.1), one can observe that the stenosis resistance, $R_{stenosis}$ [mmHg·s·ml^{-1}], defined as the ratio of the pressure drop to the flow rate, is expressed as follows:

$$R_{stenosis} = (V_L + I_L Q) . \quad (2.4)$$

Equation (2.4) has significant implications in the effect of an epicardial plaque on the perfusion pressure. More specifically, the Equation (2.4) shows that the resistance of a stenosis is dependent on the transtenotic flow rate. Therefore, the transtenotic pressure drop cannot be predicted unless the corresponding flow rate is known. Furthermore, this equation demonstrates that two stenoses with the same morphology can induce different resistances and thus, exhibit different translesional pressure drops if they are subjected to differing transtenotic flows. As will be outlined in subsequent sections, the flow-dependence of the stenosis resistance plays a significant role in the clinical manifestation of the disease, and is an important consideration in the current research.

2.3.2.b Clinical manifestation and diagnosis of coronary stenoses

For many decades, the severity of a lesion was evaluated based on its angiographic significance, or in other words, on its morphological severity (diameter reduction). Revascularization by PCI, specifically by balloon angioplasty and stent insertion, was executed for symptomatic patients with coronary plaques of diameter reductions greater than 50 percent. However, clinical studies demonstrated that there was a poor correlation between the angiographic significance and the manifestation of the disease, in particular for intermediate lesions with diameter reductions between 50 and 70 percent [17]. As such, alone, it was deemed inadequate to guide cardiologists in the decision for coronary revascularization [26-28]. More specifically, the severity of a stenosis requires a functional haemodynamic evaluation, which identifies its probability

to induce and be responsible for myocardial ischemia. Under resting conditions, the decrease in myocardial blood flow resulting from the decrease in perfusion pressure can be in part compensated for by autoregulation through the partial dilation of the myocardial capillaries thus, preventing ischemia. Symptomatic coronary artery disease presents itself when the autoregulation capacity of the myocardium is exhausted thus, eliminating its capability of further dilating to fulfill its metabolic needs.

For isolated lesions, the onset of ischemia is influenced by various factors including stenosis resistance (which is related to both the morphology of and the flow through the stenosis), lesion location, the size and the dynamics of the distal myocardial bed being perfused and the extent of collateral circulation [22-25]. Collateral circulation provides an alternative route for blood to perfuse an ischaemic myocardial domain. However, the presence and the extent of collateral coronary vessels are not completely understood and the prognostic contributions have been the topic of debate for many years. Contradicting studies on the prognostic advantages [84-89] and disadvantages [90] associated with the presence of functionally significant collateral conduits have been presented in the literature. Nevertheless, clinical studies have shown that of all patients with significant coronary artery disease, as quantified by the percent diameter stenosis, only approximately 30 percent have functionally significant collateral vessels that are capable of preventing ischemia [86, 91]. Interestingly, investigations have also shown that approximately 20 percent of healthy hearts have functionally significant collaterals that are recruited under brief coronary occlusion [92]. Nevertheless, in the presence of coronary artery disease, two prevalent factors have been associated with the development of physiologically significant collateral vessels, namely the severity of the disease (based on the percent occlusion of the stenosis) and the duration of time to which a patient is exposed to severe stenoses.

A schematic of an epicardial coronary artery supplying a myocardial domain in both healthy and diseased cases, under maximum vasodilation (induced hyperaemia) is displayed in Figure 2.7. As was presented in Figure 2.5a, when the resistance vessels are maximally dilated, coronary autoregulation is eliminated, and there is a linear relationship between the perfusion pressure and the corresponding myocardial blood

flow. Therefore, in the healthy case of Figure 2.7a, the normal myocardial flow required, under maximum hyperaemia, to fulfill the metabolic requirements of the specific domain is Q_n [ml·s^{-1}].

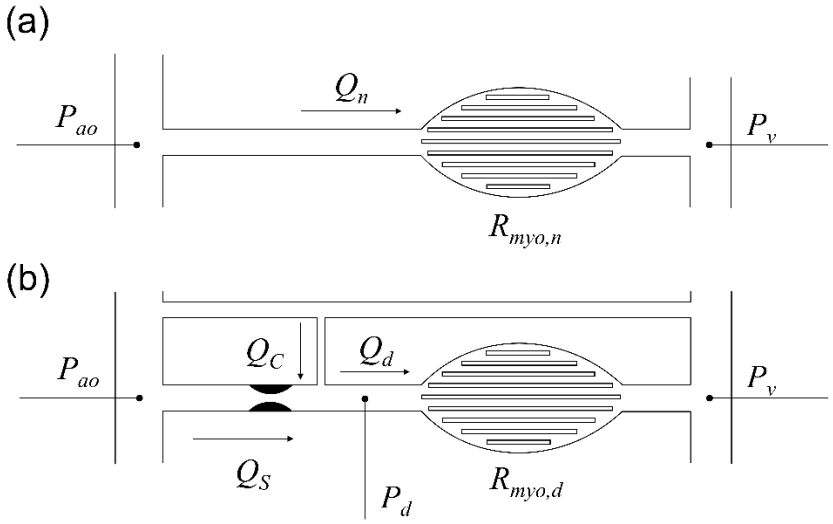

Figure 2.7: Schematic of (a) a healthy and (b) a diseased coronary artery at maximum hyperaemia. In the diseased case, a collateral conduit feeds the myocardium distal to the stenosis. P_{ao} aortic pressure [mmHg], P_d distal stenosis pressure [mmHg], P_v venous pressure [mmHg], Q_n healthy myocardial blood flow, Q_d diseased myocardial blood flow [ml·s^{-1}], Q_s stenosis flow [ml·s^{-1}], Q_c collateral flow [ml·s^{-1}], $R_{myo,n}$ healthy myocardial resistance [mmHg·s·ml^{-1}], $R_{myo,d}$ diseased myocardial resistance [mmHg·s·ml^{-1}].

When the same epicardial coronary artery is diseased (and the microvessels are still maximally vasodilated), such that there is a translesional pressure drop which decreases the effective myocardial perfusion pressure (Figure 2.7b), the flow being delivered to the myocardium is the diseased flow, Q_d [ml·s^{-1}], which results from both the flow through the stenosis, Q_S [ml·s^{-1}], and collateral flow, Q_C [ml·s^{-1}] (if present). Evidently, due to the reduced perfusion pressure, the flow being delivered to the myocardium in the diseased case is less than that required to meet the metabolic needs of the heart tissue.

The ratio of the diseased to healthy myocardial flow, at maximum hyperaemia, is referred to as the fractional flow reserve (FFR) [23]:

$$FFR = \frac{Q_d}{Q_n}. \tag{2.5}$$

Consequently, the FFR is a dimensionless index that quantifies the percent of healthy hyperaemic myocardial blood flow that is preserved when the supplying artery is diseased. As such, since it is an evaluation of myocardial perfusion, FFR is a measure of stenosis functionality [23, 24, 29-31].

When considering the direct relationship between the perfusion pressure and the flow through the myocardium at maximum hyperaemia, the diseased and healthy flow rates can be calculated as follows [23]:

$$\begin{aligned} Q_d &= (P_d - P_v)/R_{myo,d}\ , \\ Q_n &= (P_{ao} - P_v)/R_{myo,n}\ . \end{aligned} \tag{2.6}$$

Consequently, the FFR can be expressed with respect to pressure. This idea is significant as the absolute healthy myocardial blood flow is unknown in clinic:

$$FFR = \frac{(P_d - P_v)/R_{myo,d}}{(P_{ao} - P_v)/R_{myo,n}}\ . \tag{2.7}$$

Since the average venous pressure (right atrial pressure) is approximately 5mmHg [93], it can be assumed to be negligible [31]. Furthermore, the diseased and healthy myocardial resistances are equal under induced maximal hyperaemic conditions in the absence of microvascular disease (see Figure 2.5a). As such, in a clinical setting, under induced hyperaemic conditions (through the injection of a vasodilatory agent), the FFR can be approximated by [23]:

$$FFR \approx \frac{P_d}{P_{ao}}\ . \tag{2.8}$$

Figure 2.8a displays a schematic of the clinical measurement of FFR. A guiding catheter is inserted through a peripheral vessel and a solid-state pressure transducer mounted on a flexible guide-wire is fed through the guiding catheter.

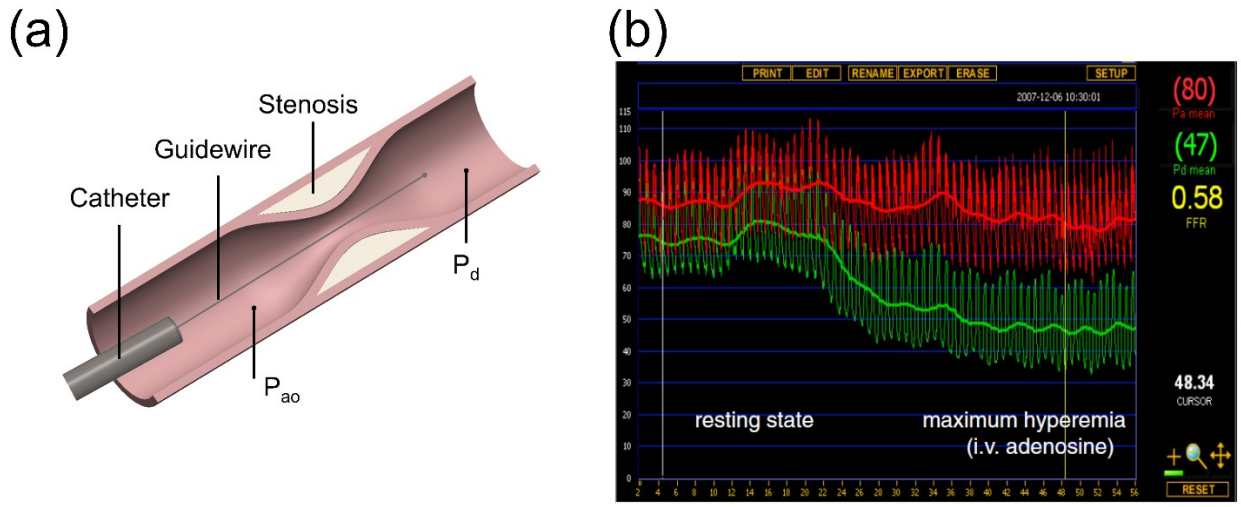

Figure 2.8: (a) Schematic of pressure-derived FFR measurement and (b) example of *in vivo* pressure recordings for the calculation of the pressure-derived FFR (with permission from [22]). The red and green lines correspond to the aortic and distal pressure measurements respectively, with the average values provided on the right-hand side of the figure.

Once the pressure recordings from the guiding catheter and the pressure wire are equalized, the pressure wire is advanced distal to the stenosis of interest. Hyperaemia is subsequently induced through the injection of adenosine, and pressure measurements over many cardiac cycles are made for the calculation of the pressure-derived FFR. Figure 2.8b provides an example of clinical data from a measurement of FFR. If multiple stenoses are present, the pressure wire is pulled back across all the stenoses to identify that which has the most significant pressure gradient [94].

Numerous clinical studies were executed upon the introduction of the pressure-derived FFR to assess its capability to discern between ischemic and non-ischemic stenoses with angiographically-significant diameter reductions [31, 32, 93, 95]. From these studies, a threshold pressure-derived FFR value between 0.75 and 0.8 was identified for the onset of ischemia on the basis of non-invasive stress and exercise tests as well as perfusion tests. This threshold value was later utilized in various clinical trials to investigate the effectiveness of FFR-guided versus angiography-guided intervention of coronary lesions. These investigations determined that interventions can be safely deferred for physiologically (functionally) nonsignificant but angiographically significant lesions [14, 96-98].

As a diagnostic index, FFR has several important features that make its use favourable. For example, FFR has a theoretical global value of one for each patient and for each vessel with a very narrow and well-defined cut-off value for the identification of ischemia. It is also independent of systemic haemodynamics (heart rate, left-ventricular contractility, etc.) while inherently taking into account the contribution of collateral circulation and the myocardial mass being perfused. Therefore, as a result of these characteristics and its unmatched capability of identifying ischemia-inducing lesions, FFR has been identified, in the recent years, as the gold-standard method for the diagnostic functional evaluation of coronary lesions [14, 22, 33].

2.3.3 Coronary bifurcation lesions

2.3.3.a Classification and statistics of CBLs

The tendency of atherosclerotic plaques to form in areas of disturbed flow, such as vessel bifurcations, has been widely accepted in the scientific world [38, 99, 100]. Coronary bifurcation lesions, which constitute their own subset of coronary artery disease, are defined as luminal narrowings that are in the vicinity of, and/or include a significant side branch [4, 7]. In order to characterize the arrangement and location of the stenoses, several classification systems have been developed over the years. In the recent years, the Medina classification, for which details are provided in Figure 2.9, has become widely adopted in clinic due to its simplicity and intuitive nature [4, 5, 7, 101].

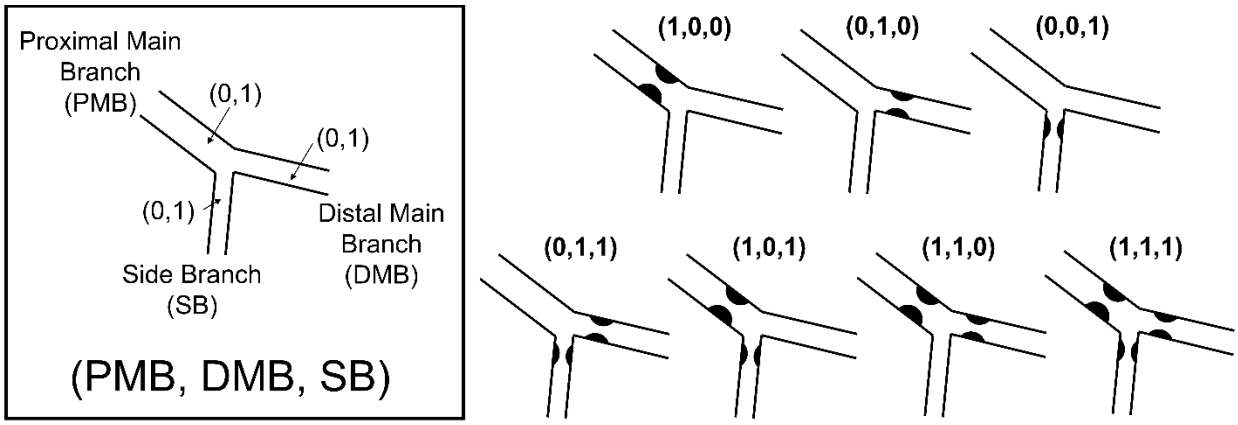

Figure 2.9: Detailed description of the Medina classification. PMB proximal main branch, DMB distal main branch, SB side branch.

The Medina classification consists of a binary system that denotes either the presence (1) or the absence (0) of a stenosis with a diameter reduction greater than 50 percent in each of the vessels of the bifurcation: (proximal main vessel, distal main vessel, side branch). For example, a configuration described by the (1,0,1) notation consists of a stenosis (with a diameter reduction greater than 50 percent) in the proximal main vessel and in the side branch and no stenosis in the distal main branch.

From a clinical perspective, coronary bifurcation lesions constitute a notable proportion, namely up to 20 percent, of all executed PCIs [4-6]. Due to the inherent technical difficulty of the procedure, which results from factors, such as the dynamic anatomic variability of the bifurcation during the procedure, plaque characteristics (plaque burden and morphology) and bifurcation characteristics (angle and vessel diameters) [5, 6], their intervention is associated with higher rates of peri- and post-procedural clinical events (major cardiac events), target-lesion revascularization, restenosis and thrombosis as compared to non-bifurcation lesions [4, 5, 7, 9-13].

There is still much uncertainty and debate with regard to the optimal interventional technique [7] as well as to the assessment of bifurcation lesion severity [8], which renders bifurcation lesions, to this day, a major limitation of interventional cardiology. In order to improve diagnostic strategies so as to reduce the risks associated with their treatment, it is essential that a good understanding of the dynamics of bifurcation lesions as well as the factors that affect the dynamics be obtained.

2.3.3.b Dynamics of CBLs

For isolated lesions, the onset of ischemia is governed by lesion morphology, the size and dynamics of the myocardium being perfused by the stenosed vessel, and the extent of collateral blood flow. However, for CBLs, the development of ischemia, and therefore the manifestation of the disease, is more involved. In addition to the factors influencing isolated lesion functionality, these types of stenoses are subject to haemodynamic interactions, both on the global and local level, which render the overall dynamics of the system more complex [102].

There are several factors that could contribute to the global haemodynamic interactions within coronary bifurcation lesions. Firstly, the resistance of a stenosis is dependent on the transtenotic flow rate. Consequently, when multiple stenoses are dispersed within the coronary tree, the resistance of each lesion contributes to the overall epicardial resistance and thus, the total myocardial flow reduction. Therefore, there is a mutual underestimation of the true resistance and haemodynamic severity of the individual lesions [102, 103]. This phenomenon has been previously demonstrated for tandem (or serial) lesions without an intermediate side branch [102, 104-108]. Furthermore, the relative epicardial resistance between the daughter vessels, which is influenced by both the relative severity of the corresponding stenoses and that of the supplying vessel lesion, influences the relative distribution of blood between the myocardial beds being perfused by the epicardial bifurcation. This idea, which can be extended to the phenomenon of branch steal, has been suggested to affect the overall physiological severity of bifurcation lesions [27, 109]. Still yet, the dynamics and relative size of the two distal myocardial beds also play a significant role in the relative distribution of blood between the two daughter vessels. More importantly, the relative extent of myocardial domain being perfused ultimately determines the criticality of the flow reduction [103, 110]. Finally, the development (if any) of collateral flow conduits depends on the magnitude and duration of exposure to myocardial ischemia. In the case of bifurcation lesions, wherein there are two potential ischemic domains, the corresponding relative extent of collateral development will further influence the ischemic state of the individual myocardia and therefore the criticality of the CBL configuration.

Local haemodynamic interactions, which are related to localized flow characteristics, arise from the close proximity of the lesions to one another and to the bifurcation carina. More specifically, pressure-flow relations of the individual lesions could be affected as a result of the overlap of the emerging fluid jet and recirculation zone of the proximal stenosis with the neck of the daughter vessel stenoses [111]. The localized flow characteristics distal to the supplying vessel stenosis are further influenced by the morphology and dynamics of the stenosis itself and therefore could have a variable effect on the downstream lesion dynamics. Additionally, these flow characteristics do not only

interact with the distal stenoses, but also with the bifurcation carina, which could further influence the flow within the two daughter vessels. Moreover, the complex geometry of the bifurcation incurs flow disturbances which affect the local haemodynamics irrespective of lesion configuration. Specifically, bifurcation geometry not only affects the level of difficulty of the procedure, but also varies significantly from patient to patient, and from bifurcation to bifurcation within a single patient [4, 13].

3

CARDIOVASCULAR COMPUTATIONAL FLUID DYNAMICS

This chapter presents an overview of computational fluid dynamics within the cardiovascular system, with emphasis on the limitations of its use. Subsequently, geometric multiscale modelling in the context of cardiovascular computational fluid dynamics is presented. Geometric multiscale modelling addresses the limitations of conventional cardiovascular computational fluid dynamics simulations and is central to the current thesis as it is the method utilized to fulfill the objectives of the research. Finally, a literature review of the numerical studies on coronary bifurcation lesions executed to date is provided. The limitations of the studies, which are addressed in the thesis, are outlined in detail.

3.1 OVERVIEW AND LIMITATIONS

For many decades, numerical simulations of blood flow have proven to be an essential and invaluable tool in the understanding of the mechanics and dynamics of the cardiovascular system. The importance of cardiovascular computational fluid dynamics (CFD) stems from the fact that medical imaging, albeit significant progress in modality technology and resolution, is neither capable of elucidating the *in vivo* haemodynamic

and mechanical environment, nor is it capable of serving as a surgical and procedural tool for predicting outcomes, and optimizing and tailoring procedures [112].

The process of numerically simulating blood flow and obtaining haemodynamic parameters in a specific cardiovascular domain consists of six main steps: generation of the geometry, meshing of the computational domain, application of fluid properties, application of boundary conditions, solution of the flow field in time and space and processing of the simulations results.

In the first step, the generation of the geometry can be achieved through computer-aided design (CAD), wherein simplified and/or analytical representations of the *in vivo* geometry of the domain of interest are created. Conversely, patient-specific geometries can also be obtained by extracting them from various imaging modalities, such as computed tomography (CT), magnetic-resonance imaging (MRI), angiography, and other. The images obtained from the modalities must be segmented and reconstructed, and usually undergo numerous stages of smoothing and correcting before being utilized for the numerical simulations. Once the finalized geometry is obtained, it is discretized in space (meshed) and the blood properties (for example, the density and viscosity) are applied.

The following step, namely the assignment of boundary conditions to the computational domain, is central to the numerical simulation of blood flow, and more specifically in the prediction of accurate flow and pressure fields within the domain of interest. Modelling the entire cardiovascular system, and in fact even the circulation in smaller cardiovascular domains is a challenge, if not impossible as it is associated with high computational costs, while still being subject to errors associated with geometric reconstruction. Therefore, only a truncated vascular domain is considered in CFD simulations. However, the localized dynamics of each portion of the vasculature are influenced by the upstream and downstream haemodynamics. Both, from a physiological and mathematical perspective, the peripheral haemodynamics are inherently considered in the boundary conditions of the numerical model. Henceforth, the selection of physiologically relevant and accurate boundary conditions that represent the *in vivo*

haemodynamic environment, is crucial in the validity of the results and remains a challenge in the field of cardiovascular CFD.

Conventional boundary conditions for cardiovascular CFD simulations most commonly consist of a prescribed flow or pressure waveform at the inlet and zero pressure/traction conditions at the outlets. In the case of multiple outlet boundaries, a predefined flow-split between the different outlets can also be prescribed. However, the application of such boundary conditions is associated with certain shortcomings. More specifically, their application requires *a priori* knowledge about the flow or pressure waveform, which is most often not available due to low resolution and/or unavailable in *in vivo* measurements. Therefore, assumptions regarding the prescribed flow or pressure waveform, which commonly are not representative of the true *in vivo* state, are made. Furthermore, zero pressure/traction outlet conditions are not capable of capturing and generating accurate pressure fields within the truncated computational domain. Consequently, the flow and pressure fields obtained from the simulations are limited in their accuracy [112]. These limitations are addressed by geometric multiscale modelling, for which details are provided in subsequent sections. Geometric multiscale modelling is central in the context of this thesis.

Once the boundary conditions are selected and applied, the system is discretized in time and the solution is obtained at each timestep in the transient simulation. More details regarding the solution methods are provided in the following chapter. Finally, the results are post-processed in order to derive and visualize haemodynamic parameters, such as WSS, flow and pressure fields, and other, which aid in the characterization of the mechanical environment and the elucidation of clinically-relevant information.

3.2 GEOMETRIC MULTISCALE MODELLING

3.2.1 Overview of geometric multiscale modelling

In order to overcome the limitations of conventional boundary conditions in cardiovascular CFD simulations, the idea of geometric multiscale modelling has been introduced. Within geometric multiscale CFD models, the vascular domain of interest, most often consisting of a 3D model, is coupled with a lower-order model (either 0D or

1D) of the surrounding and peripheral circulation. The lower-order models allow for the global dynamics of peripheral vascular domains to be accounted for in a computationally-efficient manner, such that the local haemodynamics of the domain of interest are computed in the context of global physiology [19, 112-115].

Most commonly, the 3D domains are coupled with a 0D or lumped-parameter model (LPM) representing the dynamics of the surrounding vasculature. Lumped-parameter models, wherein large and complex vascular districts are represented by a small number of hydraulic elements, are computationally inexpensive and efficient and allow for the macroscopic (spatially and temporally averaged) haemodynamic parameters to be obtained. Electrical circuit elements, for example resistances, capacitances and inductances, which have analogies within the fluid domain, are used to represent the various characteristics of the vasculature and their corresponding dynamics. The first records of lumped-parameter models for the modelling of cardiovascular dynamics date to 1733 and 1899, where they were used specifically for the study of the dynamics of the heart and its chambers (denoted as the Windkessel model) [116, 117]; since then, their use has been extended from the global modelling of individual segments, to those of entire vascular domains and even the complete cardiovascular system for various applications and with varying degrees of complexity [118-125]. Lumped-parameter models have also been of significant importance in the study of coronary artery dynamics and have been employed in various investigations for both the modelling of healthy and diseased states [27, 126-130].

Lumped-parameter models can be coupled with 3D CFD domains by means of an open-loop or closed-loop geometric multiscale configuration. In the open-loop configurations, simple resistance or impedance boundary conditions are applied at the outlets. While allowing for more physiologically-relevant pressure fields to be computed in the CFD simulations, open-loop systems require a flow or pressure waveform to be imposed at the inlet of the model. Therefore, this approach presents similar limitations to those of the generic (conventional) boundary conditions [112, 131]. Conversely, in the closed-loop configurations, both the inlet and the outlets are coupled with a lower-order model of the entire cardiovascular system in a complete feedback loop. Thus, both the

inlet and outlet boundary conditions are extracted from the solution of the lower-order model, which is in turn influenced itself by the dynamics in the 3D domain. Consequently, in closed-loop configurations, the boundary conditions dynamically change and are allowed to develop through the interaction between the two models. As such, they have the advantage of allowing the flow and pressure fields within the domain of interest to be calculated in the context of the complete global physiology of the cardiovascular system and therefore eliminate the need for *a priori* assumptions [112]. Overall, the execution of CFD simulations within a geometric multiscale framework has developed into and is proving to be a significant research tool that allows for more physiologically-relevant *in vivo* haemodynamics to be elucidated within patient-specific studies. It enables systematic evaluations of disease states and interventional procedures with the potential to serve as a clinical tool to plan, optimize, personalize and predict the outcome of treatment [112].

3.2.2 Geometric multiscale modelling of coronary arteries

Over the past decade, the use of geometric multiscale modelling within cardiovascular CFD simulations has become more prominent and has been implemented in many studies for various applications; examples include, but are not limited to, the understanding of the progression of atherosclerotic disease in the carotid bifurcation [132], risk stratification of patients suffering from aneurysmal coronary arteries [133], the prediction of short- and long-term outcomes of surgical and interventional procedures [131, 134-138] and the optimization of procedures and surgical implants [138, 139].

Computational fluid dynamics simulations under the geometric multiscale framework have also recently become of importance for the modelling of coronary haemodynamics under both healthy and diseased states [138, 140-142]. The use of closed-loop multiscale configurations within transient coronary simulations are of great importance due to the predominantly diastolic flow phenomenon; they allow the simulation of left ventricular pressure which can be imposed within the coronary myocardial model so as to account for and approximate intramyocardial pressure. The use of an open-loop model with simple resistance/impedance outlet conditions would not be able to capture such particular flow dynamics unless an inlet velocity waveform accounting for the

phenomenon were imposed. In particular, for diseased conditions, the magnitude of coronary flow is unknown as it is dependent on a complicated interplay between the stenosis resistance (which is itself dependent on the transtenotic flow) and the myocardial dynamics. Therefore, for coronary arteries, closed-loop geometric multiscale models of are central to disease evaluation.

Interestingly, the functional characterization and diagnosis of coronary stenoses using computational methods has become the interest and focus of many studies in recent years. This endeavour is motivated by the fact that, due to procedural costs, functional assessment of coronary lesions using FFR, although widely accepted as the gold-standard in coronary artery disease diagnosis, is only executed in less than 10 percent of cases undergoing PCI [14-16]. In the virtual evaluation of FFR, patient-specific anatomic data of the coronary arteries are obtained using various imaging modalities, such as coronary computed tomography angiography [142-144] and rotational coronary angiography [15] and computational fluid dynamics (CFD) simulations (as well as fluid-structure interactions simulations) are performed under a multiscale framework in order to obtain the pressure and flow fields required for the calculation of FFR.

Kim *et al.* [140, 141] developed the first closed-loop multiscale model of the coronary circulation for the simulation of coronary blood flow under both healthy [141] and disease states [140]. The resulting model and the corresponding numerical code for the implicit multiscale numerical simulation of FFR was patented in the same year [145] and later served as the basis for the only for-profit company namely, HeartFlow Inc., that is capable of numerically computing FFR [142, 143]. The models of Kim *et al.* [140, 141] consist of a patient-specific geometry of the aortic root (without the aortic valve), the aortic arch, and the descending aorta as well as the left and right coronary circulations and the main branches stemming from the aortic arch, as obtained using coronary computed tomography angiography (CTA). Within the model implemented by HeartFlow Inc., the aortic geometry was truncated to include only the root. The patient-specific geometry is coupled with LPMs of the left and right heart, which serve both as inlet boundary conditions to the aortic root (the left heart) and a means to compute left and right ventricular pressure which serve as an approximation to the intramyocardial pressure that

is applied to the coronary microcirculation during systole. Each coronary outlet model accounts for the myocardial resistance, as calculated based on scaling laws and the total myocardial resistance as well as the epicardial resistance and capacitance, and the compliance of the endocardial vessels, all calculated using literature values for the average flows, pressures and impedance spectra. The outlets of both the aorta (and its branches) and the coronary vessels, connect back to the right heart to close the system and generate a complete feedback loop.

The models of Kim *et al.* [140, 141] are capable of predicting physiologically relevant flow and pressure curves in the healthy coronary arteries under resting and light exercise conditions [141] as well as capturing the decrease in myocardial perfusion in the presence of varying LAD stenosis severity [140]. Furthermore, the ability of the HeartFlow Inc. algorithm to noninvasively assess FFR has been evaluated in a series of clinical trials [144, 146-149] which compared the results of numerical computation of FFR to that measured invasively within the catheterization lab. The results of the trials demonstrated that the numerically-computed FFR had a superior diagnostic capacity compared to the use of non-invasive tests and specifically visual evaluation from coronary CT angiography alone. The diagnostic accuracy of the non-invasive FFR was significantly improved in the most recent clinical trial [149] when strict adherence to image acquisition protocol and improvements to the computational code were implemented, ultimately granting the method U.S. Food and Drug Administration (FDA) approval [16]. Overall, closed-loop multiscale models of the coronary circulation are becoming a powerful tool to assess the functionality of coronary lesions by yielding well-validated and widely-accepted clinical index.

3.3 NUMERICAL INVESTIGATIONS OF CBLS

The dynamics of CBLs have been the focus of few studies to date. The following sections provide an in-depth evaluation of the existing literature and the state-of-the-art numerical modelling of CBL dynamics.

3.3.1 Review of the literature

In 2012, Binu *et al.* [47, 48] executed preliminary investigations on 2D and 3D models of the seven CBL configurations based on the Medina classification. For each CBL geometry, which was modelled within the LMCA bifurcation, a single diameter reduction of approximately 60 percent was employed. In both studies, steady-state CFD simulations were implemented; at the inlet of the model, healthy, average diastolic LMCA flow was applied through a fully-developed parabolic velocity profile, whereas at the outlets, a flow split between the LAD and the LCX, based on vessel diameter, was imposed. The works explored WSS patterns between the different cases in order to identify configurations which were potentially at risk for disease progression; the results found that in both the 2D and 3D cases, the (1,0,0) configuration had the highest risk for disease progression while the lowest risk was associated with the (0,0,1) case. The computed WSS within the 2D and 3D models predicted different risk levels for the multilesional configurations suggesting inconclusive findings.

In the same year, Zarandi *et al.* [46] also executed 2D CFD simulations on CBL configurations with the LMCA bifurcation. Similarly to [47, 48], lesion arrangements were based on the Medina classification, although only the (0,1,1), (1,0,1) and (1,1,1) configurations were simulated. For each configuration, Zarandi *et al*. [46] considered two diameter reductions corresponding to moderate (50 percent) and severe (75 percent) cases. Transient simulations were executed by imposing a pulsatile, fully-developed velocity profile with a time-varying flow rate corresponding to healthy conditions at the inlet and zero-traction conditions at the outlets of the LAD and the LCX. Wall shear stress within the side branch as well as the ratio of the flow in the side branch to the flow in the mother vessel, were computed. The results of the simulations showed that within the side branch, the (1,0,1) configuration had the lowest WSS over the entire cardiac cycle when compared to the (1,1,1) and (0,1,1) cases. Interestingly, at both diameter reductions, the (1,0,1) configuration also yielded the lowest flow ratio.

Between 2012 and 2014, a series of CFD investigations within patient-specific models of diseased LMCA bifurcations, from CT angiography, was executed by Chaichana *et al.* [39-44]. In two initial studies [43, 44], the (1,1,0) configuration with a

single diameter reduction of approximately 60 percent was simulated. In [44], the geometry was truncated to the proximal portions of the LAD and the LCX whereas, in [43] the geometry was extended to include the distal portions of these arteries as well as two side branches stemming from each daughter vessels. Similarly to Zarandi *et al.* [46], transient flow simulations were implemented with a pulsatile, fully-developed velocity profile based on a time-dependent healthy LMCA flow rate being applied at the inlet. The outlet boundary conditions differed between the two studies; specifically, a zero-pressure gradient as applied in the truncated LMCA bifurcation geometry of [44] while a flow-split similar to Binu *et al.,* based on diameter reductions, was applied for the extended domain of [43]. In later studies by the same group, a larger cohort of patients with differing lesion configurations, including the (0,1,1), (1,0,0), (0,1,0) and (0,0,1) cases, were considered [39, 41, 42]; in these studies, the boundary conditions for the transient flow simulations were consistent with those of their previous studies while diameter reductions ranged between 30 and 70 percent based on the specific patient.

Through the numerical studies, Chaichana *et al.* [39-44] sought changes in flow velocities, WSS and the local pressure gradient (PSG) for the different CBL configurations relative to the healthy LMCA bifurcation flow so as to assess the risk for disease progression as well as plaque rupture. As expected, the results of the studies showed high flow velocities at the minimal luminal diameter and recirculation zones both proximal and distal to the stenoses, which resulted in regions of high and low shear stresses respectively in all investigated configurations. These results implied increased rupture risk at the neck of the stenosis and increased risk for disease progression proximal and distal to the existing stenoses. Interestingly, decreased WSS was also observed in the side branches downstream the effective plaque area compared to the healthy case which implied the risk for plaque formation distal to the diseased bifurcation. Finally, compared to the healthy case, the pressure gradient was elevated in the regions of reduced luminal area which further implies increased risk for plaque rupture.

In the most recent study by Chaichana *et al.* [40], a single patient-specific geometry of the LMCA bifurcation (including the distal portions of the LAD and LCX and their side branches) was utilized and different bifurcation lesion configurations, with stenoses of 60

percent diameter reduction, were imposed. Eight stenosis arrangements were considered in that study, which included all seven Medina classification cases with stenosis placed directly at the bifurcation carina. In the eighth case, the stenoses were arranged according to the (1,1,0) configuration; however, the LMCA stenosis was shifted upstream the bifurcation carina. As in previous studies, the parameters of interest from the CFD simulations were the velocity, WSS and PSG; the study found that between most configurations, there were statistically significant differences in the investigated haemodynamic parameters. Although similar conclusions to the previous studies regarding the risk for plaque rupture and disease progression were elucidated, the consideration of various lesion configurations added value to the understanding of the complexity of bifurcation lesion haemodynamics. More specifically, through the comparison between the different configurations, the results showed that single-lesion configurations produced less severe haemodynamic changes compared to the multi-lesion cases. More importantly, the haemodynamic differences between the various multi-lesion configurations were a complicated factor of both the number and location of the stenoses within the flow divider.

Frattolin *et al.* [45] extended the work of Zarandi *et al.* [46] by considering 3D models of true bifurcation lesions, based on the Medina classification. Mild to moderate plaques, specifically with diameter reductions of 22.5, 30 and 50 percent, were simulated. All stenoses within the bifurcation had a uniform diameter reduction and were placed directly at the bifurcation carina. Similarly to all aforementioned studies, and in particular [46], a pulsatile, fully-developed velocity profile was applied at the inlet boundary, while zero-traction conditions were imposed at the outlets. Differing from previous studies, the decrease in flow as a result of the additional epicardial resistance imposed by the stenoses, was taken into account; more specifically, the time-varying volumetric flow rate applied at the inlet was scaled from the healthy condition based on average FFR values from the literature. In addition to investigating the influence of diameter reduction, the study also assessed the effect of lesion proximity to the carina. Specifically, for all configurations with a diameter reduction of 50 percent, the location of the stenoses relative to the bifurcation carina was varied between zero and six millimeters. In

accordance with previous studies, the haemodynamic parameters assessed included the WSS within the side branch and the ratio of the side branch to supplying vessel flow. Similarly to the 2D results of [46], the (1,0,1) configuration was consistently found to produce the lowest WSS and flow within the side branch. These results suggest that branch steal may play an important role in perfusion and disease progression. Furthermore, for all configurations, as the distance of the stenoses to the carina increased, both the WSS within and the flow to the side branch increased. As such, the results of the study implied that stenoses in close proximity to a bifurcation may generate more critical haemodynamic environments.

3.3.2 Limitations of existing works

To the best of the author's knowledge, the aforementioned studies constituted the first attempts to investigate localized haemodynamic changes that occur when multiple stenoses are present near a bifurcation. The results of these works have suggested the intricate relationship between the severities of lesions, the arrangement of plaques within the bifurcation, and the haemodynamics of the corresponding vasculature and emphasize the inadequacy of anatomy alone to guide and substantiate the decision for clinical intervention. The non-uniform and statistically significant haemodynamic changes that can occur within CBLs were demonstrated to be a function of the location and the severity of the lesions and were suggestive of the presence of complicated, localized haemodynamic interactions between stenoses when they are in close proximity to both one another and to a bifurcation. These interactions yielded different risk levels regarding disease progression and plaque rupture between the configurations, although the various studies drew different conclusions with regard to the most critical cases. Overall, although suggestive of the presence of complex haemodynamic interactions within CBLs, the exiting studies did not provide novel insight into the absolute haemodynamics of stenosed arteries. More specifically, increased flow velocity coupled with high WSS at the luminal narrowing and zones of flow recirculation and low WSS distal to the neck of the stenosis were elucidated over a few decades prior. In many of the studies, the observed differences between the configurations were not properly quantified so as to provide insight into the aforementioned haemodynamic interactions and their consequences.

The first main shortcoming of the current state of the art of CBL modelling is related to the assumptions made regarding the global haemodynamics of the LMCA bifurcation under diseased states. More specifically, an evaluation of the haemodynamic differences between the various lesion configurations under physiologically accurate *in vivo* diseased conditions was lacking. This limitation is related to the imposition of conventional boundary conditions (prescribed inlet healthy flow rates and either zero-pressure outlets or flow-splits between the outlet vessels), for the execution of the CFD simulations, which inherently disregard the dynamics of the distal myocardium. In a closed-loop system, such as the circulatory system, the haemodynamics upstream and downstream the simulated domain not only influence its dynamics, but are central in the notion of lesion functionality due to their correlation with the onset of ischemia. Consequently, CBL functionality could not be assessed and instead emphasis was put on disease progression. While an understanding of the prognostic attributes of this type of disease is important, there is a lack of knowledge regarding the clinical manifestation and severity of CBLs based on clinically-relevant indices; this information is necessary in order to improve diagnostic and interventional strategies and devices and thus, reduce the risks associated with their treatment.

Furthermore, the resistance of a stenosis is linearly dependent on the transtenotic flow, which signifies that the application of a predefined and healthy flow rate does not allow for the true stenosis resistance to be expressed and therefore the true effect of the lesions on the perfusion pressure to be elucidated. This idea is amplified when the outlet boundary conditions constitute a prescribed constant flow distribution between the two daughter vessels since the differences in epicardial resistance, as is influenced by the different lesion arrangements, are not taken into account (for each case, the same magnitude of flow is forced through the individual daughter vessels). Only Frattolin *et al.* [45] attempted to take into account the decreased transtenotic flow with increasing stenosis severity; however, at a specific diameter reduction, the prescribed reduced inlet flow, which was based on average FFR values from the literature for isolated lesions, was still constant between the different configurations. This shortcoming has certain important implications on the presented results and conclusions as well as the ability of the studies

to provide clinical insight into the dynamics of CBLs. More specifically, the clinical relevance of the prognostic conclusions drawn by the authors of these studies are limited due to the fact that the imposed flow conditions for the various diseased cases are not representative of the true *in vivo* haemodynamic environment.

Within coronary flow simulations, the use of conventional (predefined) boundary conditions is common due to the physiologically complex dynamics of the left coronary circulation. In order to capture the predominately diastolic flow phenomenon, either a pulsatile profile with a predefined volumetric flow rate that accounts for predominant diastolic flow (coupled with zero-pressure, flow-distribution or simple resistance outlets) or physiologically-relevant pressure profiles at all boundaries of the model must be applied. For the healthy left coronary arteries, such boundary conditions are acceptable as normal haemodynamic environments are relatively well-defined for the average human. However, under diseased states, due to the flow-dependence of the stenosis resistance and thus, the perfusion pressure as well as the influence of the dynamics of the distal myocardial circulation, neither the flow through nor the pressure distal to the stenoses are known *a priori.* Therefore, in a truncated computational domain of stenosed coronary arteries, the boundary conditions are unknown. However, by considering a larger coronary domain that allows the dynamics of the distal myocardium, including vascular resistances and changes in intramyocardial pressure to be modelled, coronary perfusion can be assessed without imposing physiologically inaccurate boundary conditions, as in the case of closed-loop multiscale models. More specifically, the flow within the epicardial arteries for the various diseased cases can develop through the interaction of the two domains which contribute to the *in vivo* haemodynamic environment. This idea not only allows for a more robust understanding of disease progression, but also permits a functional characterization of coronary plaques.

The studies that have been executed to date have not attempted a systematic, thorough and comprehensive investigation of the effect of various geometric and morphological parameters of the stenoses themselves and of the arterial bifurcation, on CBL dynamics and the corresponding haemodynamic interactions. For example, in the majority of the studies, a single diameter reduction was employed for all configurations.

Frattolin *et al.* [45], who varied the stenosis severity, only considered mild diameter reductions (in clinic, stenoses are only considered to be significant when exhibiting a minimum 50 percent diameter reduction). Most studies considered a uniform severity for all stenoses within the same configuration; physiologically, as was displayed in Chaichana *et al.* [41], who reconstructed patient-specific diseased bifurcations, there exists a variance between the severities of the different stenoses. This idea is an important consideration as it has been shown, in the case of tandem lesions and multiple stenoses within the same coronary artery, to mask the true haemodynamic severity of the individual lesions [102, 104-108].

Moreover, in all studies in which stenoses were artificially induced within the LMCA geometries, the lesions were modelled as being concentric; many clinical studies have shown that a significant proportion of coronary lesions have eccentric morphology, particularly in the case of lesions in close proximity to bifurcations [150-155]. In addition, bifurcation angle has been shown to vary significantly between patients [156], and more importantly to have a significant effect on the outcome of PCI [4-6, 157]. Nevertheless, all studies with idealized LMCA geometries considered a single bifurcation angle; those considering patient-specific geometries in which there was inherent interpatient variance, the differences in haemodynamic environment were not systematically assessed relative to the bifurcation geometry. Only the study by Frattolin *et al.* considered a single morphological parameter, namely the distance of the lesions from the bifurcation carina. The results of the study showed that when the stenoses were farther from the carina, critical haemodynamic states (both with respect to WSS and flow ratio) were alleviated. Although preliminary, these findings were indicative of the fact that morphological and geometric parameters could have a potential effect on CBL haemodynamics; therefore such investigations are merited so as to identify potential independent predictors of critical haemodynamic environments.

The above limitations concerning the current state of the art, and their corresponding implications, have been summarized in Table 3.1. The shortcomings of these studies are addressed in the research presented in the thesis. Specifically, they serve as the basis for the objectives of the work, as were presented in Chapter 1.

Table 3.1: Summary of limitations and corresponding implications of the current state of the art.

Limitation	Implications

• Execution of conventional CFD simulations
  ○ Imposed flows are not representative of diseased states
  ○ The distal myocardial dynamics are neglected
  ○ The flow-dependence of the stenosis resistance is not taken into account
	• Physiologically-relevant diseased haemodynamics could not be evaluated
	• A functional assessment based on validated clinically-relevant indices could not be obtained.

• Disregard of variable morphological and geometric parameters	• Independent predictors of critical haemodynamic environments could not be identified.

4

THE LUMPED-PARAMETER MODEL

This chapter presents the development and numerical implementation of the lumped-parameter (0D) model. An outline of the theory behind the 0D model, including details regarding the associated assumptions, is provided. The development of the lumped-parameter model constitutes the first stage in the implementation of the geometric multiscale CFD simulations of the diseased coronary bifurcation models. It is an integral part of the current research because the lumped-parameter model is coupled with the truncated 3D CBL domain so as to account for the global dynamics of the surrounding cardiovascular domains and therefore allow physiologically-relevant boundary conditions to be applied in the CFD simulations.

4.1 LUMPED-PARAMETER MODEL THEORY

Lumped-parameter models allow for large and complex cardiovascular domains to be modelled in a computationally inexpensive and efficient manner using a small number of hydraulic elements. These models yield macroscopic haemodynamic parameters, namely spatially-averaged flowrates and pressures, for the evaluation of global cardiovascular dynamics.

The basis for this type of model lies within a black-box, input-output system wherein a multicomponent cardiovascular domain can be represented by a single tube with equivalent, global fluid and vessel properties that yield, at the output of the model, flows and pressures that are physiologically-representative of those found in the full *in vivo* domain [19].

4.1.1 Electrical analogue components of lumped-parameter models

Lumped-parameter models of the cardiovascular system are represented by electrical circuits; more specifically, the global characteristics of the vasculature and the corresponding fluid and vessel dynamics have analogies within the electrical domain. A summary of the analogous domain properties and calculated parameters between the fluid and electrical models are provided in Table 4.1 [112, 113].

Table 4.1: Analogies between the fluid and electrical domains for lumped-parameter models.

	Fluid Domain	**Electrical Domain**
Calculated Parameters	Pressure	Voltage
	Flow	Current
Domain Properties	Frictional/viscous resistance	Resistance
	Arterial compliance	Capacitance
	Fluid inertia	Inductance

Within Table 4.1, one can observe that the basic components in the electrical analogue models are resistance (R), capacitance (C) and inductance (L). The resistance relates to the viscous friction at the interface between the fluid and the vessel. The capacitance denotes the compliance, or in other words the elasticity of the vessel, and therefore its ability to expand and contract (and thus, change volume) with changes in the driving pressure. Finally, the inductance is analogous to the fluid inertia and thus, the resistance of the fluid to undergo changes in flow rate with changes in driving pressure. Lumped-parameter models are also capable of representing more complex cardiovascular structures and dynamics through the inclusion of additional electrical components, such as diodes (for the modelling of the heart valves), time-dependent compliances (for the contraction of the ventricles and the atria), external pressure generators (for the representation of intramyocardial pressures), and other.

4.1.2 Governing equations of lumped-parameter models

Each basic compartment of the electrical analogue model that represents a particular vascular domain, ranging in complexity from an isolated vessel to a complex vascular district, consists of a single resistance, R, inductance, L, and capacitance, C, as is shown in Figure 4.1.

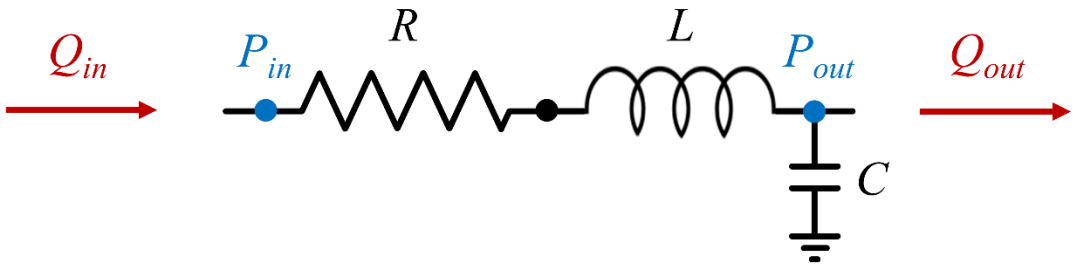

Figure 4.1: Basic compartment of the electrical analogue model, consisting of a single resistance, R [mmHg·s·ml^{-1}], and inductance, L [mmHg·s^2·ml^{-1}], in series and a single capacitance, C [cm^3·mmHg^{-1}], in parallel.

The dynamics of the basic compartmental unit are modelled by a system of two ordinary differential equations (ODEs) that correspond to the conservation of mass and momentum, as provided in Equation (4.1) [136]:

$$\begin{aligned} C\frac{dP_{out}}{dt} &= Q_{in} - Q_{out}\,, \\ L\frac{dQ_{in}}{dt} &= -RQ_{in} + P_{in} - P_{out}\,, \end{aligned} \tag{4.1}$$

where Q_{in} and Q_{out} are the inlet and outlet flow rates [ml·s^{-1}], respectively, and P_{in} and P_{out} are the inlet and outlet pressures [mmHg], respectively.

Equation (4.1) is obtained through the linearization and the subsequent spatial-averaging of the full Navier-Stokes Equations (Appendix A). In the derivation provided in Appendix A, several simplifying assumptions are made, which are related to the geometry of the vessel, the fluid and vessel properties and the nature of the flow. Table 4.2 provides a summary of the simplifying assumptions associated with these models.

Table 4.2: Summary of the simplifying assumptions considered in the derivation of the LPM governing equations.

	Assumptions
Vessel Geometry	- Straight - Circular cross-section - Tethered ends (no axial extension) - No tapering
Fluid Properties	- Newtonian - Incompressible
Vessel Properties	- Linear elastic - Incompressible
Nature of Flow	- Dominant axial flow (negligible circumferential flow) - Negligible convective acceleration - Negligible variation of axial velocity - Fully-developed (parabolic velocity profile)

Furthermore, central to the application of LPM models and the use of the electrical analogy is the notion that each domain property (R,C, and L and their fluid domain counterpart) is distinct from the others and has unique and isolated influence on the haemodynamic parameters [19].

For a single vessel modelled by the basic compartmental unit displayed in Figure 4.1, employing the assumptions outlined in Table 4.2 and simplifying the Navier-Stokes equations to produce Equation (4.1), yields theoretical expressions for the resistance [mmHg·s·ml^{-1}], inductance [mmHg·s^2·ml^{-1}] and capacitance [cm^3·mmHg^{-1}], as provided in Equation (4.2), Equation (4.3) and Equation (4.4) respectively:

$$R = f\frac{128\mu l}{\pi D^4}, \tag{4.2}$$

$$L = f\frac{4\rho l}{\pi D^2}, \tag{4.3}$$

$$C = \frac{3\pi l D^3}{16 E_m h}, \tag{4.4}$$

where l is the vessel length [cm], D is the vessel diameter [cm], μ is the fluid viscosity [g·cm^{-1}·s^{-1}], E_m is the elastic modulus of the vessel wall [mmHg] and h is the thickness of the vessel wall [cm]. In the above equations, f is a factor that converts [cPa] to [mmHg],

and is equal to 1333^{-1} mmHg·cPa^{-1}. Therefore, from these equations, it is evident that the dynamics of the compartment are dependent on the vessel geometry and the fluid and wall properties.

By combining numerous basic compartmental units into a closed-loop configuration, and by including other electrical components, such as diodes and time-varying parameters, a complete electrical analogue network describing the dynamics of a large and complex cardiovascular domain (and even the entire cardiovascular system), can be formed. The electrical analogue network is modelled by a differential-algebraic equation, which is converted to the system of nonlinear ODEs given in Equation (4.5) with the appropriate algebraic substitutions:

$$\frac{d\bar{y}}{dt} = \mathrm{A}\bar{y} + \bar{b} \,, \tag{4.5}$$

where $\bar{y}$ is a vector of unknown state variables (flowrates and pressures), A is a square matrix of parameter values (resistances, capacitances, inductances, elastances, etc.) and $\bar{b}$ is a column vector that contains forcing terms associated with the heart models. When coupling the 0D model to a distributed 3D model of a particular vascular domain, as will be outlined in subsequent sections, column vector $\bar{b}$ also contains interface conditions (forcing terms) obtained from the 3D model. The system of Equation (4.5) can be solved quickly and efficiently using conventional numerical integration schemes and solvers [19, 112-115, 158].

4.2 IMPLEMENTATION AND DEVELOPMENT OF THE MODEL

Prior to the execution of the geometric multiscale CFD simulation, which includes the 3D model of the diseased coronary bifurcation coupled with the 0D model of the rest of the cardiovascular system, the numerical simulation of the full equivalent LPM must be implemented. This stage of the multiscale model development is important in order to ensure that the dynamics obtained by the lumped-parameter representation are physiologically realistic and therefore representative of the relative upstream and downstream dynamics of the 3D domain when the multiscale coupling is accomplished.

4.2.1 Configuration of the lumped-parameter model

The full LPM of the cardiovascular system includes models of the left and right hearts, the systemic and pulmonic circulations and the left coronary circulation; the left coronary circulation is further subdivided into the left main coronary artery (LMCA) bifurcation and the epicardial, myocardial and venous circulations. The configuration of the 0D model is developed based on existing models in the literature; details regarding the configuration and parameter values of each of the aforementioned sub-models of the system are provided in subsequent sections.

4.2.1.a Heart, systemic and pulmonary models

The LPMs of the left and right sides of the heart are displayed in Figure 4.2. The left and right atria feed blood to the corresponding ventricles both actively (through their contraction) and passively (as a result of the pressure differential between the two chambers). In the models presented in Figure 4.2, the active nature of the atria is not taken into consideration in order to simplify numerics; however, the change in atrial volume and pressure over the cardiac cycle is captured through the consideration of an elastic model, which is implemented using constant elastances. The elastance is defined as the inverse of the compliance and therefore is calculated as the ratio of the pressure to the volume.

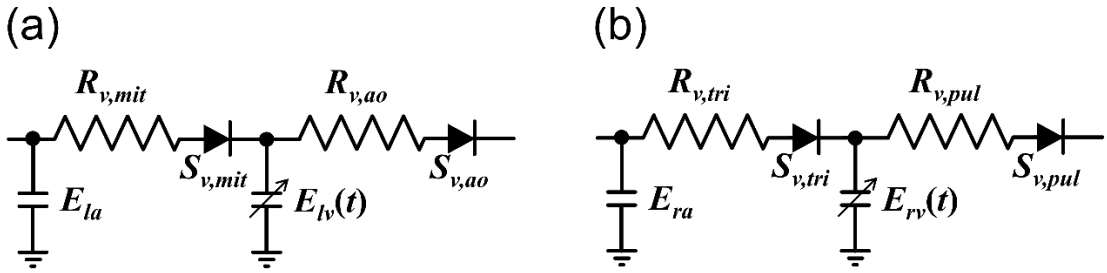

Figure 4.2: LPM of the (a) left and (b) right hearts. E the elastance [mmHg·ml^{-1}], S the valve state [-], *la* left atrium, *lv* left ventricle, *v,mit* mitral valve, *v,ao* aortic valve, *ra* right atrium, *rv* right ventricle, *v,tri* tricuspid valve, *v,pul* pulmonary valve.

Due to the passive nature of the model, atrial systole (contraction), occurring at the end of (ventricular) diastole during the P-wave of the electrocardiogram [159, 160] could not be captured. Atrial contraction primarily contributes to the end of ventricular filling

(although it is not essential) and results in a brief and small increase in atrial, ventricular and venous pressure [160]. As such, the incorporation of active atrial models would have a negligible effect on the computed coronary pressures which justified the use of a passive model.

Similarly to the atria, the change in volume and pressure within the left and right ventricles is described using elastances; however, due to the fact that it is necessary that their active nature be taken into account, a time-varying elastance function is implemented to model their corresponding contraction. The instantaneous time-varying elastance, $E(t)$ [mmHg·ml^{-1}], is defined as the ratio between the ventricular pressure and volume, as provided in Equation (4.6)

$$E(t) = \frac{P_V(t)}{V_V(t) - V_{0,V}}, \tag{4.6}$$

where $P_V(t)$ is the instantaneous ventricular pressure [mmHg], $V_V(t)$ is the instantaneous ventricular volume [ml] and $V_{0,V}$ is an empirical constant corresponding to the *x*-intercept of the pressure-volume plot [ml] [161]. The concept of ventricular time-varying elastance was first introduced by Suga and colleagues within canine hearts [162, 163] and was later shown to apply in the human heart by Senzaki and colleagues [161]. Interestingly, Senzaki *et al.* [161] demonstrated that when the patient-specific elastance curve is normalized by the maximum elastance E_{max} [mmHg·ml^{-1}], the time at which the maximum elastance occurs t_{Emax} [s], and the minimum elastance E_{min} [mmHg·ml^{-1}], the shape of the resulting curve is constant between patients, and specifically, over a range of cardiovascular diseases. The normalized time-varying elastance curve, which is provided in Figure 4.3a can be generated using Fourier series [161].

As such, the contraction of both the left and right ventricles is implemented by scaling the normalized curve, based on average values for E_{max}, E_{min}, and t_{Emax} from the literature [140, 164]; the corresponding patient-specific elastances for both ventricles can be found in Figure 4.3b and is calculated using Equation (4.7)

$$E(t) = E_{\min} + E_N(t)\left[E_{\max} - E_{\min}\right], \tag{4.7}$$

where $E_N(t)$ is the normalized time-varying elastance. By implementing the ventricular elastance model, the pressure within the corresponding chamber could be calculated based on Equation (4.8), as follows:

$$P(t) = E(t)\left[V(t) - V_0\right]. \tag{4.8}$$

Equation (4.8) is also utilized to calculate the pressure within the atria. However, in the case of the atria, as outlined above, the elastance term is not time-dependent.

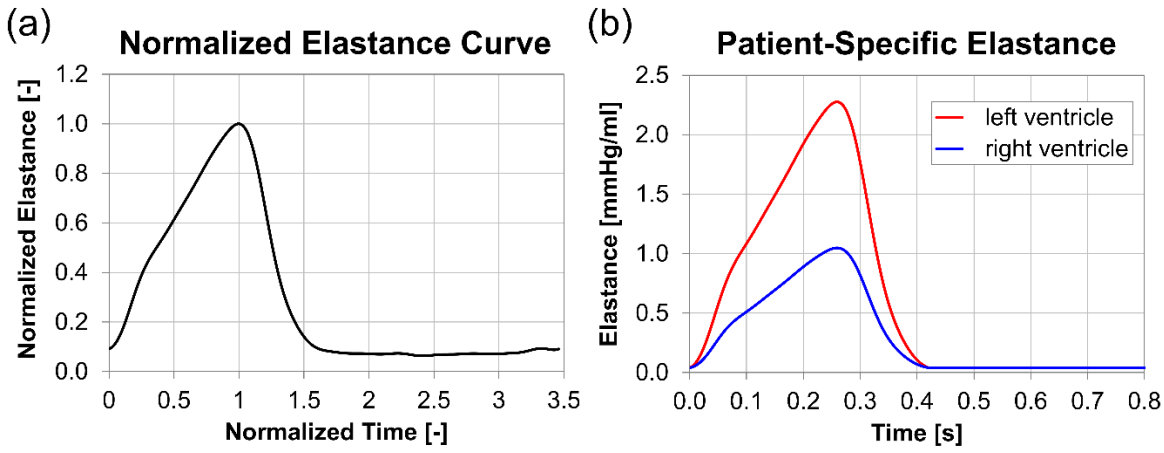

Figure 4.3: (a) Normalized elastance curve as a function of normalized time (with respect to the length of the cardiac cycle). The maximum normalized elastance (value of 1) occurs at the normalized time of 1 (b) patient-specific elastance curves for the left and right ventricles, scaled based on E_{max}, E_{min}, and t_{Emax} from the literature.

Each heart valve is modelled using a simple resistance, which represents the viscous friction across the valve orifice, and a diode, which denotes the state of the valve; linear models of the heart valves are implemented in order to simplify numerics [140, 164]. The state of the valve, which corresponds to whether it is open or closed, is governed by the transvalvular pressure gradient; therefore, with reference to Figure 4.2, the valve state, $S_{v,i}$, for valve, i, can be calculated using Equation (4.9):

$$S_{v,i} = \begin{cases} 1 & if\ \Delta P_{v,i} > 0 \\ 0 & if\ \Delta P_{v,i} \le 0 \end{cases}, \tag{4.9}$$

where $i = mit, ao, tri, pul$ for the mitral, aortic, tricuspid and pulmonary valves respectively and $\Delta P_{v,i}$ is the transvalvular pressure gradient across valve i [mmHg]:

$$\Delta P_{v,mit} = (P_{la} - P_{lv}), \tag{4.10}$$

$$\Delta P_{v,ao} = (P_{lv} - P_{ao}), \tag{4.11}$$

$$\Delta P_{v,tri} = (P_{ra} - P_{rv}), \tag{4.12}$$

$$\Delta P_{v,pul} = (P_{rv} - P_{pa}). \tag{4.13}$$

In Equations (4.10), (4.11), (4.12) and (4.13), the pressures within the heart chambers are calculated using Equation (4.8). Therefore, when the transvalvular pressure gradient is positive, the valve is open (1) and blood is allowed to flow through it, whereas when the transvalvular pressure gradient is zero or negative, the valve is closed (0) such that flow is inhibited.

Figure 4.4 displays the configurations of the systemic and pulmonary circulations. The model of the systemic circulation is based on those of Avanzolini *et al.* [165] and Mantero *et al.* [126] and consisted of a four-element Windkessel (WK) model of the aortic sinus and aorta, and a three-element WK model of the rest of the arterial system. The pulmonary circulation consisted of a three-element WK model which was shown by Kim *et al.* [140] to sufficiently model the corresponding dynamics.

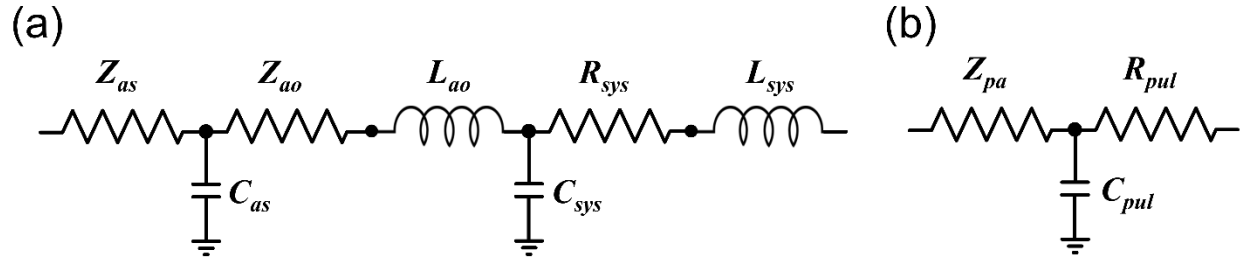

Figure 4.4: LPM of the (a) systemic and (b) pulmonic circulations. *as* aortic sinus, *ao* aortic, *sys* systemic, *pa* pulmonary artery, *pul* pulmonic.

The parameter values for the heart, systemic and pulmonary models, summarized in Table 4.3, are assigned based on literature values, and most prominently from the

models of Avanzolini *et al.* [165], Kim *et al.* [140, 141], Segers *et al*. [164] and sources therein.

Table 4.3: Parameter values for the left and right heart and systemic and pulmonic circulations. Units: E [mmHg·ml^{-1}], V [ml], P [mmHg], T [s], R [mmHg·s·ml^{-1}], C [ml·mmHg^{-1}], Z [mmHg·s·ml^{-1}], L [mmHg·s^2·ml^{-1}].

Heart			Systemic		Pulmonic	
	Left	Right				
E_{max}	2.5	1.2	Z_{cs}	0.01	Z_{pa}	0.0025
E_{min}	0.04	0.04	C_{cs}	0.1	C_p	4.5
t_{Emax}	0.26	0.26	Z_{ao}	0.07	R_p	0.3
E_a	0.08	0.07	L_{ao}	0.000825		
V_{0v}	0	20	C_s	1.1		
V_{0a}	0	20	R_s	2.0		
R_{av}	0.0005	0.0005	L_s	0.00036		
R_{vart}	0.0001	0.0001				

Systematic adjustments using an iterative procedure are made to individual parameter values based on *a priori* knowledge of the system dynamics so as to assess their effect on the flow and pressure at all points in the 0D model (in particular in the coronary circulation) and to select the values that generated flow and pressure curves that are most representative of *in vivo* conditions (as reported in the literature). In particular, a healthy hyperaemic LMCA of approximately 4.5ml·s^{-1} with a predominant diastolic flow profile and an average aortic pressure of approximately 100mmHg are sought [27, 166-168]. The parameter values are modified up to ±15 percent from their base values (as found in the literature), in increments of approximately 5 percent (values resulting from these adjustments are within physiological ranges) until the healthy hyperaemic LMCA and the average aortic pressure are within 5 percent of designated target, and the flow and pressure curves in the heart, systemic and pulmonic models displayed physiologic behaviour.

4.2.1.b Coronary model

The LPM of the coronary system, which includes only the left circulation, is subdivided into four subsections, namely the bifurcation of the LMCA into the LAD and the LCX, and the epicardial, myocardial and venous circulations, as is displayed in Figure 4.5. Right-dominant flow is considered, although the right coronary circulation is

disregarded due to the limited geometric data and ultimately for the simplification of numerics. The configuration of the coronary model is based primarily on those published by Pietrabissa *et al.* [127] and Wang *et al.* [128] as well as the coronary map provided in American Heart Association PCI guidelines [169]. The circulation of the LAD is modelled by the proximal, intermediate and distal vessel segments including the first and second diagonal branches. The *ramus intermedius* and the septal perforators are not included in order to simplify the numerics. Similarly, the proximal, intermediate and distal portions of the LCX are modelled including the first, second and third obtuse marginal branches.

In the epicardial circulation, including the LMCA bifurcation, each individual artery is represented by the 3-element WK model comprising the basic compartment unit presented in Figure 4.1.

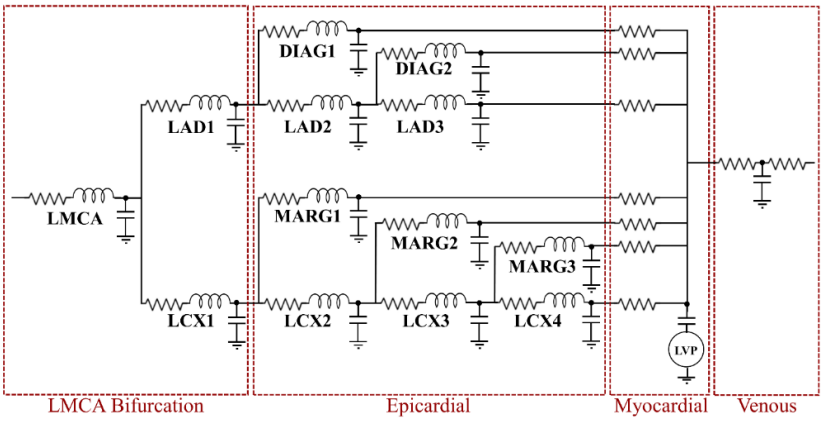

Figure 4.5: LPM of the left coronary circulation, including the LMCA bifurcation, epicardial, myocardial and venous submodels. LAD left anterior descending artery, LCX left circumflex artery, $DIAG$ diagonal, $MARG$ marginal, LVP left ventricular pressure.

This representation allowed for the parameter values to be calculated based on theoretical expressions and average geometric data from the literature. More specifically, the resistance and inductance values are calculated based on Equations (4.2) and (4.3) respectively, by employing a blood density of 1060kg·m^{-3} and a viscosity of 0.0035 Pa·s [45, 46, 136, 170, 171]; average values for the vessel diameters and lengths are taken from the literature [128, 172] and are summarized in Table 4.4 in conjunction with the corresponding resistance and inductance values. In order to eliminate assumptions regarding the material model and the vessel wall thickness, Equation (4.4) is not utilized

for the calculation of the vessel compliance. Rather, the volumetric arterial compliance, C, is deduced based on the average coronary arterial distensibility, according to Equation (4.14):

$$C = \frac{\pi D^2 l}{4} C_{norm} , \tag{4.14}$$

where C_{norm} [mmHg^{-1}] is the average distensibility, which is measured *in vivo* and assigned an average value of 0.002mmHg^{-1} from the literature [173-176]. The resulting compliance values employed in the model are also provided in Table 4.4.

Table 4.4: Epicardial coronary dimensions and parameter values used in the coronary LPM.

	Dx10^{-1} [cm]	l [cm]	R [mmHg·s·ml^{-1}]	L [mmHg·s^2·ml^{-1}]	C [ml·mmHg^{-1}]	R_{term} [mmHg·s·ml^{-1}]
LMCA	4.5	2.2	0.0580	0.0110	7.00x10^{-5}	-
LAD1	3.6	2.7	0.172	0.0211	0.000550	-
LCX1	3.4	2.3	0.160	0.0176	0.000363	-
LAD2	2.9	2.9	0.440	0.0350	0.000383	-
LAD3	1.7	6.9	8.86	0.242	0.000313	92.2
DIAG1	1.9	4.7	3.87	0.132	0.000267	76.6
DIAG2	1.9	2.2	1.81	0.0618	0.000125	76.6
LCX2	2.8	1.5	0.262	0.0194	0.000185	-
LCX3	1.7	2.1	2.70	0.0737	0.0000950	-
LCX4	1.3	3.9	14.6	0.234	0.000104	144
MARG1	1.7	3.5	4.49	0.123	0.000159	92.2
MARG2	1.7	3.0	3.85	0.105	0.000136	92.2
MARG3	1.7	3.7	4.75	0.130	0.000168	92.2

The circulation downstream each of the (terminal) epicardial arteries is modelled using a single resistance, R_{term}, representing the arterioles and arterial capillaries that provide the majority of the resistance to flow and account for the most significant pressure drop in the coronary circulation. The magnitude of the terminal resistances, which are determined for maximum hyperaemic conditions so as to calculate FFR, are approximated based on allometric scaling laws. More specifically, the total myocardial resistance, R_{tot} [mmHg·s·ml^{-1}] of the left coronary tree is estimated by assuming a direct relationship between the pressure drop and the flow:

$$\Delta P_{myo} = R_{tot} Q_{tot} , \tag{4.15}$$

where ΔP_{myo} [mmHg] is the pressure drop across the myocardium during diastole, and Q_{tot} [ml·s^{-1}] is the total average healthy myocardial flow. For the determination of the total myocardial resistance under maximal hyperaemic conditions, a total average hyperaemic healthy LMCA flow of 5.0 ml·s^{-1} is assumed. This value is based on a total average resting healthy LMCA flow of 1.0 ml·s^{-1} [46, 166, 177] and a coronary flow reserve (CFR) of 5.0 [27, 167, 168]. The CFR denotes the factor by which blood flow increases when hyperaemia is induced, and is thus defined as the ratio of the hyperaemic to resting flow.

Based on an average aortic and venous pressures of 96mmHg and 5mmHg respectively (and thus, a pressure drop of 91mmHg), the total left hyperaemic myocardial resistance is calculated to be 18mmHg·s·ml^{-1}. Each of the terminal resistances are then calculated using Equation (4.16):

$$R_{term} = R_{tot}\left[\frac{D_{term}}{D_{LMCA}}\right]^{-5/3}, \tag{4.16}$$

where R_{term} and R_{tot} are the terminal and total resistances respectively [mmHg·s·ml^{-1}] and D_{term} is the diameter of the terminal epicardial vessel [cm]. Equation (4.16) is derived based on scaling laws developed by Huo *et al.* [55, 178]. Table 4.4 presents the values of the terminal resistances.

In order to account for the predominant diastolic flow phenomenon and the compression of the endocardial arteries, a single compliance coupled with a pressure generator is added to the myocardial model distal to the terminal resistances. More specifically, the pressure generator had the same magnitude and phase as the left ventricular pressure (calculated within the heart model) and thus, accounted for the increase in intramyocardial pressure during ventricular systole. Finally, the venous circulation is represented by two resistances (corresponding to the microvascular and the epicardial veins) and a single capacitance representing venous compliance [127].

The particular coronary model configuration is developed for various reasons. This representation provides a logical analogy to the true coronary circulation and prevents

the loss of correspondence between the lumped parameters and vascular domain properties that occurs when too few parameters are used to describe a large vascular territory. This idea is especially important since the dynamics of the coronary circulation constitute the main focus of the work. Furthermore, functional significance of the coronary lesions is assessed under maximum hyperaemia which is clinically induced with the injection of adenosine within the coronary circulation. Adenosine targets the microvasculature (arterioles and primarily capillaries) and induces maximal vasodilation, while having a limited influence on the epicardial arteries and the rest of the cardiovascular system. This phenomenon is simple to implement, as it corresponded to a decrease in the downstream terminal myocardial bed resistance.

4.2.2 Results of the lumped-parameter model simulation

Figure 4.6 displays the full LPM of the cardiovascular system, obtained by combining the subsystems presented in Figure 4.2, Figure 4.4 and Figure 4.5. Appendix B provides the nonlinear system of ODEs describing the dynamics of the full LPM provided in Figure 4.6; it is solved using a fourth-order Runge-Kutta method through an in-house C++ code (details provided in Appendix C).

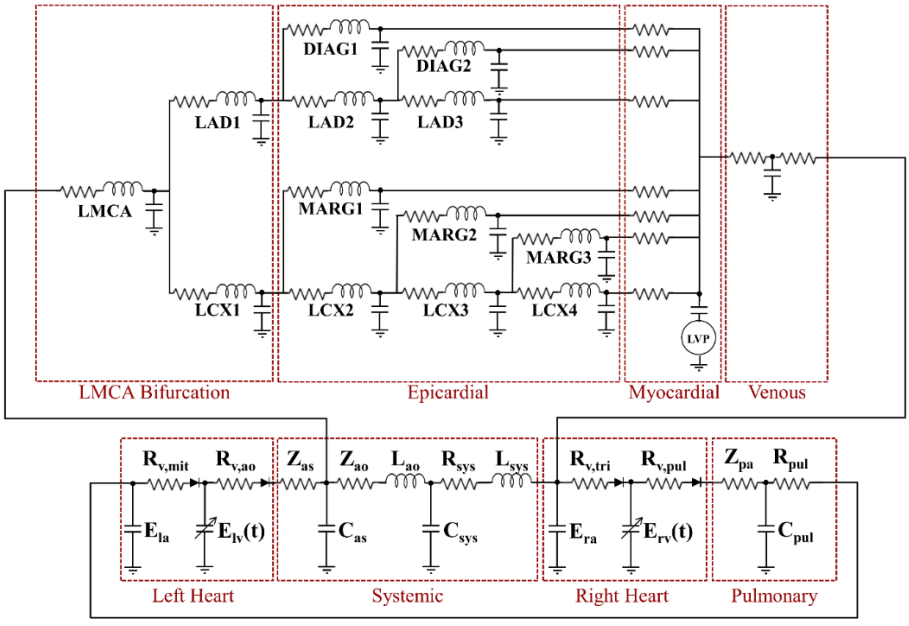

Figure 4.6: Full lumped-parameter model of the cardiovascular system including the left and right hearts, the systemic and pulmonic circulations and the left coronary circulation.

Examples of the results from the numerical integration of the full LPM are provided. Figure 4.7 displays computed parameters for the heart, systemic and pulmonary circulations. All parameters display physiological behaviour compared to values reported in the literature [126, 127, 140, 141, 159, 164, 165].

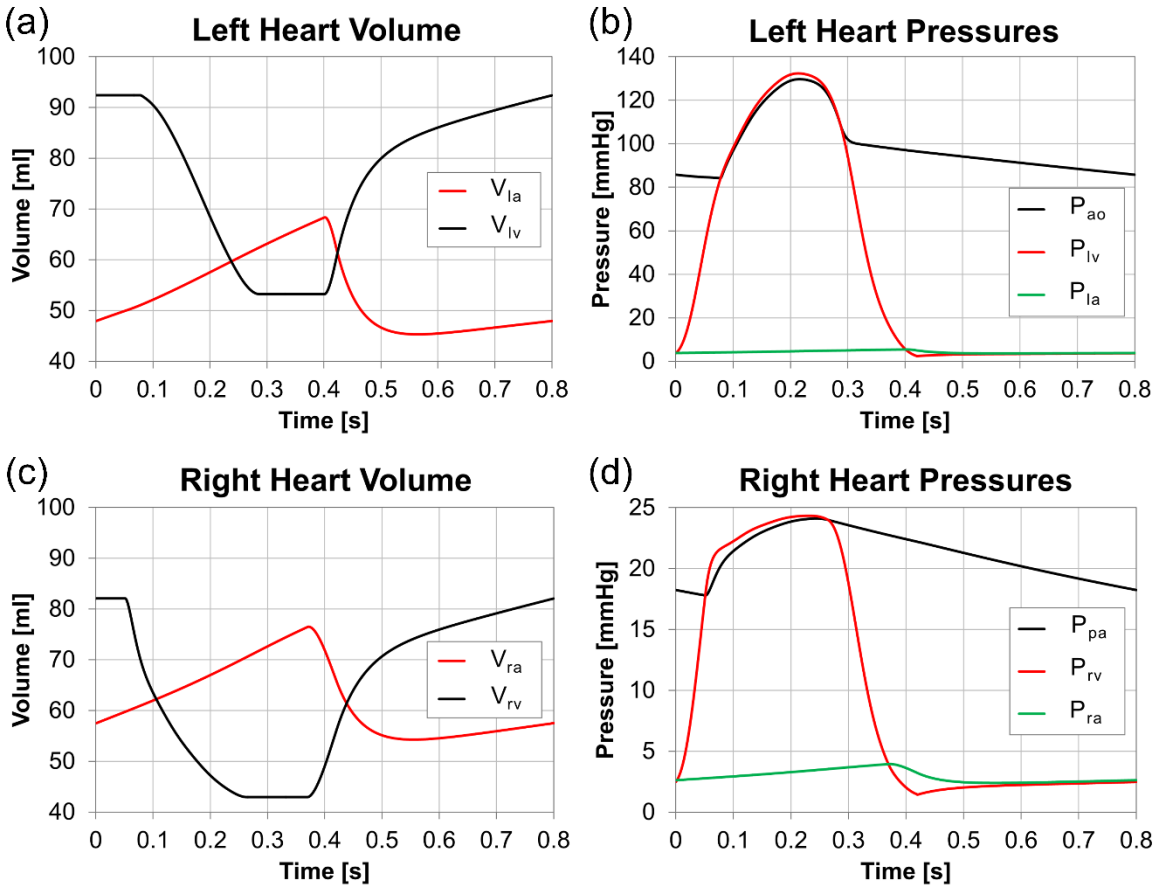

Figure 4.7: Results of the numerical integration of the full LPM model. State variables for the heart, systemic and pulmonary circulations are displayed. (a) Left heart volumes (b) left heart pressures (including aortic pressure) (c) right heart volumes and (d) right heart pressures (including the pulmonary artery pressure).

For example, in both the curves of the left and right ventricular volumes, aortic pressure varies between 85mmHg and 130mmHg during the diastolic and systolic phases, while pulmonary artery pressure, displays markedly lower pressure, ranging between 18mmHg and 24mmHg. Figure 4.8 displays the pressure-volume curves of the left and right ventricles over a single cardiac cycle; isovolumetric contraction and expansion can be readily observed.

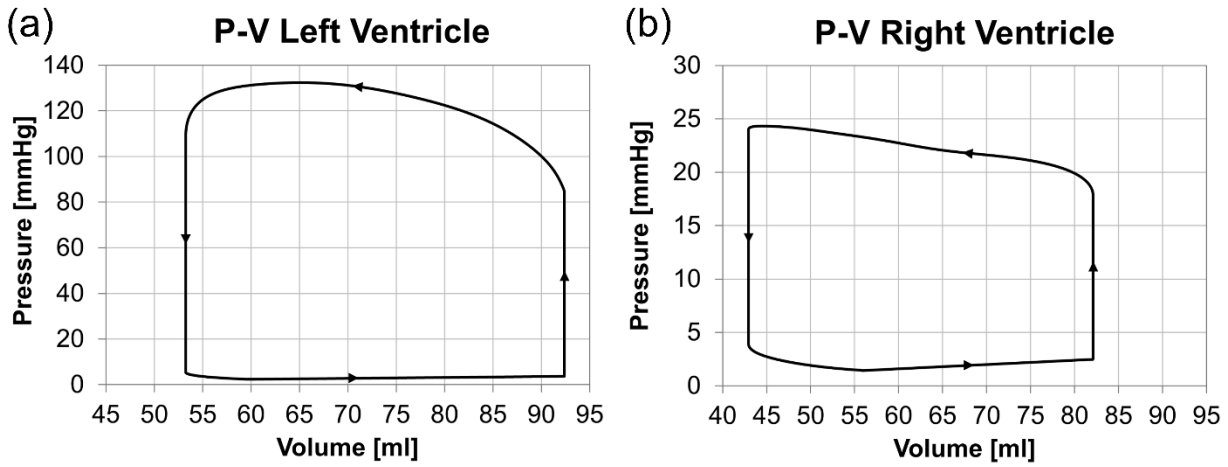

Figure 4.8: Pressure-volume curves for the (a) left and (b) right ventricles, as obtained from the numerical integration of the full LPM.

The coronary pressures obtained from the numerical integration of the full LPM are displayed in Figure 4.9. One can observe from Figure 4.9 that the time-dependent pressure profiles exhibit small deviations from aortic pressure, in particular for cases of the most proximal vessels; the terminal vessels display the largest difference from aortic pressure. These observations signify that the epicardial coronary arteries of the LPM manifest small pressure drops along their lengths. This result is further justified by the pressure-derived FFR values for the corresponding vessels, which are provided in Table 4.5. In Table 4.5, one can observe that in the most proximal epicardial vessels, namely within the second bifurcation, the FFR values remain at 0.99. The terminal portion of the LCX displays the lowest FFR value, which corresponds to a total pressure drop of 9 percent. These results are in good accordance with clinical measurement for healthy coronary vessels [22, 31].

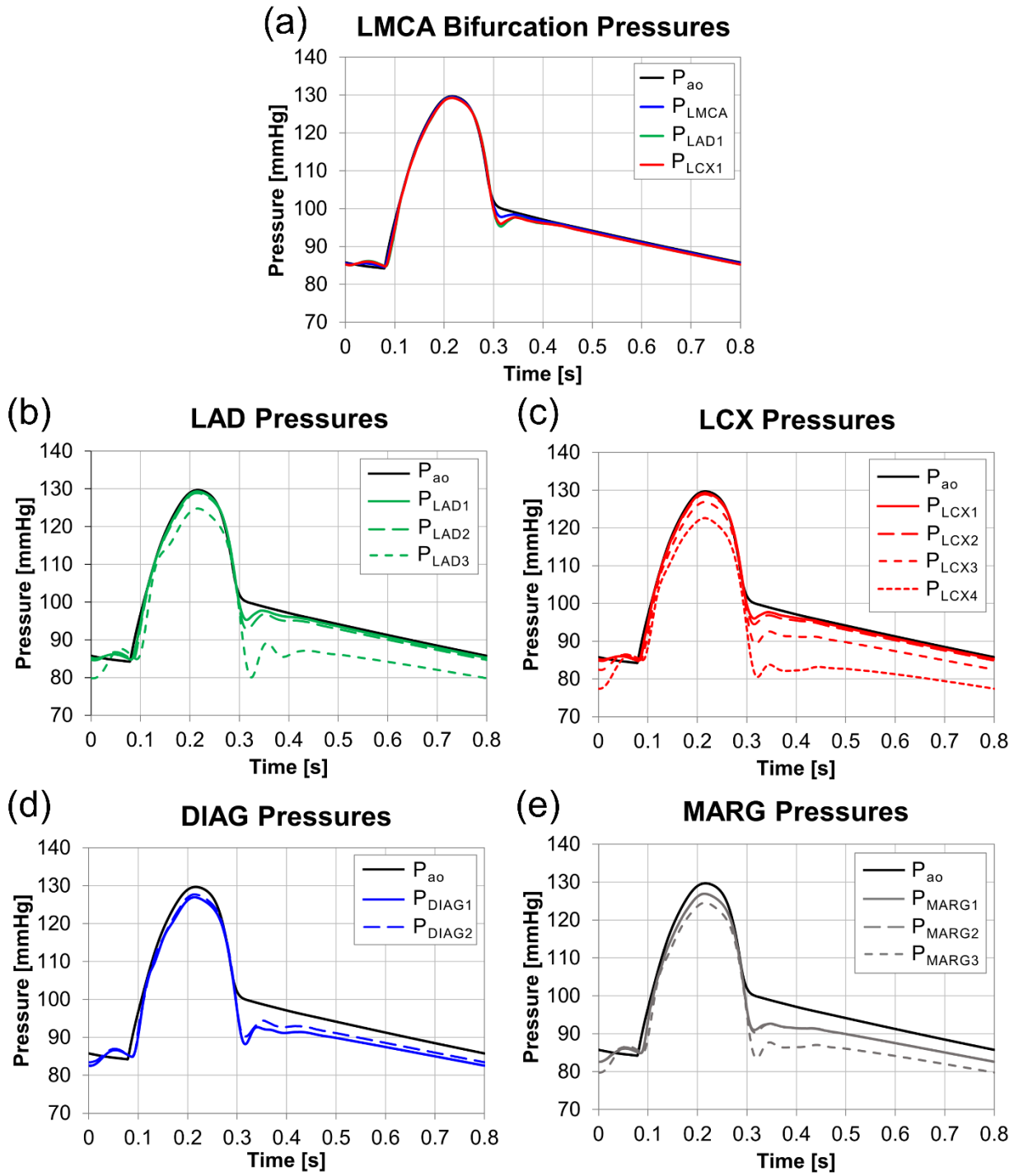

Figure 4.9: Coronary pressures in the (a) LMCA bifurcation (b) LAD (c) LCX (d) DIAG and (e) MARG as obtained from the numerical integration of the full LPM.

Table 4.5: Pressure-derived FFR values and average flow rates for each of the coronary vessels of the full LPM model.

Vessel	Pressure-Derived FFR [-]	Average Flowrates [ml·s^{-1}]
LMCA	1.00	4.42
LAD1	0.99	2.16
LCX1	0.99	2.26
LAD2	0.99	1.39
LAD3	0.93	0.607
LCX2	0.99	1.62
LCX3	0.96	0.978
LCX4	0.91	0.371
DIAG1	0.96	0.770
DIAG2	0.97	0.782
MARG1	0.96	0.641
MARG2	0.96	0.641
MARG3	0.93	0.608

The derived flowrates for each of the epicardial coronary arteries are displayed in Figure 4.10. One can observe from this figure that the peak coronary flow occurred at the onset of diastole, specifically at around t=0.4s; the flow remains high during the rest of the diastolic period thus, demonstrating the distinct flow characteristics of the left coronary system. For corroboration of the model, the computed average flow rates within the LMCA, LAD1 and LCX1 are compared to the literature due to the availability of the clinical measurement for these vessels. The resulting average healthy hyperaemic flow rates for all the epicardial coronary vessels are provided in Table 4.5; within the LMCA, LAD1 and LCX1, the computed flowrates are 4.4 ml·s^{-1}, 2.2 ml·s^{-1} and 2.3 ml·s^{-1} respectively. These values are in accordance with the range of healthy hyperaemic coronary flows found in the literature. For example, Geven *et al.* [166] reported healthy hyperaemic LMCA flows between 4.2 and 5.0 ml·s^{-1}. Furthermore, for an average resting LMCA flow of approximately 1.0 ml·s^{-1} [46, 166, 177] the computed healthy hyperaemic flow corresponds to a CFR of approximately 4.4. In the literature, the CFR has been reported to range between 4 and 6 [27, 167, 168]. The ratio of the healthy hyperaemic LAD to LCX flow is also determined in order to verify the computed daughter vessel flows. The value of 0.96 calculated for this ratio corresponds well with those reported in the literature, which range between 0.7 and 2 [110, 140, 142, 179-181].

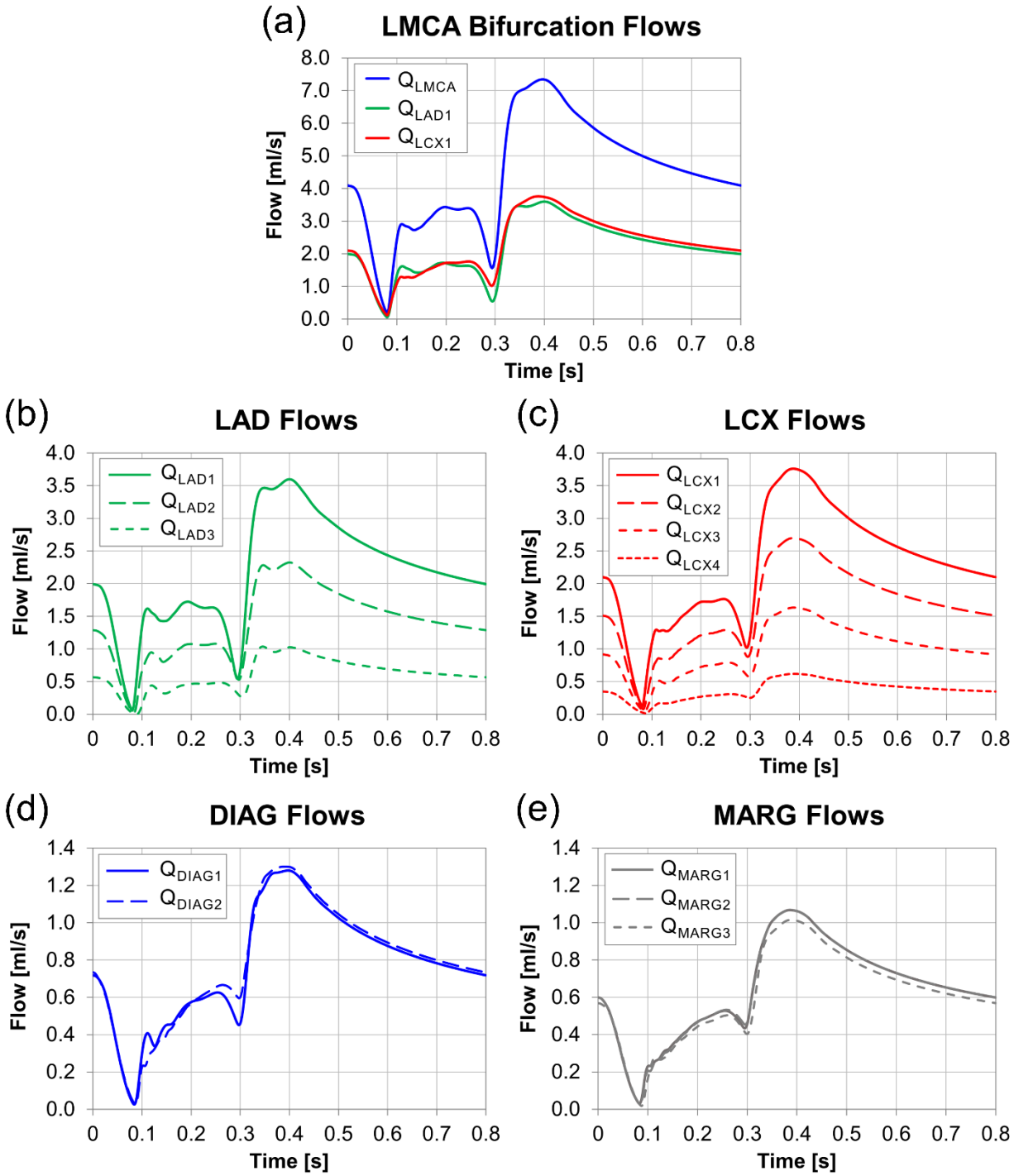

Figure 4.10: Coronary flows in the (a) LMCA bifurcation (b) LAD (c) LCX (d) DIAG and (e) MARG as obtained from the numerical integration of the full LPM.

4.2.3 Summary

In this chapter, the lumped-parameter model of the entire cardiovascular system, including the left and right hearts, the systemic and pulmonic circulations, and the left

coronary circulation, was developed. The system of ODEs modelling the dynamics of the 0D configuration were solved using an in-house code in C++. The computed dynamics display physiological behaviour, as corroborated using literature values. The development and implementation of the lumped-parameter model constitutes an integral part of the thesis as the 0D model will eventually be coupled with the 3D model of the coronary bifurcation lesions so as to assess functionality and therefore fulfill the first objective of the thesis. The physiological behaviour of the developed model, as was demonstrated in this chapter, is central to the calculation of the Fractional Flow Reserve from the multiscale simulations.

5

THE THREE-DIMENSIONAL CORONARY BIFURCATION LESION MODEL

This chapter presents the three-dimensional model of the LMCA bifurcation which is developed and utilized in the research. Specifically, it details the geometry of both the healthy and diseased bifurcation, the governing equations and assumptions associated with the numerical model, and the solution methods. The presented three-dimensional model replaces its lumped-parameter equivalent (provided in Figure 4.6) and is ultimately coupled numerically with the 0D model in order to provide localized flow characteristics in the corresponding domain.

5.1 GEOMETRY OF THE 3D CBL MODEL

Approximately 4 to 6 percent of patients presenting for coronary angiography display disease of the LMCA. This subset of disease is especially important because the LMCA is responsible, in a high proportion of patients, for the majority of the blood supply of the left ventricle and its occlusion poses a high risk of mortality. Interestingly, isolated LMCA disease is rare; at least 50 percent of patients with atherosclerosis in this vessel involves the LMCA bifurcation, which poses the greatest difficulties for intervention [182]. Consequently, the LMCA bifurcation is selected for the study of the functionality of CBLs.

5.1.1 Healthy LMCA bifurcation

An idealized and synthetic representation of the bifurcation of the LMCA is utilized in the numerical simulations; all vessels are straight, with circular cross-sections and the bifurcation is planar. The geometry of the healthy (baseline) model is displayed in Figure 5.1 and the dimensions denoted in the figure are provided in Table 5.1. These dimensions are based on average values from the literature [45, 46, 128, 156, 172, 182, 183].

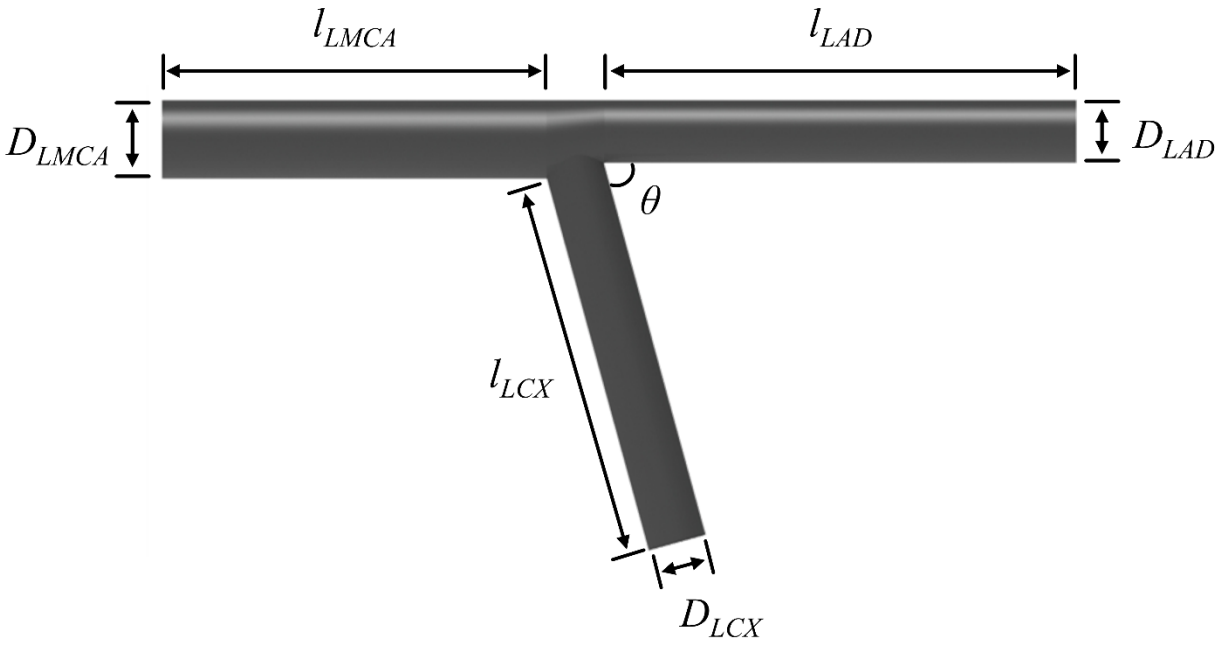

Figure 5.1: Geometry of the healthy 3D LMCA bifurcation model. D is the diameter; l is the length; θ is the angle between the LAD and the LCX.

Table 5.1: Dimensions of the 3D healthy (baseline) model of the LMCA bifurcation

Vessel	Diameter, D [cm]	Length, l [cm]	Angle, θ [º]
LMCA	0.45	2.2	-
LAD	0.36	2.7	73
LCX	0.34	2.3	

In vivo, coronary geometry is curved, tapered and tortuous [184, 185]. While a more realistic (patient-specific) geometry could potentially provide a more accurate representation of the *in vivo* flow environment, coronary vascular geometry exhibits significant inter-patient variation; as such, by using a controlled and simplified computer-generated geometry, it is possible isolate the effect of various geometric and morphological parameters of both the baseline coronary bifurcation and of the stenoses

on the corresponding flow and pressure fields. In addition, inertial pressure losses rather than viscous effects (which are most significantly influenced by vessel curvature) are expected to dominate in the translesional pressure drop as a result of the significant diameter reductions and the hyperaemic flow conditions. Therefore, the use of idealized geometries is justified.

5.1.2 Disease configurations and stenosis profile

The diseased states within the LMCA bifurcation, or in other words, the different CBL configurations, are developed here based on the Medina classification [186]. The Medina classification is selected due to the fact that its simplicity and intuitive nature have made it widely adopted in clinic [5, 101]. It constitutes a binary system that denotes either the presence (1) or the absence (0) of a stenosis with a diameter reduction greater than 50 percent in each vessel of the bifurcation as follows: (Proximal Main Vessel, Distal Main Vessel, Side Branch). Consequently, the specific classification system results in seven different lesion arrangements which are outlined in Figure 5.2.

The baseline stenosis model employed in the CBL configurations is displayed in Figure 5.3. It is taken to be concentric and axisymmetric, with a cosine profile, described by Equation (5.1) [82]:

$$R = R_0\left[1-\frac{\delta}{2R_0}\left(1+\cos\left(\frac{\pi z}{l_s}\right)\right)\right], \tag{5.1}$$

where R and R_0 are the radii of the stenosed and healthy portions of the artery respectively [cm], δ is the maximum height of the stenosis profile (based on the percent diameter reduction) [cm], z is the distance from the proximal side of the stenosis ($0 \le z \le l_s$) [cm] and l_s is the length of the base of the stenosis [cm]. In the baseline diseased model, all stenoses are placed at the bifurcation carina, and had a base length of 1.0cm [187-189].

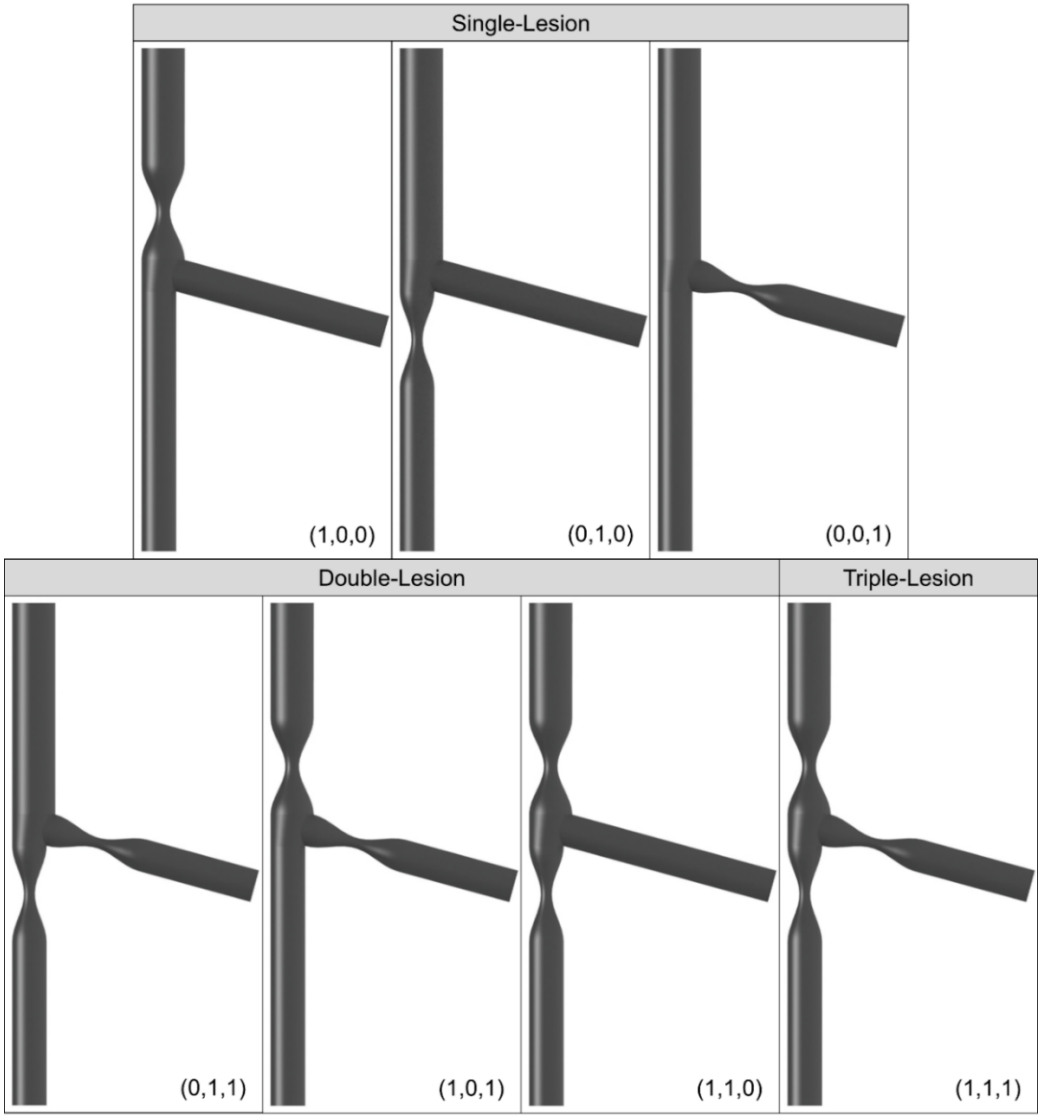

Figure 5.2: The seven baseline CBL configurations derived from the Medina classification, with diameter reductions of 68 percent.

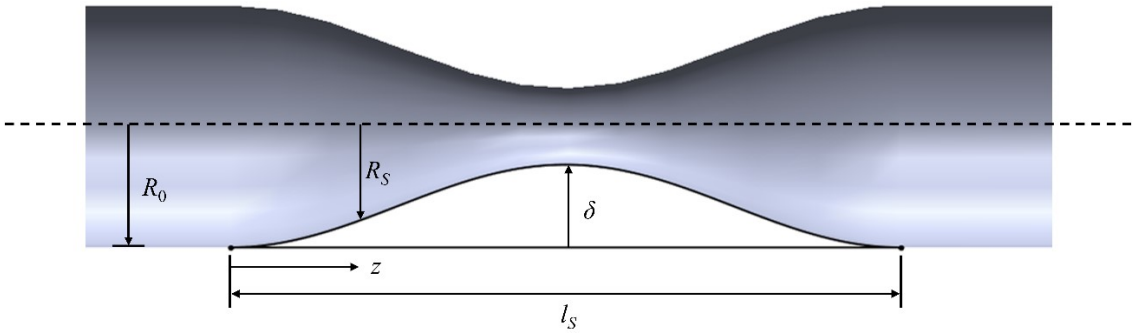

Figure 5.3: Cosine stenosis profile utilized for the CBL models. R_0 is the heathy vessel radius, R is the stenosed radius at a distance z from the proximal side of the stenosis, along its base (with total length Z_0) and δ is the maximum stenosis height.

5.2 GOVERNING EQUATIONS AND MODEL ASSUMPTIONS

The fluid domain, denoted by Ω, is displayed in Figure 5.4; its dynamics are modelled using the transient, incompressible and Newtonian Navier-Stokes equations (NSE), as provided in Equation (5.2):

$$\begin{cases} \nabla \cdot \vec{u} = 0 \\ \rho\left(\frac{\partial \vec{u}}{\partial t} + \vec{u} \cdot \nabla \vec{u}\right) + \nabla p - \mu \nabla^2 \vec{u} = 0 \end{cases} \quad \text{on } \Omega \times (0,T), \tag{5.2}$$

where $\vec{u}$ and p are the fluid velocity and pressure respectively and T is the length of one cardiac cycle (assigned a value of 0.8s based on an average heart rate of 75 beats per minute). The density of blood is taken to be 1060 kg·m^{-3} [136, 170, 171]. The boundaries of the model, Γ, consist of the inlet (LMCA), the two outlets (LAD, LCX), and the wall, as presented in Figure 5.4.

Under healthy conditions, coronary arteries have been shown to experience lumen distensions up to 10 percent and therefore circumferential strains of approximately 5 percent [190]. However, the walls of diseased vessels are stiffened and thus, experience significantly smaller distensions compared to their healthy counterparts.

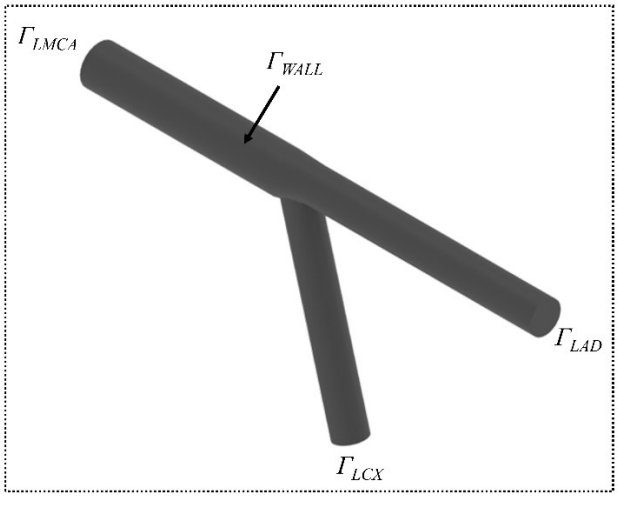

Figure 5.4: 3D model of the bifurcation of the LMCA bifurcation. Ω denotes the entire fluid domain, and Γ denotes the boundaries of the model.

Shaw *et al.* [176] and Kelle *et al.* [175] executed separate studies that measured the *in vivo* compliance of proximal coronary vessels in both diseased and healthy patients, using intravascular ultrasound (IVUS) and magnetic resonance imaging (MRI) respectively. Shaw *et al.* [176] found an average peak circumferential strain of 2.2 percent in the diseased case and 3.8 percent in the healthy case; similarly Kelle *et al.* [175] found average peak circumferential strains of 3.7 percent and 5.1 percent in the diseased and healthy cases respectively. Therefore, due to the fact that diseased coronary arteries experience very small strains under physiological conditions, the walls of the 3D LMCA bifurcation are modelled as rigid.

Blood is a fluid that constitutes a suspension of red and white blood cells, platelets and solutes and proteins within plasma. The presence of non-spherical and deformable red blood cells, which also have the tendency to aggregate and form rouleaux ("stacks" of cells), render the behaviour of whole blood non-Newtonian. More specifically, blood flow is initiated after an initial (yield) stress is overcome, which is linked to the breaking of the rouleaux. Subsequently, with increasing shear rate, the apparent viscosity of blood decreases abruptly (shear-thinning behaviour) until an asymptotically constant value (Newtonian behaviour) is reached and maintained at high shear rates [159, 191]. Figure 5.5 displays the shear dependence of the apparent blood viscosity; one can observe that the constant asymptotic apparent viscosity is reached at a shear rate between $100s^{-1}$ and $200s^{-1}$, after which blood behaves as a Newtonian fluid [159, 192-194]. Therefore, the exhibition of non-Newtonian or Newtonian properties is dependent on the nature of the flow rather than that of the blood itself. Localized and low shear phenomena (such as in the microcirculation, recirculation zones, stented arteries, etc.) require a non-Newtonian model (power law, Casson, Carreau, etc.) to be employed for accurate WSS to be computed. Conversely, flow in vessels wherein the effective length scales (vessel diameter) are orders of magnitude larger than the effective length scale of a red blood cell (such that blood can be considered a homogeneous fluid) and shear rates surpass the suggested $100s^{-1}$, the Newtonian flow assumption can be implemented [195].

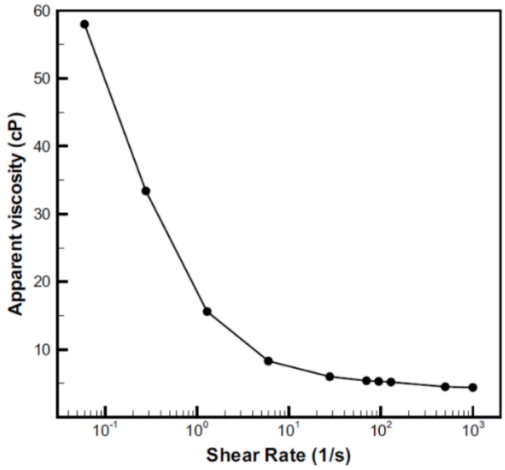

Figure 5.5: Dependence of apparent blood viscosity on shear rate (with permission from [191]).

Due to the caliber of and the flow within the epicardial coronary arteries, which result in shear rates above the determined threshold for the initiation of non-Newtonian behaviour, the assumption of Newtonian flow is justified [100, 193] and is implemented in the presented model of the LMCA bifurcation. This assumption is further supported due to the fact that hyperaemic flow conditions are simulated. Moreover, although stenoses of significant diameter reduction are simulated thus, inducing regions exhibiting low shear rates, the use of a Newtonian blood model is deemed acceptable due to the fact that localized WSS patterns are not sought in the study. The viscosity is assigned a constant value of 0.0035Pa·s based on the literature [159, 191, 195].

Studies have shown that blood flow can transition from a laminar to turbulent regime at low Reynolds numbers in stenosed vessels [196-198]; specifically a critical Reynolds number of approximately 500 has been suggested, although several studies have demonstrated this transition at both lower and higher Reynolds numbers [199-201]. Laminar flow is assumed in the numerical model, and is retrospectively justified based on the peak inlet Reynolds (Re) number, which is evaluated for the LMCA, LAD and LCX, for each configuration and stenosis severity. The peak Reynolds number is based on the peak volumetric flowrate and the diameter of the corresponding native (healthy) vessel. The results are provided in Table 5.2 for the (0,0,0) configurations, and in Table 5.3 and Table 5.4 for the single-lesion and multilesional configurations with diameter reduction of 50 percent and greater respectively.

Table 5.2: Peak Reynolds Number for the (0,0,0) configurations in the LMCA, LAD and LCX. The location of stenoses of 41 percent diameter reduction are provided.

	Peak Reynolds Number [-]						
	(0,0,0)						
	(41,0,0)	**(0,41,0)**	**(0,0,41)**	**(41,41,0)**	**(41,41,41)**	**(41,0,41)**	**(0,41,41)**
LMCA	596	611	610	593	586	591	602
LAD	396	394	404	370	369	377	373
LCX	424	443	429	402	390	392	403

Table 5.3: Peak Reynolds number for the single-lesion configurations with diameter reductions of 50 percent and greater in the LMCA, LAD and LCX.

	Peak Reynolds Number [-]								
	(1,0,0)			**(0,1,0)**			**(0,0,1)**		
	50%	**61%**	**68%**	**50%**	**61%**	**68%**	**50%**	**61%**	**68%**
LMCA	573	508	427	603	578	546	598	566	535
LAD	393	369	320	381	344	299	406	410	417
LCX	414	355	305	445	448	455	410	360	309

Table 5.4: Peak Reynolds number for the multilesional configurations with diameter reductions of 50 percent and greater in the LMCA, LAD and LCX.

	Peak Reynolds Number [-]											
	(1,1,0)			**(1,1,1)**			**(1,0,1)**			**(0,1,1)**		
	50%	**61%**	**68%**	**50%**	**61%**	**68%**	**50%**	**61%**	**68%**	**50%**	**61%**	**68%**
LMCA	567	496	281	558	471	388	563	485	404	583	524	450
LAD	361	331	171	367	325	282	378	350	311	363	330	286
LCX	383	363	191	366	294	229	357	284	214	388	345	293

From Table 5.2, Table 5.3 and Table 5.4, one can observe that for the LAD and LCX, the peak Reynolds number remains below 450 for all configurations and stenosis severities. With regard to the peak inlet (LMCA) Reynolds number, for the (0,0,0) configurations with lesions of 41 percent diameter reduction in the LMCA, it can be observed that the maximum value is 596. Similarly, in Table 5.3 and Table 5.4, for the configurations with stenoses in the LMCA, the peak inlet Reynolds number only surpasses the threshold of 500 for diameter reductions of 50 percent. For more severe stenoses, the peak Reynolds number remained below 500.

The incorporation of a turbulent regime would require a significant refinement of the spatial discretization thus, resulting in an increase in computational time [132, 202]. This assumption is therefore critical in this research due to the parametric nature of the work as well as the increase in computational time resulting from the multiscale algorithm.

Furthermore, studies have shown that many turbulence schemes available in commercial software packages, such as ANSYS Fluent, are still facing challenges to accurately capture low-Reynolds number transition to turbulence characteristics in post-stenotic regions [202, 203]. As such, due to these problems in turbulence modelling, the increased computational time, and the retrospective quantification of the Reynolds number the application of a laminar flow regime is justified for the scope of the research.

The mathematical model is initialized with conditions at time $t=0$ on the velocity, namely $\vec{u} = \vec{u}_0$. The initial conditions are obtained from a steady-state solution wherein average pressures, obtained from the solution of the full LPM of the healthy case, are applied as boundary conditions. As the vessel segment is taken to be rigid, a no-slip constraint is applied on the wall of the model, Γ_{WALL}. Details regarding the boundary conditions on $\Gamma_{LMCA,}\Gamma_{LAD}$ and Γ_{LCX} are provided in subsequent sections; these boundaries serve as interfaces between the 3D and 0D model and therefore, their conditions are dependent on the mathematical formulation of the 0D model.

5.3 SOLUTION METHODS

Analytical derivation of the solution of nonlinear partial differential equations, such as the Navier-Stokes Equations, provided in Equation (5.2), is not possible for the problem considered here. Therefore numerical integration techniques are used. More specifically, these techniques convert the continuous form of the nonlinear governing equations to a system of algebraic equations that represent the system dynamics at a finite number of discrete points within the domain of interest. Over the years, several discretization techniques have been developed and employed in various commercial flow software packages, such the Finite Element Method, the Finite Volume Method, Finite Difference Method, etc. In the present work, the commercial software package ANSYS Fluent (Canonsburg, PA, USA) is selected for the transient flow simulations of the 3D coronary bifurcation lesion models; this choice is based on the software's capabilities to robustly accommodate in-house user-defined functions, which are essential for the implementation of the multiscale algorithm (outlined in subsequent sections). The ANSYS

Fluent software package utilizes a cell-centered Finite Volume Method (FVM) for the discretization of the governing equations.

Fundamentally, this technique involves the division of the domain of interest into a finite number of control volumes, which are defined by the elements/cells of the discretized (meshed) geometry. The integral form of the conservation equations are derived over each control volume, which, using the divergence theorem, are expressed in terms of surface integrals wherein the balance of fluxes through each surface of the control volume is enforced. An overview of the Finite Volume Method, including the spatial and temporal discretization of the governing equations, the linearization of the algebraic equations and the solution method are provided in Appendix D.

5.4 SENSITIVITY ANALYSES

5.4.1 Mesh sensitivity

The geometry is discretized into unstructured viscous hybrid meshes consisting of tetrahedral and prismatic elements that are generated using ANSYS meshing. A patch-independent algorithm is employed wherein a volume tetrahedral-based mesh is first generated for the entire geometry. Subsequently, the boundary surface mesh and the boundary layer, consisting of prismatic elements, are generated using the smooth inflation option with a total of 5 layers and a growth rate of 1.2. Figure 5.6 shows a cross-section wherein both the boundary layer and the interior tetrahedral domain are displayed.

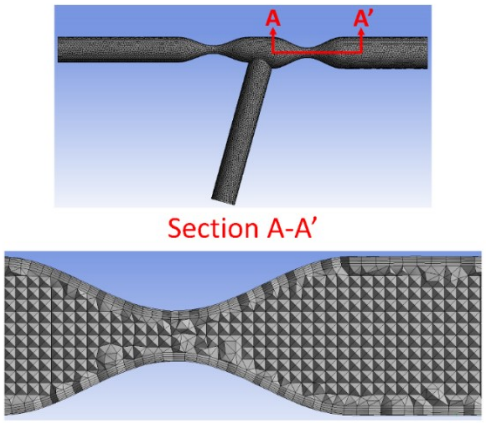

Figure 5.6: LMCA stenosis cross-section displaying the boundary layer and tetrahedral mesh.

A mesh sensitivity analysis is performed in order to determine whether the computed solution is independent of the grid resolution. Three mesh densities, namely coarse (~135,000 elements), medium (~280,000 elements) and fine (~520,000 elements), are evaluated for the (1,1,0) and (1,1,1) configurations with stenoses of 68 percent diameter reductions. Figure 5.7 and Figure 5.8 display the three meshes for the (1,1,0) and (1,1,1) configurations respectively.

Table 5.5 summarizes the mesh metrics, including element skewness and orthogonality, for the (1,1,0) and (1,1,1) configurations.

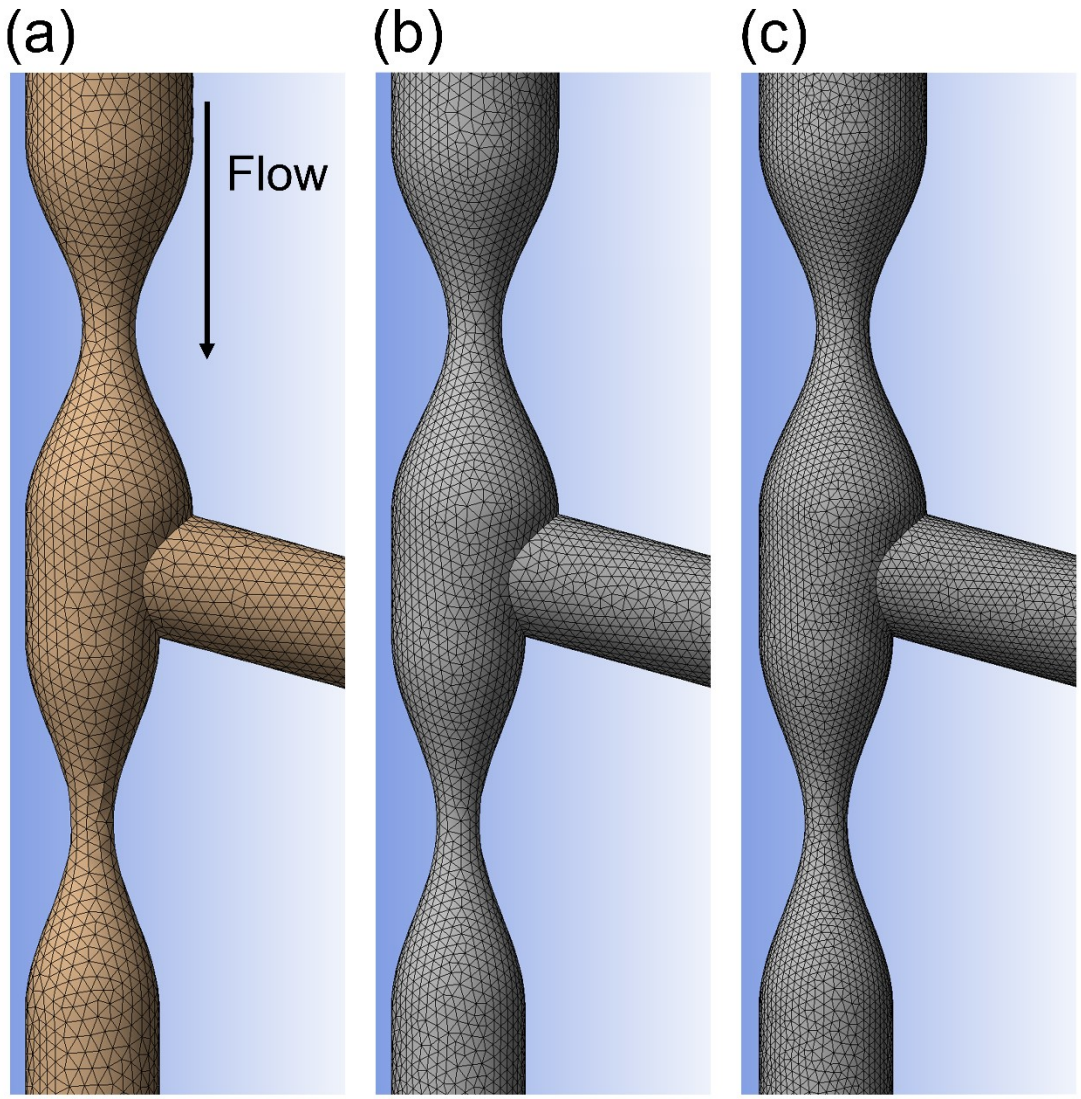

Figure 5.7: (a) Coarse (b) medium (c) fine meshes for the (1,1,0) configuration.

Table 5.5: Mesh metrics from the mesh sensitivity analysis for the (1,1,0) and (1,1,1) lesion configurations with 68 percent diameter reduction.

		(1,1,0)			(1,1,1)		
		Coarse	**Medium**	**Fine**	**Coarse**	**Medium**	**Fine**
Number of elements		134,948	280,389	525,507	136,976	282,184	519,355
Number of nodes		44,228	83,062	145,068	44,930	83,706	143,201
Skewness	**Min**	0.00251	0.00402	0.00128	0.00618	0.00376	0.00267
	Max	0.780	0.760	0.823	0.792	0.796	0.721
Orthogonality	**Min**	0.258	0.281	0.210	0.248	0.334	0.335
	Max	0.999	0.999	0.999	0.999	0.999	0.999

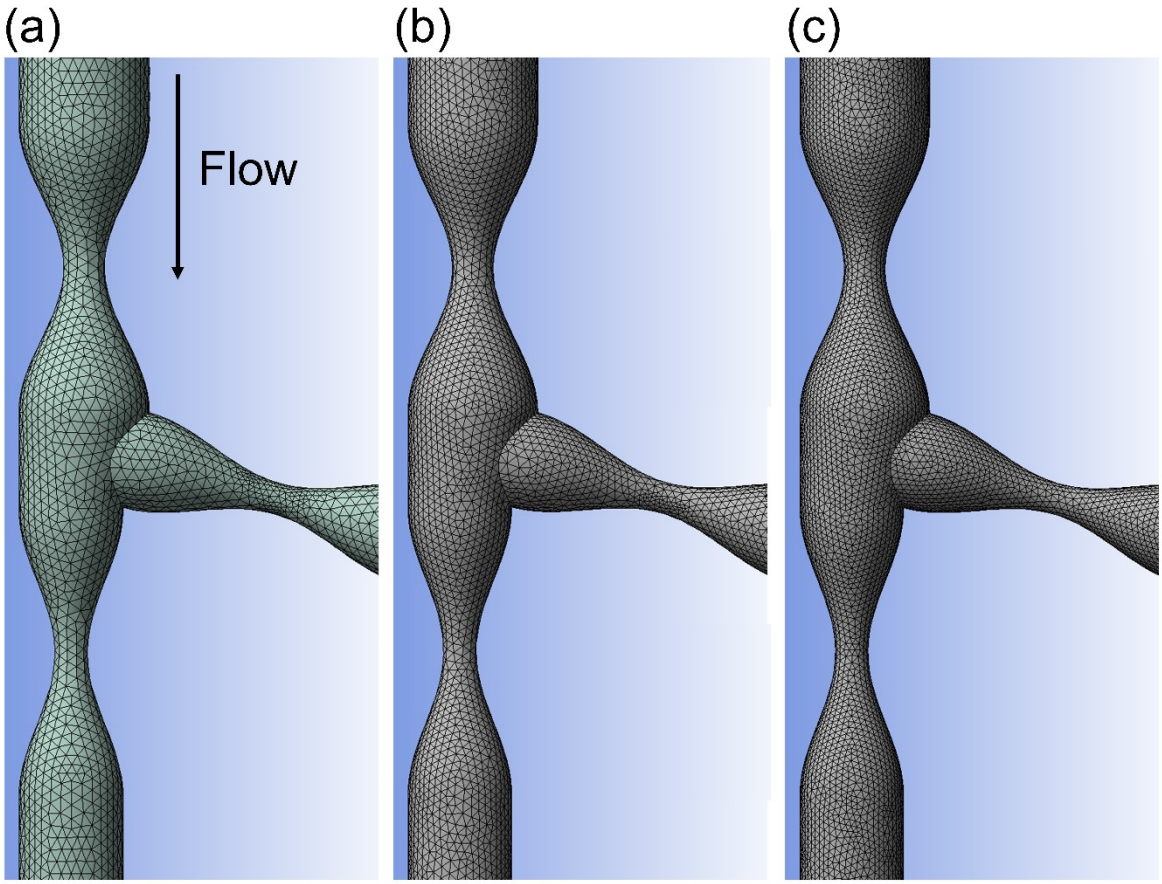

Figure 5.8: (a) Coarse (b) medium (c) fine meshes for the (1,1,1) configuration.

Transient simulations are executed for each of the mesh densities. The percent relative difference, $Diff_r$ [%] given in Equation (5.3), is used to characterize the difference in each of the parameters between each mesh density and the fine mesh:

$$Diff_r = \frac{\left| x_i - x_{fine} \right|}{x_{fine}} \times 100 \,, \tag{5.3}$$

where x is the evaluated parameter and i is the mesh density (coarse, medium). The parameters used to assess mesh convergence are the average boundary pressures and the average boundary flows, based on similar studies employing geometric multiscale models [131, 132, 134, 135, 138]. A total of six cycles (for the multiscale simulations, see Chapter 6) are simulated and the parameters are averaged over cycles 2-6 and cycles 2-4. The results of the relative difference are provided in Table 5.6 for the (1,1,0) configuration and in Table 5.7 for the (1,1,1) configuration. The differences are presented based on averages taken between cycles 2-4.

Table 5.6: Relative differences for the average boundary pressures and flows between the different mesh densities for the (1,1,0).

		Relative Difference [%]	
		Coarse-Fine	**Medium-Fine**
Average Boundary Pressures	**Aortic**	0.010	0.0010
	LAD	0.43	0.64
	LCX	0.54	0.17
Average Boundary Flowrates	**LMCA**	0.19	0.24
	LAD	1.6	0.89
	LCX	1.2	0.39

Table 5.7: Relative difference for the average boundary pressures and flows between the different mesh densities for the (1,1,1).

		Relative Difference [%]	
		Coarse-Fine	**Medium-Fine**
Average Boundary Pressures	**Aortic**	0.0035	0.011
	LAD	1.1	0.33
	LCX	0.68	0.063
Average Boundary Flowrates	**LMCA**	0.44	0.13
	LAD	2.0	0.37
	LCX	1.5	0.17

Relative differences remained below one percent for the boundary pressures and flow in both configurations between the medium and fine mesh. Between the coarse and fine mesh, percent differences up to two percent are observed for the two outlet boundary flowrates in both configurations. Similar differences are observed for the parameter

values when averaged over cycles 2-6. Based on the results of the mesh sensitivity, the medium mesh is ultimately selected and applied for the remaining simulations.

5.4.2 Timestep sensitivity

A sensitivity analysis is performed for the length of the transient simulation timestep. Three timesteps, namely 2.0×10^{-4} s, 1.0×10^{-4} s, and 0.5×10^{-4} s, are evaluated for the (1,1,0) configuration with stenoses of 68 percent diameter stenosis. Transient simulations are executed with the aforementioned timesteps and the relative difference (Equation (5.3)) is evaluated to quantify the difference in each of the evaluated parameters, relative to the smallest timestep. Specifically, the cycle-averaged boundary pressures and flows, as in the mesh sensitivity analysis, are evaluated. Averages are taken between 2-4 cycles and 2-6 cycles. Differences below 0.51 percent are determined between the timesteps of 1.0×10^{-4} s and 0.5×10^{-4} s for the cycle-averaged boundary pressures and flow between cycles 2-4. Similar differences are obtained for the cycle-averaged parameters over cycles 2-6. Therefore, a timestep of 1.0×10^{-4} s is selected for all simulations.

5.5 SUMMARY

In this chapter, the three-dimensional model of the bifurcation of the LMCA, was developed. Details regarding the geometry of the healthy vessel as well as the stenosis profile and configuration within the bifurcation, were provided. The assumptions related to the numerical implementation of the 3D model, were outlined in detail. The development and implementation of the 3D model is central to the thesis because it allows for the localized three-dimensional haemodynamics within the diseased bifurcations to be assessed. When the presented three-dimensional model is coupled with the lumped-parameter model of the rest of the cardiovascular system (presented in the previous chapter), the resulting geometric multiscale CFD model (described in detail in the subsequent chapter), will allow, for what is to the best of the author's knowledge, the first numerical assessment of the functionality of coronary bifurcation lesions. This model will take into account both local and global haemodynamic interactions thus, fulfilling the first objective of the thesis.

6

THE MULTISCALE MODEL OF CORONARY BIFURCATION LESIONS

In this chapter, the coupling between the lumped-parameter model presented in Chapter 4 and the three-dimensional model outlined in Chapter 5 is detailed. Specifically, the theory behind the numerical coupling is presented. Additionally, the results from the numerical simulation of the geometric multiscale CFD model of the healthy bifurcation are analyzed in relation to the results of the full LPM to justify the convergence of the numerically model. Finally, the results of a diseased bifurcation are presented in order to ensure the ability of the model to respond to the introduction of a stenosis in the three-dimensional model. The implementation of the geometric multiscale CFD simulations of the LMCA bifurcation constitutes the first major objective of this thesis.

6.1 THEORY

Under the multiscale framework, the localized model of the 3D domain and the global model of the 0D domain must be numerically coupled in order to allow for the communication and interaction between them. The coupling between the heterogeneously-dimensioned models can be accomplished through either monolithic or partitioned approaches. The monolithic approach was developed by Vignon-Clementel *et*

al. [204] and was initially implemented in the numerical modelling of blood flow through the abdominal aorta. This framework is best suited for multiscale models wherein the lower-dimension boundary conditions are simple and consist of few time-dependent and nonlinear components for which an analytical solution can be derived. Consequently, the derived relationship between the pressure and flow at the boundary is coded directly within the flow solver, allowing for the two numerical models to be solved simultaneously [112, 205]. The implementation of the monolithic approach can be limited due to the requirement of an in-depth knowledge of the flow solver and the simplicity of the low-dimensional models. The partitioned approach was developed by Formaggia *et al.* and Quarteroni *et al* [113-115]; it differs from the monolithic approach in that separate solvers can be used to obtain the solution of the 3D and 0D models. Consequently, in implementing this method, one can exploit commercial software packages and thus, eliminate the need for a comprehensive knowledge of the flow solver [112, 114, 115, 205]. In addition, the use of a separate solver for the solution of the lower-order model allows for more complex configurations with nonlinear and time-dependent components (for which an analytical solution cannot be derived), to be employed. Consequently, based on the requirements of the aforementioned methods as well as the complexity of the developed LPM to be coupled with the 3D domain of the LMCA bifurcation (Figure 4.2), the explicit partitioned approach is selected for the implementation of the numerical coupling of the heterogeneously-dimensioned model.

Fundamentally, the coupling consists of the enforcement of stress and flux continuity at each well-defined interfaces between the 3D and 0D models. However, this formulation results in defective boundary conditions due to the fact that the NSE require point-wise data to be imposed on the boundaries of the model so as to ensure the well-posedness of the mathematical model, whereas the 0D model, as outlined previously can only provide spatially-averaged data. The treatment of defective boundary conditions has been addressed in the work of Heywood, Ranacher and Turek [206] who demonstrated that such boundary conditions are treated implicitly with an extended variational formulation of the NSE, specifically, through the weak fulfillment of the Neumann stress boundary condition, as provided in Equation (6.1):

$$p_i \hat{n}_i - \mu \nabla \vec{u}_i \cdot \hat{n}_i = p_j(t) \hat{n}_i \,, \tag{6.1}$$

for any cell face i on boundary j=*LMCA, LAD, LCX* and where $\hat{n}_i$ is the surface normal, $\vec{u}_i$ is the velocity [cm·s^{-1}] and $p_j(t)$ is the time-dependent average pressure [mmHg]. In this work [206], it was demonstrated that when a given boundary, j, is circular, plane and perpendicular to the axis of the segment of interest, the boundary condition given by Equation (6.1) reduces to the classical mean pressure drop problem as follows:

$$p_i \hat{n}_i = p_j(t) \hat{n}_i \,. \tag{6.2}$$

The treatment of the defective boundary conditions in the context of the partitioned multiscale algorithm, including the proof of well-posedness for the heterogeneous coupling, has been extensively addressed in [114, 115, 206, 207]. Its applicability to and effectiveness for the study of blood flows using commercial software packages, has been demonstrated in various studies, for example [131, 132, 135].

The coupling interfaces between the 0D and 3D models therefore govern the entries of column vector $\bar{b}$, as provided in Equation (4.5) and the boundary conditions applied in the 3D model. The boundaries Γ_{LMCA}, Γ_{LAD}, and Γ_{LCX} of the 3D model are interfaced with the 0D model through capacitances such that Neumann stress conditions, or average, uniform, time-dependent pressures (normal stresses), as provided in Equation (6.2), are applied. As a result, the solution of the 0D model is forced by average boundary flowrates obtained from the 3D model. Consequently, in Equation (4.5), column vector $\bar{b}$ is given by:

$$\bar{b} = \begin{bmatrix} 0 & \dots & Q_{LMCA} & \dots & Q_{LAD} & \dots & Q_{LCX} & \dots & 0 \end{bmatrix}^T \,, \tag{6.3}$$

where

$$Q_j = \int_{\Gamma_j} \vec{u} \cdot \hat{n} d\gamma \,, \tag{6.4}$$

for j=*LMCA, LAD, LCX* and $\vec{u}$ obtained from the 3D model. Vector $\bar{b}$ also contains forcing terms associated with the model of the left and right hearts.

An explicit, staggered approach over the cardiac cycle $(0,T)$ is used for the coupling. More specifically, at each time step, defined between (t^n, t^{n+1}) with t^{n+1}= t^n+Δt, the system of ODEs describing the dynamics of the 0D model (Equation (4.5)) is integrated by forcing its solution with the average boundary flowrates obtained from the 3D model at the previous timestep:

$$Q_i^{t_{n+1}} = \int_{\Gamma_i} \vec{u}^{t_n} \cdot \hat{n} d\gamma \,. \tag{6.5}$$

The integration of the ODE system between (t^n, t^{n+1}) yields a set of state variables (flow and pressures) at each point in the 0D model, including the average pressures at the interfaces between it and the 3D model at time t^{n+1}; these interface pressures are subsequently applied to the 3D model, though the average pressure (Neumann stress) boundary condition of Equation (6.2), which closes the mathematical model of the localized domain and allows the computation of velocity and pressure fields within the 3D model as well as the average flow rate at each of its boundaries at time t^{n+1}. The results of the 3D flow simulation successively force the solution of the 0D model at the next time step. The transient 3D flow simulations are solved using the commercial software package ANSYS Fluent and a 4th-order Runge-Kutta method, implemented within an in-house subroutine written in C++, is employed for the solution of the nonlinear system of ODEs describing the dynamics of the 0D model, as outlined previously. The solution of the system of ODEs is coupled with the NSE within ANSYS at each timestep using a fully-automated external user-defined function written in C.

6.2 IMPLEMENTATION OF THE MULTISCALE MODEL

The configuration of the multiscale model of the LMCA bifurcation is derived by combining the LPM presented in Figure 4.6 and the 3D baseline geometry provided in Figure 5.1. Figure 6.1 displays the resulting multiscale model employed in the functional analysis of coronary bifurcation lesions. Simulations are executed based on the methodology outlined in previous sections.

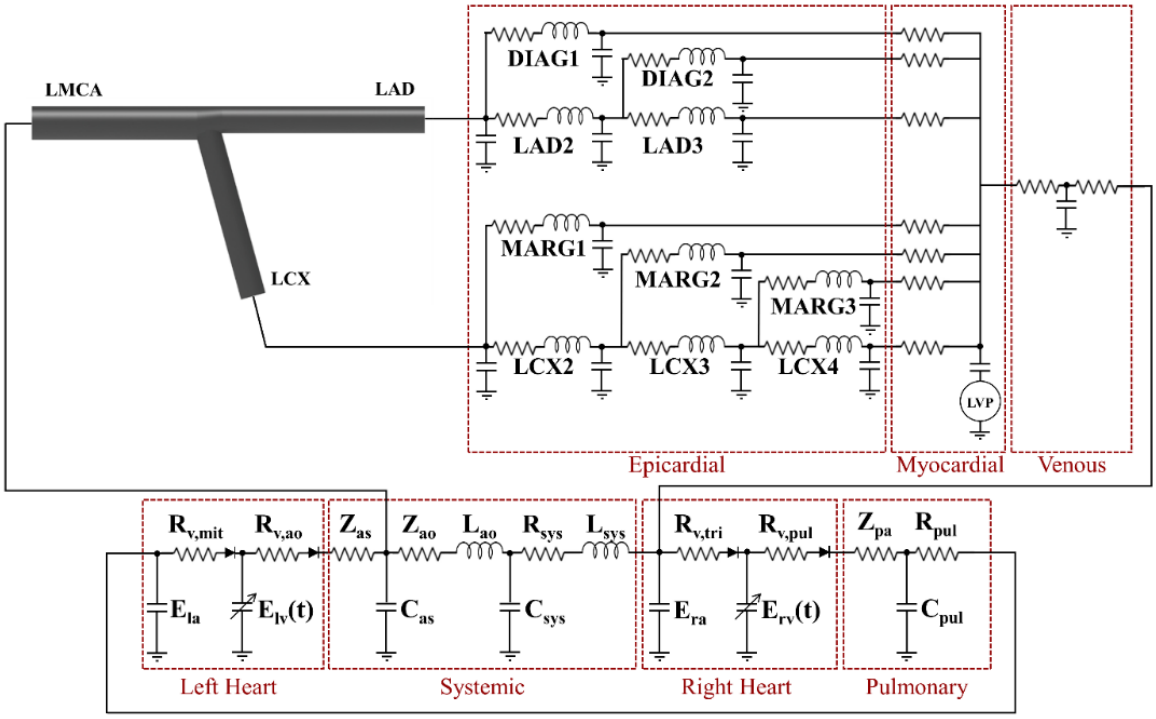

Figure 6.1: Multiscale model of the LMCA bifurcation.

In the diseased configuration of the multiscale model, collateral flow is neglected in order to simplify numerics. The presence and the extent of collateral coronary vessels is not completely understood, but has been linked, in part, to the severity of the disease and the duration of time to which a patient is exposed to severe stenoses. Clinical studies have shown that of all patients with significant coronary artery disease, as quantified by the percent diameter stenosis, only approximately 30 percent have functionally significant collateral vessels that are capable of preventing ischemia [86, 91]. Consequently, its elimination in the current model is deemed acceptable for the scope of the investigation.

6.2.1 Results of the healthy MS model of the LMCA bifurcation

The multiscale model is verified by comparing the results of the multiscale simulation of the healthy LMCA bifurcation to the results of the corresponding full LPM. The instantaneous difference of the MSM, $Diff_{inst,i}$ [%], determined at each timestep, is calculated for each state variable relative to the LPM:

$$Diff_{inst,i} = \frac{\left| x_{MSM,i} - x_{LPM,i} \right|}{x_{LPM,i}}, \tag{6.6}$$

where i is the timestep and x is the state variable being considered. In addition to the instantaneous difference, the cycle-average difference, $Diff_{avg}$ [%], utilizing cycle-averaged values, is calculated for the epicardial coronary pressures and flows; the cycle-averaged values are required for the calculation of the flow-based and pressure-based FFR.

Figure 6.2 compares the results of the two models for the left and right heart parameters. A good agreement between the presented parameters is observed and is further supported by Table 6.1 which presents the maximum instantaneous difference for the heart, systemic and pulmonic parameters. The maximum instantaneous difference recorded for all the presented state variables is 1.1 percent. Overall, the majority of the variables displayed a maximum instantaneous difference less than 0.9 percent.

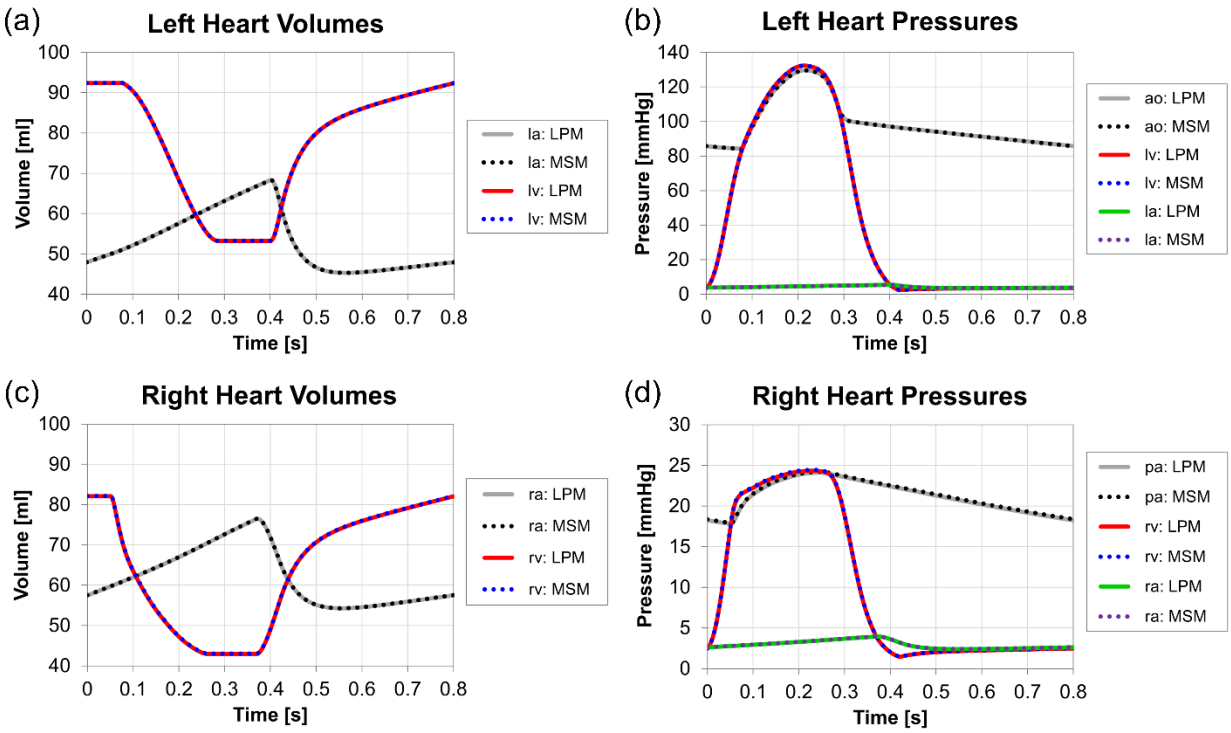

Figure 6.2: Comparison between the LPM and the healthy LMCA bifurcation MSM for the (a) left heart volumes (b) left heart pressures (c) right heart volumes and (d) right heart pressures.

Table 6.1: Maximum instantaneous differences between the LPM and MSM for each heart, systemic and pulmonic parameter.

		Max. Instantaneous Difference [%]
Left Heart	V_{la}	0.078
	V_{lv}	0.10
	P_{la}	0.078
	P_{lv}	1.1
Systemic	P_{ao}	0.088
	P_s	0.042
	Q_s	0.040
Right Heart	V_{ra}	0.12
	V_{rv}	0.26
	P_{ra}	0.19
	P_{rv}	0.68
Pulmonic	P_{pa}	0.83
	Q_{pa}	0.83
	Q_p	0.17

Figure 6.3 compares the epicardial coronary pressures between the LPM and the MSM. Four examples, namely the pressures within the LAD1, LCX3, DIAG1 and MARG3 segments are provided.

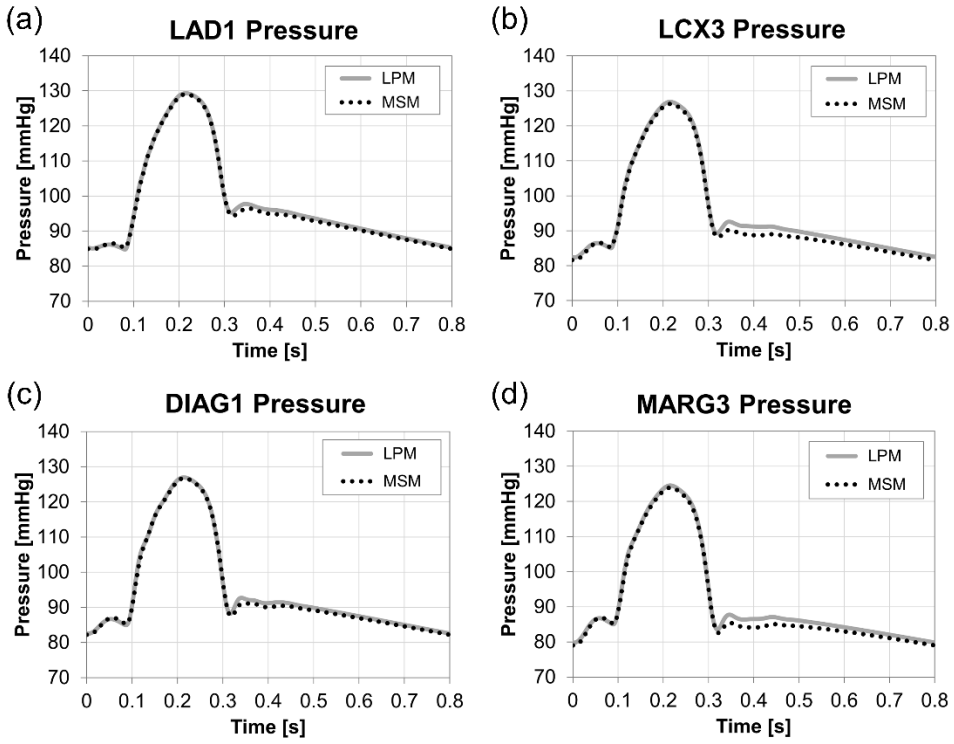

Figure 6.3: Comparison between the LPM and MSM epicardial pressures. The examples provided are within (a) LAD1 (b) LCX3 (c) DIAG1 and (d) MARG3 branches.

The maximum instantaneous difference and the cycle-averaged difference for the epicardial coronary pressures are provided in Table 6.2. For all the pressure state variables, the maximum instantaneous difference is 2.8 percent; the cycle-averaged differences did not surpass 1.2 percent.

Table 6.2: Maximum instantaneous and cycle-averaged differences between the LPM and the healthy LMCA bifurcation MSM for the epicardial coronary pressures.

		Maximum Instantaneous Difference [%]	**Average Difference [%]**
LAD	P_{LAD1}	1.7	0.50
	P_{LAD2}	0.58	0.50
	P_{LAD3}	0.62	0.51
LCX	P_{LCX1}	2.7	1.2
	P_{LCX2}	2.7	1.2
	P_{LCX3}	2.7	1.1
	P_{LCX4}	2.8	1.1
DIAG	P_{DIAG1}	2.0	0.5
	P_{DIAG2}	1.9	0.5
MARG	P_{MARG1}	2.7	1.1
	P_{MARG2}	2.7	1.1
	P_{MARG3}	2.8	1.1

Figure 6.4 and Figure 6.5 compare the epicardial coronary flows between the LPM and MSM. More specifically, the results are presented for the LMCA, LAD1, LCX2, DIAG2 and MARG3 branches. The left-hand panel provides the flowrates while the right-hand panel presents the corresponding instantaneous differences. The opening and closing of the aortic valve are also denoted in the figures. All computed epicardial coronary flows, including those not presented in the figures, display two distinct peaks in the instantaneous difference occurring near the opening and the closing of the aortic valve. Differences for the first peak (aortic valve opening) range between 10 and 26 percent, while difference for the second peak (near aortic valve closing) range between three and 11 percent.

The maximum instantaneous differences and cycle-averaged difference for the epicardial coronary flows are summarized in Table 6.3. Interestingly, as the vessel becomes more distal to the LMCA, the peak instantaneous difference occurs later than the initial peak observed within the LMCA. It is important to note that at all other points in

the cardiac cycle, the instantaneous difference remains below 3 percent for all coronary flows. This fact is further justified by the results presented in Table 6.3, wherein the maximum cycle-averaged difference between the LPM and MSM is 1.4 percent.

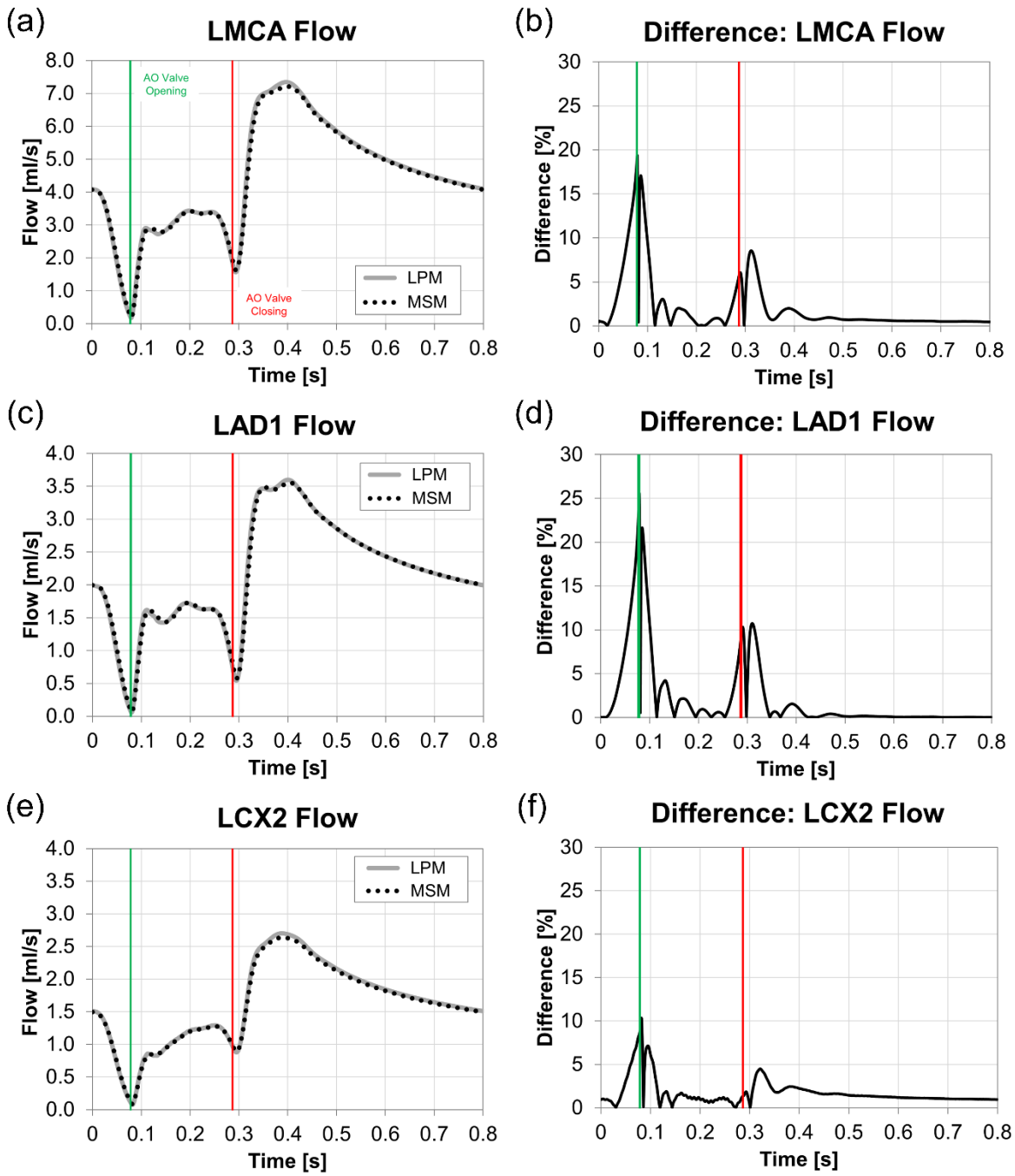

Figure 6.4: Comparison between the LPM and MSM for the (a) LMCA (c) LAD1 and (e) LCX2 flows. The corresponding instantaneous differences are provided in (b), (d), and (f) respectively. The green and red lines denote aortic valve opening and closing respectively.

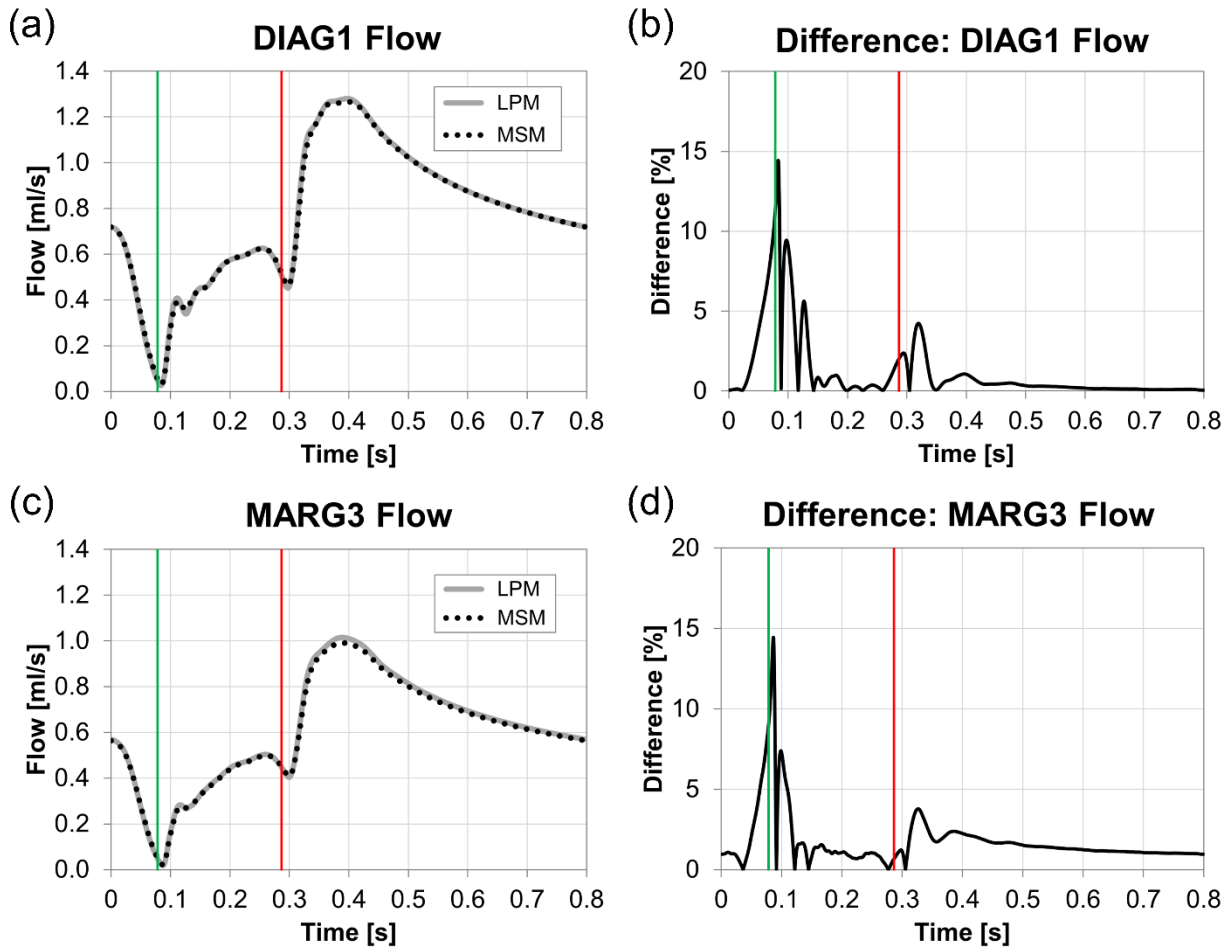

Figure 6.5: Comparison between the LPM and MSM for the (a) DIAG1 and (c) MARG3 flows. The corresponding instantaneous differences are provided in (b) and (d) respectively. The green and red lines denote aortic valve opening and closing respectively.

Table 6.3: Maximum instantaneous differences and cycle-averaged differences between the LPM and MSM for the epicardial coronary flows

		Maximum Instantaneous Difference [%]	Average Difference [%]
LMCA	Q_{LMCA}	19	0.86
LAD	Q_{LAD1}	26	0.33
	Q_{LAD2}	19	0.33
LCX	Q_{LCX1}	16	1.4
	Q_{LCX2}	10	1.4
	Q_{LCX3}	12	1.4
	Q_{LCX4}	14	1.4
DIAG	Q_{DIAG1}	14	0.33
	Q_{DIAG2}	19	0.33
MARG	Q_{MARG1}	11	1.4
	Q_{MARG2}	13	1.4
	Q_{MARG3}	14	1.4

The peaks in the instantaneous differences observed for the coronary flows occurred after the opening and the closing of the aortic valve. During systole, after the opening of the aortic valve, blood flows from the left ventricle to the aortic root and thus, the coronary arteries (which stem from the aortic root). Initially, the acceleration of the blood flowing into the coronary arteries is significant as can be displayed in Figure 6.4, wherein the LMCA flowrate increases from nearly zero to $3.5ml \cdot s^{-1}$ over 30ms. After the closing of the aortic valve, left ventricular pressure drops significantly over a time period of approximately 0.08s due to ventricular relaxation. The decrease in ventricular pressure is associated with a decrease in the intramyocardial pressure acting on the coronary microcirculation, which allows blood to accelerate into the coronary arteries. Therefore, the observed peak instantaneous differences occur during these high acceleration phases.

Pressure-flow relations and overall system dynamics during phases of fluid acceleration are affected significantly by capacitance and inductance effects. Capacitance effects relate to the compliance/elasticity of the vessels and denote the change in pressure gradient required to generate a change in vessel volume. These effects become most prominent when the rate of change of the pressure gradient is high, in particular during accelerative and decelerative phases. The inductance of the vessel encompasses fluid inertial effects and therefore the response of the system to changes in the pressure gradients; as in the case of capacitance effects, inductance effects contribute to the dynamics when the flow is in an accelerative state, wherein the rate of change of the pressure gradient is high.

With regard to compliance, as a result of changes in vessel volume (due to vessel elasticity) which acts as a fluid volume reserve, the response of the system to a change in pressure gradient is not instantaneous, as it would be in the case of a rigid vessel. As such, for elastic vessels, there is a time lag between the pressure gradient and the flow, such that the total inlet flow is not equal to the total outlet flow in a vessel. Fluid inertia has a similar effect of system response to pressure changes; due to inertial effects, the response of the fluid to a change in pressure gradient is not instantaneous as it would be

in the case of a purely resistive vessel (wherein the pressure and flow curves are superimposed [19]).

Therefore, due to the fact that the peak instantaneous differences occur during times of high fluid acceleration, they can be attributed to differences in capacitive and inductive effects between the two models. More specifically, in the LPM, the LAD and LCX are modelled as compliant vessels whereas in the MSM, the corresponding 3D vessels are rigid and therefore did not include any capacitive effects. Furthermore, the inductance of the vessels in the LPM is calculated assuming that a bolus of fluid with volume equal to that of the designated vessel is able to accelerate solely in the direction of the vessel axis free of any viscous resistance; in the MSM, the inertial response of the system is altered due to the contribution of viscous resistance. Capacitive and inductive effects are also responsible for the aforementioned mismatch in the positive to negative flow transition (and vice versa) between the two models for the LAD3.

Overall, differences in the results between the LPM and the MSM are expected due to discrepancies in the model assumptions (Appendix A elucidates the assumptions associated with the derivation of the LPM). In the LPM the underlying assumption concerning the viscous resistance (R) of the vessel is that the flow is fully-developed and therefore that the velocity profile is parabolic. Conversely, in the CFD multiscale simulations of the healthy LMCA bifurcation, the velocity profile is not forced, but rather is allowed to develop. Based on the entrance length, l_e [cm] which is defined for laminar flow in Equation (6.7):

$$l_e = 0.06 D \,\mathrm{Re}, \tag{6.7}$$

where D is the vessel diameter [cm] and Re is the Reynolds number as is given in Equation (6.8):

$$\mathrm{Re} = \frac{4\rho Q}{\pi \mu D}, \tag{6.8}$$

where Q is the volumetric flowrate [ml·s^{-1}], the flow is in the development region and therefore, a uniform (plug) profile is maintained in the 3D CFD multiscale simulations of the LMCA bifurcation. Here, the average entrance length is approximately 10cm whereas the length of the LMCA in the 3D model is 2.2cm. In the entrance region where the flow is developing (as in the case of the multiscale CFD simulation), the pressure drop is nonlinear and greater than the pressure drop for the fully-developed flow (as in the case of the LPM) along the same length of vessel [159]. Consequently, additional pressure losses are expected in the MSM in comparison to the LPM for the LMCA, LAD and LCX. Furthermore, the LPM does not take into account losses that occur at the vessel bifurcations due to disturbed flow, and therefore additional pressure losses are expected in the MSM, particularly for the LCX. This phenomenon can be observed from Table 6.2 and Table 6.3, where the cycle-averaged differences for the pressures and flows in the LCX and MARG branches are higher compared to those of the LAD and DIAG branches. As such, instantaneous differences of 3 percent found for the coronary pressures and flows can be attributed to the additional pressure losses occurring in the MSM and are within reason.

Based on the above justifications and the globally low instantaneous and cycle-averaged differences for the coronary parameters between the LPM and MSM models, the simulation of the multiscale healthy LMCA bifurcation is confirmed.

6.2.2 Results of a diseased MS model of the LMCA bifurcation

The ability of the MS model to capture the decrease in flow and perfusion pressure upon the introduction of a stenosis is assessed through the comparison of the diseased flows and pressures to the healthy case as well as the evaluation of the corresponding flow- and pressure-derived FFR values. Here, the results for the (1,0,0) configuration, over a range of mild to severe diameter reductions are presented. Specifically, four diameter reductions, namely 41, 50, 61 and 68 percent are simulated.

The simulated time-dependent flow rates in each of the vessels of the bifurcation are displayed in Figure 6.6 while the corresponding pressures distal to the LAD and the LCX are displayed in Figure 6.7.

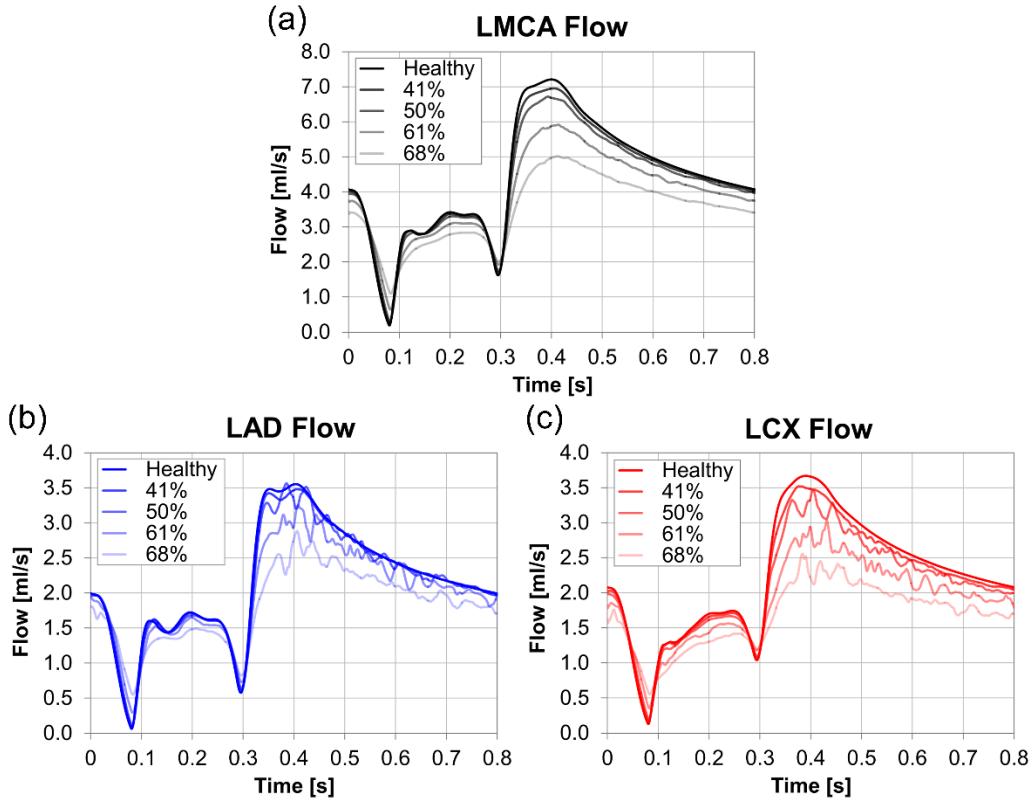

Figure 6.6: Flow in the (a) LMCA (b) LAD (c) LCX in the (1,0,0) configuration with increasing stenosis severity.

One can observe that as the stenosis severity increases, the total perfusion of the left coronary tree, as is evaluated through the LMCA flow, decreases. The decrease in perfusion is correspondingly demonstrated through the flow reduction in each of the daughter vessels.

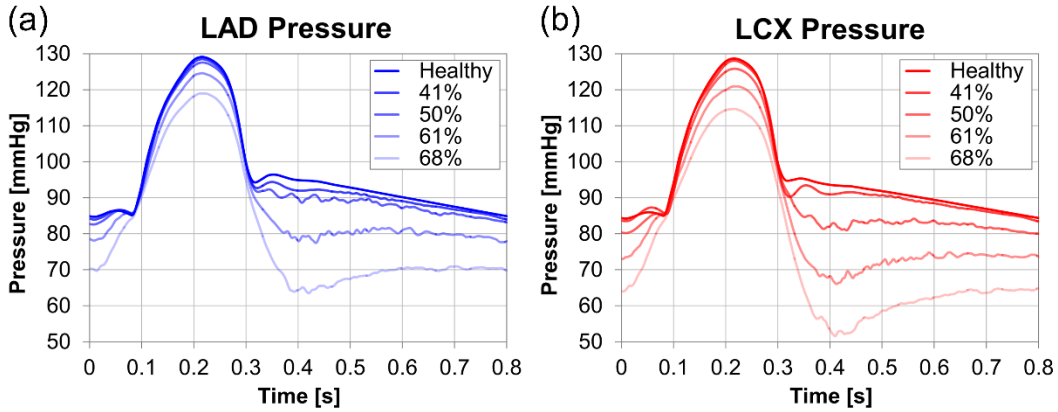

Figure 6.7: Pressure at the outlet of the (a) LAD and (b) LCX for the (1,0,0) configuration with increasing stenosis severity.

Figure 6.8a presents the flow-based FFR values in the LMCA, LAD and LCX for the (1,0,0) configuration as a function of stenosis severity. At a 68 percent diameter reduction, the configuration becomes globally critical, and exhibits an FFR value below 0.8 within the LMCA. In the LAD, the FFR remains above the critical value over the entire range of stenosis severities, while in the LCX, it is critical at a diameter reduction of 68 percent.

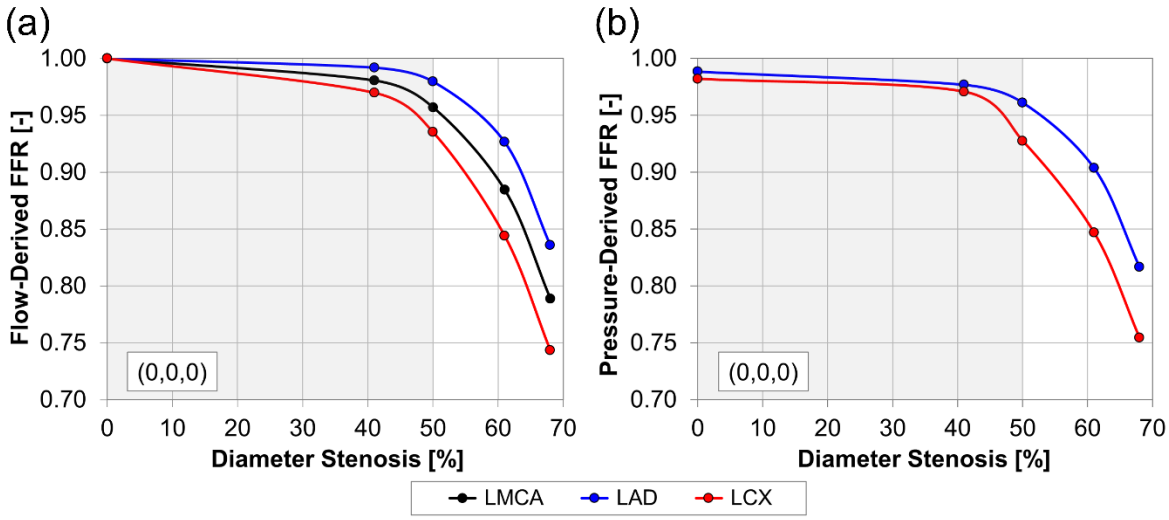

Figure 6.8: (a) Flow-derived and (b) pressure-derived FFR for the (1,0.0) configuration in each of the vessels of the bifurcation with increasing stenosis severity. The shaded area corresponds to the range of diameter reduction for which the configuration is (0,0,0).

Similar trends are observed for the pressures in the distal portions of the LAD and LCX; as the diameter reduction increases, the time-dependent pressure curves begin to deviate from the healthy case, which is approximately equal to aortic pressure thus, exhibiting a pressure drop. The corresponding pressure-derived FFR values are displayed in Figure 6.8b, where with increasing stenosis severity, the FFR decreases in both the LAD and the LCX. Similarly to the flow-derived FFR, the pressure-derived FFR is found to be critical (below 0.8) for the LCX and non-critical within the LAD. The results of the multiscale simulation of the (1,0,0) configuration display FFR values that ranged between 0.74 and 0.93 for diameter reductions between 61 and 68 percent. These FFR values are in good accordance with the FFR values reported in the literature for similar ranges of stenosis severities (presented in Table 6.4).

Table 6.4: Literature and study values for FFR (lesions with diameter reductions between 60 and 80 percent)

	Diameter Reduction [%]	FFR [-]
Multiscale Model	*61-68*	*0.74-0.93*
Takagi *et al.* [208]	60-80	0.35-0.75
Hamilos *et al.* [189]	60-70	0.68-0.97
Meimoun *et al.* [188]	70	0.68-0.76
Iguchi *et al. [187]*	60-70	0.60-0.96

Table 6.5: Average lesion lengths reported in the literature

	Lesion Length [cm]
Multiscale Model	*1.0*
Takagi *et al.* [208]	1.42±0.75
Meimoun *et al.* [188]	1.41±0.65
Iguchi *et al.* [187]	1.35±0.80
Koo *et al.* [209]	0.64±0.30

Furthermore, Fischer *et al.* [210] reported in their study that of all stenoses with diameter reductions greater than 60 percent, only 38 percent had FFR values less than 0.75 while Koo *et al.* [209] found that for an average diameter reduction of 79±11 percent the average FFR was 0.81±0.12 with only 31 percent of lesions having an FFR below 0.75. Consequently, the results of the multiscale simulations are representative of *in vivo* conditions. The fact that the computed values are on the higher-end of the reported ranges can be justified based on the stenosis length; in the current model, the stenoses are modelled with a base length of 10mm, which is shorter than the average lesion lengths reported in the literature (summarized in Table 6.5). In Koo *et al.* [209], where higher FFR values compared to the rest of the referenced clinical studies were reported, noticeably shorter lesion lengths were also observed. Furthermore, both Meimoun *et al.* [188] and Iguchi *et al.* [187] found a significant negative correlation between the FFR and the lesion length, signifying that shorter lesions are associated with higher FFR values.

In Figure 6.6, one can observe oscillations in the diastolic flow of the LAD and the LCX for the moderate to severe diameter reductions. Similar oscillations are observed for the multilesional configurations with stenoses in the LMCA, but not for the cases where the LMCA is healthy, as can be observed in Figure 6.9 for the (0,1,1) and (0,0,1) configurations.

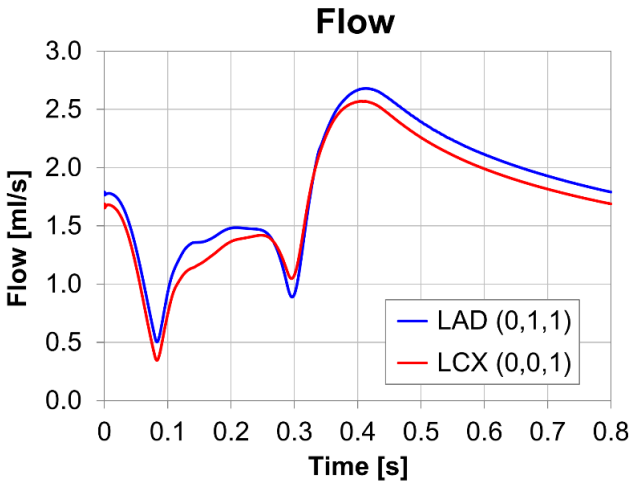

Figure 6.9: Flow in the LAD for the (0,1,1) configuration and in the LCX for the (0,0,1) configuration at a 68 percent diameter reduction.

Several additional simulations are executed in order to determine the origin of the oscillations. Firstly, the spatial and temporal resolution of the models are refined. The flows from the resulting numerical simulations still displayed oscillations which confirmed that they are not a result of the lack of convergence of the model. Furthermore, the outlets of the LCX and the LAD are both extended by a length equivalent to 10 diameters. The flows within the extended outlet CFD simulations still displayed oscillations in the LAD and LCX flow as is determined for the baseline geometry.

Consequently, based on these results, the oscillations are attributed to the disturbed flow field distal to the stenoses and are not to numerical instabilities. The average boundary flows of the extended model are compared to the average boundary flows of the baseline model and are found to have differences of one, zero and two percent in the LMCA, LAD and LCX respectively, corresponding to one, zero and two percent differences in the FFR within the corresponding vessels. Moreover, an additional geometry with extended outlets, wherein a five degree angle is introduced for the LAD relative to the axis of the LMCA, is simulated. The resulting flow curves displayed very small amplitude oscillations, with small differences in the average boundary flows compared to the original geometry. These results further justify that the oscillations originate from the complex flow field in the distal portions of the daughter vessels.

6.3 SUMMARY

In this chapter, the development of the geometric multiscale model of the LMCA bifurcation was presented. The geometric multiscale CFD simulation was executed for the healthy LMCA bifurcation. The results displayed physiological behaviour and are corroborated based on the full LPM simulation and literature values. The multiscale CFD simulations for a single diseased case were also implemented in order to confirm the ability of the model to capture the decrease in myocardial perfusion. The resulting FFR values were in good accordance with clinical studies from the literature. Therefore, the presented simulations demonstrated the ability of the developed CFD multiscale model to provide physiologically-relevant dynamics within coronary bifurcation lesions. Thus, the first objective of the work is fulfilled. Specifically, this chapter presented, what is to the best of the author's knowledge, the first computational model of a diseased coronary bifurcation that incorporates both local (within the bifurcation) and global (within the surrounding cardiovascular domains) haemodynamic effects while inherently accounting for the haemodynamic interactions. This model will be utilized, as part of the second objective of the thesis, to investigate the effect of various geometric parameters, both of the bifurcation and the stenoses, on the functional manifestation of the disease.

7

EFFECT OF STENOSIS CONFIGURATION

This chapter outlines the study of the effect of stenosis configuration on the functionality of coronary bifurcation lesions. It provides the motivation behind the investigation of this particular parameter, the corresponding cases that are considered in the work and the results and clinical relevance of the findings. The results presented in the chapter have been published in the Journal of Biomechanics [211].

7.1 MOTIVATION

The development of ischemia in coronary bifurcation lesions and consequently the manifestation of the particular disease is more involved than that of isolated lesions. This phenomenon results from the fact that CBLs are subject to both global and local haemodynamic interactions, which render the overall dynamics of the system more complex [102].

The global haemodynamic interactions can result from various factors. As outlined in Chapter 2, the resistance of a stenosis is dependent on the transtenotic flow. When multiple stenoses are dispersed within the coronary tree, the resistance of each individual lesion contributes to the overall epicardial resistance and thus, the total myocardial flow reduction. Therefore, there is a mutual underestimation of the true resistance and

haemodynamic severity of the individual lesions [102, 103]. In addition to its flow-dependence, the stenosis resistance is also governed by the morphology of the lesion and therefore, the extent to which the true stenosis resistance is masked differs between lesions. This idea was previously demonstrated for tandem (or serial) lesions [102, 104-108]. However, for bifurcation lesions, this phenomenon is more complicated due to the fact that there are three vessels which can have varying resistance as a result of the presence or the absence of a stenosis within them.

The relative epicardial resistance between the daughter vessels, which is influenced by both the relative severity of the corresponding stenoses and that of the supplying vessel lesion, governs the relative distribution of blood between the myocardial beds being perfused by the epicardial bifurcation. This idea, which can be extended to the phenomenon of branch steal, has been previously suggested to affect the flow distribution between the daughter vessels in bifurcation lesions [27, 109]; however, its influence on the functionality of CBLs has not been studied. Still yet, the dynamics and relative size of the two distal myocardia also play a significant role in the relative distribution of blood between the two daughter vessels. More importantly, the relative extent of myocardial domain being perfused ultimately determines the criticality of the flow reduction [103, 110]. These aforementioned global factors, which contribute to the haemodynamic interactions within CBLs, are affected by the location and number of stenoses within the bifurcation, or conversely the CBL configuration.

The significance of stenosis configuration in the haemodynamics of coronary bifurcation lesions has been suggested in previous numerical studies. For example, Binu *et al.* [47, 48] found that the wall shear stress pattern varied between the different bifurcation lesion configurations thus, implying variance in the risk for disease progression. Similarly, by using conventional CFD simulations, Zarandi *et al.* [46] computed wall shear stress distributions in the side branches of true bifurcation lesion configurations as well as the flow ratio between the side branch and mother vessel; both parameters were found to be influenced by the number and location of the stenoses. Chaichana *et al.* [39-44] executed a series of CFD simulation within patient-specific models of diseased LMCA bifurcations [39-44] and sought changes in flow velocities,

WSS and the local pressure gradient (PSG) for the different CBL configurations relative to the healthy LMCA bifurcation flow so as to assess the risk for disease progression as well as plaque rupture. The studies found statistically significant differences in all investigated parameters between the various configurations, with these differences being a complicated factor of both the number and location of the stenoses within the flow divider.

To the best of the author's knowledge, the effect of lesion configuration, with varying stenosis severity, on the haemodynamic impact and clinical manifestation of the disease has not been studied to date. Consequently, as an initial study, it is hypothesized that the configuration of the stenoses within the bifurcation, alone, impacts the haemodynamic interactions between the stenoses in the bifurcation and therefore plays a central role in the physiological severity of this type of coronary artery disease. Thus, the objective of this investigation is to characterize and compare, for the first time, the functional impact, as quantified by the flow-based and pressure-based FFR, of different bifurcation lesion configurations.

7.2 GEOMETRY OF THE CBL CONFIGURATIONS

Four multilesional CBL configurations based on the Medina classification are considered. Additionally, four diameter reductions, namely 41, 50, 61 and 68 percent are modelled for each case, which accounts for a range from mild to severe stenoses. All stenoses in a given configuration have the same diameter reduction. Therefore, a total of 16 cases are simulated in this research. Details regarding the stenosis profile are provided in Chapter 5. Examples of the multilesional configurations with different stenosis severities are provided in Figure 7.1. In order to comply with the definition of the Medina classification, all configurations with a diameter reduction of 41 percent have been denoted as (0,0,0).

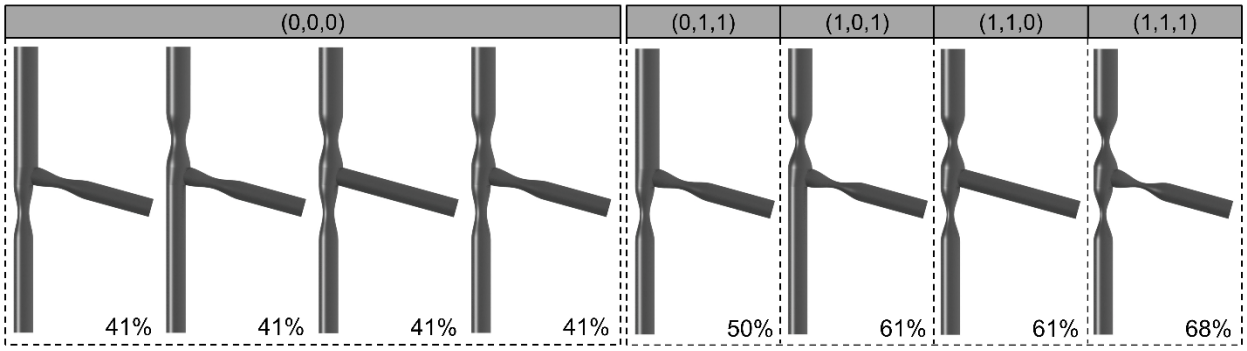

Figure 7.1: Examples of the multi-lesion configurations, based on the Medina classification that are considered in the study.

7.3 RESULTS

Average pressures and flows at each of the boundaries of the bifurcation are obtained at every timestep of the 16 different multiscale simulations; these values are processed and used in the calculation of the flow-based and pressure-based FFR in order to study the functionality of CBLs with respect to lesion configuration.

7.3.1 Flow and pressure profiles

Figure 7.2 presents the time-dependent flow in each of the vessels of the bifurcation for the (1,1,1) configuration with varying stenosis severity. The corresponding boundary pressures distal to the LAD and the LCX are presented in Figure 7.3.

Similarly to the case study of the (1,0,0) configuration presented in Chapter 6, as the percent diameter stenosis increases, the magnitude of the flow curves as well as the cycle-averaged flow, decreases, while the shape of the flow curve remains constant. This signifies that perfusion is decreased in all myocardial beds of the model with increasing stenosis severity. A similar trend is displayed in the pressure curves wherein, as the diameter reduction increases, the time-dependent LAD and LCX pressures (and corresponding cycle-averaged pressures) deviate from the aortic pressure. This result signifies that the myocardial perfusion pressure decreases with increasing stenosis severity.

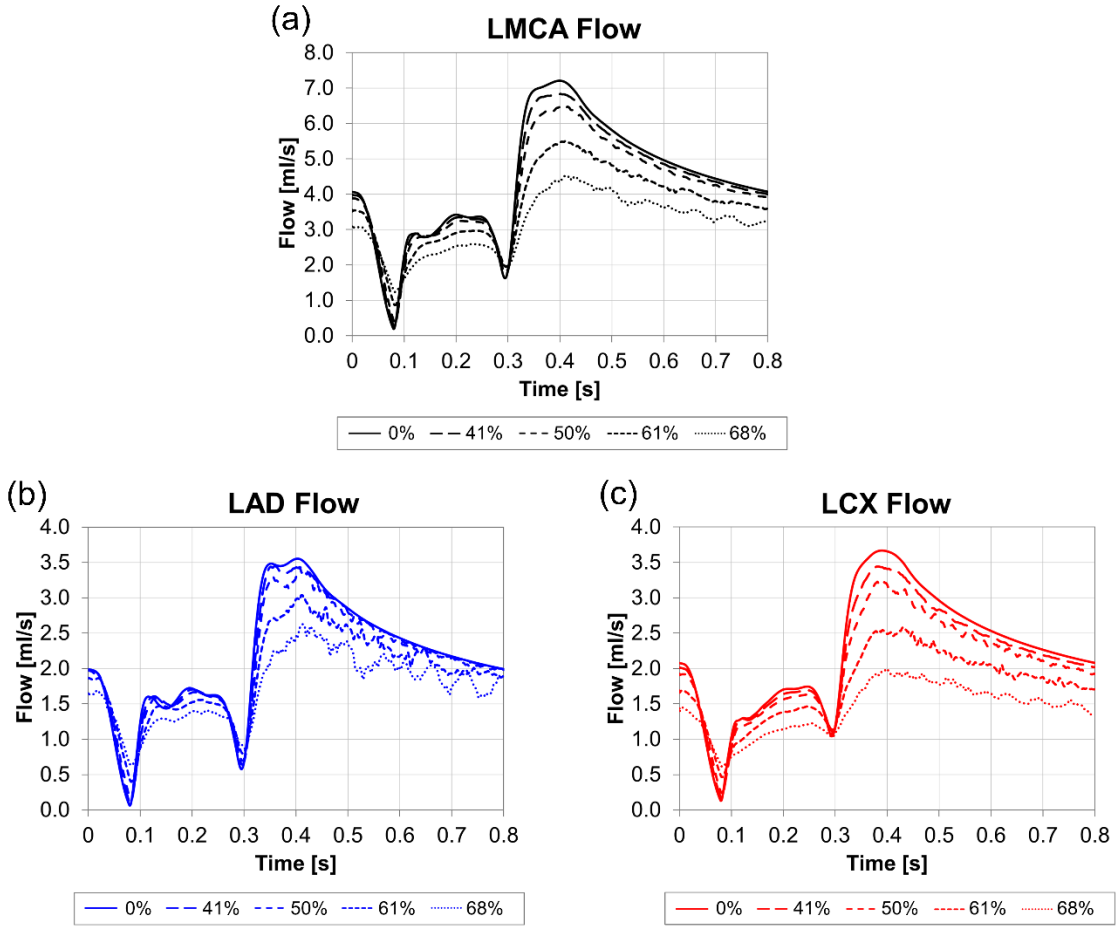

Figure 7.2: Flow in the (a) LMCA (b) LAD and (c) LCX for the (1,1,1) configuration with varying stenosis severity.

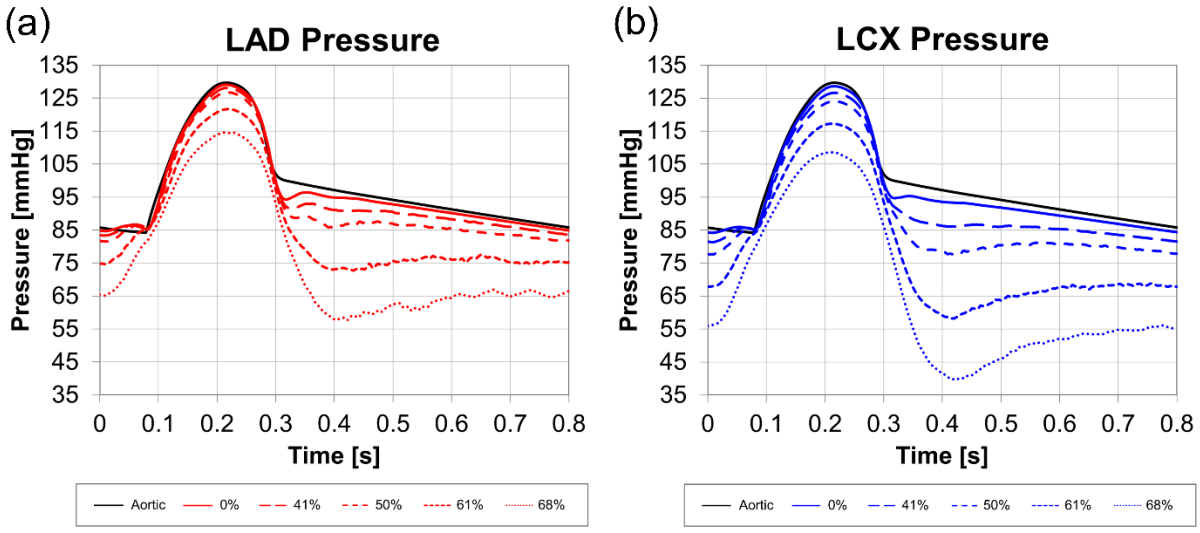

Figure 7.3: Time-dependent, face-averaged pressure in the (a) LAD and (b) LCX for the (1,1,1) configuration with varying stenosis severity.

Furthermore, while the shape of the time-dependent curves at low diameter reductions are similar to that of aortic pressure, with increasing diameter stenosis, the shape of the time-dependent curves begins to resemble that of the left ventricular pressure. One can also observe from these figures that the decrease in perfusion is greater in the LCX than in the LAD; the corresponding pressure- and flow-derived FFR values are provided in subsequent sections.

7.3.2 Flow-based FFR

Figure 7.4 displays the flow-based FFR in the LMCA, LAD and LCX for each multilesional configuration as a function of diameter stenosis.

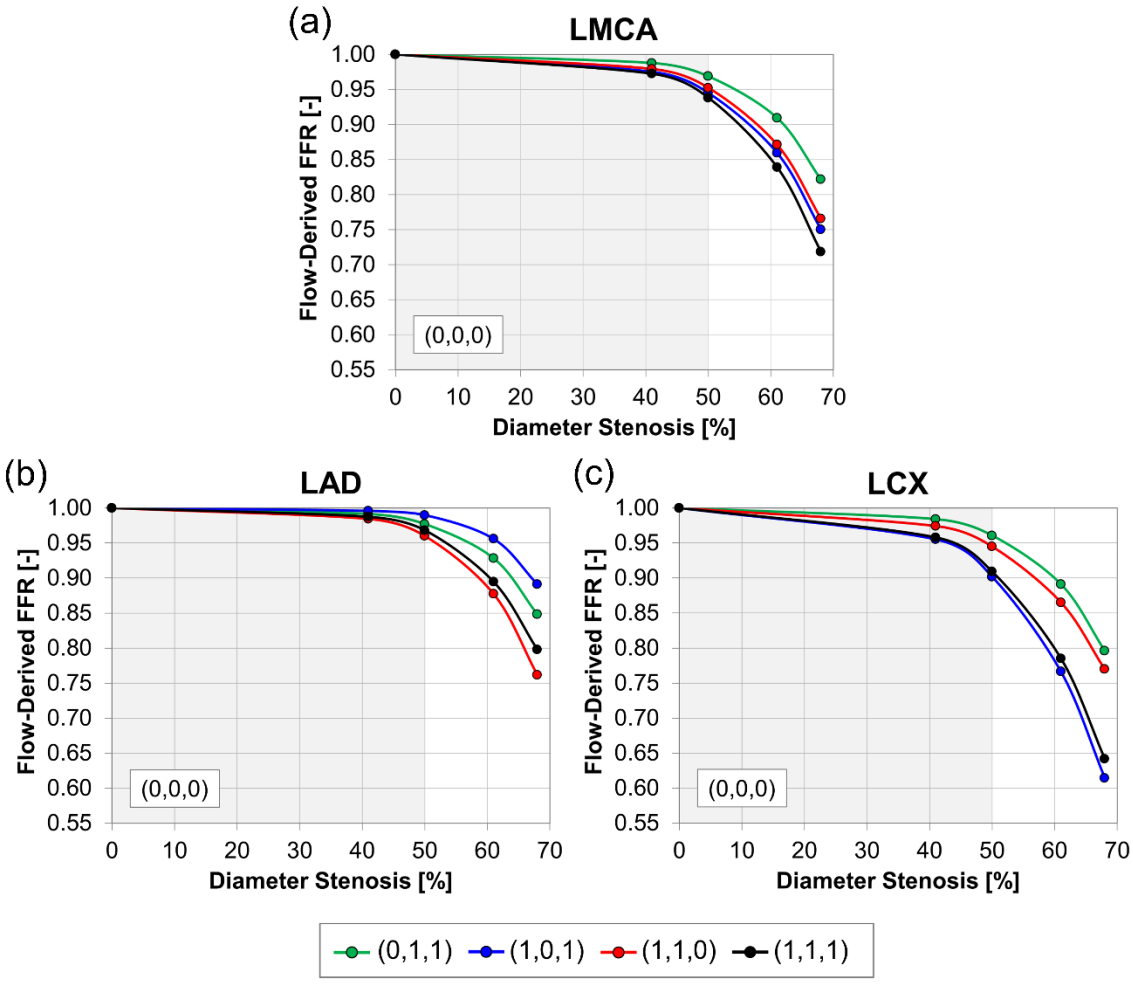

Figure 7.4: Comparison of the flow-based FFR in the (a) LMCA (b) LAD and (c) LCX as a function of diameter stenosis between the different multilesional CBL configurations. The shaded area corresponds to the (0,0,0) configurations (diameter reduction less than 50 percent).

The results of the upper panel elucidate the global effect of the bifurcation lesion configuration as a function of diameter reduction as it corresponds to the flow in the LMCA and therefore the perfusion of the entire myocardial bed supplied by the left coronary circulation. At any diameter reduction, the (1,1,1) configuration produces the lowest FFR values and therefore the most significant decrease in myocardial perfusion. The (0,1,1) configuration, which is the only arrangement that does not have a stenosis in the LMCA, produces the highest FFR values at any stenosis severity. The flow-based FFR values of the (1,0,1) and (1,1,0) cases are within the range of values of the two aforementioned configurations, with the (1,0,1) configuration displaying slightly lower FFR values as compared to the (1,1,0).

In the lower panel of Figure 7.4, the flow-based FFR values for each of the daughter vessels are displayed. Interestingly, in both the LAD and the LCX, the (1,1,1) configuration does not result in the lowest FFR values and therefore does not produce the most critical flow reduction, regardless of the fact that it has the greatest number of stenoses; instead, at any diameter stenosis, the (1,1,0) and the (1,0,1) configurations exhibit the most significant reduction in perfusion in the myocardia supplied by the LAD and the LCX, respectively. The difference in FFR of the LAD between the (1,1,0) and the (1,1,1) configurations becomes larger as the severity of the stenosis increases; at a diameter reduction of 61 percent the FFR values differ by 0.01, whereas at a 68 percent diameter reduction, they differ by 0.04. A similar trend can be observed in the LCX between the (1,0,1) and (1,1,1) configurations, such that at 61 percent diameter reduction, the FFR values differ by 0.02 and at a severity of 68 percent they differ by 0.03. Interestingly, in the LCX, it is the (0,1,1) configuration and not the (1,1,0) case that displays the highest FFR values, regardless of the fact that the particular configuration is stenosed in the LCX while the (1,1,0) configuration is not.

By considering a critical flow-based FFR of 0.8, globally, the (1,1,1) configuration becomes critical at a diameter reduction of 64 percent. The (1,0,1) and (1,1,0) configurations closely follow the (1,1,1) configuration and become critical at 65 percent and 66 percent diameter reductions respectively. Therefore, globally, it is suggested that these configurations, although different in the location and number of stenoses, have

similar haemodynamic severities. When accounting for the daughter vessels individually, from a local perspective, the (1,0,1) configuration is the first case to reach a critical FFR (within the LCX), specifically at a 59 percent diameter stenosis. The (1,1,1) configuration then becomes critical (in the myocardium supplied by the LCX) at a 60 percent diameter reduction while the (1,1,0) and (0,1,1) configurations require much higher stenosis severities, namely 66 percent and 68 percent, respectively, to reach a critical FFR (again, in the LCX). Therefore, from a global perspective, the bifurcation lesion configurations become critical at higher severities compared to the daughter vessels being considered individually. Furthermore, global criticality does not appear to correspond to local criticality.

Figure 7.5 compares the flow-based FFR between the LAD and the LCX in each individual bifurcation lesion configuration, as a function of diameter reduction. One can observe that in all configurations, in particular the (0,1,1), (1,1,1) and (1,0,1) cases, the flow-based FFR is lower in the LCX, at any stenosis severity. This observation is interesting for the configurations of the upper panel of Figure 7.5, both of which have a stenosis in each of the daughter vessels and therefore show a level of symmetry in their lesion configuration yet no symmetry in their dynamics. Furthermore, when comparing the (0,1,1) and (1,1,1) configurations, it is observed that the introduction of a stenosis in the LMCA results in a nonlinear effect on the FFR within the two daughter vessels. For example, at a 68 percent diameter stenosis, the difference in the flow-based FFR between the two configurations is 0.05 in the LAD and 0.16 in the LCX, and at a 61 percent stenosis, the difference is 0.04 in the LAD and 0.10 in the LCX.

In the lower panel of Figure 7.5, the two configurations presented, namely (1,1,0) and the (1,0,1) each have a stenosis in the LMCA and a stenosis in one of the daughter vessels and therefore exhibit a level of similarity in their configuration. It can be observed that, for the (1,0,1) configuration, with increasing stenosis severity, the curves of the flow-based FFR in the LAD and the LCX diverge and also differ significantly in magnitude, with the FFR values in the LCX (which is stenosed) being significantly lower than those in the LAD.

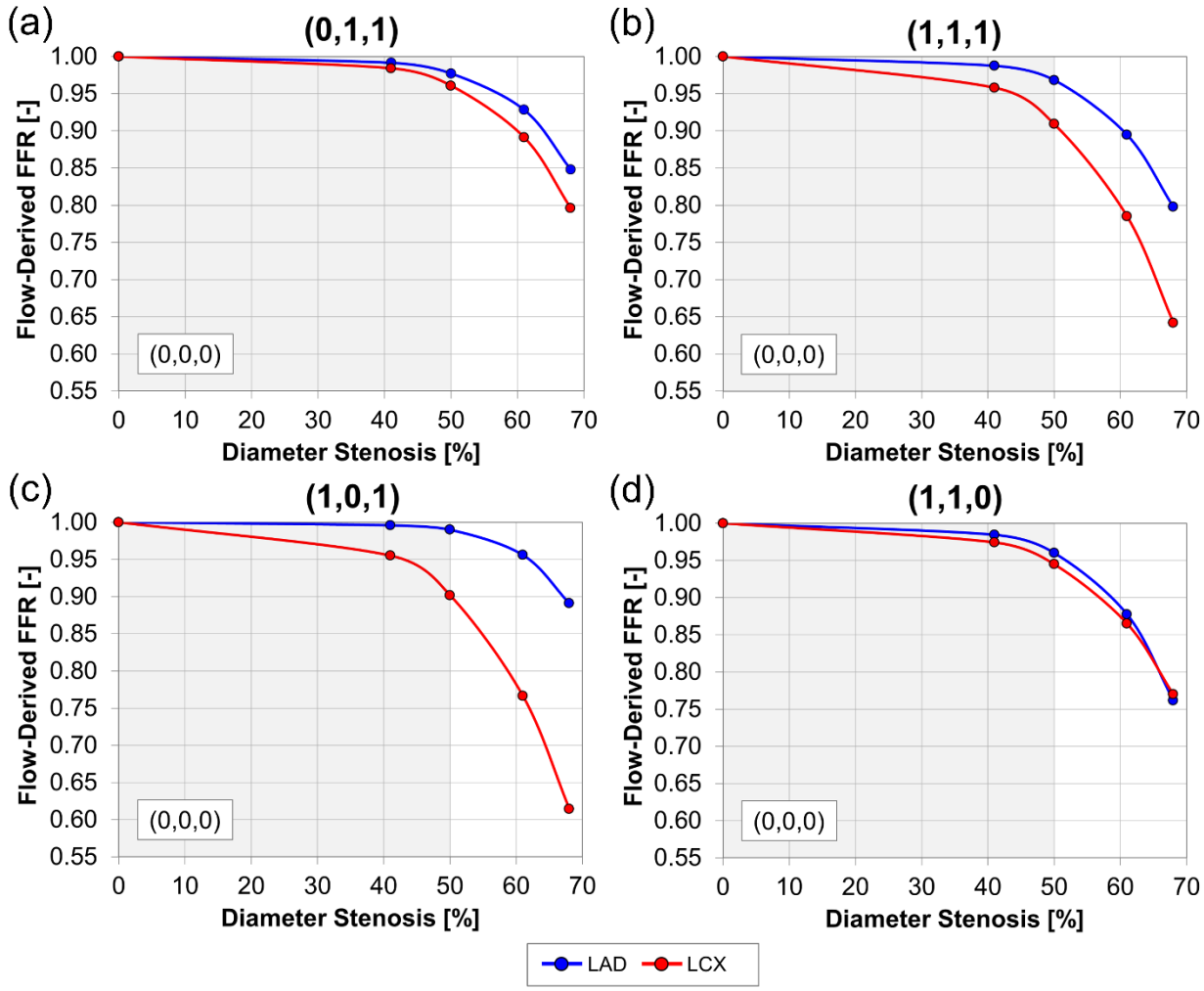

Figure 7.5: Comparison between the flow-based FFR in the LAD and LCX for the (a) (0,1,1) (b) (1,1,1) (c) (1,0,1) and (d) (1,1,0) as a function of percent diameter stenosis.

Conversely, the (1,1,0) configuration displays significantly different behaviour; as the stenosis severity increases, the flow-based FFR curves of the LAD and the LCX converge and eventually intersect at a diameter reduction of 66 percent. As such, unlike the (1,0,1) configuration the flow-based FFR values in the LAD and LCX do not differ significantly (a maximum of 0.02 at a stenosis of 50 percent) regardless of the fact that the LAD is not stenosed.

7.3.3 Pressure-based FFR

The pressure-based FFR, given by the ratio between the distal stenosis pressure and the aortic pressure, is calculated for each configuration and stenosis severity. Figure

7.6 compares the pressure-based FFR (FFR_P) and flow-based FFR (FFR_Q) in the LCX and LAD for each configuration.

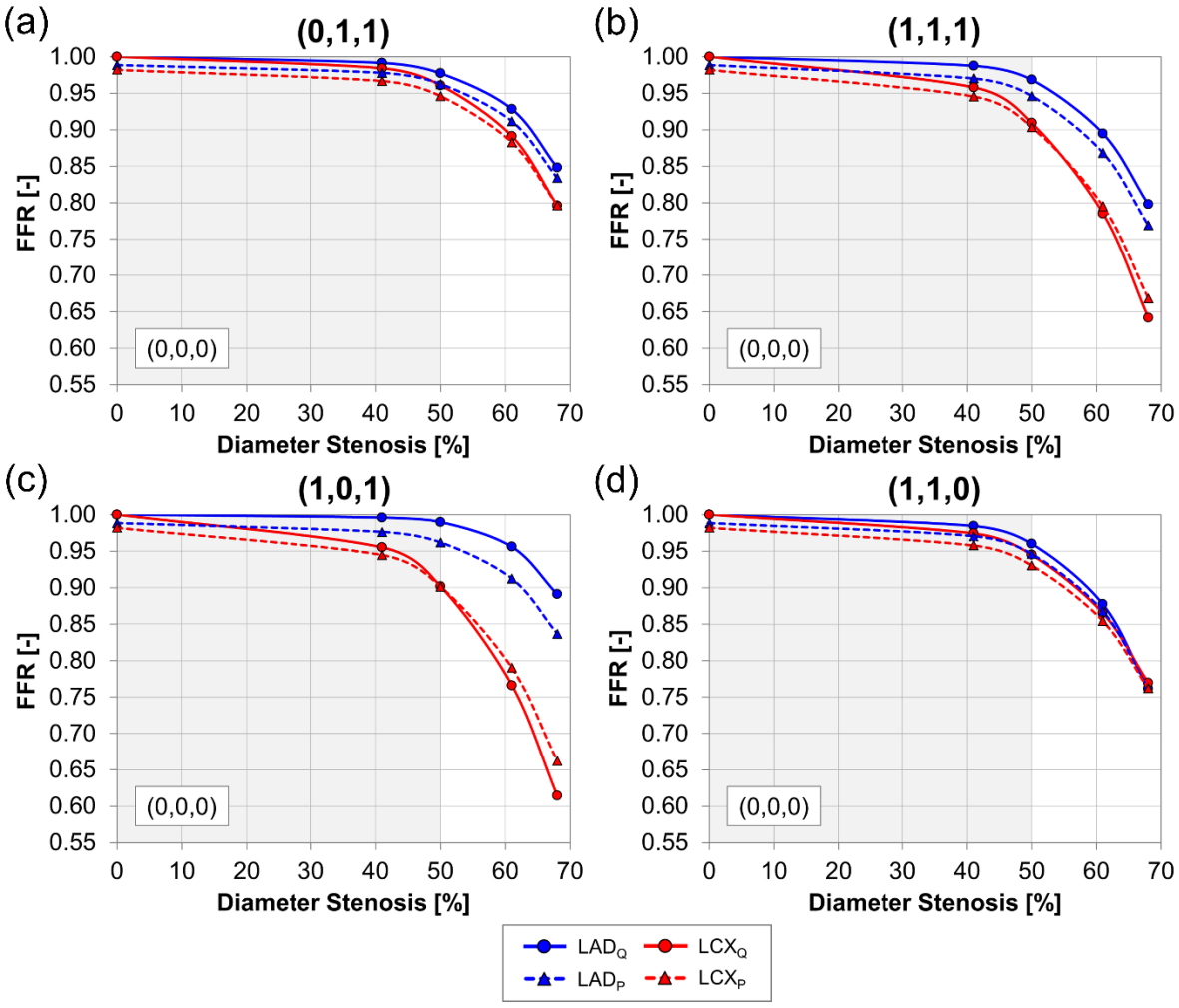

Figure 7.6: Comparison between the flow-derived FFR (FFR_Q) and the pressure-derived FFR (FFR_P) for the (a) (0,1,1) (b) (1,1,1) (c) (1,0,1) and (d) (1,1,0) configurations as a function of diameter stenosis.

One can observe that the trends displayed by the pressure-based FFR are similar to those for the flow derived-FFR. Specifically, the pressure-based FFR is consistently lower in the LCX as compared to the LAD. A nonlinear increase in the FFR between the LAD and the LCX is still observed between the (0,1,1) and (1,1,1) configurations. Within the LAD, the pressure-based FFR differs by 0.04 and 0.07 at a stenosis severity of 61 percent and 68 percent, respectively, between the two configurations, whereas in the LCX, the corresponding differences are 0.09 and 0.13 at diameter stenoses of 61 percent

and 68 percent respectively. A significant difference between the pressure-based FFR in the LAD and LCX is observed for the (1,0,1) although the difference between the two curves is smaller when compared to the corresponding differences in the curves of the flow-based FFR; at diameter reductions of 61 percent and 68 percent, the respective difference in the flow-based FFR between the LAD and LCX is 0.19 and 0.28, whereas for the pressure-based FFR values, these differences are 0.12 and 0.18 respectively. Finally, the LAD and LCX pressure-based FFR curves converge (rather than diverge) for the (1,1,0) configuration as is determined for the flow-based FFR, although the curves intersect at a slightly larger diameter reduction, namely 68 percent (as compared to 66 percent stenosis). As such, for the range of stenosis severities investigated, with respect to the pressure-based FFR, the flow is consistently more critically reduced in the LCX in the (1,1,0) configuration as compared to the LAD, although there is no stenosis in the LCX.

Differences between the flow- and pressure-based FFR values can be observed, specifically for the (1,0,1) configuration in both the LAD and LCX and the (1,1,1) configuration in the LCX. Within the LCX, for the (0,1,1) and (1,1,0) configurations, the pressure-based FFR overestimates the functional impact as compared to the flow-based FFR when the percent diameter reduction is less than 62 percent. Above this threshold, the functional impact for these configurations is underestimated. The (1,0,1) and (1,1,1) configurations show the same behaviour, although the transition threshold is around 50 percent. Overall, for these configurations in the LCX, when the flow-based FFR is at the ischemic threshold of 0.8, the pressure-based FFR value range between 0.81 and 0.82. In the LAD, different trends are seen between the two indices; for the (1,0,1), (0,1,1) and (1,1,1) configurations, the pressure-based FFR consistently overestimates the severity. Both the pressure- and flow-based FFR are, however, above 0.8 for the range of stenoses severities which show the greatest discrepancies. Conversely, the (1,1,0) configuration shows the same trends as those in the LCX; at high percent diameter reduction the functional severity is underestimated by the pressure-based FFR and vice versa at low percent diameter reduction. The threshold for this transition occurs at a 66 percent diameter stenosis.

7.4 DISCUSSION

In this study, the geometric multiscale model of the LMCA bifurcation is utilized, for the first time, to investigate the effect of lesion configuration on the functional impact of coronary bifurcation lesions.

7.4.1 Flow and pressure profiles

Figure 7.2 and Figure 7.3 displayed the progression of the flow and pressure curves in the (1,1,1) case as a function of stenosis severity. A similar decrease in amplitude in the flow curves with increasing stenosis severity was also reported by Kim *et al.* [140] in the corresponding computational study. Although in a clinical setting, the flow through the epicardial arteries does not correspond to the perfusion of the myocardium (in other words the myocardial FFR), in this research, due to the fact that collateral flow is not included, there is a direct correlation between epicardial and myocardial flow and therefore myocardial perfusion as a result of the conservation of mass. As such, in the context of CBLs, the model developed in this research is capable of capturing the decrease in myocardial perfusion with increasing stenosis severity, consequently making it possible to report flow-based FFR values.

The computed pressure curves at the outlets of the LAD and the LCX could be compared with *in vivo* data due to the fact that in a clinical setting, the pressure-based FFR is utilized for diagnostic purposes. The shape of the pressure curves computed for the diseased cases correlate well with those presented in the literature [22, 26, 188]. In particular, still in regard to Figure 7.3, one can observe that for stenosis severities with computed high FFR values, as in the LAD with a 41 percent diameter reduction and a corresponding 0.97 pressure-based FFR, the aortic and distal pressure curves overlap during the majority of the cardiac cycle, as was displayed in Pijls *et al.* [22] for a stenosis with an FFR of 0.97. Clinically, Meimoun *et al.* [188] and Tonino *et al.* [26] showed that for stenoses with intermediate FFR values namely, 0.87 and 0.90, the distal pressure curves begin to differ from the aortic pressure, in particular at peak systole and during diastole. This correlates well with the computed curves of the particular study with the corresponding pressure-based FFR values, specifically in the LAD at a 61 percent diameter reduction and in the LCX at a 50 percent diameter reduction. Finally, for more

severe cases, clinical studies show that distal pressure deviates from aortic pressure over the majority of the cycle [26] as is computed in our study in the case of LCX at a 68 percent diameter reduction with an FFR of 0.68. It is also interesting to observe that in the *in vivo* pressure measurements of the aforementioned studies, certain fluctuations in the pressure are present during diastole and are also detected in the present study, at high stenosis severities.

7.4.2 Flow-based FFR

The first important finding from the simulations in this research is that coronary bifurcation lesions display different behaviour when compared to their functional impact from global and local perspectives. This idea is shown by the fact that, globally, all configurations with a stenosis in the LMCA showed similar haemodynamic behaviour and became critical within a very small range of percent diameter reductions. However, the (1,1,1) configuration became critical at the lowest diameter reduction as compared to the rest of the configurations. This finding is logical due to the fact that this configuration had the greatest number of stenoses. Conversely, when considering the configurations from a local perspective by investigating the haemodynamic impact of the lesions on the individual daughter vessel myocardia, the results are significantly different; in each of the daughter vessels, the (1,1,1) configuration, which had the greatest number of stenoses, did not generate the most critical haemodynamic environment for any given stenosis severity. Furthermore, the (1,1,0) configuration became critical in the LCX at significantly higher stenosis severities as compared to the (1,0,1) and (1,1,1) configurations and showed more similar haemodynamic behaviour to that of the (0,1,1) configuration, a behaviour that is not evident from the global perspective. As such, the (1,0,1) and the (1,1,1) configurations reached a critical FFR in the LCX at a similar diameter reduction, although the (1,0,1) ultimately reached criticality before the (1,1,1) case.

The aforementioned results are very significant and impactful because they are suggestive of the importance of branch steal and its impact of the haemodynamic severity of coronary bifurcation lesions. Branch steal is a phenomenon that occurs in the vicinity of a vessel bifurcation, wherein a lower resistance daughter vessel diverts flow away from the higher resistance daughter vessel. Gould *et al.* [27] displayed through a linearized

and spatially-averaged model of a diseased coronary bifurcation that this phenomenon can occur in daughter vessels between which there is a relative difference in the corresponding resistance. As such, a completely occluded vessel is not required for this phenomenon to occur. In Gould *et al.* [27] it was shown that with increasing stenosis severity in the proximal main branch, the CFR of the healthy (low-resistance) daughter vessel was decreasing. However, for any given stenosis severity in the proximal main branch, as the severity of the stenosis in the distal main branch increased, the CFR of the healthy daughter vessel also increased. Thus, as the stenosis in the distal main branch became more severe, the healthy daughter vessel was increasingly stealing flow away from it as a result of its low resistance.

In this research, the phenomenon of branch steal is captured and shown through the fact that the (1,1,0) and (1,0,1) configurations create a more critical haemodynamic environment in the corresponding diseased daughter vessel as compared to the (1,1,1) configuration which has a greater number of stenoses overall. Interestingly, our results correlated well with those of Gould *et al.* [27] which showed that branch steal becomes more significant as the severity of the proximal main branch stenosis increases. The results of the current study also correlate well with those of Zarandi *et al*. [46] and Frattolin *et al.* [45] who obtained a significantly lower flow ratio between the side branch and the proximal main branch in the (1,0,1) configuration as compared to the (1,1,1) configuration. Zarandi *et al*. [46] and Frattolin *et al.* [45] did however find greater differences in the flow ratio between the two-lesion and three-lesion configurations in comparison to this research. The discrepancies between the results are attributed to the nature of the boundary conditions utilized in [45, 46].

The results of the current study also correlate well with the FFR values measured by Yong *et al.* [103] in the LAD and the LCX of ovine when the same stenosis configurations are induced. Branch steal is displayed to occur in both configurations, although in this particular study the two configurations showed similar behaviour, a result that can be attributed to the particular ovine model. An important finding of [103] which is particularly pertinent to the present study is that branch steal is found to be more prominent in the cases where the two lesions are closest to the bifurcation.

As mentioned above, the (1,0,1) configuration displayed the expected behaviour in the FFR with regard to branch steal, such that with increasing stenosis severity, the FFR in the LCX is lower for the (1,0,1) configuration as compared to the (1,1,1) configuration due to the fact that the LAD, which is not stenosed, is stealing blood flow away from the LCX which had a higher resistance path to follow due to the presence of the stenosis. Correspondingly, due to the flow diversion into the LAD, the FFR of the (1,0,1) configuration within the LAD is the highest of the rest of the configurations. The (1,1,0) configuration, which had a similar configuration to that of the (1,0,1) but with a stenosis in the LAD as opposed to the LCX, also showed some signs of branch steal in that, within the LAD, the FFR is lower for the (1,1,0) than for the (1,1,1) configuration. However, in this case, within the LCX which is not stenosed, the FFR is not the highest of the rest of the configurations which signifies that the flow diverted away from the LAD by the LCX is not as significant as in the case of the (1,0,1) configuration. This is further denoted by the fact that for the (1,1,0) configuration, the FFR within the LAD and the LCX is very similar, with a slightly more significant value within the LCX even though the LCX is free of lesions.

The results obtained in this research have potentially very significant clinical implications. Due to branch steal, it is suggested in this study that a two-lesion configuration could have an equal if not more significant haemodynamic impact compared to a three-lesion configuration, a phenomenon that deviates from intuitive judgement. As such, this finding suggests that in a clinical setting, two-lesion configurations should be considered just as significant as three-lesion configurations. Furthermore, the results of this study indicate that branch steal, which has been shown to have a greater effect in bifurcation lesions due to the close proximity of the stenoses to the bifurcation as well as to one another, can be a complicated phenomenon; more specifically, a misinterpretation of its contribution to the functional impact could result in a misguided and/or incorrect diagnosis (false negative) as is suggested through the case of the (1,1,0) configuration. Here, it is expected that the perfusion of the myocardium of the LAD would significantly be affected. However, the flow reduction to the LCX, which is free of disease, is just as, if not more, significant. The differences calculated between the (0,1,1) and (1,1,1)

configurations could also have some important clinical considerations. The results showed that the introduction of a moderate stenosis in the LMCA can significantly and nonlinearly increase the haemodynamic impact of the (0,1,1) configuration. Consequently, this finding suggests that even a mild to moderate degree of narrowing in the LMCA should be considered to be significant, particularly due to the fact that small changes in its severity as a result of disease progression could greatly influence the functional impact and therefore affect the diagnosis and prognosis.

7.4.3 Pressure-based FFR

The pressure-based FFR, as is employed clinically for the diagnosis of coronary stenoses, is compared to the flow-based FFR, which constitutes the fundamental definition of the fractional flow reserve. The results of the study showed some discrepancies between the two values over the range of stenosis severities considered. In milder stenosis severities, where the pressure-based FFR is lower than the flow-based FFR, the differences between the two values can be attributed to the initial discrepancy in the healthy case; whereas the flow-based FFR has a theoretical healthy value of one, as a result of the small pressure drop that occurs in the epicardial arteries relative to aortic pressure, the pressure-based FFR has a slightly lower healthy value. At more severe diameter reductions, the differences between the pressure- and flow-based FFR can be attributed to the assumption of the direct relationship between the pressure drop and the flow within the myocardium at maximum hyperaemia that is employed in the derivation of the pressure-based FFR.

The results of the study displayed that the epicardial and myocardial resistances are the main determinants of the flow magnitude within the epicardial arteries. However, their corresponding compliances are not neglected and therefore can account for the differences between the pressure- and flow-based FFR. Discrepancies between flow- and pressure-based FFR values have been reported in the literature. For example, De Bruyne *et al.* [93] registered a mean difference of 0.042 ± 0.092 between the pressure-based FFR and myocardial perfusion using positron-emission topography. In the current study, the maximum difference between the pressure- and flow-based FFR is 0.07, with the majority of the cases displaying a difference of approximately 0.03. Therefore, these differences

in the current study correlate well with those reported in the literature. Overall, the important finding is that both the pressure- and flow-based FFR values displayed the same general trends and allowed for the same conclusions to be drawn about the functional impact of the different coronary bifurcation lesion configurations.

7.5 SUMMARY

In this chapter, the developed geometric multiscale CFD model was utilized to investigate the effect of lesion configuration on the functional impact of CBLs. The results of the investigation corroborate the hypothesis that the lesion configuration alone significantly impacts the haemodynamic interactions between the stenoses within the bifurcation and influences the functional impact of the corresponding configuration. More specifically, the study found that branch steal plays a central role in the functionality of the different lesion configurations. As such, one of the main findings of this investigation is that a two-lesion configuration can be just as, if not more haemodynamically significant as compared to a three-lesion configuration at any given percent diameter stenosis. The results were also supportive of the complexity of the branch steal phenomenon. Consequently, another significant finding of the investigation is that the (1,1,0) and the (1,0,1) configurations displayed significantly different dynamics, with the possibility of diagnostic false negatives arising in the case of the (1,1,0) configuration, regardless of the similarity in their configurations.

8

EFFECT OF RELATIVE STENOSIS SEVERITY

This chapter outlines the study of the effect of relative stenosis severity on the functionality of coronary bifurcation lesions. It provides the motivation behind the investigation of this particular parameter, an overview of the methods and the results and clinical relevance of the findings.

8.1 MOTIVATION

The development of fractional flow reserve and its subsequent clinical validation have emphasized the inadequacy of angiographic severity to identify stenoses that induce functional ischemia [26, 28]. Nevertheless, research is ongoing regarding the identification of angiographic characteristics that are independent predictors of functionally significant lesions. Several studies have demonstrated that a correlation between stenosis severity and FFR exists [25, 189, 212, 213], and tends to be dominant compared to correlations of other angiographic parameters with the clinical index [214]. Consequently, these studies suggest that stenosis severity could be an important predictor of CBL functionality.

The resistance of a stenosis, and therefore the corresponding transtenotic pressure drop, is dependent on morphological parameters, as outlined in Chapter 2 (Equations (2.2) and (2.3)) and thus, the contribution of stenosis severity is inherent. However, stenosis resistance is additionally dependent on the transtenotic flow. Consequently, the presence of multiple stenoses in the coronary tree results in the mutual underestimation of the true individual stenosis resistance due to the fact that each lesion contributes to the overall epicardial resistance and thus, the total myocardial flow reduction [102-108].

Interestingly, the extent of the interactions and the corresponding degree of the underestimation of FFR has been shown to be complicated; for example, through a clinical study, Pijls *et al.* [102] demonstrated that the effect of the distal stenosis on the apparent (masked) FFR of the proximal stenosis is more significant than that of the proximal stenosis on the corresponding apparent FFR of the distal stenosis. Park *et al.* [215] observed a similar phenomenon through computational studies of tandem lesions with varying proximal and distal stenosis severities. In [215], it was also found that for either a proximal or distal stenosis with a mild severity, increasing the severity of the adjacent stenosis results in a general monotonic increase in its apparent FFR. However, as the severity of the reference stenosis increases, a nonlinear relationship between its apparent FFR and the (increasing) severity of the adjacent stenosis is observed. These results are in good accordance with the computation results of D'Souza *et al.* [104].

Overall, the underestimation of the apparent haemodynamic severity of a stenosis can be significant. Relative differences in FFR from two to above 15 percent have been recorded and can thus have important implications for revascularization [102, 104, 106]. The total haemodynamic impact of tandem lesions is governed by a relative contribution from the two stenoses, which in turn could be affected by the extent of the haemodynamic masking of the individual lesion severity.

The aforementioned studies have emphasized the complexity of the haemodynamic interactions between tandem lesions and the corresponding masking of the true functional severity of the individual stenoses found in series to one another. Yet,

in the case of bifurcation lesions, the complexity of this phenomenon can be further amplified due to the presence of an intermediate branch and thus, the involvement of two or more stenoses and branches in these interactions; the haemodynamic severity of an isolated stenosis within a CBL configuration can be masked by up to two adjacent lesions, each of which can exhibit its own haemodynamic severity and thus, contribute variably to the masking of the adjacent stenoses.

Moreover, due to the involvement of a bifurcation, the relative epicardial resistance between the daughter vessels, which is influenced by both the relative severity of the corresponding stenoses and that of the supplying vessel lesion, governs the relative distribution of blood between the myocardial beds being perfused by the epicardial bifurcation. This phenomenon, which can be extended to the notion of branch steal, further complicates the manifestation of the disease as it works in conjunction to the masking effect. In Chapter 7, branch steal was shown to amplify the flow reduction within the corresponding diseased daughter vessel such that from a localized perspective, a two-lesion configuration was rendered more haemodynamically critical than a three-lesion configuration. The importance of branch steal in the clinical manifestation of CBLs has also been previously suggested [27, 109]. More specifically, the distribution of blood between the two daughter vessels, as determined by both the relative epicardial resistance and the relative size and resistance of the two distal myocardial domains being perfused by the bifurcation, would affect the apparent FFR of the corresponding myocardial beds. In turn, the cumulative effect of branch steal and haemodynamic masking within the two daughter vessels would impact the total transtenotic flow through the supplying vessel stenosis thus, further influencing the apparent FFR and subsequently the overall functionality of the configuration.

Consequently, for coronary bifurcation lesions, there is a complicated interplay between branch steal and the masking effect of sequential stenoses. This idea could have an important effect on the global and local haemodynamic manifestation of the various configurations, yet has not been assessed to date; computational studies of CBLs thus far modelled a constant severity between all lesions in the bifurcation [39-48]. Therefore, the objective of the present study is to systematically quantify and compare, for the first

time, the functionality of different CBL configurations with varying stenosis severity within each of the individual vessels of the bifurcation.

8.2 METHODS

The seven bifurcation lesion configurations of the Medina classification are considered in this study. Three diameter reductions, corresponding to mild (41 percent), moderate (55 percent) and severe (68 percent) diameter reductions are modelled so as to capture a wide range of severities. Figure 8.1 displays examples of the geometries considered in the study, including the single-, double- and triple-lesion configurations.

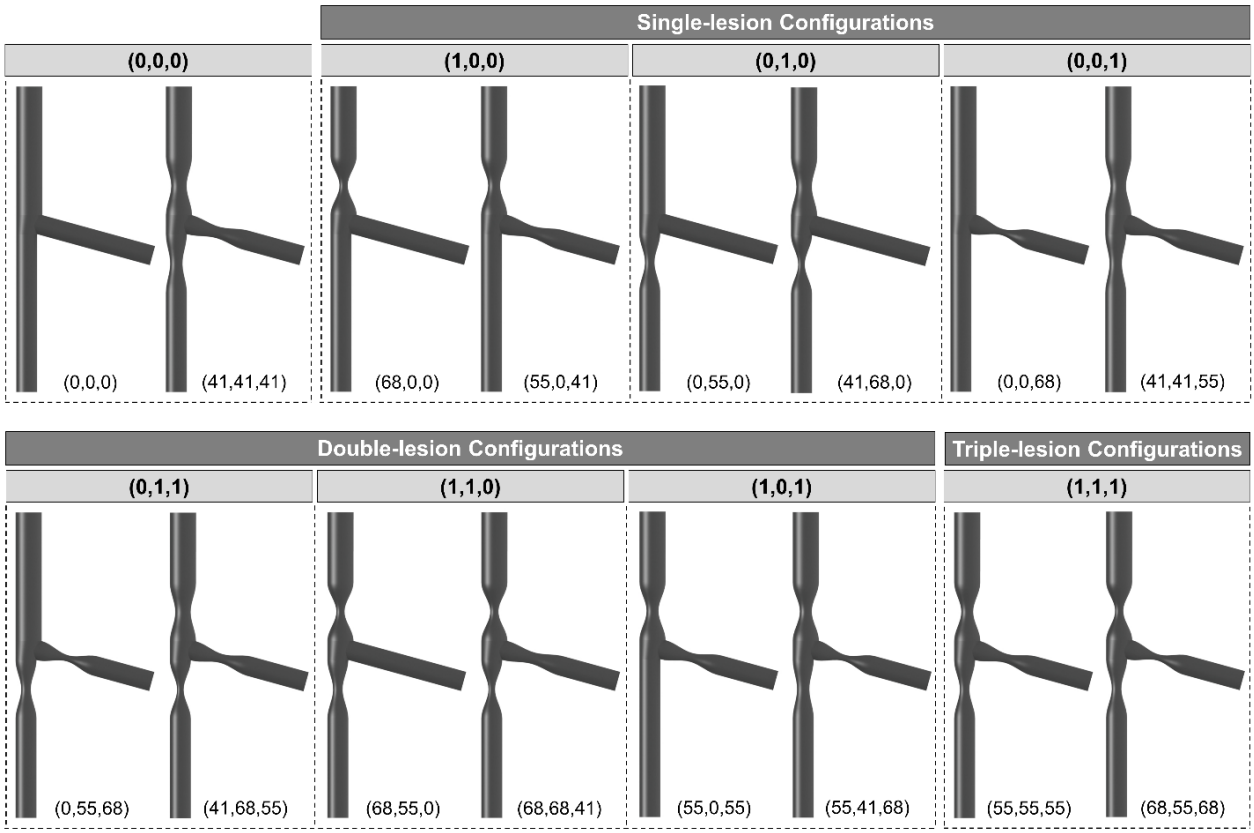

Figure 8.1: Examples of healthy and single-, double- and triple-lesion configurations with varying stenosis severity. The diameter reductions of the stenoses within each vessel are provided. Vessels with stenoses of 41 percent diameter reduction are considered healthy.

In order to assess the effect of stenosis severity as well as the effect of the relative severity of the stenoses between the vessels of the bifurcation, the diameter reductions of the stenoses within a single case are not uniform. More specifically, all possible

combinations of stenosis severities within the various vessels of the bifurcation are considered thus, resulting in a total of 63 simulations. One must note that when the Medina classification is used, stenoses with diameter reductions of 41 percent are considered healthy and are assigned a binary value of 0. Therefore, single-lesion configurations can have up to two vessels with mild diameter reductions while double-lesion configurations can have up to one stenosed vessel with a mild diameter reduction (this idea is demonstrated in Figure 8.1).

Due to the significant number of simulations, a slightly coarser mesh is utilized in the current study in comparison to the mesh implemented in all other simulations. More specifically, the coarse mesh considered for the sensitivity analysis (Chapter 5) is used. In the mesh sensitivity analysis, the coarse mesh displayed a maximum two percent difference in the boundary flows and pressures, relative to the corresponding value with the fine-mesh simulations. Due to the fact that the simulations of the current study would not be used for comparative purposes in subsequent chapters (this investigation is independent of the other geometric parameters) the coarse mesh is deemed sufficient. The use of a coarser mesh allows a notable decrease in computational time. To further decrease computational time, a total of four cycles (rather than six) are simulated for each of the 63 cases.

8.3 RESULTS

The flow-derived FFR for the single-lesion configurations is displayed in Figure 8.2. One can observe that globally (Figure 8.2a), only the (1,0,0) configuration with a diameter reduction of 68 percent reaches a critical FFR. In the LMCA, the FFR of the (1,0,0) configuration is significantly lower than that of the (0,1,0) and (0,0,1) configurations, displaying differences up to 20 percent at the maximum diameter reductions. When considering the flow in the individual daughter vessels, none of the single-lesion configurations become critical in the LAD, whereas both the (1,0,0) and (0,0,1) configurations display an FFR value below 0.8 at a diameter reduction of 68 percent. In Figure 8.2b and Figure 8.2c, one can also observe that for the (0,1,0) configuration, with increasing LAD stenosis severity, the FFR within the LCX increases. The same behaviour occurs for the (0,0,1) configuration, in the LAD, with increasing LCX stenosis severity.

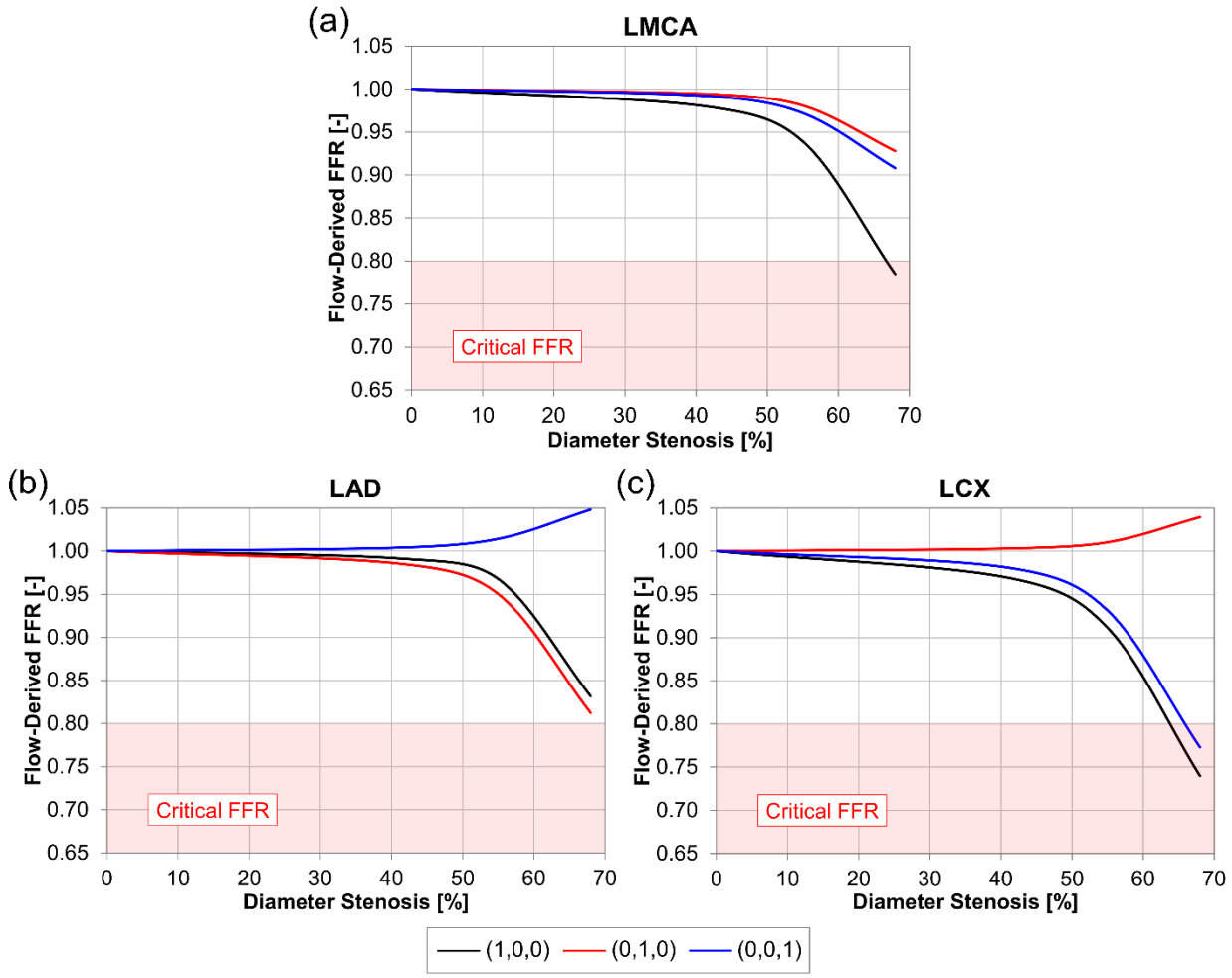

Figure 8.2: Flow-derived FFR in the (a) LMCA (b) LAD and (c) LCX for the single-lesion configurations. The shaded area corresponds to critical FFR values.

Figure 8.3 presents the flow-derived FFR in the LMCA, LAD and LCX for the (1,1,0) and (1,0,1) configurations. The (1,0,0), (0,1,0) and (0,0,1) configurations are provided for reference. The independent axis refers to varying LAD or LCX diameter stenosis in the corresponding configurations; in the (1,0,0) case, the varying stenosis severity corresponds to the LMCA lesion. One can observe that with increasing LMCA severity, the FFR within all vessels of the bifurcation decreases. Globally, increasing the LAD and LCX severity also results in a decrease in FFR. Interestingly, from a global perspective, only configurations with a 68 percent diameter reduction in the LMCA reach a critical FFR, irrespective of the severity of the stenoses within the LAD and LCX. In fact, the (1,0,0) configuration with a 68 percent diameter reduction generated a more globally critical haemodynamic environment than the (1,1,0) and (1,0,1) configurations with a moderate

diameter reduction in the supplying artery and severe diameter reductions in the diseased daughter vessels. As such, a single-lesion configuration is globally more critical than a two-lesion configuration.

From the local perspective (Figure 8.3b and Figure 8.3c), when considering each of the daughter vessels individually, the FFR decreases as the severity of the stenosis in the supplying vessel increases. In the (1,1,0) and the (1,0,1) configurations, with increasing severity of the LAD and LCX stenoses respectively, the FFR in the corresponding vessel decreases while the FFR in the adjacent healthy vessel increases.

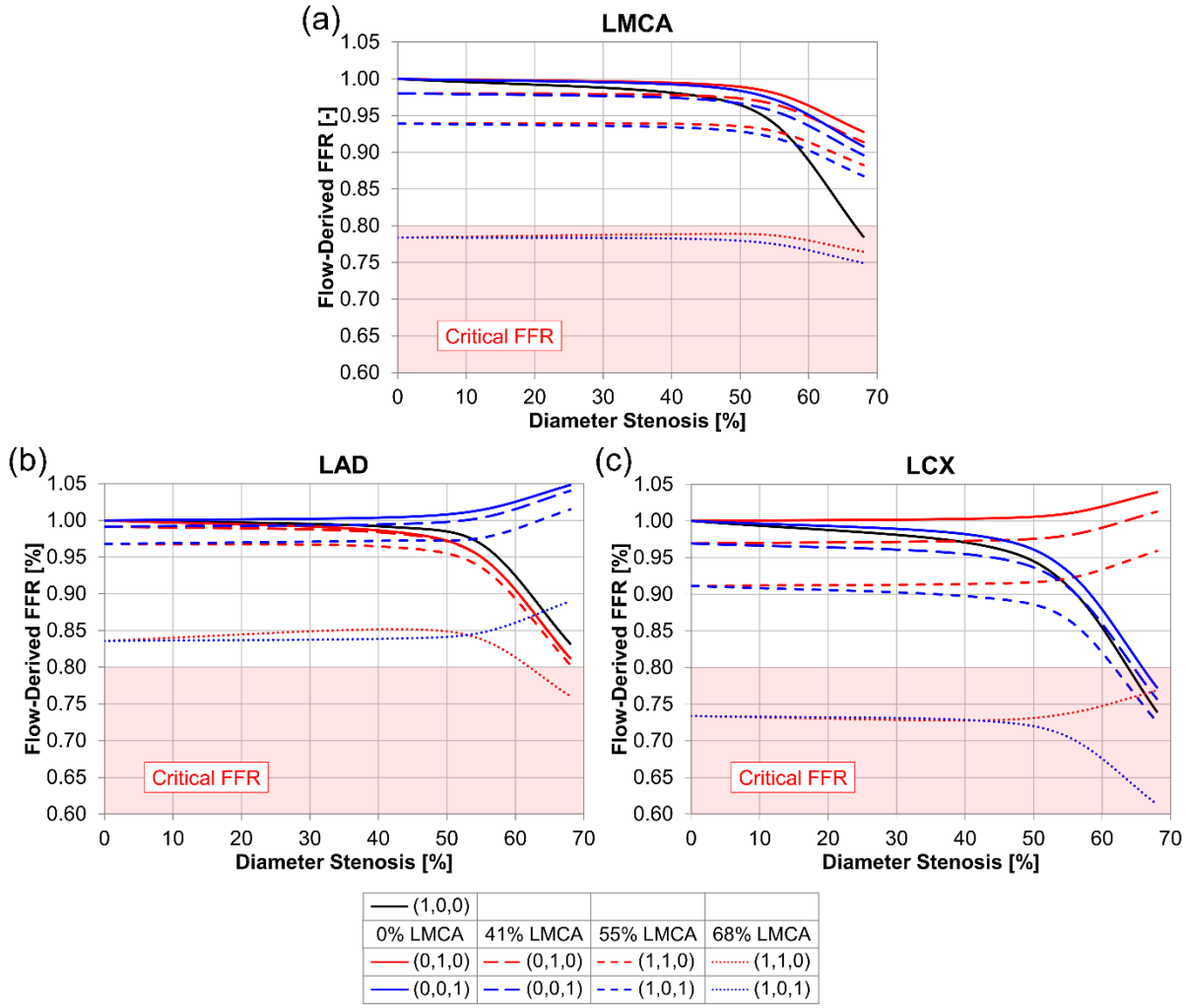

Figure 8.3: Flow-derived FFR in the (a) LMCA (b) LAD and (c) LCX for the (1,1,0) and (1,0,1) configurations. The FFR of the (1,0,0) configuration has been included as a reference. The x-axis corresponds to the diameter reduction of the LMCA, LAD and LCX in the (1,0,0), (1,1,0) and (1,0,1) configurations respectively. The shaded area corresponds to critical FFR values.

The FFR in the LMCA is lower for the (1,0,0) case with a severe constriction in the supplying artery compared to many two-lesion configurations with moderate diameter reductions in the supplying vessel. However, when considering the FFR in the LAD and the LCX individually, the two-lesion configurations with moderate LMCA stenoses presented lower values compared to the (1,0,0) case with a 68 percent diameter reduction. Within the LAD, only the (1,1,0) configuration with severe diameter reductions in both the LMCA and LAD generated a haemodynamically critical environment, although many of the cases with the same configuration that had mild-moderate diameter reductions in the LMCA are borderline functional. However, in the LCX, similar to the LMCA, all configurations with severe diameter reductions in the supplying artery had FFR values below 0.8 for all ranges of LAD and LCX stenosis severities.

This observation is particularly interesting as the (1,1,0) configuration, wherein the LCX is free of disease and the LAD has mild-to moderate severity stenoses, is critical in the LCX rather than in the LAD. One can also observe from Figure 8.3b and Figure 8.3c that as the stenosis severity of the LMCA increases, the change in FFR with subsequently increasing LAD or LCX stenosis severity decreases. For example, for the (1,0,1) with a 41 percent diameter reduction in the LMCA, as the severity of the LCX stenosis increases from 0 percent to 68 percent, the FFR within the LCX ranges from 0.97 to 0.76 thus, displaying a maximum absolute difference of 0.21. Conversely, when the LMCA is severely stenosed, an increase in LCX severity between 0 percent and 68 percent results in absolute drop of 0.12 in the LCX FFR.

Figure 8.4 displays the flow-derived FFR in the LMCA, LAD and LCX for the multilesional configurations. Many single-lesion configurations are included for reference purposes. The independent axis presents varying diameter reduction in the LCX. Varying severity of the LMCA stenosis is accounted for by the different line colours whereas, varying LAD stenosis severity is displayed by different line types. Within all the vessels of the bifurcation, increasing the severity of the supplying vessel results in a decrease in FFR; an increase in LCX and LAD stenosis severity also globally reduces the FFR.

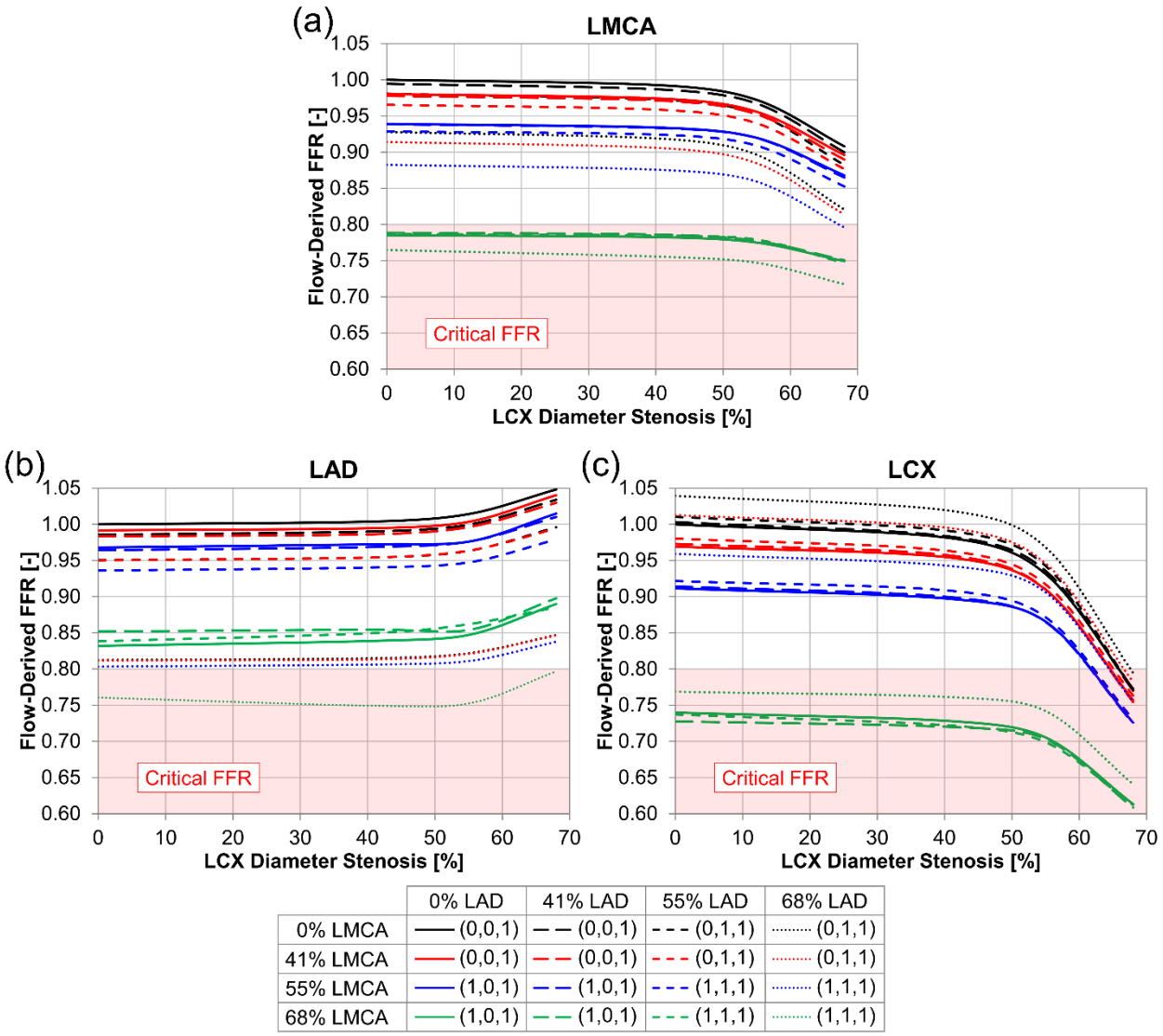

Figure 8.4: Flow-derived FFR in the (a) LMCA (b) LAD and (c) LCX for the multilesional configurations. The shaded area corresponds to critical FFR values. The severity of the LCX stenosis is presented on the x-axis whereas the different colours and line types correspond to varying LMCA and LAD stenosis severity respectively.

From the global perspective (Figure 8.4a), all configurations with a severe diameter reduction in the supplying artery result in a critical haemodynamic environment. For all other LMCA stenosis severities, an FFR below the threshold is not generated, in exception to the (1,1,1) configuration with a moderate diameter reduction in the supplying artery and severe diameter reductions in both daughter vessels. One can also observe that within the LMCA, the most significant changes in FFR are observed with increasing LMCA diameter reduction rather than increasing LAD or LCX severity, in particular when

the supplying vessel itself is severely stenosed. Specifically, at higher degrees of LMCA constriction, significant diameter reductions in the LAD and LCX are required to induce a notable decrease in FFR.

The functionality within the individual daughter vessels is presented in Figure 8.4b and Figure 8.4c. Overall, one can observe that with increasing LCX stenosis severity, the FFR in the LAD increases, whereas that in the LCX decreases. Similar behaviour is determined with increasing LAD stenosis severity wherein, correspondingly, the FFR in the LAD decreases whereas that in the LCX increases. Within the LAD, only configurations with a severe diameter reduction in both the LMCA and LAD, irrespective of LCX stenosis severity, generate a haemodynamically critical environment, although configurations with mild-moderate constrictions in the LMCA are found to be borderline critical. Conversely, in the LCX, all configurations with a 68 percent diameter reduction in the LMCA have an FFR below the ischemic threshold, irrespective of the number of stenoses and the severity of the lesions within the two daughter vessels. In addition, for mild to moderate supplying vessel stenoses, relatively severe diameter reductions in both daughter vessels are required in order to induce a haemodynamically critical environment.

Similarly to the two-lesion configurations presented in Figure 8.3, as the severity of the constriction increases in the LMCA, increasing the diameter reduction in the LAD and/or the LCX results in a smaller change in FFR compared to cases where the constriction in the LMCA is less severe. For example, in the (1,1,1) configuration with a 68 percent diameter reduction in both the LMCA and LAD, increasing the LCX constriction from 0 percent to 68 percent results in an absolute decrease in FFR of 0.12. Conversely, when the LMCA is healthy, and the stenosis in the LAD has a diameter reduction of 68 percent, the same increase in LCX stenosis severity results in absolute decrease in FFR of 0.26.

By comparing the FFR in the LAD and LCX for different configurations with a variable number of stenoses and a varying lesion severity, as is presented in Figure 8.4, one can make several important observations. For example, the results of the numerical

simulation displayed that the (0,0,1) configuration with a severe diameter reduction induce a lower FFR in the LCX compared to the FFR in the LAD and LCX generated by the (0,1,1) configurations with severe diameter reductions in both daughter vessels and even mild constrictions within the supplying vessel. Furthermore, the FFR in the LCX is found to be more critical for the (1,0,0) configuration with a single severe constriction in the supplying vessel in comparison to the FFR within both the LCX and LAD in the case of the (1,1,1) configuration with a moderate diameter reduction in the supplying vessel and mild-severe diameter reductions in both of the daughter vessels.

8.4 DISCUSSION

Previous studies have demonstrated that tandem lesions are subject to complicated haemodynamic interactions. More specifically, due to the flow-dependence of the translesional pressure drop, the presence of multiple stenoses results in the mutual underestimation of the true functional severity of the individual stenoses, in a manner dependent on the relative severity between the stenoses. In the presence of an intermediate branch, as in the case of CBLs, this phenomenon is further complicated due to the variable number and arrangement of stenoses with differing severities and the interaction of three vessel and their corresponding myocardia. This chapter presents, what is, to the best of the author's knowledge, the first systematic investigation of the functionality of different CBLs configurations with relative stenosis severities between the lesions within the bifurcation.

Sixty-three cases, consisting of the seven different CBL configurations of the Medina classification and three diameter reductions corresponding to a range of mild to severe constrictions are simulated. The particular set of simulations allows for a more systematic evaluation of the contribution of both branch steal and haemodynamic masking (resulting from the flow dependence of the translesional pressure drop) to the functionality of CBLs. The occurrence of branch steal is clear in the results; as the stenosis severity of one of the daughter vessels increased, the FFR in the adjacent daughter vessel increased thus, implying an improvement in the perfusion of the corresponding myocardial domain. Interestingly, branch steal is not only shown to occur in the cases where one of the daughter vessels is completely free of disease, as has been

suggested previously [27], but rather between two daughter vessels that display a relative resistance between them. For example, the (0,1,1) configuration with a severe diameter reduction in the LCX has a higher FFR when the diameter reduction of the adjacent LAD is also severe (68 percent) compared to when it is mild (41 percent) to moderate (55 percent). In fact, in the case where the LAD is not severely diseased, the FFR in the LCX is noticeably within the critical ischemic range, whereas when there is a severe constriction in the LAD, the corresponding FFR in the LCX is borderline critical. This signifies that a CBL configuration could potentially be destabilized in the presence of branch steal and could render what would be considered (logically) a more angiographically significant case less functionally significant. This idea was also demonstrated in Chapter 7, wherein a two-lesion configuration had a lower FFR than a three-lesion configuration.

The masking effect, wherein the true haemodynamic severity of a lesion is underestimated due to the dependence of its resistance on the transtenotic flow, is less apparent compared to the effect induced by branch steal. For example, the FFR in the LCX induced by the (1,0,0) configuration with a severe diameter reduction is lesser than the FFR in both the LAD and the LCX that is generated by the (1,1,0) configuration with severe diameter reductions in both the LMCA and the LAD and a mild diameter reduction in the LCX. This idea is further demonstrated by the fact that the total effect of a particular combination of lesions is not equal to the sum of the effects of its individual components. In the LCX, the FFR for the (1,1,0) configuration with the aforementioned stenosis severities is 0.76; conversely, the FFR in the LCX for the (1,0,0) configuration with a 68 percent diameter reduction is 0.74 while that of the (0,1,0) configuration with a severe diameter in the LAD and a mild stenosis in the LCX is approximately 1.0. In the LAD, the FFR for the respective cases is 0.83 and 0.82. Thus, the masking effect appeared to have a less dominant effect (on the order of a relative difference of two percent) compared to the effect of branch steal, which is on the order of five to six percent.

The comparison of all configurations with varying stenosis severities in the LMCA, LAD and LCX allowed for a global overview of the effect of the haemodynamic interactions that take place within CBLs and their consequent effect on the functionality and clinical

manifestation of the disease. As a result of this comparison, the results showed that the number of lesion does not govern the haemodynamic severity of CBLs; this idea was suggested in the previous chapter for multilesional configurations although is more strongly emphasized through this particular work wherein single-lesion configurations are even found to be more haemodynamically significant than triple lesion configurations. This idea is important because it is counter-intuitive, as it would be expected that a greater number of stenoses would have a more significant effect on myocardial perfusion than would a smaller number of stenoses.

An extension to this finding, the results of the simulation showed that all configurations with a severe diameter reduction in the supplying vessel produced a haemodynamically critical environment in at least one of the daughter vessels, irrespective of the diameter reductions within the LAD and/or LCX. In addition, it is demonstrated that for less severe stenoses in the LMCA, relatively significant constrictions are required in the daughter vessels to induce an FFR less than 0.8. Still yet, as the severity of the constriction in the supplying vessel increased, the absolute change in FFR with increasing daughter vessel stenosis severity is lesser. These ideas suggest that the severity of the supplying vessel stenosis could play a dominant role in the functionality of CBLs.

In the previous chapter, where the effect of lesion configuration on the functionality of CBLs was investigated, the (1,1,0) configuration displayed the possibility for false-negatives in diagnosis, wherein the FFR in the LCX was found to reach a critical value before that of the LAD, regardless of the fact that the LCX was free of disease. However, in Chapter 7, the onset of ischemia in the LAD closely followed that of the LCX suggesting such that the window of stenoses severities where diagnostic false negatives could occur was small. In the present study, this idea is better demonstrated, specifically for the cases where there is a severe constriction in the supplying vessel and mild to moderate constriction in the LAD. Here, the FFR in the LAD and the LCX displayed significant differences (up to approximately 12 percent); specifically, the FFR in the LCX is well within the ischemic range (0.74) whereas that in the LAD is noticeably above the threshold (0.84). Consequently, based on the standard pull-back tests, it would be expected that

the FFR would be lower in the LAD compared to that in the LCX thus, introducing the risk for false negatives in diagnosis. These findings also emphasize the intricacy of the haemodynamic interactions that are present within CBLs, and the complicated interplay between the masking of the true haemodynamic severity of a particular lesion and branch steal, and its consequence of the clinical manifestation of the disease.

The findings of the current study could have important clinical implications. The results suggest that the functional severity of CBLs is not governed by the number of stenoses within the configuration. Consequently, in a clinical setting, single- and double-lesion configurations should be considered just as significant as three-lesion configurations. More specifically, configurations wherein the supplying vessel is significantly stenosed could be an indication of a functionally significant configurations. Furthermore, due to the complicated interactions induced by the flow-dependence of the stenosis resistance and the involvement of multiple vessels with different perfused myocardial domains, the results also suggested that the presence of a large relative severity between daughter vessels could functionally de-stabilize a CBL configuration. This could have important implications from the treatment perspective as increasing the relative resistance between the two daughter vessels could generate a more haemodynamically critical environment. In addition, a misinterpretation of the contribution of the haemodynamic interaction to the functional impact could result in a misguided and/or incorrect diagnosis (false negative) as is suggested through the case of the (1,1,0) configuration. Finally, although hyperaemic conditions are simulated in the current study, the results could also imply that configurations that display a significant difference in the resistance between the daughter vessels could be at a greater risk for disease progression.

8.5 SUMMARY

In this chapter, the seven bifurcation lesion configurations of the Medina classification were simulated with stenoses ranging between mild and severe diameter reduction. More specifically, the relative severity between the stenoses in each configuration was varied in order to investigate its effect on the functionality. To the best of the author’s knowledge, the current study is the first to systematically investigate the

effect of relative stenosis severity from a functional perspective. More specifically, the results showed that the number of lesions does not govern the functional impact of coronary bifurcation lesions such that in a clinical setting, single- and double-lesion configurations should be considered just as significant as three-lesion configuration, particularly when the mother vessel has relatively severe constriction. The results are also suggestive of the complexity of the haemodynamic interactions within CBLs. As such certain configurations displayed the possibility of false negatives in diagnosis using the current diagnostic guidelines.

9

EFFECT OF LUMINAL ECCENTRICITY

This chapter outlines the study of the effect of stenosis (luminal) eccentricity on the functionality of coronary bifurcation lesions. It provides the motivation behind the investigation of this particular parameter, the corresponding cases that are considered in the work and the results and clinical relevance of the findings.

9.1 MOTIVATION

To date, numerical investigations of coronary bifurcation lesion have modelled the stenoses within the configurations as concentric and axisymmetric [39-48]. However, many clinical studies have found that a significant proportion of coronary lesions have eccentric morphology. More specifically, eccentric stenosis morphology is particularly observed in the cases of lesions that are in close proximity to bifurcations [150-155]. More specifically, in bifurcations, the flow divider has been shown to be spared of disease in a high proportion of reported cases [152, 153, 216]. Furthermore, in a study of LMCA bifurcation plaque distribution, Oviedo *et al.* [152] showed that approximately 35 percent of lesions in the supplying artery were eccentric.

Several studies have investigated the effect of plaque eccentricity on the corresponding haemodynamics. Early *in vitro* investigations by Young and Tsai [82, 83]

revealed that non-symmetric arterial constrictions resulted in higher pressure losses compared to the axis-symmetric counterpart. Still using *in vitro* methods, Poepping *et al.* [217] demonstrated that in diseased carotid bifurcations, there was an increase in the size of the recirculation zone and a change in fluid jet directionality in the eccentric lesion cases compared to the concentric morphologies.

Most recently, Javadzadegan *et al.* [218, 219] carried out numerical studies on both idealized and patient-specific coronary models comparing the haemodynamics of concentric and eccentric lesions. In the idealized geometries, it was shown that eccentricity resulted in an increase in the strength of the emerging jet and in the length of the distal recirculation zone. In the patient-specific models, although recirculation zone length appeared to be larger in the eccentric cases, statistical significance for this observation over the entire cohort of patients was not determined. Other studies, such as those by Griffith *et al.* [220], Guleren [221] and Varghese *et al.* [197], have looked at localized flow characteristics, such as velocity profiles and their sensitivity to flow perturbations (such as the skewness of the inlet velocity profile) as well as transition to turbulence, etc. within both concentric and eccentric constrictions. However, in all these studies, the lesions and constrictions were isolated or physiological flow conditions pertaining to coronary arteries were not employed. Furthermore, a functional perspective on the effect of eccentricity, relating to clinical manifestation of the disease, was not provided.

From a clinical perspective, several studies have sought to identify stenosis morphological parameters, including eccentricity that are independent predictors of lesion functionality. Using *in vivo* porcine models, Huo *et al*. [222] demonstrated that lesion eccentricity had a minimal effect on myocardial FFR. Opolski *et al.* [25] correlated coronary computed-tomography angiography-derived plaque morphological parameters (such as lesion length, diameter stenosis, lumen eccentricity etc.) to FFR measurements and determined that there was no difference in the average luminal eccentricity between the positive and negative FFR group. Conversely, in a study correlating morphological lesion characteristics obtained from quantitative coronary angiography to FFR,

Takashima *et al.* [223] found that FFR was significantly lower, statistically, for eccentric stenosis cases compared to non-eccentric ones.

These studies demonstrate that the effect of lesion eccentricity on the functionality of coronary lesion is still not well understood. The aforementioned numerical studies elucidate that luminal eccentricity results in localized haemodynamic changes which, in the case of bifurcation lesions could be important due to the close proximity of the stenoses to each other and the flow divider. Although from the clinical studies it is suggested that eccentricity may not have a dominant effect of coronary lesion functionality compared to other morphological characteristics, only isolated stenoses have been considered to date. As such, the effect of eccentricity on CBL functionality, wherein stenoses haemodynamically interact, remains unknown, and has not been systematically investigated. In the current study, it is hypothesized that lesion eccentricity could influence the functionality of CBLs. Thus, the objective is to compare the functional impact, as quantified by the flow-based and pressure-based FFR, between different CBL configurations with eccentric and concentric stenoses.

9.2 GEOMETRY OF THE CBL CONFIGURATIONS

Seven coronary bifurcation lesion configurations, including single-, double-, and triple-stenosis arrangements, based on the Medina classification are modelled in the present study. Mild and intermediate lesions, with diameter reductions of 41, 50, 61 and 68 percent are simulated for each configuration, as outlined in Chapter 5.

All stenoses within a given configuration have the same severity. For each configuration and stenosis severity both eccentric and concentric stenosis profiles are modelled. In the LAD and the LCX, eccentric stenosis profiles are placed opposite to the flow divider. In the LMCA, the eccentric stenosis profile is located on the side of the LAD for all configurations. Figure 9.1 provides examples of all the configurations and diameter reductions with eccentric stenosis profiles. Examples of the geometries for the concentric cases are provided in Chapter 5. Both the eccentric and concentric stenoses have circular cross-sections; Figure 9.2 displays the cross-section of an eccentric LMCA stenosis with a 50 percent diameter reduction.

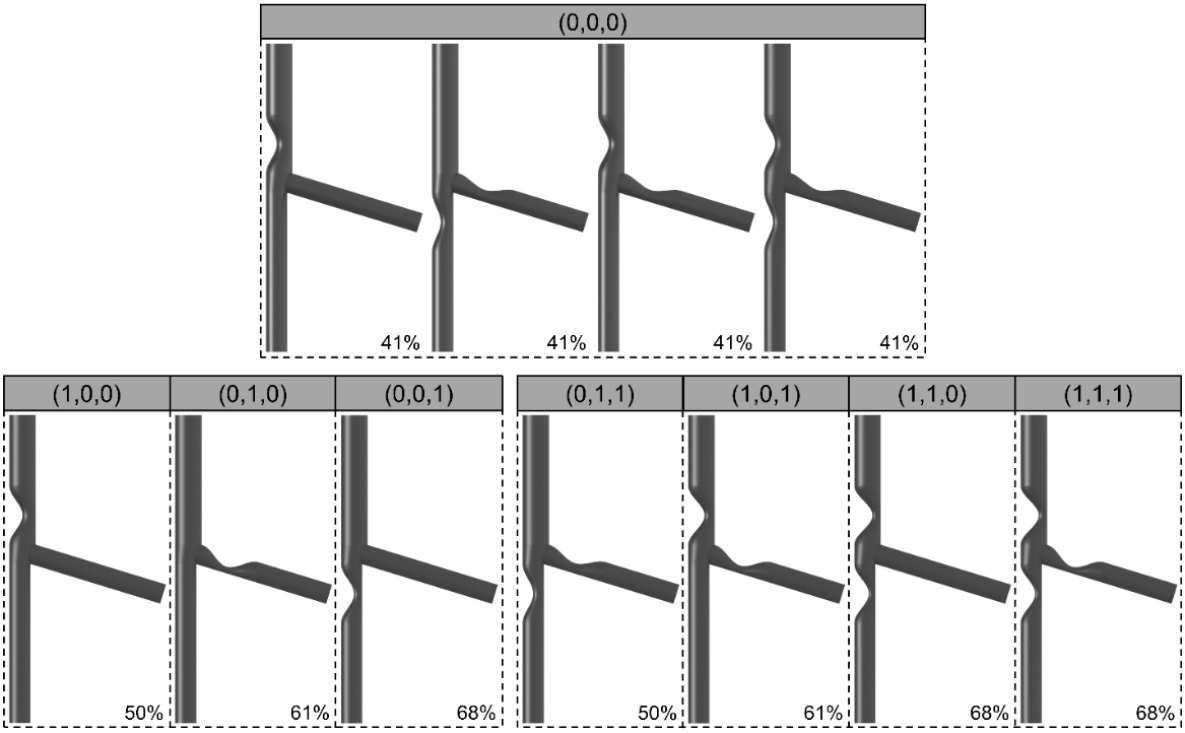

Figure 9.1: Examples of the modelled Medina classification bifurcation lesion configurations with eccentric stenosis profiles.

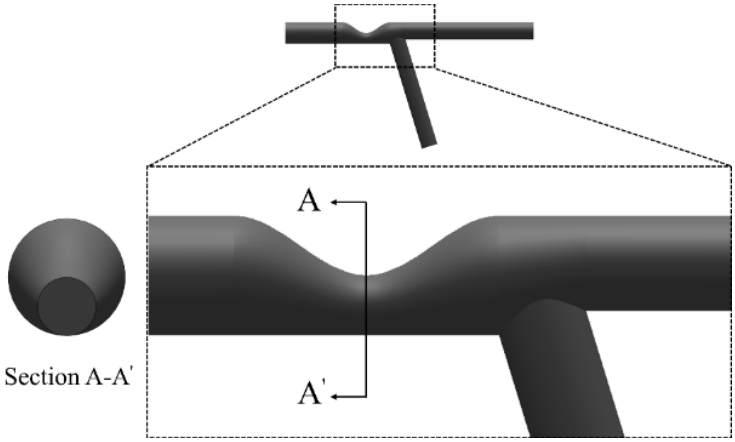

Figure 9.2: Cross section of minimal lumen diameter in the eccentric lesion morphology with 50 percent diameter reduction.

9.3 RESULTS

The average pressures and flows computed at the boundaries of each case are utilized in the calculation of the pressure- and flow-based FFR respectively. The comparison between the FFR values of the concentric and eccentric stenosis profiles is provided.

9.3.1 Flow-based FFR

Figure 9.3 compares the flow-based FFR in the LAD and LCX between the eccentric and concentric stenosis profiles within the single-lesion configurations. The left-hand panel displays the computed FFR values, while the corresponding percent differences in FFR relative to the concentric profile are given in the right-hand panel.

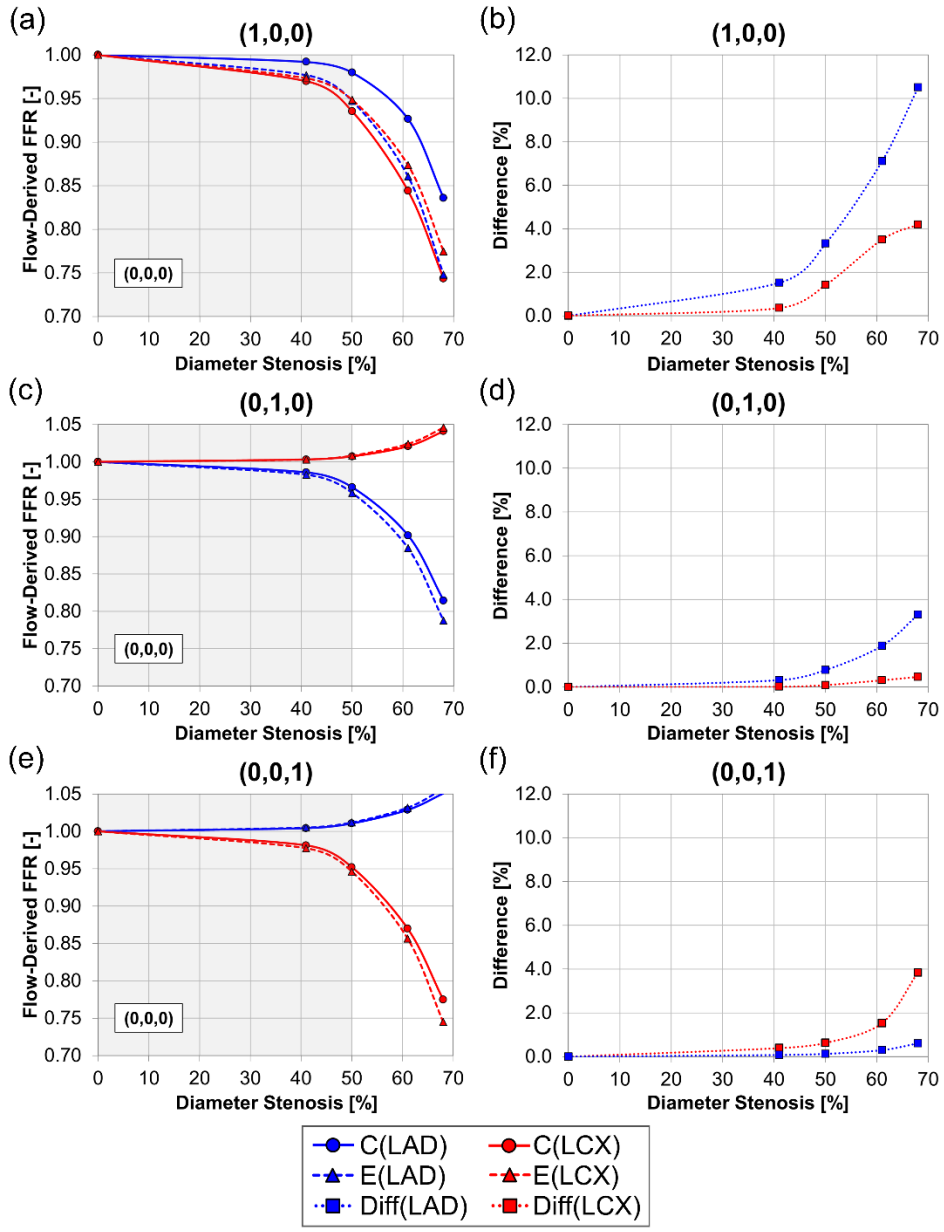

Figure 9.3: Comparison of the flow-derived FFR in the LAD and LCX for the (a) (1,0,0) (c) (0,1,0) and (e) (0,0,1) configurations between concentric (C) and eccentric (E) stenosis profiles. Percent difference (Diff) between the concentric and eccentric flow-based FFR in the LAD and LCX for the corresponding configurations are shown in (b), (d), and (f).

In the (1,0,0) configuration, a decrease in LAD FFR is observed for the eccentric case relative to the concentric one. The maximum decrease, occurring at the most severe diameter reduction is 10.5 percent. Conversely, in the LCX, the eccentric profile displays an increase in FFR relative to the concentric case; the corresponding maximum difference is below 5 percent. For the (0,1,0) and (0,0,1) configurations, within the LAD and LCX, respectively, the FFR is lower for the eccentric case compared to the concentric profile. In both configurations, the maximum difference remains below 4 percent. The maximum percent difference between the eccentric and concentric profiles for the single-lesion configurations are summarized in Table 9.1.

Table 9.1: Maximum percent difference in the flow-based FFR within the LAD and LCX between the eccentric and concentric stenosis profiles, relative to the concentric case.

		Maximum Difference [%]	
		LAD	**LCX**
Single-Lesion	**(1,0,0)**	10.5	4.20
	(0,1,0)	3.31	0.460
	(0,0,1)	0.609	3.84
Multi-Lesion	**(0,1,1)**	2.00	1.55
	(1,0,1)	10.1	8.71
	(1,1,0)	15.8	6.97
	(1,1,1)	14.3	7.95

Figure 9.4 compares the flow-based FFR in the LAD and LCX between eccentric and concentric stenosis profiles for the multilesional configurations. The left-hand panel displays the flow-derived FFR values while the right-hand panel presents the corresponding percent difference between the concentric and eccentric cases. A lower FFR is observed for the eccentric case compared to its concentric counterpart in both the LAD and LCX in the (0,1,1) configuration (Figure 9.4a,b). This configuration is the only multilesional case without a stenosis in the supplying artery; similarly to the single daughter vessel lesion configurations (Figure 9.3c-f), the maximum percent difference between the two cases is small (less than 2.0 percent within both daughter vessels). Conversely, for all multilesional cases with a stenosis is the LMCA, a significant decrease in LAD FFR is computed; in the LCX, the FFR for the eccentric case is higher than that of the concentric profile.

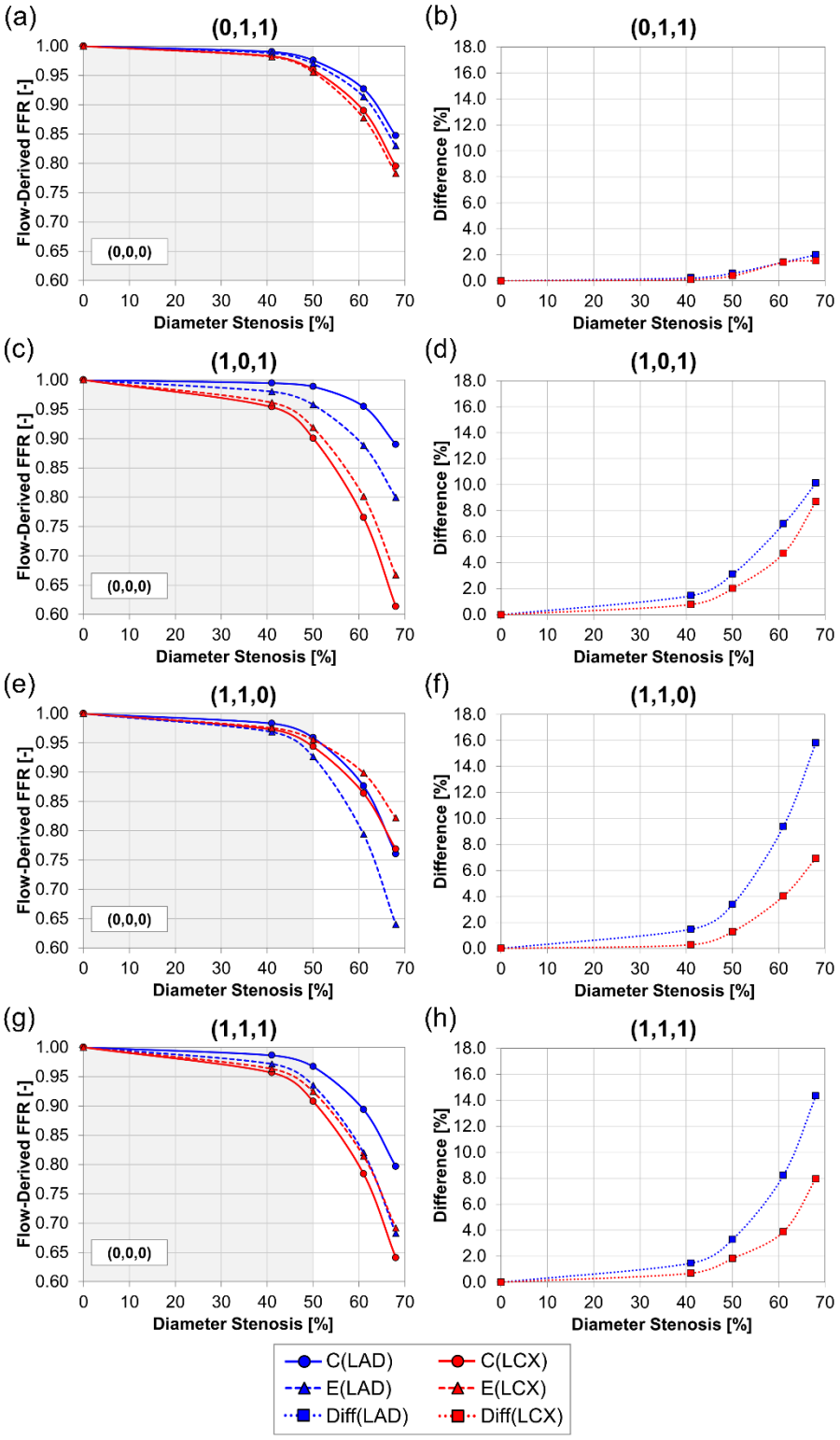

Figure 9.4: Comparison of the flow-derived FFR in the LAD and LCX for the (a) (0,1,1) (c) (1,0,1) (e) (1,1,0) and (g) (1,1,1) configurations between concentric (C) and eccentric (E) stenosis profiles. Percent difference (Diff) between the concentric and eccentric flow-based FFR in the LAD and LCX for the corresponding configurations are shown in (b), (d), (f), and (h).

The maximum difference in FFR between the eccentric and concentric cases for the (1,0,1), (1,1,0) and (1,1,1) configurations occurs at the maximum diameter reduction, within the LAD, and are 10, 16 and 14 percent respectively. The corresponding increase in FFR within the LCX is 8.1, 6.9 and 8.0 percent for the same configurations respectively. The maximum percent difference between the eccentric and concentric profiles for the multilesional cases are summarized in Table 9.1.

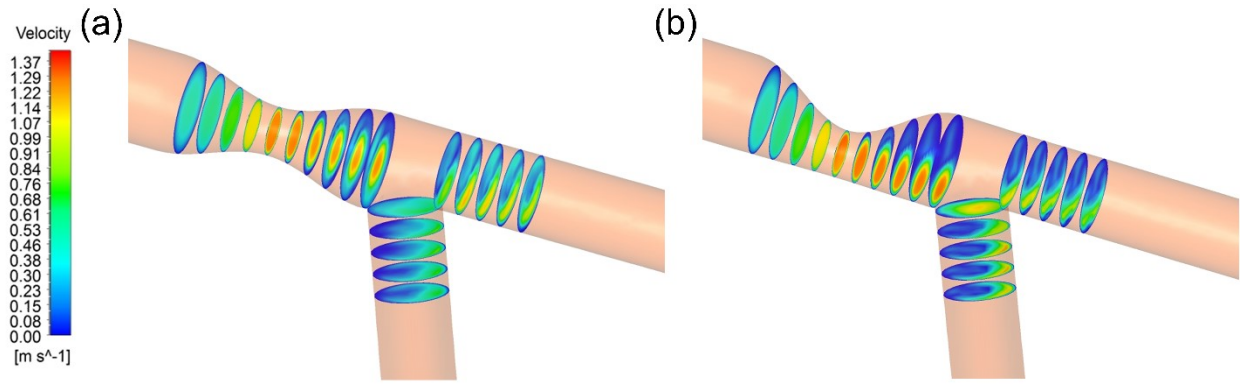

Figure 9.5: Velocity contours in the (1,0,0) configuration with a 50 percent diameter reduction for the (a) concentric and (b) eccentric profiles at t=0.7s.

Figure 9.5 displays the velocity contours near the bifurcation carina in the (1,0,0) configuration with a stenosis of 50 percent for both the concentric and eccentric stenosis profiles at time t=0.7s. It can be observed that for the concentric case, the emerging jet is centered at the axis of the vessel whereas, for the eccentric case, it is shifted towards the wall of the vessel opposite the stenosis. Furthermore, in the concentric case, the velocity in the LAD is higher than in the LCX as the momentum of the emerging jet drives the flow into the LAD. Conversely, in the eccentric case, the flow appears to be distributed more equally between the two daughter vessels, with a significantly weaker jet being observed in the LAD.

9.3.2 Pressure-based FFR

Figure 9.6 displays the pressure-based FFR in the LAD and the LCX for each multilesional configuration for both the eccentric and concentric cases. The trends observed for the pressure-derived FFR are similar to those observed for the flow-derived FFR.

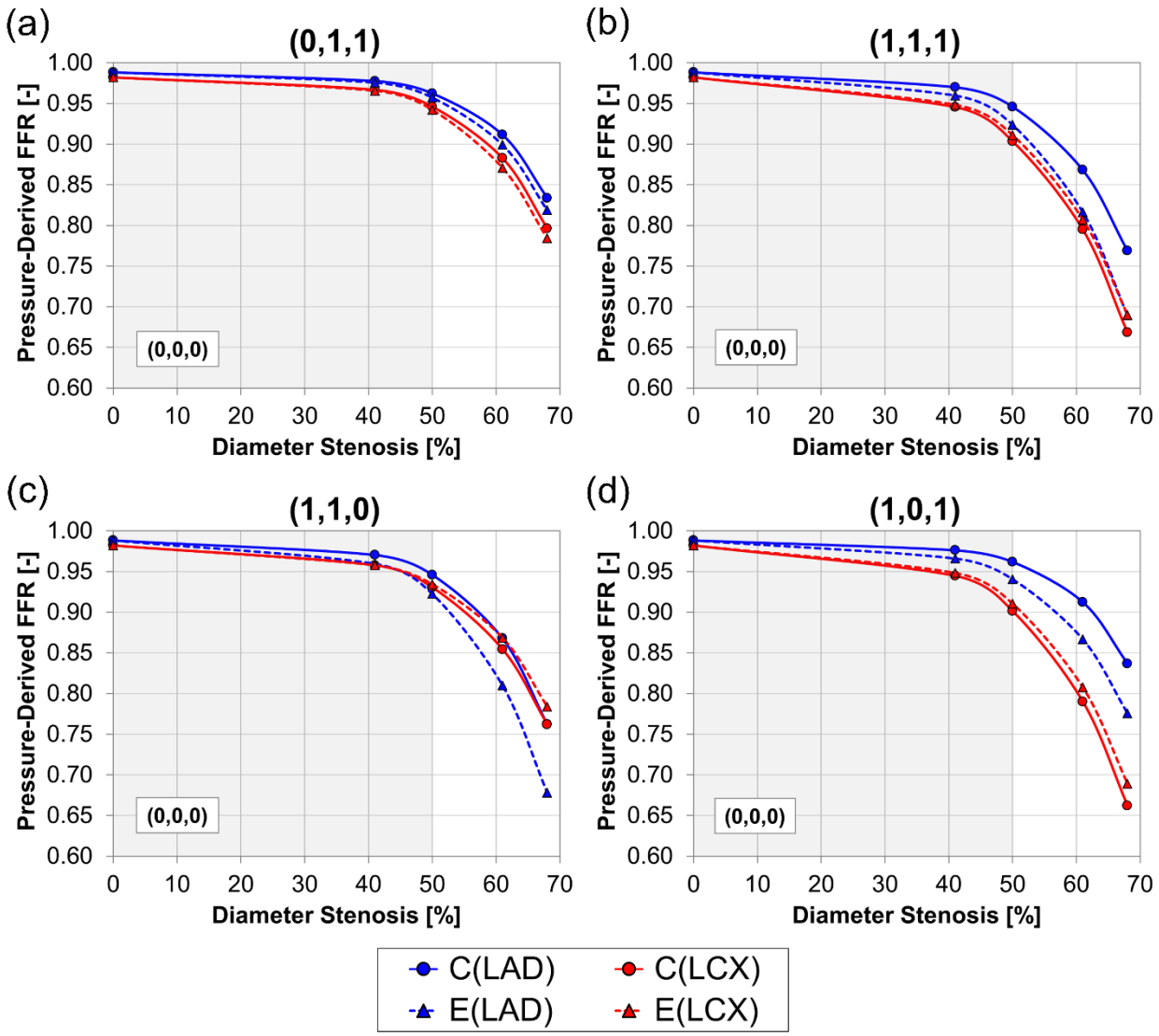

Figure 9.6: Comparison of pressure-derived FFR between concentric (C) and eccentric (E) stenosis profiles in the LAD and LCX for the (a) (0,1,1) (b) (1,1,1) (c) (1,1,0) and (d) (1,0,1) configurations.

Table 9.2: Maximum percent difference in the pressure-based FFR within the LAD and LCX between the eccentric and concentric stenosis profiles, relative to the concentric case

		Maximum Difference [%]	
		LAD	**LCX**
Single-Lesion	**(1,0,0)**	7.72	1.49
	(0,1,0)	2.39	0.0752
	(0,0,1)	0.00261	2.72
Multi-Lesion	**(0,1,1)**	1.82	1.54
	(1,0,1)	7.31	4.06
	(1,1,0)	11.1	2.86
	(1,1,1)	10.3	3.21

Specifically, for the multilesional cases with a stenosis in the supplying artery, a decrease in LAD FFR and an increase in the corresponding LCX FFR is observed for the eccentric stenosis profiles relative to the concentric cases. However, it is important to note that the magnitude of the differences in the pressure-based FFR is smaller than those computed for the flow-based FFR. Specifically, in the (1,0,1), (1,1,0) and (1,1,1) configurations, the maximum differences are 7.3, 11 and 10 percent respectively. Table 9.2 presents the maximum percent difference in the pressure-based FFR between the eccentric and concentric stenosis profiles within the LAD and LCX for all configurations.

9.4 DISCUSSION

Clinical studies have shown that coronary stenoses tend to be eccentric. Yet, to the best of the author's knowledge, the effect of eccentricity on stenosis functionality, specifically in the case of bifurcation lesions wherein plaques are found in close proximity to one another, has not been systematically investigated. In this study, the flow- and pressure-derived FFR is compared between the concentric and eccentric profiles.

9.4.1 Comparison of FFR between eccentric and concentric stenoses

The numerical simulations carried out in this study yielded differences in flow- and pressure-derived FFR between the eccentric and concentric stenosis profiles up to 3.8 percent for the configurations with lesions only within the daughter vessel lesions ((0,1,1), (0,1,0) and (0,0,1)). These configurations are the most representative of isolated-lesion cases as there are no proximal or distal stenoses with which they immediately interact. For all these aforementioned cases, the FFR is lower in the eccentric cases compared to the concentric ones which signifies that eccentric stenoses are associated with higher pressure losses. Higher pressure losses for eccentric stenosis profiles relative to concentric ones have been suggested previously in the literature, for example through *in vitro* methods by Young and Tsai [82, 83] in isolated straight vessels and by Poepping *et al.* [217] within carotid bifurcation models. Similarly, in idealized numerical models of isolated concentric and eccentric constrictions within the right coronary artery and LAD, Guleren [221] demonstrated a consistently greater pressure drop during both systole and diastole for lesions with eccentric lumens. Clinically, Takashima *et al.* [223] compared the average FFR in the presence and absence of eccentricity and found that the FFR values

were approximately 6 percent lower for eccentric cases compared to non-eccentric ones (0.79±0.10 and 0.84±0.10 respectively). Therefore, the decrease in FFR recorded in the present study is in good accordance with other literature works.

While in this study, a decrease in FFR is observed for the eccentric stenosis profiles relative to the concentric ones for the aforementioned configurations, is it important to note the magnitude of both the computed percent and absolute differences. More specifically, the recorded maximum 3.8 percent difference corresponds to a maximum absolute difference of 0.03 in the FFR values. In clinic, the measurement of FFR has been shown to be subject to some variance; a coefficient of variance (95 percent) of 4.8 percent corresponding to a mean absolute difference of 0.01±0.04 between successive FFR measurements was determined by De Bruyne *et al.* [30]. Similar observations were made by Berry *et al.* [224] who recorded absolute differences of 0±0.04 between successive *in vivo* FFR measurements. Consequently, the differences computed numerically in the present study fall within the reported clinical variance. Interestingly, several clinical studies have shown that lesion eccentricity does not play a dominant role in the isolated coronary lesion functionality. For example, Opolski *et al.* [25] found that the average lumen eccentricity index in patients was similar between patients with positive (<0.8) and negative (>0.8) FFR values (0.27±0.13 and 0.28±0.14 respectively). Lumen eccentricity was also shown by Huo *et al*. [222], in *in vivo* porcine models, to have a negligible effect on myocardial FFR. Therefore, the results of the current study appear to be in line with clinical observation.

In this research, configurations with a supplying vessel stenosis showed markedly different behaviour from those with a healthy LMCA. More specifically, a decrease in LAD FFR and an increase in LCX FFR is observed for the eccentric profiles with respect to the concentric ones. In the LAD, the maximum decrease (at the maximum diameter reduction) ranged between 10-16 percent and between 7-11 percent for the flow-based and pressure-based FFR respectively. In the LCX, the maximum increase in FFR ranged between 4-9 percent and between 1.5-4.1 percent for the flow-based and pressure-based FFR respectively. Therefore, the differences in FFR are lesser for the pressure-based FFR compared to the flow-based one. This discrepancy can be attributed to the fact that

in the derivation of pressure-derived FFR, zero-compliance is assumed in the myocardium at maximal hyperaemia whereas the present model did not disregard compliance.

Furthermore, the magnitude of the decrease in LAD FFR is greater than the corresponding increase in LCX FFR, suggesting that eccentricity has a nonlinear effect on the daughter vessel functionality. The corresponding maximum absolute changes in FFR within the LAD and LCX are 0.09-0.12 and 0.03-0.05 for the flow-based FFR and of 0.06-0.08 and 0.02-0.03 for the pressure-based FFR. Furthermore, the results displayed cases where LAD FFR is non-critical for the concentric case, but critical for the eccentric profile. For example, the (1,0,1) configuration at a 68 percent diameter reduction had a concentric flow-derived FFR of 0.89 whereas for the eccentric case, it is 0.79. Similarly, for the (1,1,0) configuration at a 61 percent diameter reduction, the concentric profile generated an FFR of 0.88 whereas in the eccentric case, it is 0.79. Finally, a borderline critical FFR of 0.8 is computed for the (1,1,1) configuration with concentric stenoses of 68 percent diameter reduction, which is reduced to 0.68 when the profiles are eccentric. In one instance (the (1,1,0) configuration at a 68 percent diameter reduction), the increase in LCX FFR between the concentric and eccentric profiles is significant enough to render a critical FFR (concentric case) to a non-critical FFR (eccentric case). Consequently, in particular within the LAD, the absolute changes in FFR computed in the current study notably surpassed the reported variance associated with clinical FFR measurements [30, 224]; for severe diameter reductions, the differences in LCX are also above clinical variance ranges.

The decrease in LAD FFR in conjunction with the increase of the LCX FFR between the concentric and eccentric stenosis profiles that is observed in this study can be attributed to the offset of the supplying vessel stenosis jet directionality in the eccentric case relative to the concentric one. In the case of the eccentric profile, the jet emerging from the neck of the supplying vessel stenosis is shifted towards the bifurcation carina which permitted more flow to be diverted to the LCX compared to the concentric profile case where the emerging jet is directed towards the lumen of the LAD. Jet skewness in eccentric constrictions has been previously reported in numerical and *in vitro* studies for

eccentricity indices ranging from the level of manufacturing tolerances [221] to intermediate and maximal lumen deflection in both straight [197, 218, 220] and bifurcating vessels [217]. Therefore, the results presented in this study are in agreement with literature.

The results of this research suggest that the altered haemodynamics, including emerging jet skewness, induced distal to stenoses with luminal eccentricity may not have a significant impact on the translesional pressure drop and thus, the functionality of lesions that are not in close proximity to and not proximal to other lesions and vessel bifurcations, for example in the (0,1,0), (0,0,1) and (0,1,1) configurations. Conversely, when a stenosis is located near and proximal to a bifurcation carina, as is the case for the supplying vessel stenosis in the (1,0,0), (1,0,1), (1,1,0) and (1,1,1) configurations presented in the current study, the flow patterns distal to the lesions overlap and therefore closely interact with the flow divider. As such, altered haemodynamics induced by eccentricity of the stenosed lumen could significantly influence the flow within the individual daughter vessels and thus, have an effect of the functionality of the configuration. This idea is suggested by the results, which displayed up to a 16 percent difference in the daughter vessel FFR values between the eccentric and concentric stenosis profiles.

9.4.2 Potential clinical implications

The results of this research have potentially significant clinical implications. More specifically, the findings suggest that for isolated stenoses, in particular cases that are not proximal to a bifurcation, the effect of eccentricity on lesion functionality is within clinical measurement error and therefore could be negligible, which signifies that eccentricity may not be an independent/dominant determinant haemodynamic impact. This phenomenon has been suggested in clinical studies [25], although, to the best of the authors' knowledge, a systematic numerical investigation demonstrating this behaviour had not been executed to date. Conversely, for CBL configurations wherein the mother vessel is diseased, eccentricity of the supplying vessel stenosis, directionality of the supplying vessel stenosis jet, as is influenced by the eccentricity of the corresponding stenosis lumen, could have a notable effect on the distribution of blood between the

daughter vessels. Therefore, the findings suggest that lumen eccentricity of the supplying vessel in close proximity to the bifurcation carina, could have an important effect on the clinical manifestation of the disease.

9.5 SUMMARY

In this chapter, both concentric and eccentric profiles for stenoses ranging between mild and diseased diameter reductions were considered in order to investigate the effect of lesion eccentricity on the functional impact of the CBLs. To the best of the author's knowledge, the current study is the first to systematically investigate the effect of lesion eccentricity (both for isolated and interacting stenoses) from a functional perspective. Overall, the results are in good accordance with clinical observations. More specifically, this study found that eccentricity had a negligible effect (within clinical measurement error) on the functionality of lesions which are not close to other stenoses and not proximal to a bifurcation carina. Conversely, for configurations where the supplying vessel is stenosed, eccentricity was found to have a significant effect on the FFR of the two daughter vessels. These findings are attributed to the change in directionality of the jet emerging from the supplying vessel stenosis between the concentric and eccentric cases. Therefore, from a clinical perspective, these results suggest that for bifurcation lesions with a stenosed supplying vessel, luminal eccentricity could be an important predictor of functionality.

10

EFFECT OF BIFURCATION ANGLE

This chapter presents the study of the effect of bifurcation angle on the functionality of coronary bifurcation lesions. It provides the motivation behind the investigation of this particular parameter, the corresponding cases that are considered in the work and the results and clinical relevance of the findings.

10.1 MOTIVATION

In vivo, coronary geometry has been shown to be highly curved and tortuous and to display significant interpatient variability [184, 185, 225]. In particular, the bifurcation of the LMCA is a location of significant anatomical variation, as quantified by various morphological parameters including the bifurcation angle [78, 153, 183, 225-231]. Table 10.1 presents measurements of the angles within the LMCA bifurcations from a series of *in vivo* and *ex vivo* studies from which interpatient anatomic variability is evident.

The development of atherosclerotic lesions has been accepted to be focalized in vascular locations where the local haemodynamics are complex and are characterized by low and oscillatory shear stress (such as in vessel bifurcations) [34-38]. The association of localized flow characteristics with disease development and progression, in conjunction with the significant interpatient variability of vascular morphology

introduced the notion of geometric risk factors [232] that predispose patients to the atherosclerotic disease.

Table 10.1: Measurements of the LMCA bifurcation angle from the literature

	Bifurcation Angle, mean±SD (range) [°]		
Study	**LMCA-LAD**	**LMCA-LCX**	**LAD-LCX**
Brinkman *et al.* [225]	-	-	76.4±16.7 (40-100)
Craiem *et al.* [226]	137±19.0	126±20.1	59.5±20.4
Dvir *et al.* [227]	-	129.4±20.2	70.7±17.1
Girasis *et al.* [228]	-	-	95.6±23.6 (44-165)
Godino *et al.* [229]	151±28	131±32	78±28
Malve *et al.* [78]	171.6±7.58	104.1±19.1	81.7±17.2 (44-101)
Pflederer *et al.* [230]	-	-	80±27 (34-180)
Rubinshtein *et al.* [183]	-	-	74±25 (7-136)

Many studies to date have investigated the effect of geometric parameters, including bifurcation angle, on the corresponding flow characteristics [72-79]. Specifically, in the LMCA bifurcation, Chaichana *et al.* [156] simulated blood flow in both synthetic and patient-specific geometries with variable angulations. The results showed that as the bifurcation angle increased, the size of the flow separation region also increased; correspondingly, for greater angulations, larger areas of the bifurcation were subjected to low WSS. Similar observations were made within the patient-specific arterial geometries. These results correlate with those of early studies of flow within the carotid bifurcation by Perktold *et al.* [233], where bifurcation angle was shown to affect the axial and secondary flow fields as well as the WSS and the size of the recirculation zone, in idealized geometries.

Still within idealized bifurcation models, Tadjifar [234] observed larger regions of low WSS in the daughter vessels with increasing bifurcation angle. Malve *et al.* [78] also found a positive correlation between bifurcation angle and regions of high WSS near the bifurcation carina through numerical models within patient-specific geometries. Therefore these studies suggest that bifurcation angle has an effect on the localized haemodynamics near the carina. Interestingly, some works have found increased plaque burden within the LMCA bifurcation with increasing angle [153, 226], although these findings contradict others that have suggested that bifurcation angle may not be a dominant geometric predictor for the localization of the atherosclerosis [72, 78, 235].

From a clinical perspective, the angle of a coronary bifurcation has important implications for diagnosis and treatment. Particularly, the bifurcation has an influence on the type of stenting technique employed during percutaneous coronary interventions, and affects the difficulty of the procedure [4, 6, 157, 236]. More importantly, several clinical studies have shown that the specific geometric parameter can also have an effect on the outcome of the procedure; specifically, certain angulations can increase the risk for post-procedural major adverse cardiac events, restenosis and/or thrombosis [157, 237, 238], which may be linked to observed changes in bifurcation angle post-stent insertion relative to the pre-procedural state [227, 229]. Furthermore, from the diagnostic perspective, the complex geometry of the bifurcation, as influenced in part from the angle, renders visualization using coronary angiography difficult and most commonly results in an inaccurate classification and understanding of the lesion configuration and severity [4].

Consequently, from a clinical perspective, bifurcation angle is an important morphological parameter associated with CBLs. While the effect of the bifurcation angle on the haemodynamics of healthy bifurcations as well as its corresponding implications for disease progression and initiation have been suggested, to date, the effect of bifurcation angle on the haemodynamics within diseased bifurcations has not been elucidated. More specifically, a functional evaluation of the effect of bifurcation angle on CBLs is lacking. This idea is important because the stenoses are found in close proximity to the bifurcation; as such, disturbed flow patterns distal to the supplying vessel stenosis overlap with the bifurcation carina, the proximal portions of the daughter vessels and their corresponding stenoses. Additional flow disturbances induced by the bifurcation itself also interact with the daughter vessels and their lesions, which could in turn affect the corresponding viscous and inertial pressure losses. The contribution of these interactions to the clinical manifestation of CBLs remains unknown. Therefore, the objective of the current study is to systematically compare the functionality, as quantified by the flow- and pressure-derived FFR, of different CBL configurations with varying angulations.

10.2 GEOMETRY OF THE CBL CONFIGURATIONS

Four multilesional coronary bifurcation lesion configurations based on the Medina classification are modelled in the present study. Mild, intermediate and severe lesions,

with diameter reductions of 41, 50, 61 and 68 percent are simulated for each configuration. All stenoses within a given configuration are concentric and axisymmetric and had the same severity. For each configuration and stenosis severity, five different bifurcation angles are modelled, as presented in Table 10.2 and are based on the ranges of values reported in the literature (Table 10.1).

Table 10.2: Combination of LAD and LCX angles employed in the study

	Angle [°]		
Case	**LMCA-LAD**	**LMCA-LCX**	**LAD-LCX**
1	0	73	73
2	0	50	50
3	0	90	90
4	20	50	70
5	40	50	90

More specifically, the absolute angle between the LAD and the LCX as well as the angles between the individual daughter vessels and the centerline axis of the LMCA are varied. In Table 10.2, the LMCA-LAD and LMCA-LCX angles refer to the internal angulation between the centerline axis of the LMCA and the corresponding daughter vessel. The five bifurcation angles considered, with examples of the lesion configurations and the stenosis severities are presented in Figure 10.1.

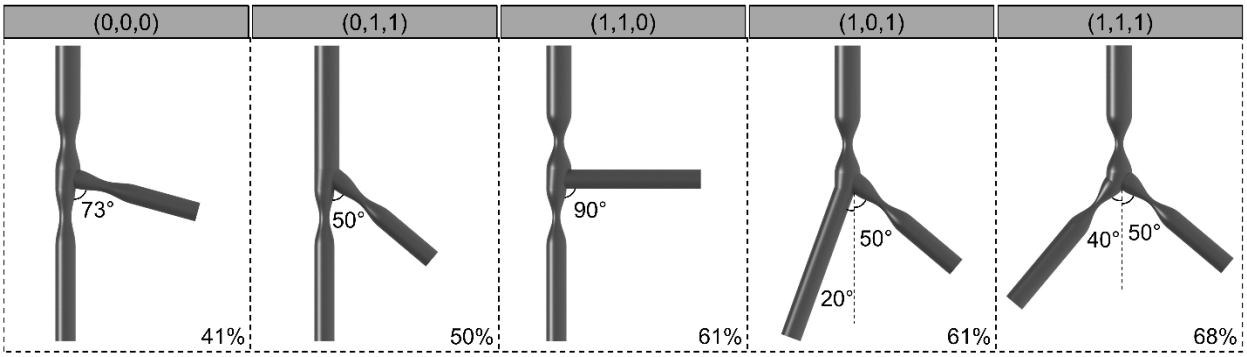

Figure 10.1: Examples of the multilesional configurations with different bifurcation angles and varying stenosis severities that are considered in the study. The configurations had concentric stenosis profiles.

10.3 RESULTS

The average pressures and flows computed at the boundaries of each case are utilized in the calculation of the pressure- and flow-based FFR respectively. The

comparison between the FFR values for the different configurations with varying bifurcation angle is provided.

Figure 10.2 presents the flow-derived FFR in the LAD and LCX of the multilesional configurations with varying LCX angle. One can observe that for all configurations, small differences are calculated in the FFR within both the LAD and the LCX. The maximum computed difference, measured at 1.5 percent, is found between the minimum and maximum LCX angles, within the LAD, for the (1,1,0) configuration at the maximum diameter. Specifically, as the angle of the LCX increases from 50 degrees to 90 degrees, the FFR within the LAD decreases. The corresponding difference in the LCX FFR is 0.94 percent and constitutes an increase in FFR with increasing bifurcation angle from 50 degrees to 90 degrees. For the reported maximum percent difference, the corresponding absolute difference in FFR is 0.01 within the LAD. For all other configurations and diameter reductions, the differences in FFR with varying LCX angle remain below 1.0 percent within both daughter vessels.

Figure 10.3 presents the flow-derived FFR in the LAD and LCX of each multilesional configurations with varying LAD angle. For all diameter reductions, the (1,1,0), (0,1,1), and (1,1,1) configurations display differences in FFR that remain below 1.0 percent when the angle is increased from zero to 20 degrees. Within the LAD, the (1,0,1) configuration displays a difference in FFR of 1.7 percent; for this case, in the LCX, the difference in FFR between angles of zero and 20 degrees is 1.0 percent. Interestingly, for the (1,0,1) configuration, when the angle of the LAD is increased to 20 degrees, the LAD FFR decreases, while the LCX FFR increases.

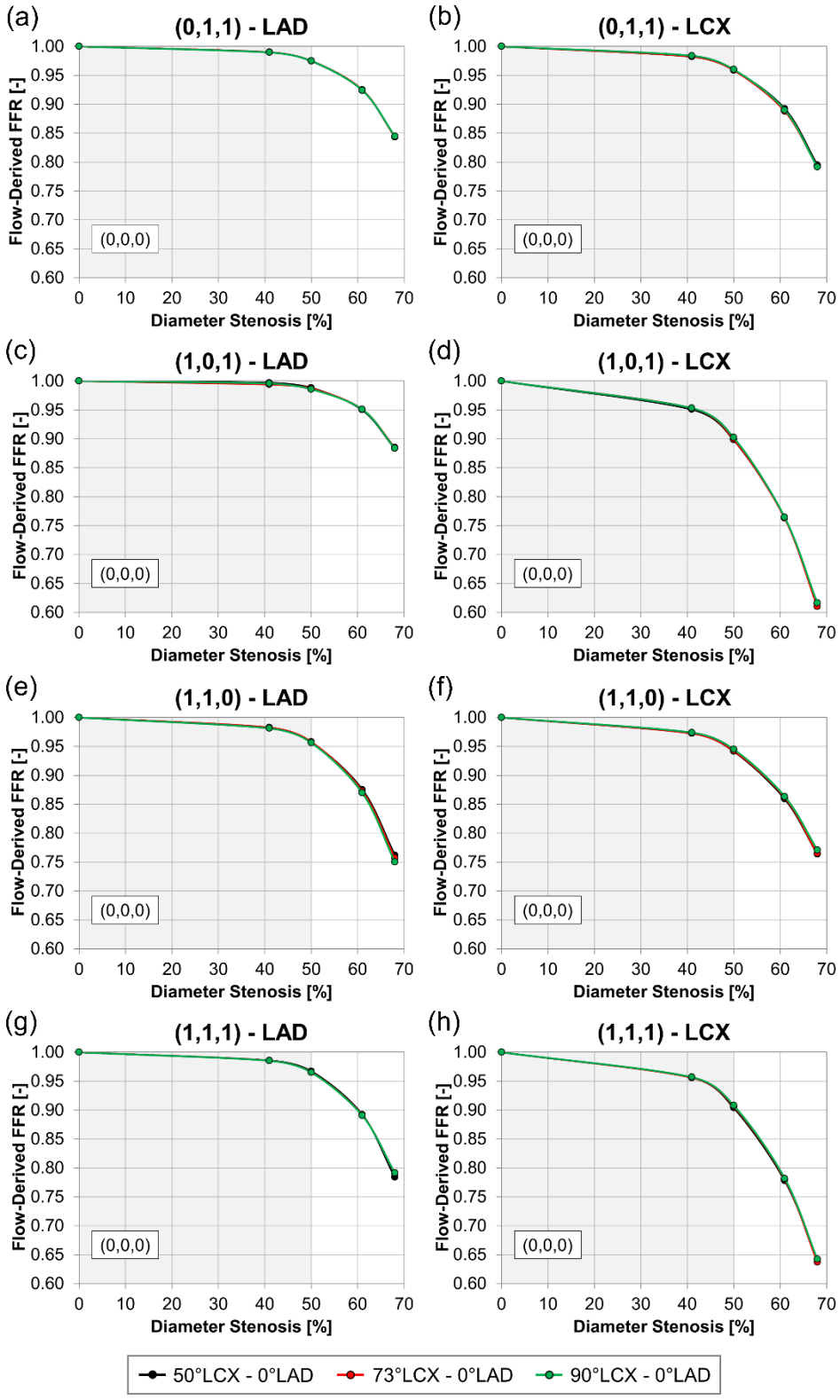

Figure 10.2: Flow-derived FFR with varying LCX angle. The FFR in the LAD is displayed for the (a) (0,1,1) (c) (1,0,1) (e) (1,1,0) and (g) (1,1,1) configurations. The FFR in the LCX is displayed for the (b) (0,1,1) (d) (1,0,1) (f) (1,1,0) and (h) (1,1,1) configurations.

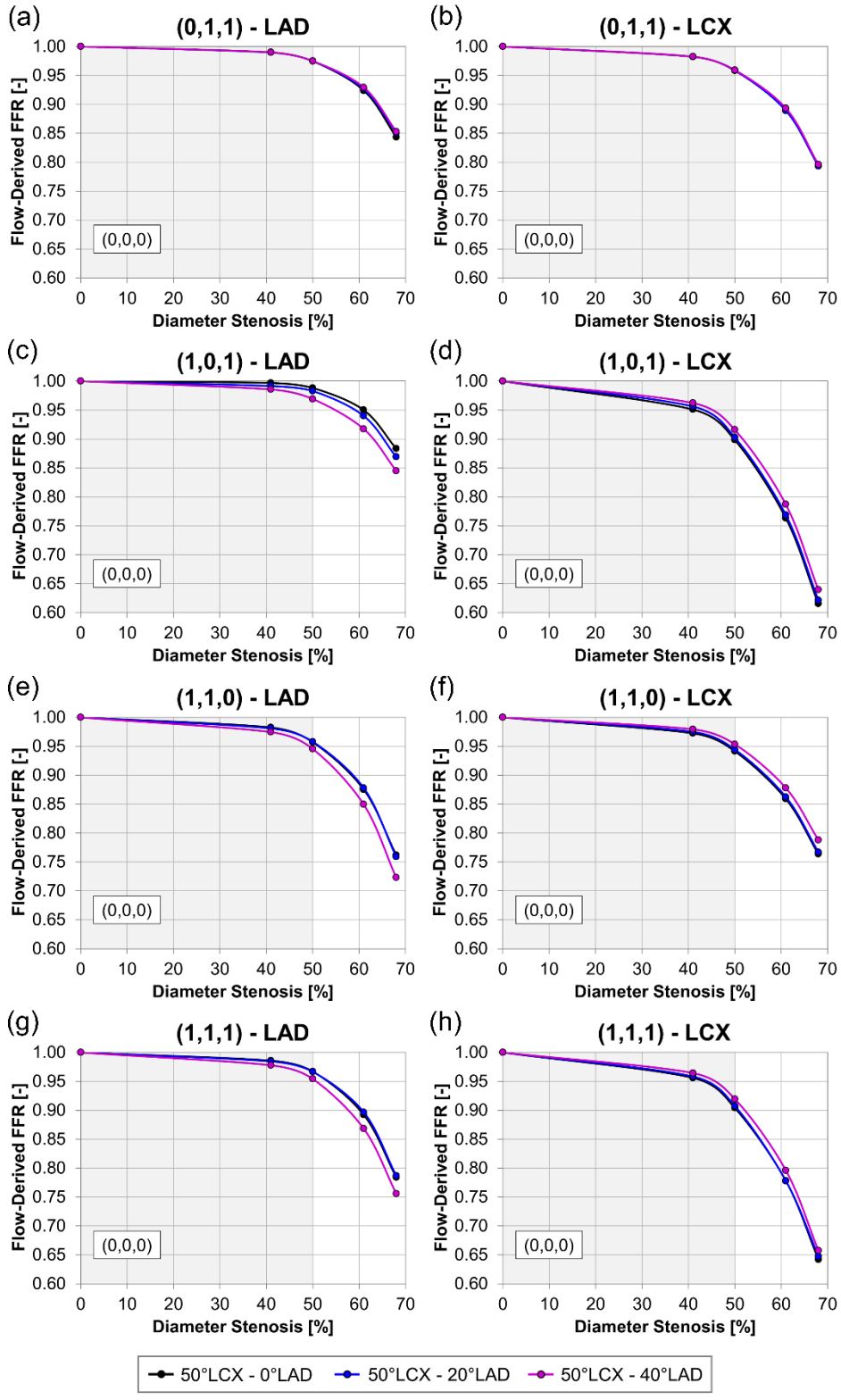

Figure 10.3: Flow-derived FFR with varying LAD angle. The FFR in the LAD is displayed for the (a) (0,1,1) (c) (1,0,1) (e) (1,1,0) and (g) (1,1,1) configurations. The FFR in the LCX is displayed for the (b) (0,1,1) (d) (1,0,1) (f) (1,1,0) and (h) (1,1,1) configurations.

When the angle of the LAD is further increased to 40 degrees relative to the centerline of the LMCA, increased differences in the FFR relative to the zero degree LAD are observed for all multilesional configurations with a stenosis in the LMCA. The maximum percent difference between the zero degree and 40 degree LAD cases occurs in the (1,1,0) configuration at the maximum diameter reduction, within the LAD. Specifically, a maximum decrease in FFR of 5.2 percent is recorded within the LAD. A corresponding decrease in LCX FFR of 3.1 percent is measured for the (1,1,0) configuration. The maximum percent differences in the LAD and LCX FFR within the (1,1,0) configuration correspond to absolute differences of 0.04 and 0.02 respectively. Within the (1,0,1) configuration, the maximum relative percent difference in the LAD FFR between the zero degree and 40 degree LAD angle is 4.5 percent.

This relative percent difference corresponds to an absolute decrease in the LAD FFR of 0.04 with increasing LAD angle. The LCX FFR decreases accordingly within the 40 degree LAD angle configuration by 3.9 percent (absolute difference of 0.02) relative to the configuration with a zero degree LAD angle. Finally, for the (1,1,1) configuration, a decrease in the LAD FFR of 3.7 percent is measured for the zero degree LAD angle relative to the 40 degree angle. The corresponding increase in LCX FFR is 2.3 percent. The measured maximum absolute differences in FFR within the LAD and the LCX for the (1,1,1) configuration are 0.03 and 0.02 respectively. The percent difference in the LAD and LCX FFR for the (0,1,1) configurations are negligible, and are measured at 1.2 and 0.13 percent respectively. The corresponding maximum absolute differences in the LAD and the LCX FFR for the (0,1,1) configuration are 0.01 and 0.01 respectively. Table 10.3 summarizes the maximum differences in the LAD and LCX FFR for the various multilesional configuration between the zero and 40 degree LAD angle.

Table 10.3: Maximum percent difference and absolute difference in flow-derived FFR within the LAD and LCX between the zero degree LAD and 40 degree LAD angles.

	Maximum Percent Difference [%]		**Maximum Absolute Difference [-]**	
	LAD	**LCX**	**LAD**	**LCX**
(0,1,1)	1.2	0.13	0.02	0.001
(1,0,1)	4.5	3.9	0.04	0.02
(1,1,0)	5.2	3.1	0.04	0.02
(1,1,1)	3.7	2.3	0.03	0.02

The pressure-based FFR in the LAD and the LCX for each multilesional configuration is displayed in Figure 10.4 for all bifurcation angles.

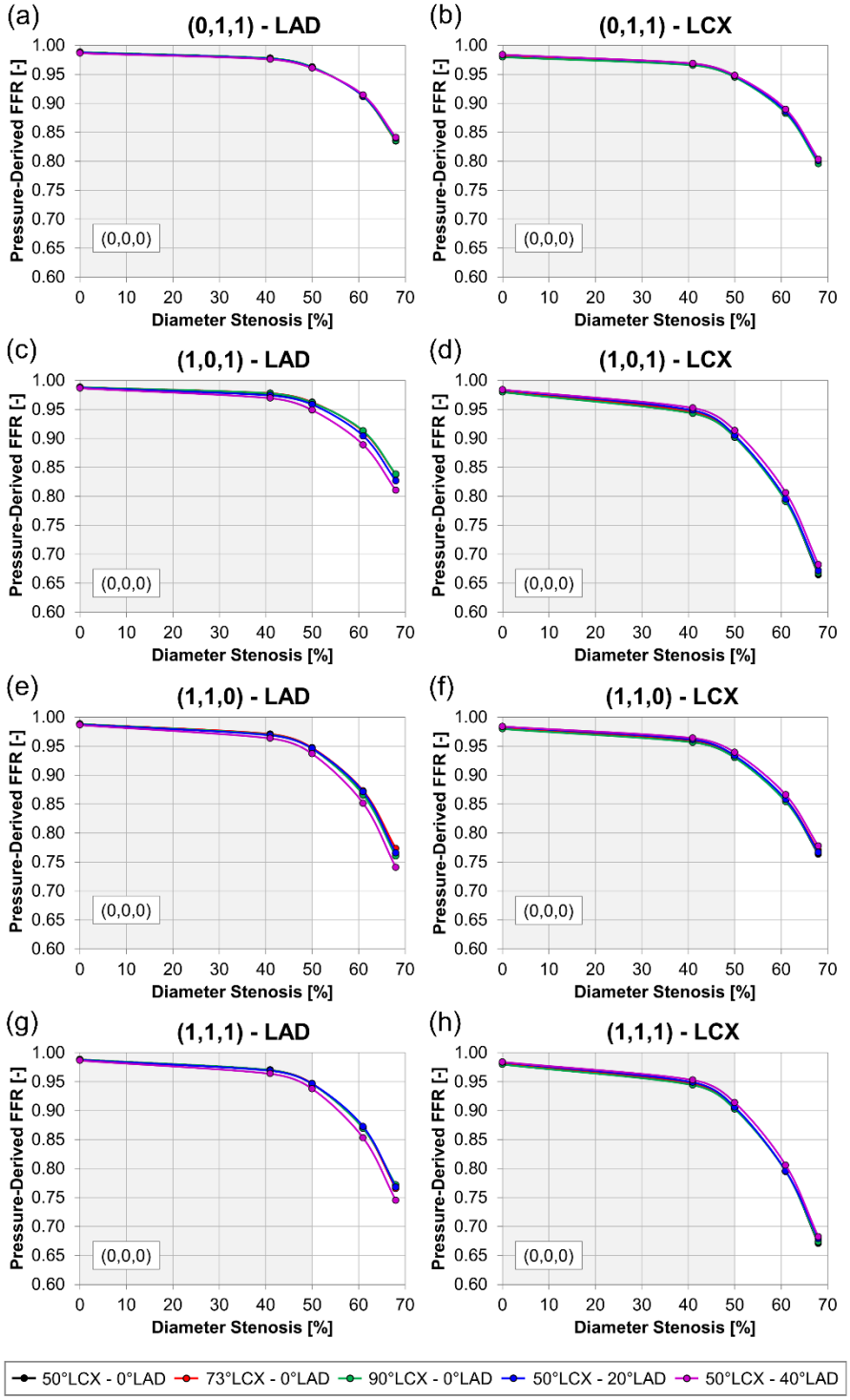

Figure 10.4: Pressure-derived FFR with varying bifurcation angle. The FFR in the LAD is displayed for the (a) (0,1,1) (c) (1,0,1) (e) (1,1,0) and (g) (1,1,1) configurations. The FFR in the LCX is displayed for the (b) (0,1,1) (d) (1,0,1) (f) (1,1,0) and (h) (1,1,1) configurations.

One can observe that the trends within the pressure-based FFR are in good accordance with those presented for the flow-based FFR. The maximum difference in pressure-based FFR is observed between the zero degree LAD angle and the 40 degree LAD angle, and occurs within LAD for the (1,1,0) configuration. More specifically, the maximum relative decrease in the LAD FFR is computed to be 4.3 percent, which corresponds to an absolute difference in FFR of 0.03. In the adjacent LCX, the corresponding relative percent difference is 0.98 which corresponds to an absolute increase of 0.01 in the LCX FFR. Negligible differences in the pressure-derived FFR are measured with changes in the angle of the LCX; specifically, as is observed for the flow-derived FFR, the maximum difference is measured with the LAD of the (1,1,0) configuration, with a magnitude of 1.7 percent between the 50 degree LCX angle and the 90 degree LCX angle. Overall, the maximum computed differences occur as the angle of the LAD is increased from zero to 40 degrees, within the configurations with a stenosis in the supplying artery. While the magnitudes of the differences are lesser for the pressure-derived FFR in comparison to the flow-derived FFR, the trends between the two indices are the same. Table 10.4 presents the maximum differences in the LAD and LCX pressure-derived FFR for the various multilesional configuration between the zero and 40 degree LAD angle.

Table 10.4: Maximum percent difference and absolute difference in pressure-derived FFR within the LAD and LCX between the zero degree LAD and 40 degree LAD angles.

	Maximum Percent Difference [%]		**Maximum Absolute Difference [-]**	
	LAD	**LCX**	**LAD**	**LCX**
(0,1,1)	0.74	0.32	0.01	0.003
(1,0,1)	3.3	2.0	0.03	0.01
(1,1,0)	4.3	0.98	0.03	0.01
(1,1,1)	2.7	1.4	0.02	0.01

10.4 DISCUSSION

The angle of an arterial bifurcation has been suggested to affect the localized flow dynamics and consequently to impact the risk for the development and progression of atherosclerosis. This idea is important for the left coronary bifurcation, which shows significant anatomical variability between patients. From the clinical standpoint, in

coronary arteries, the bifurcation angle influences the difficulty of percutaneous coronary interventions, and has been suggested to affect the risk for post-procedural major adverse cardiac events, restenosis and/or thrombosis. Overall, the angle of a bifurcation is an important morphological parameter for atherosclerotic disease. However, to the best of the author's knowledge, the effect of bifurcation angle on the functionality CBLs has not been systematically investigated. Therefore, in this study, for the first time, the flow- and pressure-derived FFR is compared between the various multilesional CBL configurations with varying bifurcation angle.

10.4.1 Effect of bifurcation angle on FFR

The effect of changes in the localized flow field on the functionality of CBLs, as induced by changes in the bifurcation angle, is observed by considering the changes in FFR within the two daughter vessels of the (0,1,1) configuration with varying LAD and LCX angle. Both the angles of the LCX and the LAD relative to the centerline axis of the LMCA are varied individually to assess their effect on the corresponding FFR in the daughter vessels for each configuration. The (0,1,1) case is the only configuration for which the flow patterns within the daughter vessels are not influenced by a stenosis in the supplying vessel. Interestingly, for all bifurcation angles considered, the recorded differences with varying angle, for all diameter reductions and both daughter vessels, remained below 1.2 percent relative to the baseline case (50 degree LCX – zero degree LAD). This percent difference corresponded to an absolute difference in FFR less than 0.01. As was outlined in Chapter 9, the clinical measurement of FFR is associated with variance between successive readings. Specifically, differences up to 5 percent have been recorded, which correspond to absolute differences of 0.01±0.04 [30]. As such, the differences recorded for the (0,1,1) configuration with varying bifurcation angle are well within clinical measurement error (and in fact within computational error). Consequently, in absolute terms, the results of the simulations of this study imply that bifurcation angle does not affect the functionality of CBLs.

This novel finding is further supported by the results from the simulations where the angle of the LCX is varied relative to the centerline of the LMCA. For all multilesional configurations, including those where the supplying artery is stenosed, the maximum

difference in FFR occurred within the LAD of the (1,1,0) configuration, between the 50 degree and 90 degree LCX angles. Similarly to the (0,1,1) configuration, the magnitude of the relative difference in LAD flow-derived FFR is 1.5 percent which corresponded to an absolute difference of 0.01, which is well within clinical measurement error. Therefore, these results further suggest such that the functionality of CBLs is not affected by the bifurcation angle, and would thus not influence the manifestation of the disease. These results are in good accordance with the preliminary results of Zarandi [239], who investigated the effect of varying LCX angle on the ratio of the LCX flow to the LMCA flow within the (0,1,1), (1,0,1) and (1,1,1) configurations using conventional CFD simulations. In the work of Zarandi [239], negligible changes in the flow ratio are computed for these configurations. However, only mild diameter reductions (up to 30% diameter reduction were considered, and conventional CFD simulations were executed thus, not accounting for the effect of bifurcation angle on CBL functionality.

Interestingly, for the configurations with a stenosis in the LMCA, when the angle of the LAD is varied with respect to the centerline axis of the LMCA, larger differences in the LAD and LCX FFR are observed than the differences with varying LCX angles. More specifically, the maximum difference in FFR, which occurs between the cases with a zero degree and 40 degree LAD angle, is 5.2 percent (an absolute difference of 0.04). These differences are still within clinical measurement error, as in the case of the varying LCX angle, which implies that bifurcation angle would not manifest differences in the functionality of CBLs. However, the computed trends suggest that further increases in the LAD angle could induce differences in FFR that affect clinical manifestation. Interestingly, these differences correspond to a decrease in FFR within the LAD and an increase in FFR in the LCX, which is similar to the trends observed for the eccentric stenosis profiles presented in Chapter 9. These findings are attributed to the change in the position of the carina relative to the axis of the LMCA as the angle of the LAD increased. Specifically, the location of the bifurcation carina shifts towards the centerline axis of the LMCA with increasing LAD angle, which influences the distribution of blood within the two daughter vessel. This phenomenon is important and is expected to be most prominent when the supplying vessel is stenosed as a result of the high linear inertia of the jet emerging from

the neck of the LMCA lesion. With the shift of the carina towards the centerline of LMCA, more blood could flow into the LCX thus, increasing the LCX FFR and decreasing the LAD FFR. Consequently, despite the measurable differences in FFR with increasing LAD angle, and the recorded differences with increasing LCX angle, the results of the simulations suggest that the bifurcation angle does not affect CBL functionality.

10.4.2 Potential clinical implications

The results of the current study have potentially important clinical implications. More specifically, the findings suggest that differences in FFR within the daughter vessels induced by varying bifurcation angle are within clinical measurement error and could therefore be negligible from the clinical standpoint. This signifies that bifurcation angle may not be a determinant of haemodynamic impact and therefore may not influence the clinical manifestation of the disease regardless of the fact that the specific morphological parameter plays an important role in the difficulty of percutaneous coronary intervention as well as the risk for the development of atherosclerotic plaques.

In addition, the results of the study further support the findings presented in Chapter 9 with regard to the effect of lesion eccentricity on CBL functionality. In Chapter 9, the directionality of the supplying vessel stenosis jet relative to the carina was found to notably change the functionality of a CBL configuration, well above clinical measurement error. Here, the shift in the carina that is induced with the change in bifurcation angle results in more notable changes than the differences with the varying angle alone. Therefore, from a clinical standpoint, these results suggest that when there is a severe stenosis in the supplying artery, the position of the carina relative to the jet could have a significant influence the relative distribution of the blood between the daughter vessels and therefore the clinical manifestation of the disease. This is a significant and novel finding as it is the relative resistance of the downstream myocardia and not the localized flow dynamics that is thought to play the dominant role in the distribution of blood between the daughter vessels. The results of these simulations provide new insight into the importance of the interaction of the localized flow dynamics and the geometry of the vessel bifurcation on the functionality of CBLs.

10.5 SUMMARY

The angle of the LMCA bifurcation has been shown to display significant inter-patient variability. To the best of the author's knowledge, its effect on the functionality of CBLs has not been investigated to date. In this chapter, for the first time, different multilesional CBL configurations with stenoses ranging from mild to severe reductions were simulated with varying bifurcation angle. Specifically, the angle between the LAD and the LCX as well as the angles between the centerline axis of the LMCA and each of the daughter vessels were varied based on reported measurements from the literature. The study found that the bifurcation angle had a negligible effect on the functionality of CBLs. More specifically, for all configurations, the relative differences in FFR ranged between zero and 5.2 percent, with the majority of cases displaying a difference less than 1.5 percent. The computed differences are not only within computational error, but more importantly well within the reported range of clinical measurement error. Therefore, these results suggest that bifurcation angle, while an important geometric parameter from the treatment perspective, may not influence CBL functionality. However, the findings also suggest that the location of the carina relative to the high inertia jet emerging from the supplying vessel stenosis could be an important determinant of the distribution of blood between the daughter vessels and therefore the clinical manifestation of the disease.

11

DISCUSSION AND CONCLUSIONS

This chapter provides an overview of the original contributions of this research, in the context of the hypotheses and objectives presented in Chapter 1. In addition, a discussion of the obtained results and their corresponding clinical significance and impact are outlined. The limitations of the research are acknowledged and recommendations for future works are discussed.

11.1 ORIGINAL CONTRIBUTIONS

The dynamics of coronary bifurcation lesions are complicated and the factors that affect their clinical functionality have not been investigated to date. In this thesis, it was hypothesized that haemodynamic interactions at both local and global levels, play a significant role in the functionality of coronary bifurcation lesions and therefore their clinical manifestation. As such, the main objective was to provide insight on and an understanding of the haemodynamic impact of coronary bifurcation lesions from a clinically-relevant perspective, while taking into account local and global haemodynamic interactions. Therefore, in the context of the hypothesis and objectives, the novel contributions of the thesis are outlined in the sequel.

To the best of the author's knowledge, this thesis presented the first computational model of a diseased coronary bifurcation that incorporated both local (within the bifurcation) and global (within the surrounding cardiovascular domains) haemodynamic effects while inherently accounting for haemodynamic interactions. More specifically, this work presented the first successful attempt to study CBL dynamics within a geometric multiscale framework, where the boundary conditions of the computational fluid dynamics simulations were not known *a priori,* but were rather obtained at each time step of the transient simulation through the interaction of a localized 3D model with a 0D model of the surrounding cardiovascular domains.

The computed flow- and pressure-derived FFR values were in good agreement with FFR measurements reported in clinical studies for similar ranges of stenosis severities thus, confirming the ability of the multiscale model to simulate decreases in perfusion and to capture physiologically-relevant flow and pressure fields within diseased coronary bifurcations. This idea is especially important for the study of coronary lesions whose resistance and therefore functionality is dependent on the transtenotic flow as well as the dynamics of the distal myocardium. Consequently, unlike previous studies of CBLs, the flow and pressure fields within the diseased bifurcation were calculated, for the first time, within the context of the complete global physiology of the cardiovascular system thus, providing the first functional evaluation of CBLs.

Moreover, with the use of the developed geometric multiscale model, the author executed, what is to the best of her knowledge, the first systematic investigation of the effect of various geometric and morphological parameters on the haemodynamic severity of CBLs. The geometric and morphological parameters that were investigated were selected in order to provide a thorough and comprehensive evaluation of the effects of global and local haemodynamic interactions which had not been previously studied. The main results of the research, as discussed below, provided novel insight with regard to the influence of the different morphological parameters on the haemodynamic interactions within CBLs and the corresponding functionality. These original findings, outlined in Table 11.1, present potentially important clinical implications which could help improve diagnostic procedures, and therefore ameliorate patient care.

Table 11.1: Summary of the main and original findings of the systematic investigation of the effect of geometric parameters on the functionality of CBLs

Parameter	Main Findings	Clinical Implications
Lesion configuration	• Branch steal renders a two-lesion configuration more functionally significant than a three-lesion configuration • There is a possibility for false negatives in diagnosis, based on the current diagnostic guidelines	• The number of lesions does not govern the criticality of CBLs ○ single- and double-lesion configurations should be considered just as significant as three-lesion configurations ○ the presence of a large relative severity between daughter vessel could functionally de-stabilize a CBL configuration (implications to treatment) • The severity of the supplying vessel stenosis may be an important predictor of CBL functionality • A misinterpretation of the contribution of haemodynamic interactions could result in a misguided and/or incorrect diagnosis
Relative stenosis severity	• A single-lesion configuration can produce a more functionally critical environment compared to double- and triple-lesion arrangements • The severity of the supplying vessel stenosis plays a dominant role in the overall functionality of the configuration	
Luminal eccentricity	• Eccentricity has a negligible effect on the functionality of isolated lesions • Eccentricity has a notable effect on the FFR for configurations where the supplying vessel is stenosed	• The location of the carina relative to the jet emerging from the supplying vessel stenosis influences the distribution of blood between the daughter vessels ○ Eccentricity may be an important predictor of functionality for CBL configurations with a supplying vessel stenosis ○ Bifurcation angle may not be a predictor of CBL functionality
Bifurcation angle	• Bifurcation angle has a negligible effect on the functionality of CBLs	

11.2 DISCUSSION OF THE MODEL ASSUMPTIONS

The main and novel findings of the thesis and the corresponding clinical implications, as presented in Table 11.1, are stated within the limits of the model assumptions. *In vivo*, coronary geometry is curved and tortuous [78, 184, 185]; coronary bifurcations display significant variance in their geometry and are nonplanar [78, 153, 183, 225-231]. In the current study, linear and planar geometries of the LMCA bifurcation were utilized. While an anatomically-relevant geometry could potentially provide a more accurate representation of the *in vivo* flow environment, the use of a controlled and

simplified computer-generated geometry allowed for the effect of the various geometric and morphological parameters on the functional impact of CBLs to be isolated, without influencing the results by patient-specific flow patterns. This idea is especially important due to the fact that coronary geometry displays significant interpatient variation. Overall, idealized geometric models lend themselves well to parametric studies, as the one presented in the thesis.

The choice to utilize idealized geometries was justified based on validated expressions for the translesional pressure drop [80] wherein the morphology of and the volumetric flow through the stenosis are shown to have the most dominant effect on the translesional pressure drop, and not the proximal flow profile which would be altered with the introduction of curvature and tortuosity. This phenomenon is most prominent at higher flows (for example, during maximum hyperaemia) wherein inertial pressure losses become more dominant compared to viscous pressure losses (which would be influenced by the flow profile) and in particular for severe stenoses. Furthermore, disturbed flow profiles proximal to the LAD and the LCX stenoses are induced by the bifurcation geometry; this phenomenon is amplified in the case where the LMCA is stenosed due to the fact that the recirculation zone distal to the stenosis is found within the bifurcation region and thus, the induced disturbances interact with the stenoses within the LAD and LCX. As such, flow disturbances induced by curvature would have a less prominent effect for the LAD and LCX stenoses compared to a hypothetically isolated stenosis in a curved portion of vessel far from a bifurcation. Consequently, as the resulting flow and pressure profiles were in good accordance with clinical reports, the use of simplified geometries was justified for the scope of the current work.

Moreover, coronary arteries are subjected to dynamic motion (in space) as a result of the ventricular contraction and expansion. This phenomenon was not considered in order to reduce computational costs. Its exclusion from the current model was justified by the fact that in the proximal epicardial coronary arteries, as were modelled in the current study, regions of small curvature changes have been shown to exist [240]. Furthermore, flow disturbances induced by bifurcations have been shown to have a dominant effect on flow patterns compared to disturbances generated by dynamic curvature changes [241].

This idea is expected to be amplified due to the presence of arterial constrictions, which themselves induce flow disturbances in the post-stenotic regions.

Simplifying assumptions (geometry, fluid and vessel properties, boundary conditions, etc.) are inherent in cardiovascular numerical modelling due to computational cost and lack of available *in vivo* data. Geometric multiscale modelling was developed for the purpose of integrating, in a computationally efficient manner, the influence of peripheral (upstream and downstream) haemodynamics within the simulations of a truncated localized domain. Physiologically-relevant boundary conditions that allow for the haemodynamics of a truncated portion of the cardiovascular system to be simulated in the context of global physiology are crucial in the validity of the presented results. Whereas the multiscale approach allows for more robust simulations to be executed, and in many cases for haemodynamic conditions that are not known *a priori* to be predicted (as was the case for the model presented in the thesis), they are still subject to some limitations that are worth noting. Specifically, during the transient simulations, the flow and pressure within the truncated domain are determined based on the interaction between the 3D model and the 0D model, and therefore depend on the configuration and the parameter values of the LPM coupled with the boundaries. Lumped model parameter selection is an important part of the development of such models to ensure that physiologically-relevant results are obtained. This idea is especially important for patient-specific simulations that require parameter values to be matched to clinically-measured data [242].

In the development of the model presented in the thesis, parameter values for the heart, systemic and pulmonary circulations were selected based on literature values and were adjusted in a systematic, yet manual approach until physiologically-relevant flows were obtained. Coronary parameter values were also adjusted in a similar manner to obtain the desired output for the healthy model. Here, it is acknowledged that the choices of parameter values influence the results; however, due to model verification with respect to clinical data, the model yields reliable results that could be representative of *in vivo* conditions. The use of the manual, iterative procedure for parameter identification was tedious and thus, perhaps not the ideal method; however, this approach was previously

employed in similar models in the literature [243, 244] and was deemed acceptable for the scope of the present study since patient-specific simulations were not being executed and a single lumped-parameter model was being employed. Here, it must be recognized that significant work is being executed in the field of parameter estimation for multiscale modelling applications [242] and therefore, future work on this model could benefit from corresponding approaches and clinical measurement.

From the numerical standpoint, a potential limitation of the current study involves assumptions with regard to the flow regime. Specifically, a laminar regime was assumed in the developed model whereas studies have shown that in stenotic vessels, transition to turbulence can occur at low Reynolds number. This simplification was implemented in order to reduce the computational expense as the incorporation of a turbulent model would require significant spatial discretization. The laminar flow assumption was also retrospectively justified based on the peak Reynolds number, which did not surpass the reported threshold for diameter reductions greater than 50 percent. Nevertheless, due to the significant constrictions and hyperaemic flow conditions employed in the thesis, the work could potentially benefit from the employment of a turbulence model, to investigate its effect on the corresponding FFR values.

In addition, with respect to biophysical phenomena, the model did not incorporate collateral flow. The overall configuration, extent, and response of collaterals to maximum vasodilation vary significantly between patients and are still not fully understood. Moreover, studies have shown that collateral circulation is only present in approximately 30% of patients that have functionally significant coronary lesions [84]. Therefore, the disregard of collateral circulation was deemed acceptable for the scope of the current study. It also allowed to investigate the true haemodynamic severity of a particular lesion configuration as collateral flow provides an alternative conduit for myocardial perfusion. Still from the biophysical perspective, both the downstream epicardial arteries and the microvasculature were assumed to be free of disease. Disease of the downstream epicardial arteries would impose additional resistance in the epicardial tree thus, contributing to the overall flow reduction and ultimately masking the true haemodynamic severity of the upstream bifurcation lesion configuration. Microvascular disease increases

the overall myocardial resistance; not only does this signify that under induced hyperaemic conditions, total microvascular vasodilation is inhibited, but also that the increased resistance of the microvasculature itself reduces perfusion. Therefore, the true functionality of an epicardial stenosis is underestimated. The presence of peripheral coronary artery disease was disregarded in order to elucidate the true haemodynamic severity of the bifurcation lesion configurations and to isolate the true effect of each of the investigated geometric parameters on the corresponding FFR.

Finally, due to the parametric nature of the thesis, hundreds of numerical simulations regarding the functionality of CBLs with varying geometric parameters were presented. Measurements of the FFR from numerous clinical studies presented in the literature were utilized to corroborate the results obtained from the developed model. The flows and pressures computed within the diseased bifurcations and the corresponding FFR values displayed physiologically-relevant behaviour and were in good accordance with values reported in the literature. Nevertheless, further validation of the model would be required in order to maximize the impact of the obtained results for clinical applications. However, such an endeavour, which includes various methods, such as patient-specific simulations, *in vitro* hydraulic setups, animal work and ultimately clinical studies, requires significant resources (time, financial support) which currently places them out of the scope of the current thesis. To date, *in vitro* validation using an experimental hydraulic setup based on the works of Geven *et al.* [166] and Gaillard *et al.* [245] have been initiated. Nevertheless, due to the correspondence of the computed values with clinical and numerical data from the literature, the presented model yields reliable results that could be representative of clinically-relevant cases.

11.3 RECOMMENDATIONS FOR FUTURE WORKS

Based on the presented limitations, several recommendations for future works can be made. The use of idealized vascular geometries was justified for the scope and purpose of the thesis. However, the incorporation of more realistic coronary anatomy is recommended in future work. This idea could be implemented in various stages, firstly through the synthetic incorporation of curvature, tortuosity and non-planarity in the idealized geometries which would provide insight on their relative contribution to the

overall dynamics of CBLs, particularly in relation to the effect of localized flow characteristics on the corresponding functionality. Subsequently, patient-specific geometries reconstructed from various imaging modalities can be implemented which would allow, as a preliminary initiative, a verification of the results obtained in the thesis. It would account for differences in flow dynamics resulting from interpatient variation in the geometry and thus, facilitate a multivariate analysis so as to understand, from a statistical standpoint, the geometric parameters that influence the clinical manifestation of the disease. As outlined previously, the use of patient-specific geometries would eventually be coupled with clinical measurements in order to allow the tailoring of the lumped model parameters for each individual case so as to get an accurate *in vivo* representation of the corresponding haemodynamics.

Furthermore, additional geometric and morphological parameters of both the arterial bifurcation and of the lesion themselves could be considered in future works. In addition to curvature, tortuosity and non-planarity in the vicinity of the bifurcation, which could affect the localized flow patterns, the effect of lesion length, inter-lesion distance, the relative distance of the stenoses from the bifurcation carina, the relative sizes of the daughter vessels (and thus, the relative sizes of the perfusion territories) and the reference vessel diameters should be considered in the context of FFR. These morphological parameters are derived from quantitative coronary angiography and other imaging modalities, and their relationship to the FFR of isolated lesions is often sought [25, 223].

Finally, as outlined previously, the results obtained in the study were corroborated against literature data. However, due to the potentially significant clinical implications of the results, and their prospective application in clinic for the improvement of diagnostic procedure for coronary bifurcation lesions, it is essential that validation efforts be conducted in the future. This procedure would be initiated by the verification of the numerical results through *in vitro* testing followed by the integration of patient-specific models from a large cohort into the numerical model. Eventually, for clinical use, animal and clinical studies would have to be executed.

11.4 SUMMARY

In conclusion, the thesis presented the first numerical functional evaluation of coronary bifurcation lesions with a systematic evaluation of the effect of geometric and morphological parameters on the ischemic manifestation of the disease. The functional evaluation was facilitated through the use of computational fluid dynamics simulations executed within a geometric multiscale algorithm, which enabled the calculation of the gold-standard diagnostic index, namely the Fractional Flow Reserve. The results showed that clinical manifestation is a complex factor of both local and global haemodynamic interactions. Within the limitations of the work, the findings have potentially important clinical implications which, with future validation, could improve the current diagnostic guidelines.

LIST OF SYMBOLS

Symbol	Description	Units
δ	Maximum height of the stenosis profile	[cm]
θ	Angle between the left anterior descending artery and the left circumflex artery	[°]
μ	Dynamic viscosity of blood	[g·cm^{-1}·s^{-1}]
ρ	Density of blood	[g·cm^{-3}]
Γ	Boundary of three-dimensional model	[-]
Γ_{LMCA}	Inlet boundary of the left main coronary artery	[-]
Γ_{LAD}	Outlet boundary of the left anterior descending artery	[-]
Γ_{LCX}	Outlet boundary of the left circumflex artery	[-]
ΔP_{myo}	Diastolic pressure drop across the myocardium	[mmHg]
$\Delta P_{stenosis}$	Translesional pressure drop	[mmHg]
$\Delta P_{v,i}$	Transvalvular pressure gradient for *i=mit,ao,tri,pul* for the mitral, aortic, triscuspid and pulmonary valves respectively	[mmHg]
Ω	Fluid domain	[-]
$\overline{b}$	Column vector of forcing terms in the multiscale model	[-]
h	Thickness of vessel wall	[cm]
l	Length of vessel	[cm]
l_e	Entrance length for flow development	[cm]
l_{LAD}	Length of proximal left anterior descending artery	[cm]
l_{LCX}	Length of proximal left circumflex artery	[cm]
l_{LMCA}	Length of left main coronary artery	[cm]
l_S	Length of the stenosis base	[cm]
$\hat{n}_i$	Normal of boundary surface i	[-]
p	Localized fluid pressure	[mmHg]
$\overline{p}_j(t)$	Time-dependent face-average pressure	[mmHg]
r_0	Radius of healthy vessel	[cm]
r_S	Radius of stenosis	[cm]
t_{Emax}	Time at which the maximum elastance occurs	[s]
$\vec{u}$	Fluid velocity	[cm·s^{-1}]
x	Parameter of interest for the relative percent difference	[-]
$\overline{y}$	Vector of unknown state variables (flowrates and pressures)	[-]
z	Distance from the proximal side of the stenosis ($0 \leq z \leq l_S$)	[cm]
$\mathbf{A}$	Square matrix of 0D model parameter values	[-]
A_0	Healthy vessel cross-sectional area	[cm^2]
A_S	Area of the stenosis throat	[cm^2]
C	Volumetric arterial compliance	[cm^3·mmHg^{-1}]
C_{as}	Compliance of aortic sinus	[ml·mmHg^{-1}]
C_{norm}	Average distensibility of vessel	[mmHg^{-1}]
C_{pul}	Compliance of pulmonary circulation	[ml·mmHg^{-1}]
C_{sys}	Compliance of systemic circulation	[ml·mmHg^{-1}]
D	Diameter of vessel	[cm]
D_0	Healthy vessel diameter	[cm]
D_{LAD}	Diameter of proximal left anterior descending artery	[cm]
D_{LCX}	Diameter of proximal left circumflex artery	[cm]
D_{LMCA}	Diameter of the left main coronary artery	[cm]
$Diff_r$	Relative percent difference	[%]
D_{term}	Diameter of the terminal epicardial vessel	[cm]

Symbol	Description	Unit
$E(t)$	Instantaneous time-varying elastance	[mmHg·ml^{-1}]
E_{la}	Left atrial elastance	[mmHg·ml^{-1}]
$E_{lv}(t)$	Time-varying left ventricular elastance	[mmHg·ml^{-1}]
E_m	Elastic modulus of vessel wall	[mmHg]
E_{max}	Maximum elastance	[mmHg·ml^{-1}]
E_{min}	Minimum elastance	[mmHg·ml^{-1}]
$E_N(t)$	Normalized time-varying elastance	[-]
E_{ra}	Elastance of right atrium	[mmHg·ml^{-1}]
$E_{rv}(t)$	Time-varying elastance of right ventricle	[mmHg·ml^{-1}]
FFR	Fractional Flow Reserve	[-]
FFR_P	Pressure-derived FFR	[-]
FFR_Q	Flow-derived FFR	[-]
I_L	Inertial pressure loss coefficient	[mmHg·s^2·ml^{-2}]
K_E	Dimensionless empirical inertial pressure loss coefficient	[-]
K_v	Dimensionless empirical viscous pressure loss coefficient	[-]
L	Blood inertia	[mmHg·s^2·ml^{-1}]
L_{ao}	Inductance of aorta	[mmHg·s^2·ml^{-1}]
L_{sys}	Inductance of systemic circulation	[mmHg·s^2·ml^{-1}]
P_{ao}	Aortic pressure	[mmHg]
P_d	Distal stenosis pressure	[mmHg]
P_{DIAG1}	First diagonal branch pressure	[mmHg]
P_{DIAG2}	Second diagonal branch pressure	[mmHg]
P_{in}	Inlet pressure (to basic compartmental lumped-parameter model unit)	[mmHg]
P_{la}	Pressure of left atrium	[mmHg]
P_{LAD1}	Proximal left anterior descending artery pressure	[mmHg]
P_{LAD2}	Intermediate left anterior descending artery pressure	[mmHg]
P_{LAD3}	Distal left anterior descending artery pressure	[mmHg]
P_{LCX1}	Proximal left circumflex artery pressure	[mmHg]
P_{LCX2}	Proximal-intermediate left circumflex artery pressure	[mmHg]
P_{LCX3}	Distal-intermediate left circumflex artery pressure	[mmHg]
P_{LCX4}	Distal left circumflex artery pressure	[mmHg]
P_{LMCA}	Left main coronary artery pressure	[mmHg]
P_{MARG1}	First marginal branch pressure	[mmHg]
P_{MARG2}	Second marginal branch pressure	[mmHg]
P_{MARG3}	Third marginal branch pressure	[mmHg]
P_{lv}	Pressure of left ventricle	[mmHg]
P_{pa}	Pulmonary artery pressure	[mmHg]
P_{out}	Outlet pressure (to basic compartmental LPM unit)	[mmHg]
P_{ra}	Pressure of right atrium	[mmHg]
P_{rv}	Pressure of right ventricle	[mmHg]
P_{sys}	Systemic pressure	[mmHg]
P_v	Venous pressure	[mmHg]
$P_V(t)$	Instantaneous ventricular pressure	[mmHg]
Q	Volumetric flow rate	[ml·s^{-1}]
Q_C	Collateral flow	[ml·s^{-1}]
Q_d	Diseased hyperaemic myocardial flow	[ml·s^{-1}]
Q_{DIAG1}	First diagonal branch flow	[ml·s^{-1}]
Q_{DIAG2}	Second diagonal branch flow	[ml·s^{-1}]
Q_{in}	Inlet flow rate (to basic compartmental LPM unit)	[ml·s^{-1}]
Q_{LAD1}	Proximal left anterior descending artery flow	[ml·s^{-1}]
Q_{LAD2}	Intermediate left anterior descending artery flow	[ml·s^{-1}]

Symbol	Description	Unit
Q_{LAD3}	Distal left anterior descending artery flow	[ml·s^{-1}]
Q_{LCX1}	Proximal left circumflex artery flow	[ml·s^{-1}]
Q_{LCX2}	Proximal-intermediate left circumflex artery flow	[ml·s^{-1}]
Q_{LCX3}	Distal-intermediate left circumflex artery flow	[ml·s^{-1}]
Q_{LCX4}	Distal left circumflex artery flow	[ml·s^{-1}]
Q_{LMCA}	Left Main Coronary Artery flow	[ml·s^{-1}]
Q_{MARG1}	First marginal branch flow	[ml·s^{-1}]
Q_{MARG2}	Second marginal branch flow	[ml·s^{-1}]
Q_{MARG3}	Third marginal branch flow	[ml·s^{-1}]
Q_n	Normal (healthy) hyperaemic myocardial flow	[ml·s^{-1}]
Q_{pa}	Pulmonary artery flow	[ml·s^{-1}]
Q_{pul}	Pulmonary flow	[ml·s^{-1}]
Q_{out}	Outlet flow rate (to basic compartmental LPM unit)	[ml·s^{-1}]
Q_S	Transtenotic flow	[ml·s^{-1}]
Q_{sys}	Systemic flow	[ml·s^{-1}]
Q_{tot}	Total average healthy myocardial flow	[ml·s^{-1}]
R	Viscous resistance	[mmHg·s·ml^{-1}]
R_{av}	Resistance of atrio-ventricular (mit, tri) valves	[mmHg·s·ml^{-1}]
Re	Reynolds number	[-]
$R_{myo,d}$	Diseased myocardial resistance	[mmHg·s·ml^{-1}]
$R_{myo,n}$	Healthy myocardial resistance	[mmHg·s·ml^{-1}]
R_{pul}	Resistance of pulmonary circulation	[mmHg·s·ml^{-1}]
$R_{stenosis}$	Stenosis resistance	[mmHg·s·ml^{-1}]
R_{sys}	Resistance of systemic circulation	[mmHg·s·ml^{-1}]
R_{term}	Resistance of terminal (myocardial) vessel	[mmHg·s·ml^{-1}]
R_{tot}	Total myocardial resistance	[mmHg·s·ml^{-1}]
$R_{v,ao}$	Resistance of aortic valve	[mmHg·s·ml^{-1}]
R_{vart}	Resistance of ventriculo-arterial (ao, pul) valves	[mmHg·s·ml^{-1}]
$R_{v,mit}$	Resistance of mitral valve	[mmHg·s·ml^{-1}]
$R_{v,pul}$	Resistance of pulmonary valve	[mmHg·s·ml^{-1}]
$R_{v,tri}$	Resistance of tricuspid valve	[mmHg·s·ml^{-1}]
$S_{v,ao}$	State of aortic valve	[-]
$S_{v,mit}$	State of mitral valve	[-]
$S_{v,pul}$	State of pulmonary valve	[-]
$S_{v,tri}$	State of tricuspid valve	[-]
T	Duration of one cardiac cycle	[s]
$V_{0,V}$	Empirical constant corresponding to the x-intercept of the ventricular pressure-volume plot	[ml]
V_L	Viscous pressure loss coefficient	[mmHg·s·ml^{-1}]
V_{la}	Left atrial volume	[ml]
V_{lv}	Left ventricular volume	[ml]
V_{ra}	Right atrial volume	[ml]
V_{rv}	Right ventricular volume	[ml]
$V_V(t)$	Instantaneous ventricular volume	[ml]
Z_{ao}	Impedance of aorta	[mmHg·s·ml^{-1}]
Z_{as}	Impedance of aortic sinus	[mmHg·s·ml^{-1}]
Z_{pa}	Impedance of pulmonary artery	[mmHg·s·ml^{-1}]

REFERENCES

[1] Nichols, M., Townsend, N., Scarborough, P., and Rayner, M. (2014), "Cardiovascular disease in Europe 2014: epidemiological update," Eur. Heart J., 35(42): 2950-2959. DOI: 10.1093/eurheartj/ehu299.

[2] Mozaffarian, D., Benjamin, E.J., Go, A.S., Arnett, D.K., Blaha, M.J., Cushman, M., *et al.* (2015), "Heart disease and stroke statistics - 2015 update: a report from the American Heart Association," Circulation, 131(4): e29-e322. DOI: 10.1161/CIR.0000000000000152.

[3] Lozano, R., Naghavi, M., Foreman, K., Lim, S., Shibuya, K., Aboyans, V., *et al.* (2012), "Global and regional mortality from 235 causes of death for 20 age groups in 1990 and 2010: a systematic analysis for the Global Burden of Disease Study 2010," Lancet, 380(9859): 2095-2128. DOI: 10.1016/S0140-6736(12)61728-0.

[4] Louvard, Y., Thomas, M., Dzavik, V., Hildick-Smith, D., Galassi, A.R., Pan, M., *et al.* (2008), "Classification of coronary artery bifurcation lesions and treatments: time for a consensus!," Catheter. Cardiovasc. Interv., 71(2): 175-183. DOI: 10.1002/ccd.21314.

[5] Windecker, S., Kolh, P., Alfonso, F., Collet, J.P., Cremer, J., Falk, V., *et al.* (2014), "2014 ESC/EACTS Guidelines on myocardial revascularization: The Task Force on Myocardial Revascularization of the European Society of Cardiology (ESC) and the European Association for Cardio-Thoracic Surgery (EACTS) developed with the special contribution of the European Association of Percutaneous Cardiovascular Interventions (EAPCI)," Eur. Heart J., 35(37): 2541-2619. DOI: 10.1093/eurheartj/ehu278.

[6] Patel, Y., Depta, J.P., Novak, E., Yeung, M., Lavine, K., Banerjee, S., *et al.* (2012), "Long-term outcomes with use of intravascular ultrasound for the treatment of coronary bifurcation lesions," Am. J. Cardiol., 109(7): 960-965. DOI: 10.1016/j.amjcard.2011.11.022.

[7] De Vries, T., and Kaplan, A.V., (2014), "Coronary bifurcation lesions," Textbook of cardiovascular intervention, C. Thompson, ed., London: Springer.

[8] Tu, S., Echavarria-Pinto, M., von Birgelen, C., Holm, N.R., Pyxaras, S.A., Kumsars, I., *et al.* (2015), "Fractional flow reserve and coronary bifurcation anatomy: a novel quantitative model to assess and report the stenosis severity of bifurcation lesions," J. Am. Coll. Cardiol.: Cardiovasc. Interv., 8(4): 564-574. DOI: 10.1016/j.jcin.2014.12.232.

[9] Colombo, A., Bramucci, E., Sacca, S., Violini, R., Lettieri, C., Zanini, R., *et al.* (2009), "Randomized study of the crush technique versus provisional side-branch stenting in true coronary bifurcations: the CACTUS (Coronary Bifurcations: Application of the Crushing Technique Using Sirolimus-Eluting Stents) Study," Circulation, 119(1): 71-78. DOI: 10.1161/CIRCULATIONAHA.108.808402.

[10] Koo, B.K., Waseda, K., Kang, H.J., Kim, H.S., Nam, C.W., Hur, S.H., *et al.* (2010), "Anatomic and functional evaluation of bifurcation lesions undergoing percutaneous coronary intervention," Circ. Cardiovasc. Interv., 3(2): 113-119. DOI: 10.1161/CIRCINTERVENTIONS.109.887406.

[11] Ferenc, M., Buettner, H.J., Gick, M., Comberg, T., Rothe, J., Khoury, F., *et al.* (2016), "Clinical outcome after percutaneous treatment of de novo coronary bifurcation lesions using first or second generation of drug-eluting stents," Clin. Res. Cardiol., 105(3): 230-238. DOI: 10.1007/s00392-015-0911-7.

[12] Yang, P.S., Ha, J., Kim, J.S., Park, S., Bae, J., Shin, D.H., *et al.* (2015), "Eccentric morphology of jailed side-branch ostium after stent crossover in coronary bifurcation lesions: a three-dimensional optical coherence tomographic analysis," J. Cardiol., 65(4): 305-310. DOI: 10.1016/j.jjcc.2014.12.004.

[13] Latib, A., and Colombo, A. (2008), "Bifurcation disease: what do we know, what should we do?," J. Am. Coll. Cardiol.: Cardiovasc. Interv., 1(3): 218-226. DOI: 10.1016/j.jcin.2007.12.008.

[14] Li, J., Elrashidi, M.Y., Flammer, A.J., Lennon, R.J., Bell, M.R., Holmes, D.R., *et al.* (2013), "Long-term outcomes of fractional flow reserve-guided vs. angiography-guided percutaneous coronary intervention in contemporary practice," Eur. Heart J., 34(18): 1375-1383. DOI: 10.1093/eurheartj/eht005.

[15] Morris, P.D., Ryan, D., Morton, A.C., Lycett, R., Lawford, P.V., Hose, D.R., *et al.* (2013), "Virtual fractional flow reserve from coronary angiography: modeling the significance of coronary lesions: results from the VIRTU-1 (VIRTUal Fractional Flow Reserve From Coronary Angiography) study," J. Am. Coll. Cardiol.: Cardiovasc. Interv., 6(2): 149-157. DOI: 10.1016/j.jcin.2012.08.024.

[16] Morris, P.D., van de Vosse, F.N., Lawford, P.V., Hose, D.R., and Gunn, J.P. (2015), ""Virtual" (computed) fractional flow reserve: current challenges and limitations," J. Am. Coll. Cardiol.: Cardiovasc. Interv., 8(8): 1009-1017. DOI: 10.1016/j.jcin.2015.04.006.

[17] White, C.W., Wright, C.B., Doty, D.B., Hiratza, L.F., Eastham, C.L., Harrison, D.G., *et al.* (1984), "Does visual interpretation of the coronary arteriogram predict the physiologic importance of a coronary stenosis?," N. Engl. J. Med., 310(13): 819-824. DOI: 10.1056/NEJM198403293101304.

[18] WHO, 2012, "The top 10 causes of death," http://www.who.int/mediacentre/factsheets/fs310/en/.

[19] Zamir, M., (2005), "Static design issues," The physics of coronary blood flow, Springer US, Boston, MA, pp. 1-34.

[20] Pagiatakis, C., Galaz, R., Tardif, J.C., and Mongrain, R. (2015), "A comparison between the principal stress direction and collagen fiber orientation in coronary

atherosclerotic plaque fibrous caps," Med. Biol. Eng. Comput., 53(6): 545-555. DOI: 10.1007/s11517-015-1257-z.

[21] Iaizzo, P.A., (2005), Handbook of cardiac anatomy, physiology, and devices, Humana Press, Totowa, N.J.

[22] Pijls, N.H., and Sels, J.W. (2012), "Functional measurement of coronary stenosis," J. Am. Coll. Cardiol., 59(12): 1045-1057. DOI: 10.1016/j.jacc.2011.09.077.

[23] Pijls, N.H., van Son, J.A., Kirkeeide, R.L., De Bruyne, B., and Gould, K.L. (1993), "Experimental basis of determining maximum coronary, myocardial, and collateral blood flow by pressure measurements for assessing functional stenosis severity before and after percutaneous transluminal coronary angioplasty," Circulation, 87(4): 1354-1367. DOI: 10.1161/01.CIR.87.4.1354

[24] Yong, A.S., Ng, A.C., Brieger, D., Lowe, H.C., Ng, M.K., and Kritharides, L. (2011), "Three-dimensional and two-dimensional quantitative coronary angiography, and their prediction of reduced fractional flow reserve," Eur. Heart J., 32(3): 345-353. DOI: 10.1093/eurheartj/ehq259.

[25] Opolski, M.P., Kepka, C., Achenbach, S., Pregowski, J., Kruk, M., Staruch, A.D., *et al.* (2014), "Advanced computed tomographic anatomical and morphometric plaque analysis for prediction of fractional flow reserve in intermediate coronary lesions," Eur. J. Radiol., 83(1): 135-141. DOI: 10.1016/j.ejrad.2013.10.005.

[26] Tonino, P.A., Fearon, W.F., De Bruyne, B., Oldroyd, K.G., Leesar, M.A., Ver Lee, P.N., *et al.* (2010), "Angiographic versus functional severity of coronary artery stenoses in the FAME study fractional flow reserve versus angiography in multivessel evaluation," J. Am. Coll. Cardiol., 55(25): 2816-2821. DOI: 10.1016/j.jacc.2009.11.096.

[27] Gould, K.L., Kirkeeide, R., and Johnson, N.P. (2010), "Coronary branch steal: experimental validation and clinical implications of interacting stenosis in branching coronary arteries," Circ. Cardiovasc. Imag., 3(6): 701-709. DOI: 10.1161/CIRCIMAGING.110.937656.

[28] Fischer, J.J., Samady, H., McPherson, J.A., Sarembock, I.J., Powers, E.R., Gimple, L.W., *et al.* (2002), "Comparison between visual assessment and quantitative angiography versus fractional flow reserve for native coronary narrowings of moderate severity," Am. J. Cardiol., 90(3): 210-215. DOI: 10.1016/S0002-9149(02)02456-6.

[29] Sen, S., Escaned, J., Malik, I.S., Mikhail, G.W., Foale, R.A., Mila, R., *et al.* (2012), "Development and validation of a new adenosine-independent index of stenosis severity from coronary wave-intensity analysis: results of the ADVISE (ADenosine Vasodilator Independent Stenosis Evaluation) study," J. Am. Coll. Cardiol., 59(15): 1392-1402. DOI: 10.1016/j.jacc.2011.11.003.

[30] De Bruyne, B., Bartunek, J., Sys, S.U., Pijls, N.H., Heyndrickx, G.R., and Wijns, W. (1996), "Simultaneous coronary pressure and flow velocity measurements in humans.

Feasibility, reproducibility, and hemodynamic dependence of coronary flow velocity reserve, hyperemic flow versus pressure slope index, and fractional flow reserve," Circulation, 94(8): 1842-1849. DOI: 10.1161/01.CIR.94.8.1842.

[31] Pijls, N.H.J., Vangelder, B., Vandervoort, P., Peels, K., Bracke, F.A.L.E., Bonnier, H.J.R.M., *et al.* (1995), "Fractional flow reserve - a useful index to evaluate the influence of an epicardial coronary stenosis on myocardial blood-flow," Circulation, 92(11): 3183-3193. DOI: 10.1161/01.CIR.92.11.3183.

[32] De Bruyne, B., Bartunek, J., Sys, S.U., and Heyndrickx, G.R. (1995), "Relation between myocardial fractional flow reserve calculated from coronary pressure measurements and exercise-induced myocardial ischemia," Circulation, 92(1): 39-46. DOI: 10.1161/01.CIR.92.1.39

[33] Pijls, N.H. (2013), "Fractional flow reserve to guide coronary revascularization," Circ. J., 77(3): 561-569. DOI: 10.1253/circj.CJ-13-0161.

[34] Caro, C.G., Fitz-Gerald, J.M., and Schroter, R.C. (1971), "Atheroma and arterial wall shear. Observation, correlation and proposal of a shear dependent mass transfer mechanism for atherogenesis," Proc. R. Soc. Lond. B Biol. Sci., 177(1046): 109-159. DOI: 10.1098/rspb.1971.0019.

[35] Caro, C.G., Fitz-Gerald, J.M., and Schroter, R.C. (1969), "Arterial wall shear and distribution of early atheroma in man," Nature, 223(5211): 1159-1160. DOI: 10.1038/2231159a0.

[36] Friedman, M., Hutchins, G., Brentbargeron, C., Deters, O., and Mark, F. (1981), "Correlation between intimal thickness and fluid shear in human arteries," Atherosclerosis, 39(3): 425-436.

[37] Zarins, C.K., Giddens, D.P., Bharadvaj, B.K., Sottiurai, V.S., Mabon, R.F., and Glagov, S. (1983), "Carotid Bifurcation Atherosclerosis Quantitative Correlation of Plaque Localization with Flow Velocity Profiles and Wall Shear-Stress," Circ. Res., 53(4): 502-514. DOI: 10.1161/01.RES.53.4.502.

[38] Ku, D.N., Giddens, D.P., Zarins, C.K., and Glagov, S. (1985), "Pulsatile flow and atherosclerosis in the human carotid bifurcation. Positive correlation between plaque location and low oscillating shear stress," Arteriosclerosis, 5(3): 293-302. DOI: 10.1161/01.ATV.5.3.293.

[39] Chaichana, T., Sun, Z., and Jewkes, J. (2013), "Hemodynamic impacts of left coronary stenosis: a patient-specific analysis," Acta. Bioeng. Biomech., 15(3): 107-112. DOI: 10.5277/abb130313.

[40] Chaichana, T., Sun, Z., and Jewkes, J. (2013), "Haemodynamic analysis of the effect of different types of plaques in the left coronary artery," Comput. Med. Imaging Graph., 37(3): 197-206. DOI: 10.1016/j.compmedimag.2013.02.001.

[41] Chaichana, T., Sun, Z., and Jewkes, J. (2013), "Hemodynamic impacts of various types of stenosis in the left coronary artery bifurcation: a patient-specific analysis," Phys. Med., 29(5): 447-452. DOI: 10.1016/j.ejmp.2013.02.001.

[42] Chaichana, T., Sun, Z., and Jewkes, J. (2012), "Investigation of the haemodynamic environment of bifurcation plaques within the left coronary artery in realistic patient models based on CT images," Australas. Phys. Eng. Sci. Med., 35(2): 231-236. DOI: 10.1007/s13246-012-0135-3.

[43] Chaichana, T., Sun, Z., and Jewkes, J. (2014), "Impact of plaques in the left coronary artery on wall shear stress and pressure gradient in coronary side branches," Comput. Methods Biomech. Biomed. Engin., 17(2): 108-118. DOI: 10.1080/10255842.2012.671308.

[44] Chaichana, T., Sun, Z., and Jewkes, J. (2012), "Computational fluid dynamics analysis of the effect of plaques in the left coronary artery," Comput. Math. Methods Med., 2012. DOI: 10.1155/2012/504367.

[45] Frattolin, J., Zarandi, M.M., Pagiatakis, C., Bertrand, O.F., and Mongrain, R. (2015), "Numerical study of stenotic side branch hemodynamics in true bifurcation lesions," Comput. Biol. Med., 57: 130-138. DOI: 10.1016/j.compbiomed.2014.11.014.

[46] Zarandi, M., Mongrain, R., and Bertrand, O. (2012), "Determination of flow conditions in coronary bifurcation lesions in the context of the Medina classification," Model. Simulat. Eng., 2012(2012). DOI: 10.1155/2012/419087.

[47] Binu, L.S., and Kumar, A.S., 2012, "Simulation of left main coronary bifurcation lesions using 3D computational fluid dynamics model and its comparison with 2D," World Congress on Engineering 2012, p. 631.

[48] Binu, L.S., and Kumar, A.S., 2012, "Simulation of left main coronary bifurcation under different cases of stenosis and assessing the possibility of plaque proliferation using computational fluid dynamics.," International Simulation Conference of India 2012.

[49] Thiriet, M., and Parker, K.H., (2009), "Physiology and pathology of the cardiovascular system: a physical perspective," Cardiovascular mathematics: modeling and simulation of the circulatory system, L. Formaggia, A. Quarteroni, and A. Veneziani, eds., Springer-Verlag, Milan; New York.

[50] Mulroney, S.E., and Myers, A.K., (2009), "Overview of the heart and circulation," Netter's essential physiology, S. E. Mulroney, A. K. Myers, and F. H. Netter, eds., Saunders/Elsevier, Philadelphia, PA.

[51] Maximilian Buja, L., (2007), "Anatomy of the Heart," Cardiovascular Medicine, J. T. Willerson, H. J. J. Wellens, J. N. Cohn, and D. R. Holmes, eds., Springer London, London, pp. 3-17.

[52] Jonge, G.J., Ooijen, P.M.A., Sablayrolles, J.-L., Ligabue, G., and Zijlstra, F., (2009), "Coronary radiology," Medical radiology, M. Oudkerk, and M. Reiser, eds., Springer, Berlin, pp. 1-24.

[53] Duncker, D.J., and Bache, R.J. (2008), "Regulation of coronary blood flow during exercise," Physiol. Rev., 88(3): 1009-1086. DOI: 10.1152/physrev.00045.2006.

[54] Fioranelli, M., Gonnella, C., and Tonion, S., (2009), "Clinical anatomy of the coronary circulation," CT evaluation of coronary artery disease, P. Pavone, M. Fioranelli, and D. A. Dowe, eds., Springer, Milan.

[55] Huo, Y., and Kassab, G.S. (2012), "Intraspecific scaling laws of vascular trees," J. R. Soc. Interface., 9(66): 190-200. DOI: 10.1098/rsif.2011.0270.

[56] Ramanathan, T., and Skinner, H. (2005), "Coronary blood flow," Contin. Educ. Anaesth. Crit. Care Pain., 5(2): 61-64. DOI: 10.1093/bjaceaccp/mki012.

[57] Pappano, A.J., and Wier, W.G., (2012), "Coronary circulation," Cardiovascular physiology, A. J. Pappano, and W. G. Wier, eds., Elsevier/Mosby, Philadelphia, PA, pp. 223-236.

[58] Faxon, D.P., Fuster, V., Libby, P., Beckman, J.A., Hiatt, W.R., Thompson, R.W.*, et al.* (2004), "Atherosclerotic Vascular Disease Conference: Writing Group III: pathophysiology," Circulation, 109(21): 2617-2625. DOI: 10.1161/01.CIR.0000128520.37674.EF.

[59] Tarbell, J.M., Shi, Z.D., Dunn, J., and Jo, H. (2014), "Fluid Mechanics, Arterial Disease, and Gene Expression," Annu. Rev. Fluid. Mech., 46: 591-614. DOI: 10.1146/annurev-fluid-010313-141309.

[60] Sitia, S., Tomasoni, L., Atzeni, F., Ambrosio, G., Cordiano, C., Catapano, A.*, et al.* (2010), "From endothelial dysfunction to atherosclerosis," Autoimmun. Rev., 9(12): 830-834. DOI: 10.1016/j.autrev.2010.07.016.

[61] Simionescu, M., and Sima, A.V., (2012), "Morphology of atherosclerotic lesions," Inflammation and atherosclerosis, G. Wick, and C. Grundtman, eds., Springer-Verlag/Wien, Wien; New York.

[62] Mizuno, Y., Jacob, R.F., and Mason, R.P. (2011), "Inflammation and the development of atherosclerosis," J. Atheroscler. Thromb., 18(5): 351-358. DOI: 10.5551/jat.7591.

[63] Finn, A.V., Nakano, M., Narula, J., Kolodgie, F.D., and Virmani, R. (2010), "Concept of vulnerable/unstable plaque," Arterioscler. Thromb. Vasc. Biol., 30(7): 1282-1292. DOI: 10.1161/ATVBAHA.108.179739.

[64] Kolodgie, F.D., Virmani, R., Burke, A.P., Farb, A., Weber, D.K., Kutys, R.*, et al.* (2004), "Pathologic assessment of the vulnerable human coronary plaque," Heart, 90(12): 1385-1391. DOI: 10.1136/hrt.2004.041798.

[65] Madder, R.D., Smith, J.L., Dixon, S.R., and Goldstein, J.A. (2012), "Composition of Target Lesions by Near-Infrared Spectroscopy in Patients With Acute Coronary Syndrome Versus Stable Angina," Circ. Cardiovasc. Interv., 5(1): 55-61. DOI: 10.1161/Circinterventions.111.963934.

[66] Mauriello, A., Servadei, F., Zoccai, G.B., Giacobbi, E., Anemona, L., Bonanno, E.*, et al.* (2013), "Coronary calcification identifies the vulnerable patient rather than the vulnerable plaque," Atherosclerosis, 229(1): 124-129. DOI: 10.1016/j.atherosclerosis.2013.03.010.

[67] Moreno, P.R., Falk, E., Palacios, I.F., Newell, J.B., Fuster, V., and Fallon, J.T. (1994), "Macrophage infiltration in acute coronary syndromes. Implications for plaque rupture," Circulation, 90(2): 775-778. DOI: 10.1161/01.CIR.90.2.775

[68] Saremi, F., and Achenbach, S. (2015), "Coronary plaque characterization using CT," Am. J. Roentgenol., 204(3): W249-260. DOI: 10.2214/AJR.14.13760.

[69] Thieme, T., Wernecke, K.D., Meyer, R., Brandenstein, E., Habedank, D., Hinz, A.*, et al.* (1996), "Angioscopic evaluation of atherosclerotic plaques: Validation by histomorphologic analysis and association with stable and unstable coronary syndromes," J. Am. Coll. Cardiol., 28(1): 1-6. DOI: 10.1016/0735-1097(96)00108-8.

[70] Virmani, R., Kolodgie, F.D., Burke, A.P., Farb, A., and Schwartz, S.M. (2000), "Lessons from sudden coronary death: a comprehensive morphological classification scheme for atherosclerotic lesions," Arterioscler. Thromb. Vasc. Biol., 20(5): 1262-1275. DOI: 10.1161/01.ATV.20.5.1262.

[71] Fishbein, M.C., and Fishbein, G.A. (2015), "Arteriosclerosis: Facts and Fancy," Cardiovasc. Pathol. DOI: 10.1016/j.carpath.2015.07.007.

[72] Bijari, P.B., Wasserman, B.A., and Steinman, D.A. (2014), "Carotid bifurcation geometry is an independent predictor of early wall thickening at the carotid bulb," Stroke, 45(2): 473-478. DOI: 10.1161/STROKEAHA.113.003454.

[73] Sousa, L.C., Castro, C.F., Antonio, C.C., Sousa, F., Santos, R., Castro, P.*, et al.* (2016), "Computational simulation of carotid stenosis and flow dynamics based on patient ultrasound data - A new tool for risk assessment and surgical planning," Adv. Med. Sci., 61(1): 32-39. DOI: 10.1016/j.advms.2015.07.009.

[74] van Wyk, S., Prahl Wittberg, L., and Fuchs, L. (2014), "Atherosclerotic indicators for blood-like fluids in 90-degree arterial-like bifurcations," Comput. Biol. Med., 50: 56-69. DOI: 10.1016/j.compbiomed.2014.03.006.

[75] Gallo, D., Steinman, D.A., and Morbiducci, U. (2015), "An insight into the mechanistic role of the common carotid artery on the hemodynamics at the carotid bifurcation," Ann. Biomed. Eng., 43(1): 68-81. DOI: 10.1007/s10439-014-1119-0.

[76] Corban, M.T., Eshtehardi, P., Suo, J., McDaniel, M.C., Timmins, L.H., Rassoul-Arzrumly, E.*, et al.* (2014), "Combination of plaque burden, wall shear stress, and plaque phenotype has incremental value for prediction of coronary atherosclerotic plaque progression and vulnerability," Atherosclerosis, 232(2): 271-276. DOI: 10.1016/j.atherosclerosis.2013.11.049.

[77] Timmins, L.H., Mackie, B.D., Oshinski, J.N., Giddens, D.P., and Samady, H. (2013), "Colocalization of low and oscillatory coronary wall shear stress with subsequent culprit lesion resulting in myocardial infarction in an orthotopic heart transplant patient," J. Am. Coll. Cardiol.: Cardiovasc. Interv., 6(11): 1210-1211. DOI: 10.1016/j.jcin.2013.03.024.

[78] Malve, M., Gharib, A.M., Yazdani, S.K., Finet, G., Martinez, M.A., Pettigrew, R.*, et al.* (2015), "Tortuosity of coronary bifurcation as a potential local risk factor for atherosclerosis: CFD steady state study based on in vivo dynamic CT measurements," Ann. Biomed. Eng., 43(1): 82-93. DOI: 10.1007/s10439-014-1056-y.

[79] Timmins, L.H., Molony, D.S., Eshtehardi, P., McDaniel, M.C., Oshinski, J.N., Samady, H.*, et al.* (2015), "Focal association between wall shear stress and clinical coronary artery disease progression," Ann. Biomed. Eng., 43(1): 94-106. DOI: 10.1007/s10439-014-1155-9.

[80] Kirkeeide, R., (1991), "Coronary obstructions, morphology and physiologic significance," Quantitative Coronary Arteriography, J. C. Reiber, and P. Serruys, eds., Springer Netherlands, pp. 229-244.

[81] Seeley, B.D., and Young, D.F. (1976), "Effect of geometry on pressure losses across models of arterial stenoses," J. Biomech., 9(7): 439-448. DOI: 10.1016/0021-9290(76)90086-5.

[82] Young, D.F., and Tsai, F.Y. (1973), "Flow characteristics in models of arterial stenoses — I. Steady flow," J. Biomech., 6(4): 395-410. DOI: 10.1016/0021-9290(73)90099-7.

[83] Young, D.F., and Tsai, F.Y. (1973), "Flow characteristics in models of arterial stenoses. II. Unsteady flow," J. Biomech., 6(5): 547-559. DOI: 10.1016/0021-9290(73)90012-2.

[84] Seiler, C. (2010), "The human coronary collateral circulation," Eur. J. Clin. Invest., 40(5): 465-476. DOI: 10.1111/j.1365-2362.2010.02282.x.

[85] Traupe, T., Gloekler, S., de Marchi, S.F., Werner, G.S., and Seiler, C. (2010), "Assessment of the human coronary collateral circulation," Circulation, 122(12): 1210-1220. DOI: 10.1161/CIRCULATIONAHA.109.930651.

[86] Meier, P., Gloekler, S., Zbinden, R., Beckh, S., de Marchi, S.F., Zbinden, S.*, et al.* (2007), "Beneficial effect of recruitable collaterals: a 10-year follow-up study in patients with stable coronary artery disease undergoing quantitative collateral measurements," Circulation, 116(9): 975-983. DOI: 10.1161/CIRCULATIONAHA.107.703959.

[87] Habib, G.B., Heibig, J., Forman, S.A., Brown, B.G., Roberts, R., Terrin, M.L.*, et al.* (1991), "Influence of coronary collateral vessels on myocardial infarct size in humans. Results of phase I thrombolysis in myocardial infarction (TIMI) trial. The TIMI Investigators," Circulation, 83(3): 739-746. DOI: 10.1161/01.CIR.83.3.739.

[88] Hansen, J.F. (1989), "Coronary collateral circulation: clinical significance and influence on survival in patients with coronary artery occlusion," Am. Heart J., 117(2): 290-295. DOI: 10.1016/0002-8703(89)90771-0

[89] Billinger, M., Kloos, P., Eberli, F.R., Windecker, S., Meier, B., and Seiler, C. (2002), "Physiologically assessed coronary collateral flow and adverse cardiac ischemic events: a follow-up study in 403 patients with coronary artery disease," J. Am. Coll. Cardiol., 40(9): 1545-1550. DOI: 10.1016/S0735-1097(02)02378-1.

[90] Koerselman, J., de Jaegere, P.P., Verhaar, M.C., Grobbee, D.E., van der Graaf, Y., and Group, S.S. (2005), "Prognostic significance of coronary collaterals in patients with coronary heart disease having percutaneous transluminal coronary angioplasty," Am. J. Cardiol., 96(3): 390-394. DOI: 10.1016/j.amjcard.2005.03.083.

[91] Pohl, T., Wustmann, K., Zbinden, S., Windecker, S., Mehta, H., Meier, B.*, et al.* (2003), "Exercise-induced human coronary collateral function: quantitative assessment during acute coronary occlusions," Cardiology, 100(2): 53-60. DOI: 10.1159/00007303.

[92] Wustmann, K., Zbinden, S., Windecker, S., Meier, B., and Seiler, C. (2003), "Is there functional collateral flow during vascular occlusion in angiographically normal coronary arteries?," Circulation, 107(17): 2213-2220. DOI: 10.1161/01.CIR.0000066321.03474.DA.

[93] De Bruyne, B., Baudhuin, T., Melin, J.A., Pijls, N.H.J., Sys, S.U., Bol, A.*, et al.* (1994), "Coronary flow reserve calculated from pressure measurements in humans - validation with positron emission tomography," Circulation, 89(3): 1013-1022. DOI: 10.1161/01.CIR.89.3.1013.

[94] Vranckx, P., Cutlip, D.E., McFadden, E.P., Kern, M.J., Mehran, R., and Muller, O. (2012), "Coronary pressure-derived fractional flow reserve measurements: recommendations for standardization, recording, and reporting as a core laboratory technique. Proposals for integration in clinical trials," Circ. Cardiovasc. Interv., 5(2): 312-317. DOI: 10.1161/CIRCINTERVENTIONS.112.968511.

[95] Watkins, S., McGeoch, R., Lyne, J., Steedman, T., Good, R., McLaughlin, M.J.*, et al.* (2009), "Validation of magnetic resonance myocardial perfusion imaging with fractional flow reserve for the detection of significant coronary heart disease," Circulation, 120(22): 2207-2213. DOI: 10.1161/CIRCULATIONAHA.109.872358.

[96] Pijls, N.H., De Bruyne, B., Peels, K., Van Der Voort, P.H., Bonnier, H.J., Bartunek, J.K.J.J.*, et al.* (1996), "Measurement of fractional flow reserve to assess the functional severity of coronary-artery stenoses," N. Engl. J. Med., 334(26): 1703-1708. DOI: 10.1056/NEJM199606273342604.

[97] Pijls, N.H., Fearon, W.F., Tonino, P.A., Siebert, U., Ikeno, F., Bornschein, B.*, et al.* (2010), "Fractional flow reserve versus angiography for guiding percutaneous coronary intervention in patients with multivessel coronary artery disease: 2-year follow-up of the FAME (Fractional Flow Reserve Versus Angiography for Multivessel Evaluation) study," J. Am. Coll. Cardiol., 56(3): 177-184. DOI: 10.1016/j.jacc.2010.04.012.

[98] Pijls, N.H., van Schaardenburgh, P., Manoharan, G., Boersma, E., Bech, J.W., van't Veer, M.*, et al.* (2007), "Percutaneous coronary intervention of functionally nonsignificant stenosis: 5-year follow-up of the DEFER Study," J. Am. Coll. Cardiol., 49(21): 2105-2111. DOI: 10.1016/j.jacc.2007.01.087.

[99] Samady, H., Eshtehardi, P., McDaniel, M.C., Suo, J., Dhawan, S.S., Maynard, C.*, et al.* (2011), "Coronary artery wall shear stress is associated with progression and transformation of atherosclerotic plaque and arterial remodeling in patients with coronary artery disease," Circulation, 124(7): 779-788. DOI: 10.1161/CIRCULATIONAHA.111.021824.

[100] Asakura, T., and Karino, T. (1990), "Flow patterns and spatial distribution of atherosclerotic lesions in human coronary arteries," Circ. Res., 66(4): 1045-1066. DOI: 10.1161/01.RES.66.4.1045

[101] Papadopoulou, S.L., Girasis, C., Gijsen, F.J., Rossi, A., Ottema, J., van der Giessen, A.G.*, et al.* (2014), "A CT-based Medina classification in coronary bifurcations: does the lumen assessment provide sufficient information?," Catheter. Cardiovasc. Interv., 84(3): 445-452. DOI: 10.1002/ccd.25496.

[102] Pijls, N.H., De Bruyne, B., Bech, G.J., Liistro, F., Heyndrickx, G.R., Bonnier, H.J.*, et al.* (2000), "Coronary pressure measurement to assess the hemodynamic significance of serial stenoses within one coronary artery: validation in humans," Circulation, 102(19): 2371-2377. DOI: 10.1161/01.CIR.102.19.2371

[103] Yong, A.S., Daniels, D., De Bruyne, B., Kim, H.S., Ikeno, F., Lyons, J.*, et al.* (2013), "Fractional flow reserve assessment of left main stenosis in the presence of downstream coronary stenoses," Circ. Cardiovasc. Interv., 6(2): 161-165. DOI: 10.1161/CIRCINTERVENTIONS.112.000104.

[104] D'Souza, G.A., Peelukhana, S.V., and Banerjee, R.K. (2014), "Diagnostic uncertainties during assessment of serial coronary stenoses: an in vitro study," J. Biomech. Eng., 136(2): 021026. DOI: 10.1115/1.4026317.

[105] Kim, H.L., Koo, B.K., Nam, C.W., Doh, J.H., Kim, J.H., Yang, H.M.*, et al.* (2012), "Clinical and physiological outcomes of fractional flow reserve-guided percutaneous

coronary intervention in patients with serial stenoses within one coronary artery," J. Am. Coll. Cardiol.: Cardiovasc. Interv., 5(10): 1013-1018. DOI: 10.1016/j.jcin.2012.06.017.

[106] Fearon, W.F., Yong, A.S., Lenders, G., Toth, G.G., Dao, C., Daniels, D.V.*, et al.* (2015), "The impact of downstream coronary stenosis on fractional flow reserve assessment of intermediate left main coronary artery disease: human validation," J. Am. Coll. Cardiol.: Cardiovasc. Interv., 8(3): 398-403. DOI: 10.1016/j.jcin.2014.09.027.

[107] Siogkas, P.K., Sakellarios, A.I., Papafaklis, M.I., Stefanou, K.A., Athanasiou, L.M., Exarchos, T.P.*, et al.* (2014), "Assessing the hemodynamic influence between multiple lesions in a realistic right coronary artery segment: A computational study," Conf. Proc. IEEE Eng. Med. Biol. Soc., 2014: 5643-5646. DOI: 10.1109/embc.2014.6944907.

[108] Bing, R., Yong, A.S., and Fearon, W.F. (2015), "Assessment of left main artery stenosis with fractional flow reserve is affected by downstream stenosis in the left anterior descending artery," Coron. Artery Dis., 26 Suppl 1: e35-37. DOI: 10.1097/MCA.0000000000000202.

[109] Zhang, J.M., Zhong, L., Luo, T., Huo, Y., Tan, S.Y., Wong, A.S.*, et al.* (2014), "Numerical simulation and clinical implications of stenosis in coronary blood flow," Biomed. Res. Int., 2014: 514729. DOI: 10.1155/2014/514729.

[110] Daniels, D.V., van't Veer, M., Pijls, N.H., van der Horst, A., Yong, A.S., De Bruyne, B.*, et al.* (2012), "The impact of downstream coronary stenoses on fractional flow reserve assessment of intermediate left main disease," J. Am. Coll. Cardiol.: Cardiovasc. Interv., 5(10): 1021-1025. DOI: 10.1016/j.jcin.2012.07.005.

[111] Gould, K., (1999), Coronary Artery Stenosis and Reversing Atherosclerosis, London: Arnold Publishers Distributed by Oxford University Press, USA.

[112] Marsden, A.L., and Esmaily-Moghadam, M. (2015), "Multiscale Modeling of Cardiovascular Flows for Clinical Decision Support," Appl. Mech. Rev., 67(3): 030804-030804. DOI: 10.1115/1.4029909.

[113] Formaggia, L., Nobile, F., Quarteroni, A., and Veneziani, A. (1999), "Multiscale modelling of the circulatory system: a preliminary analysis," Comput. Vis. Sci., 2(2-3): 75-83. DOI: 10.1007/s007910050030.

[114] Quarteroni, A., Ragni, S., and Veneziani, A. (2001), "Coupling between lumped and distributed models for blood flow problems," Comput. Vis. Sci., 4(2): 111-124. DOI: 10.1007/s007910100063.

[115] Quarteroni, A., and Veneziani, A. (2003), "Analysis of a geometrical multiscale model based on the coupling of ODEs and PDEs for blood flow simulations," Multiscale Model. Sim., 1(2): 173-195. DOI: 10.1137/S1540345902408482.

[116] Olufsen, M.S., and Nadim, A. (2004), "On deriving lumped models for blood flow and pressure in the systemic arteries," Math. Biosci. Eng., 1(1): 61-80.

[117] Shi, Y., Lawford, P., and Hose, R. (2011), "Review of zero-D and 1-D models of blood flow in the cardiovascular system," Biomed. Eng. Online, 10: 33. DOI: 10.1186/1475-925X-10-33.

[118] Beyar, R., Hausknecht, M.J., Halperin, H.R., Yin, F.C., and Weisfeldt, M.L. (1987), "Interaction between cardiac chambers and thoracic pressure in intact circulation," Am. J. Physiol., 253(5 Pt 2): H1240-1252.

[119] Burkhoff, D., and Tyberg, J.V. (1993), "Why does pulmonary venous pressure rise after onset of LV dysfunction: a theoretical analysis," Am. J. Physiol., 265(5 Pt 2): H1819-1828.

[120] Chen, S., Zhang, S., Gong, Y., Dai, K., Sui, M., Yu, Y.*, et al.* (2008), "The role of the autonomic nervous system in hypertension: a bond graph model study," Physiol. Meas., 29(4): 473-495. DOI: 10.1088/0967-3334/29/4/005.

[121] Heldt, T., Shim, E.B., Kamm, R.D., and Mark, R.G. (2002), "Computational modeling of cardiovascular response to orthostatic stress," J. Appl. Physiol., 92(3): 1239-1254. DOI: 10.1152/japplphysiol.00241.2001.

[122] Lu, K., Clark, J.W., Jr., Ghorbel, F.H., Ware, D.L., and Bidani, A. (2001), "A human cardiopulmonary system model applied to the analysis of the Valsalva maneuver," Am. J. Physiol. Heart Circ. Physiol., 281(6): H2661-2679.

[123] Pennati, G., Bellotti, M., and Fumero, R. (1997), "Mathematical modelling of the human foetal cardiovascular system based on Doppler ultrasound data," Med. Eng. Phys., 19(4): 327-335. DOI: 10.1016/S1350-4533(97)84634-6.

[124] Santamore, W.P., and Burkhoff, D. (1991), "Hemodynamic consequences of ventricular interaction as assessed by model analysis," Am. J. Physiol., 260(1 Pt 2): H146-157.

[125] Ursino, M., Fiorenzi, A., and Belardinelli, E. (1996), "The role of pressure pulsatility in the carotid baroreflex control: a computer simulation study," Comput. Biol. Med., 26(4): 297-314. DOI: 10.1016/0010-4825(96)00012-1.

[126] Mantero, S., Pietrabissa, R., and Fumero, R. (1992), "The coronary bed and its role in the cardiovascular system: a review and an introductory single-branch model," J. Biomed. Eng., 14(2): 109-116. DOI: 10.1016/0141-5425(92)90015-D.

[127] Pietrabissa, R., Mantero, S., Marotta, T., and Menicanti, L. (1996), "A lumped parameter model to evaluate the fluid dynamics of different coronary bypasses," Med. Eng. Phys., 18(6): 477-484. DOI: 10.1016/1350-4533(96)00002-1.

[128] Wang, J.Z., Tie, B., Welkowitz, W., Kostis, J., and Semmlow, J. (1989), "Incremental network analogue model of the coronary artery," Med. Biol. Eng. Comput., 27(4): 416-422. DOI: 10.1007/BF02441434.

[129] Manor, D., Sideman, S., Dinnar, U., and Beyar, R. (1994), "Analysis of coronary circulation under ischaemic conditions," Med. Biol. Eng. Comput., 32(4 Suppl): S123-132. DOI: 10.1007/BF02523338.

[130] Maasrani, M., Verhoye, J.P., Corbineau, H., and Drochon, A. (2008), "Analog electrical model of the coronary circulation in case of multiple revascularizations," Ann. Biomed. Eng., 36(7): 1163-1174. DOI: 10.1007/s10439-008-9500-5.

[131] Baretta, A., Corsini, C., Yang, W., Vignon-Clementel, I.E., Marsden, A.L., Feinstein, J.A*., et al.* (2011), "Virtual surgeries in patients with congenital heart disease: a multi-scale modelling test case," Phil. Trans. R. Soc. A, 369(1954): 4316-4330. DOI: 10.1098/rsta.2011.0130.

[132] Balossino, R., Pennati, G., Migliavacca, F., Formaggia, L., Veneziani, A., Tuveri, M*., et al.* (2009), "Computational models to predict stenosis growth in carotid arteries: which is the role of boundary conditions?," Comput. Methods Biomech. Biomed. Engin., 12(1): 113-123. DOI: 10.1080/10255840903080802.

[133] Sengupta, D., Kahn, A.M., Burns, J.C., Sankaran, S., Shadden, S.C., and Marsden, A.L. (2012), "Image-based modeling of hemodynamics in coronary artery aneurysms caused by Kawasaki disease," Biomech. Model. Mechanobiol., 11(6): 915-932. DOI: 10.1007/s10237-011-0361-8.

[134] Hsia, T.Y., Cosentino, D., Corsini, C., Pennati, G., Dubini, G., Migliavacca, F*., et al.* (2011), "Use of mathematical modeling to compare and predict hemodynamic effects between hybrid and surgical Norwood palliations for hypoplastic left heart syndrome," Circulation, 124(11 Suppl): S204-210. DOI: 10.1161/CIRCULATIONAHA.110.010769.

[135] Lagana, K., Balossino, R., Migliavacca, F., Pennati, G., Bove, E.L., de Leval, M.R*., et al.* (2005), "Multiscale modeling of the cardiovascular system: application to the study of pulmonary and coronary perfusions in the univentricular circulation," J. Biomech., 38(5): 1129-1141. DOI: 10.1016/j.jbiomech.2004.05.027.

[136] Migliavacca, F., Balossino, R., Pennati, G., Dubini, G., Hsia, T.Y., de Leval, M.R*., et al.* (2006), "Multiscale modelling in biofluidynamics: application to reconstructive paediatric cardiac surgery," J. Biomech., 39(6): 1010-1020. DOI: 10.1016/j.jbiomech.2005.02.021.

[137] Morlacchi, S., Chiastra, C., Gastaldi, D., Pennati, G., Dubini, G., and Migliavacca, F. (2011), "Sequential structural and fluid dynamic numerical simulations of a stented bifurcated coronary artery," J. Biomech. Eng., 133(12): 121010. DOI: 10.1115/1.4005476.

[138] Sankaran, S., Esmaily Moghadam, M., Kahn, A.M., Tseng, E.E., Guccione, J.M., and Marsden, A.L. (2012), "Patient-specific multiscale modeling of blood flow for coronary artery bypass graft surgery," Ann. Biomed. Eng., 40(10): 2228-2242. DOI: 10.1007/s10439-012-0579-3.

[139] Moghadam, M.E., Migliavacca, F., Vignon-Clementel, I.E., Hsia, T.Y., Marsden, A.L., and Modeling of Congenital Hearts Alliance, I. (2012), "Optimization of shunt placement for the Norwood surgery using multi-domain modeling," J. Biomed. Eng., 134(5): 051002. DOI: 10.1115/1.4006814.

[140] Kim, H.J., Vignon-Clementel, I.E., Coogan, J.S., Figueroa, C.A., Jansen, K.E., and Taylor, C.A. (2010), "Patient-specific modeling of blood flow and pressure in human coronary arteries," Ann. Biomed. Eng., 38(10): 3195-3209. DOI: 10.1007/s10439-010-0083-6.

[141] Kim, H.J., Vignon-Clementel, I.E., Figueroa, C.A., Jansen, K.E., and Taylor, C.A. (2010), "Developing computational methods for three-dimensional finite element simulations of coronary blood flow," Finite Elem. Anal. Des., 46(6): 514-525. DOI: 10.1016/j.finel.2010.01.007.

[142] Taylor, C.A., Fonte, T.A., and Min, J.K. (2013), "Computational fluid dynamics applied to cardiac computed tomography for noninvasive quantification of fractional flow reserve. Scientific basis," J. Am. Coll. Cardiol., 61(22): 2233-2241. DOI: 10.1016/j.jacc.2012.11.083.

[143] Zarins, C.K., Taylor, C.A., and Min, J.K. (2013), "Computed fractional flow reserve (FFTCT) derived from coronary CT angiography," J. Cardiovasc. Transl. Res., 6(5): 708-714. DOI: 10.1007/s12265-013-9498-4.

[144] Min, J.K., Leipsic, J., Pencina, M.J., Berman, D.S., Koo, B.K., van Mieghem, C.*, et al.* (2012), "Diagnostic accuracy of fractional flow reserve from anatomic CT angiography," JAMA, 308(12): 1237-1245. DOI: 10.1001/2012.jama.11274.

[145] Taylor, C.A., Kim, H.J., and Coogan, J.S., 2010, "Patient-specific hemodynamics of the cardio vascular system," Google Patents.

[146] Koo, B.K., Erglis, A., Doh, J.H., Daniels, D.V., Jegere, S., Kim, H.S.*, et al.* (2011), "Diagnosis of ischemia-causing coronary stenoses by noninvasive fractional flow reserve computed from coronary computed tomographic angiograms. Results from the prospective multicenter DISCOVER-FLOW (Diagnosis of Ischemia-Causing Stenoses Obtained Via Noninvasive Fractional Flow Reserve) study," J. Am. Coll. Cardiol., 58(19): 1989-1997. DOI: 10.1016/j.jacc.2011.06.066.

[147] Nakazato, R., Park, H.B., Berman, D.S., Gransar, H., Koo, B.K., Erglis, A.*, et al.* (2013), "Noninvasive fractional flow reserve derived from computed tomography angiography for coronary lesions of intermediate stenosis severity: results from the DeFACTO study," Circ. Cardiovasc. Imag., 6(6): 881-889. DOI: 10.1161/CIRCIMAGING.113.000297.

[148] Gaur, S., Achenbach, S., Leipsic, J., Mauri, L., Bezerra, H.G., Jensen, J.M.*, et al.* (2013), "Rationale and design of the HeartFlowNXT (HeartFlow analysis of coronary blood flow using CT angiography: NeXt sTeps) study," J. Cardiovasc. Comput. Tomogr., 7(5): 279-288. DOI: 10.1016/j.jcct.2013.09.003.

[149] Norgaard, B.L., Leipsic, J., Gaur, S., Seneviratne, S., Ko, B.S., Ito, H.*, et al.* (2014), "Diagnostic performance of noninvasive fractional flow reserve derived from coronary computed tomography angiography in suspected coronary artery disease: the NXT trial (Analysis of Coronary Blood Flow Using CT Angiography: Next Steps)," J. Am. Coll. Cardiol., 63(12): 1145-1155. DOI: 10.1016/j.jacc.2013.11.043.

[150] Brown, B.G., Bolson, E.L., and Dodge, H.T. (1984), "Dynamic mechanisms in human coronary stenosis," Circulation, 70(6): 917-922. DOI: 10.1161/01.CIR.70.6.917

[151] Badak, O., Schoenhagen, P., Tsunoda, T., Magyar, W.A., Coughlin, J., Kapadia, S.*, et al.* (2003), "Characteristics of atherosclerotic plaque distribution in coronary artery bifurcations: an intravascular ultrasound analysis," Coron. Artery Dis., 14(4): 309-316. DOI: 10.1097/01.mca.0000076511.29238.f1.

[152] Oviedo, C., Maehara, A., Mintz, G.S., Araki, H., Choi, S.Y., Tsujita, K.*, et al.* (2010), "Intravascular ultrasound classification of plaque distribution in left main coronary artery bifurcations. Where is the plaque really located?," Circ. Cardiovasc. Interv., 3(2): 105-112. DOI: 10.1161/Circinterventions.109.906016.

[153] Rodriguez-Granillo, G.A., Rosales, M.A., Degrossi, E., Durbano, I., and Rodriguez, A.E. (2007), "Multislice CT coronary angiography for the detection of burden, morphology and distribution of atherosclerotic plaques in the left main bifurcation," Int. J. Cardiovasc. Imaging, 23(3): 389-392. DOI: 10.1007/s10554-006-9144-1.

[154] Maehara, A., Mintz, G.S., Castagna, M.T., Pichard, A.D., Satler, L.F., Waksman, R.*, et al.* (2001), "Intravascular ultrasound assessment of the stenoses location and morphology in the left main coronary artery in relation to anatomic left main length," Am. J. Cardiol., 88(1): 1-4. DOI: 10.1016/S0002-9149(01)01575-2.

[155] Toggweiler, S., Urbanek, N., Schoenenberger, A.W., and Erne, P. (2010), "Analysis of coronary bifurcations by intravascular ultrasound and virtual histology," Atherosclerosis, 212(2): 524-527. DOI: 10.1016/j.atherosclerosis.2010.06.045.

[156] Chaichana, T., Sun, Z., and Jewkes, J. (2011), "Computation of hemodynamics in the left coronary artery with variable angulations," J. Biomech., 44(10): 1869-1878. DOI: 10.1016/j.jbiomech.2011.04.033.

[157] Dzavik, V., Kharbanda, R., Ivanov, J., Ing, D.J., Bui, S., Mackie, K.*, et al.* (2006), "Predictors of long-term outcome after crush stenting of coronary bifurcation lesions: importance of the bifurcation angle," Am. Heart J., 152(4): 762-769. DOI: 10.1016/j.ahj.2006.04.033.

[158] Westerhof, N., Bosman, F., De Vries, C.J., and Noordergraaf, A. (1969), "Analog studies of the human systemic arterial tree," J. Biomech., 2(2): 121-143. DOI: 10.1016/0021-9290(69)90024-4.

[159] Caro, C.G., Pedley, T.J., Schroter, R.C., Seed, W.A., and Parker, K.H., (2011), The Mechanics of the Circulation, Cambridge University Press, Cambridge.

[160] Levy, M.N., Pappano, A.J., and Berne, R.M., (2007), "The cardiac pump.," Cardiovascular Physiology, Mosby Elsevier, Philadelphia, PA, p. 74.

[161] Senzaki, H., Chen, C.H., and Kass, D.A. (1996), "Single-beat estimation of end-systolic pressure-volume relation in humans. A new method with the potential for noninvasive application," Circulation, 94(10): 2497-2506. DOI: 10.1161/01.CIR.94.10.2497

[162] Suga, H., and Sagawa, K. (1974), "Instantaneous pressure-volume relationships and their ratio in the excised, supported canine left ventricle," Circ. Res., 35(1): 117-126. DOI: 10.1161/01.RES.35.1.117.

[163] Suga, H., Sagawa, K., and Shoukas, A.A. (1973), "Load independence of the instantaneous pressure-volume ratio of the canine left ventricle and effects of epinephrine and heart rate on the ratio," Circ. Res., 32(3): 314-322. DOI: 10.1161/01.RES.32.3.314.

[164] Segers, P., Stergiopulos, N., Westerhof, N., Wouters, P., Kolh, P., and Verdonck, P. (2003), "Systemic and pulmonary hemodynamics assessed with a lumped-parameter heart-arterial interaction model," J. Eng. Math., 47(3-4): 185-199. DOI: 10.1023/B:Engi.0000007975.27377.9c.

[165] Avanzolini, G., Barbini, P., Cappello, A., and Cevenini, G. (1988), "CADCS simulation of the closed-loop cardiovascular system," Int. J. Biomed. Comput., 22(1): 39-49. DOI: 10.1016/0020-7101(88)90006-2.

[166] Geven, M.C.F., Bohte, V.N., Aarnoudse, W.H., van den Berg, P.M.J., Rutten, M.C.M., Pijls, N.H.J.*, et al.* (2004), "A physiologically representative in vitro model of the coronary circulation," Physiol. Meas., 25(4): 891-904. DOI: 10.1088/0967-3334/25/4/009.

[167] Kern, M.J., Lerman, A., Bech, J.W., De Bruyne, B., Eeckhout, E., Fearon, W.F.*, et al.* (2006), "Physiological assessment of coronary artery disease in the cardiac catheterization laboratory - A scientific statement from the American Heart Association Committee on Diagnostic and Interventional Cardiac Catheterization, Council on Clinical Cardiology," Circulation, 114(12): 1321-1341. DOI: 10.1161/Circulationaha.106.177276.

[168] Heusch, G. (2010), "Adenosine and maximum coronary vasodilation in humans: myth and misconceptions in the assessment of coronary reserve," Basic Res. Cardiol., 105(1): 1-5. DOI 10.1007/s00395-009-0074-7.

[169] Scanlon, P.J., Faxon, D.P., Audet, A.M., Carabello, B., Dehmer, G.J., Eagle, K.A.*, et al.* (1999), "ACC/AHA guidelines for coronary angiography. A report of the American College of Cardiology/American Heart Association Task Force on practice guidelines (Committee on Coronary Angiography). Developed in collaboration with the Society for Cardiac Angiography and Interventions," J. Am. Coll. Cardiol., 33(6): 1756-1824. DOI: 10.1161/01.CIR.99.17.2345.

[170] Nichols, W.W., O'Rourke, M.F., and McDonald, D.A., (2005), McDonald's blood flow in arteries : theoretic, experimental, and clinical principles, Hodder Arnold ; Distributed in the U.S.A. by Oxford University Press, London; New York.

[171] Brutin, D., Sobac, B., Loquet, B., and Sampol, J. (2011), "Pattern formation in drying drops of blood," J. Fluid. Mech., 667(01): 85-95. DOI: 10.1017/S0022112010005070.

[172] Dodge, J.T., Jr., Brown, B.G., Bolson, E.L., and Dodge, H.T. (1992), "Lumen diameter of normal human coronary arteries. Influence of age, sex, anatomic variation, and left ventricular hypertrophy or dilation," Circulation, 86(1): 232-246. DOI: 10.1161/01.CIR.86.1.232.

[173] Alfonso, F., Macaya, C., Goicolea, J., Hernandez, R., Segovia, J., Zamorano, J., *et al.* (1994), "Determinants of coronary compliance in patients with coronary artery disease: an intravascular ultrasound study," J. Am. Coll. Cardiol., 23(4): 879-884. DOI: 10.1016/0735-1097(94)90632-7.

[174] Williams, M.J., Stewart, R.A., Low, C.J., and Wilkins, G.T. (1999), "Assessment of the mechanical properties of coronary arteries using intravascular ultrasound: an in vivo study," Int. J. Card. Imaging, 15(4): 287-294. DOI: 10.1023/A:1006279228534.

[175] Kelle, S., Hays, A.G., Hirsch, G.A., Gerstenblith, G., Miller, J.M., Steinberg, A.M., *et al.* (2011), "Coronary artery distensibility assessed by 3.0 Tesla coronary magnetic resonance imaging in subjects with and without coronary artery disease," Am. J. Cardiol., 108(4): 491-497. DOI: 10.1016/j.amjcard.2011.03.078.

[176] Shaw, J.A., Kingwell, B.A., Walton, A.S., Cameron, J.D., Pillay, P., Gatzka, C.D., *et al.* (2002), "Determinants of coronary artery compliance in subjects with and without angiographic coronary artery disease," J. Am. Coll. Cardiol., 39(10): 1637-1643. DOI:10.1016/S0735-1097(02)01842-9.

[177] Chaichana, T., Sun, Z., and Jewkes, J. (2014), "Impact of plaques in the left coronary artery on wall shear stress and pressure gradient in coronary side branches," Computer methods in biomechanics and biomedical engineering, 17(2): 108-118. 10.1080/10255842.2012.671308.

[178] Huo, Y., and Kassab, G.S. (2009), "The scaling of blood flow resistance: from a single vessel to the entire distal tree," Biophys. J., 96(2): 339-346. DOI: 10.1016/j.bpj.2008.09.038.

[179] He, Z.X., Hartley, G.J., Cwajg, E., Michael, L.H., and Verani, M.S. (2000), "Myocardial blood flow and uptake of Tl-201 and Tc-99m MIBI during a bolus injection of CGS-21680, a potent selective adenosine A2 agonist," Circulation, 98(17): 95-95. DOI: 10.1161/01.CIR.102.4.438.

[180] Villanueva, F.S., Gertz, E.W., Csikari, M., Pulido, G., Fisher, D., and Sklenar, J. (2001), "Detection of coronary artery stenosis with power Doppler imaging," Circulation, 103(21): 2624-2630. DOI: 10.1161/01.CIR.103.21.2624

[181] Pacella, J.J., and Villanueva, F.S. (2006), "Effect of coronary stenosis on adjacent bed flow reserve - Assessment of microvascular mechanisms using myocardial contrast echocardiography," Circulation, 114(18): 1940-1947. DOI: 10.1161/Circulationaha.106.641779.

[182] Ragosta, M. (2015), "Left main coronary artery disease: importance, diagnosis, assessment, and management," Curr. Probl. Cardiol., 40(3): 93-126. DOI: 10.1016/j.cpcardiol.2014.11.003.

[183] Rubinshtein, R., Lerman, A., Spoon, D.B., and Rihal, C.S. (2012), "Anatomic features of the left main coronary artery and factors associated with its bifurcation angle: a 3-dimensional quantitative coronary angiographic study," Catheter. Cardiovasc. Interv., 80(2): 304-309. DOI: 10.1002/ccd.23425.

[184] Turgut, O., Yilmaz, A., Yalta, K., Yilmaz, B.M., Ozyol, A., Kendirlioglu, O.*, et al.* (2007), "Tortuosity of coronary arteries: an indicator for impaired left ventricular relaxation?," Int. J. Cardiovasc. Imaging, 23(6): 671-677. DOI: 10.1007/s10554-006-9186-4.

[185] Zhu, H., Ding, Z., Piana, R.N., Gehrig, T.R., and Friedman, M.H. (2009), "Cataloguing the geometry of the human coronary arteries: a potential tool for predicting risk of coronary artery disease," Int. J. Cardiol., 135(1): 43-52. DOI: 10.1016/j.ijcard.2008.03.087.

[186] Medina, A., Suarez de Lezo, J., and Pan, M. (2006), "[A new classification of coronary bifurcation lesions]," Rev. Esp. Cardiol., 59(2): 183. DOI: 10.1016/S1885-5857(06)60130-8.

[187] Iguchi, T., Hasegawa, T., Nishimura, S., Nakata, S., Kataoka, T., Ehara, S.*, et al.* (2013), "Impact of lesion length on functional significance in intermediate coronary lesions," Clin. Cardiol., 36(3): 172-177. DOI: 10.1002/clc.22076.

[188] Meimoun, P., Sayah, S., Luycx-Bore, A., Boulanger, J., Elmkies, F., Benali, T.*, et al.* (2011), "Comparison Between Non-Invasive Coronary Flow Reserve and Fractional Flow Reserve to Assess the Functional Significance of Left Anterior Descending Artery Stenosis of Intermediate Severity," J. Am. Soc. Echocardiogr., 24(4): 374-381. DOI: 10.1016/j.echo.2010.12.007.

[189] Hamilos, M., Muller, O., Cuisset, T., Ntalianis, A., Chlouverakis, G., Sarno, G.*, et al.* (2009), "Long-term clinical outcome after fractional flow reserve-guided treatment in patients with angiographically equivocal left main coronary artery stenosis," Circulation, 120(15): 1505-1512. DOI: 10.1161/CIRCULATIONAHA.109.850073.

[190] Kural, M.H., Cai, M., Tang, D., Gwyther, T., Zheng, J., and Billiar, K.L. (2012), "Planar biaxial characterization of diseased human coronary and carotid arteries for computational modeling," J. Biomech., 45(5): 790-798. DOI: 10.1016/j.jbiomech.2011.11.019.

[191] Robertson, A.M., Sequeira, A., and Kameneva, M.V., (2008), "Hemorheology," Hemodynamical flows modeling, analysis and simulation, G. P. Galdi, R. Rannacher, A. M. Robertson, and S. Turek, eds., Birkhäuser, Basel, Basel, pp. 63-120.

[192] Pedley, T.J., (1980), The fluid mechanics of large blood vessels, Cambridge University Press, Cambridge; New York.

[193] Johnston, B.M., Johnston, P.R., Corney, S., and Kilpatrick, D. (2004), "Non-Newtonian blood flow in human right coronary arteries: steady state simulations," J. Biomech., 37(5): 709-720. DOI: 10.1016/j.jbiomech.2003.09.016.

[194] Berger, S.A., and Jou, L.D. (2000), "Flows in stenotic vessels," Annu. Rev. Fluid. Mech., 32: 347-382. DOI: 10.1146/annurev.fluid.32.1.347.

[195] Ambrosi, D., Quarteroni, A., and Rozza, G., 2012, "Modeling of physiological flows," Springer, Milan; New York.

[196] Sherwin, S.J., and Blackburn, H.M. (2005), "Three-dimensional instabilities and transition of steady and pulsatile axisymmetric stenotic flows," J. Fluid. Mech., 533: 297-327. DOI: 10.1017/S0022112005004271.

[197] Varghese, S.S., Frankel, S.H., and Fischer, P.F. (2007), "Direct numerical simulation of stenotic flows. Part 2. Pulsatile flow," J. Fluid. Mech., 582: 281-318. DOI: 10.1017/S0022112007005836.

[198] Mittal, R., Simmons, S.P., and Najjar, F. (2003), "Numerical study of pulsatile flow in a constricted channel," J. Fluid. Mech., 485: 337-378. DOI: 10.1017/S002211200300449x.

[199] Ferrari, M., Werner, G.S., Bahrmann, P., Richartz, B.M., and Figulla, H.R. (2006), "Turbulent flow as a cause for underestimating coronary flow reserve measured by Doppler guide wire," Cardiovasc. Ultrasound, 4(14). DOI: 10.1186/1476-7120-4-14.

[200] Mallinger, F., and Drikakis, D. (2002), "Instability in three-dimensional, unsteady, stenotic flows," Int. J. Heat. Fluid. Fl., 23(5): 657-663. DOI: 10.1016/S0142-727x(02)00161-3.

[201] Cho, Y.I., Back, L.H., and Crawford, D.W. (1985), "Effect of simulated hyperemia on the flow field in a mildly atherosclerotic coronary artery casting of man," Aviat. Space Environ. Med., 56(3): 212-219.

[202] Varghese, S.S., Frankel, S.H., and Fischer, P.F. (2008), "Modeling transition to turbulence in eccentric stenotic flows," J. Biomech. Eng., 130(1): 014503. DOI: 10.1115/1.2800832.

[203] Jeon, B.J., Kim, J., and Choi, H.G. (2015), "A finite element analysis of turbulent eccentric stenotic flows by large eddy simulation," J. Mech. Sci. Technol., 29(5): 1869-1874. DOI: 10.1007/s12206-015-0407-4.

[204] Vignon-Clementel, I.E., Alberto Figueroa, C., Jansen, K.E., and Taylor, C.A. (2006), "Outflow boundary conditions for three-dimensional finite element modeling of blood flow and pressure in arteries," Comput. Method. Appl. Mech. Eng., 195(29–32): 3776-3796. DOI: 10.1016/j.cma.2005.04.014.

[205] Esmaily Moghadam, M., Vignon-Clementel, I.E., Figliola, R., and Marsden, A.L. (2013), "A modular numerical method for implicit 0D/3D coupling in cardiovascular finite element simulations," J. Comput. Phys., 244(0): 63-79. DOI: 10.1016/j.jcp.2012.07.035.

[206] Heywood, J.G., Rannacher, R., and Turek, S. (1996), "Artificial boundaries and flux and pressure conditions for the incompressible Navier-Stokes equations," Int. J. Numer. Meth. Fl., 22(5): 325-352. DOI: 10.1002/(Sici)1097-0363(19960315)22:5<325::Aid-Fld307>3.0.Co;2-Y.

[207] Formaggia, L., Gerbeau, J.F., Nobile, F., and Quarteroni, A. (2003), "Numerical Treatment of Defective Boundary Conditions for the Navier-Stokes Equations," SIAM J. Numer. Anal., 40(1): 376-401. DOI:10.1137/S003614290038296X.

[208] Takagi, A., Tsurumi, Y., Ishii, Y., Suzuki, K., Kawana, M., and Kasanuki, H. (1999), "Clinical potential of intravascular ultrasound for physiological assessment of coronary stenosis: relationship between quantitative ultrasound tomography and pressure-derived fractional flow reserve," Circulation, 100(3): 250-255. DOI: 10.1161/01.CIR.100.3.250

[209] Koo, B.K., Park, K.W., Kang, H.J., Cho, Y.S., Chung, W.Y., Youn, T.J.*, et al.* (2008), "Physiological evaluation of the provisional side-branch intervention strategy for bifurcation lesions using fractional flow reserve," Eur. Heart J., 29(6): 726-732. DOI: 10.1093/eurheartj/ehn045.

[210] Fischer, J.J., Samady, H., McPherson, J.A., Sarembock, I.J., Powers, E.R., Gimple, L.W.*, et al.* (2002), "Comparison between visual assessment and quantitative angiography versus fractional flow reserve for native coronary narrowings of moderate severity," The American journal of cardiology, 90(3): 210-215.

[211] Pagiatakis, C., Tardif, J.C., L'Allier, P.L., and Mongrain, R. (2015), "A numerical investigation of the functionality of coronary bifurcation lesions with respect to lesion configuration and stenosis severity," J. Biomech., 48(12): 3103-3111. DOI: 10.1016/j.jbiomech.2015.07.018.

[212] Ben-Dor, I., Torguson, R., Deksissa, T., Bui, A.B., Xue, Z., Satler, L.F.*, et al.* (2012), "Intravascular ultrasound lumen area parameters for assessment of physiological

ischemia by fractional flow reserve in intermediate coronary artery stenosis," Cardiovasc. Revasc. Med., 13(3): 177-182. DOI: 10.1016/j.carrev.2011.12.003.

[213] Hoole, S.P., Seddon, M.D., Poulter, R.S., Starovoytov, A., Wood, D.A., and Saw, J. (2012), "Development and validation of the fractional flow reserve (FFR) angiographic scoring tool (FAST) to improve the angiographic grading and selection of intermediate lesions that require FFR assessment," Coron. Artery Dis., 23(1): 45-50. DOI: 10.1097/MCA.0b013e32834e4f71.

[214] Natsumeda, M., Nakazawa, G., Murakami, T., Torii, S., Ijichi, T., Ohno, Y.*, et al.* (2015), "Coronary angiographic characteristics that influence fractional flow reserve," Circ. J.(0). DOI: 10.1253/circj.CJ-14-0931.

[215] Park, S.J., Ahn, J.M., Pijls, N.H., De Bruyne, B., Shim, E.B., Kim, Y.T.*, et al.* (2012), "Validation of functional state of coronary tandem lesions using computational flow dynamics," Am. J. Cardiol., 110(11): 1578-1584. DOI: 10.1016/j.amjcard.2012.07.023.

[216] Medina, A., Martin, P., Suarez de Lezo, J., Novoa, J., Melian, F., Hernandez, E.*, et al.* (2011), "Ultrasound study of the prevalence of plaque at the carina in lesions that affect the coronary bifurcation. Implications for treatment with provisional stent," Rev. Esp. Cardiol., 64(1): 43-50. DOI: 10.1016/j.recesp.2010.07.006.

[217] Poepping, T.L., Rankin, R.N., and Holdsworth, D.W. (2010), "Flow patterns in carotid bifurcation models using pulsed Doppler ultrasound: effect of concentric vs. eccentric stenosis on turbulence and recirculation," Ultrasound Med. Biol., 36(7): 1125-1134. DOI: 10.1016/j.ultrasmedbio.2010.02.005.

[218] Javadzadegan, A., Shimizu, Y., Behnia, M., and Ohta, M. (2013), "Correlation between Reynolds number and eccentricity effect in stenosed artery models," Technol. Health Care, 21(4): 357-367. DOI: 10.3233/THC-130736.

[219] Javadzadegan, A., Yong, A.S., Chang, M., Ng, A.C., Yiannikas, J., Ng, M.K.*, et al.* (2013), "Flow recirculation zone length and shear rate are differentially affected by stenosis severity in human coronary arteries," Am. J. Physiol. Heart Circ. Physiol., 304(4): H559-566. DOI: 10.1152/ajpheart.00428.2012.

[220] Griffith, M.D., Leweke, T., Thompson, M.C., and Hourigan, K. (2013), "Effect of small asymmetries on axisymmetric stenotic flow," J. Fluid. Mech., 721: R1. DOI: 10.1017/jfm.2013.109

[221] Melih Guleren, K. (2013), "Numerical flow analysis of coronary arteries through concentric and eccentric stenosed geometries," J. Biomech., 46(6): 1043-1052. DOI: 10.1016/j.jbiomech.2013.02.001.

[222] Huo, Y., Svendsen, M., Choy, J.S., Zhang, Z.D., and Kassab, G.S. (2012), "A validated predictive model of coronary fractional flow reserve," J. R. Soc. Interface., 9(71): 1325-1338. DOI: 10.1098/rsif.2011.0605.

[223] Takashima, H., Waseda, K., Gosho, M., Kurita, A., Ando, H., Sakurai, S.*, et al.* (2015), "Severity of morphological lesion complexity affects fractional flow reserve in intermediate coronary stenosis," J. Cardiol., 66(3): 239-245. DOI: 10.1016/j.jjcc.2014.11.004.

[224] Berry, C., van 't Veer, M., Witt, N., Kala, P., Bocek, O., Pyxaras, S.A.*, et al.* (2013), "VERIFY (VERification of Instantaneous Wave-Free Ratio and Fractional Flow Reserve for the Assessment of Coronary Artery Stenosis Severity in EverydaY Practice): a multicenter study in consecutive patients," J. Am. Coll. Cardiol., 61(13): 1421-1427. DOI: 10.1016/j.jacc.2012.09.065.

[225] Brinkman, A.M., Baker, P.B., Newman, W.P., Vigorito, R., and Friedman, M.H. (1994), "Variability of human coronary artery geometry: an angiographic study of the left anterior descending arteries of 30 autopsy hearts," Ann. Biomed. Eng., 22(1): 34-44. DOI: 10.1007/BF02368220.

[226] Craiem, D., Casciaro, M.E., Graf, S., Glaser, C.E., Gurfinkel, E.P., and Armentano, R.L. (2009), "Coronary arteries simplified with 3D cylinders to assess true bifurcation angles in atherosclerotic patients," Cardiovasc. Eng., 9(4): 127-133. DOI: 10.1007/s10558-009-9084-1.

[227] Dvir, D., Marom, H., Assali, A., and Kornowski, R. (2007), "Bifurcation lesions in the coronary arteries: early experience with a novel 3-dimensional imaging and quantitative analysis before and after stenting," EuroIntervention, 3(1): 95-99.

[228] Girasis, C., Serruys, P.W., Onuma, Y., Colombo, A., Holmes, D.R., Jr., Feldman, T.E.*, et al.* (2010), "3-Dimensional bifurcation angle analysis in patients with left main disease: a substudy of the SYNTAX trial (SYNergy Between Percutaneous Coronary Intervention with TAXus and Cardiac Surgery)," J. Am. Coll. Cardiol.: Cardiovasc. Interv., 3(1): 41-48. DOI: 10.1016/j.jcin.2009.10.019.

[229] Godino, C., Al-Lamee, R., La Rosa, C., Morici, N., Latib, A., Ielasi, A.*, et al.* (2010), "Coronary left main and non-left main bifurcation angles: how are the angles modified by different bifurcation stenting techniques?," J. Intervent. Cardiol., 23(4): 382-393. DOI: 10.1111/j.1540-8183.2010.00562.x.

[230] Pflederer, T., Ludwig, J., Ropers, D., Daniel, W.G., and Achenbach, S. (2006), "Measurement of coronary artery bifurcation angles by multidetector computed tomography," Invest. Radiol., 41(11): 793-798. DOI: 10.1097/01.rli.0000239318.88270.9f.

[231] Handran, C.B., Garberich, R.F., Lesser, J.R., Henry, T.D., Gilmore, M., and Schwartz, R.B. (2015), "The left main bifurcation angle and changes throughout the cardiac cycle: quantitative implications for left main bifurcation stenting and stents," J. Invasive Cardiol., 27(9): 401-404.

[232] Friedman, M.H., Deters, O.J., Mark, F.F., Bargeron, C.B., and Hutchins, G.M. (1983), "Arterial geometry affects hemodynamics. A potential risk factor for athersoclerosis," Atherosclerosis, 46(2): 225-231.

[233] Perktold, K., Peter, R.O., Resch, M., and Langs, G. (1991), "Pulsatile non-Newtonian blood flow in three-dimensional carotid bifurcation models: a numerical study of flow phenomena under different bifurcation angles," J. Biomed. Eng., 13(6): 507-515.

[234] Tadjfar, M. (2004), "Branch angle and flow into a symmetric bifurcation," J. Biomech. Eng., 126(4): 516-518. DOI: 10.1115/1.1785809.

[235] Lee, S.W., Antiga, L., Spence, J.D., and Steinman, D.A. (2008), "Geometry of the carotid bifurcation predicts its exposure to disturbed flow," Stroke, 39(8): 2341-2347. 10.1161/STROKEAHA.107.510644.

[236] Movahed, M.R. (2008), "Coronary artery bifurcation lesion classifications, interventional techniques and clinical outcome," Expert Rev. Cardiovasc. Ther., 6(2): 261-274. DOI: 10.1586/14779072.6.2.261.

[237] Aliabadi, D., Tilli, F.V., Bowers, T.R., Benzuly, K.H., Safian, R.D., Goldstein, J.A.*, et al.* (1997), "Incidence and angiographic predictors of side branch occlusion following high-pressure intracoronary stenting," Am. J. Cardiol., 80(8): 994-997.

[238] Amemiya, K., Domei, T., Iwabuchi, M., Shirai, S., Ando, K., Goya, M.*, et al.* (2014), "Impact of the bifurcation angle on major cardiac events after cross-over single stent strategy in unprotected left main bifurcation lesions: 3-dimensional quantitative coronary angiographic analysis," Am. J. Cardiovasc. Dis., 4(4): 168-176.

[239] Molavi-Zarandi, M., (2013), "Characterization of physiological flow in stenosed and stented coronary artery bifurcations," McGill University, Department of Mechanical Engineering, Doctor of Philosophy

[240] Choi, G., Cheng, C.P., Wilson, N.M., and Taylor, C.A. (2009), "Methods for quantifying three-dimensional deformation of arteries due to pulsatile and nonpulsatile forces: implications for the design of stents and stent grafts," Ann. Biomed. Eng., 37(1): 14-33. DOI: 10.1007/s10439-008-9590-0.

[241] Prosi, M., Perktold, K., Ding, Z., and Friedman, M.H. (2004), "Influence of curvature dynamics on pulsatile coronary artery flow in a realistic bifurcation model," J. Biomech., 37(11): 1767-1775. DOI: 10.1016/j.jbiomech.2004.01.021.

[242] Pant, S., Fabreges, B., Gerbeau, J.F., and Vignon-Clementel, I.E. (2014), "A methodological paradigm for patient-specific multi-scale CFD simulations: from clinical measurements to parameter estimates for individual analysis," Int. J. Numer. Method. Biomed. Eng., 30(12): 1614-1648. DOI: 10.1002/cnm.2692.

[243] Kim, H.J., Vignon-Clementel, I.E., Figueroa, C.A., LaDisa, J.F., Jansen, K.E., Feinstein, J.A.*, et al.* (2009), "On coupling a lumped parameter heart model and a three-

dimensional finite element aorta model," Ann. Biomed. Eng., 37(11): 2153-2169. DOI: 10.1007/s10439-009-9760-8.

[244] Pennati, G., Corsini, C., Cosentino, D., Hsia, T.Y., Luisi, V.S., Dubini, G.*, et al.* (2011), "Boundary conditions of patient-specific fluid dynamics modelling of cavopulmonary connections: possible adaptation of pulmonary resistances results in a critical issue for a virtual surgical planning," Interface Focus, 1(3): 297-307. DOI: 10.1098/rsfs.2010.0021.

[245] Gaillard, E., Garcia, D., Kadem, L., Pibarot, P., and Durand, L.G. (2010), "In vitro investigation of the impact of aortic valve stenosis severity on left coronary artery flow," J. Biomech. Eng., 132(4): 044502. DOI: 10.1115/1.4000990.

[246] ANSYS, (2012), ANSYS FLUENT Theory Guide, SAS IP, Inc., U.S.A.

Appendix A : Derivation of LPM governing equations

In this appendix, the governing equations of the lumped-parameter model are derived. Specifically, the Navier-Stokes Equations (NSE) are linearized and spatially averaged.

The following assumptions are made in the derivation:

1. Negligible circumferential flow (no swirl) and dominant axial flow
2. Negligible convective acceleration
3. Cylindrical vessel geometry with tethered ends (no axial extension)
4. Variation of velocity change in the axial direction is negligible compared to other terms

The incompressible Navier-Stokes equations for a Newtonian fluid are:

$$\begin{cases} \nabla \cdot \vec{u} = 0 , & \text{(A.1)} \\ \rho\left(\dfrac{\partial \vec{u}}{\partial t} + \vec{u} \cdot \nabla \vec{u} \right) + \nabla p - \mu \nabla^2 \vec{u} = 0 . & \text{(A.2)} \end{cases}$$

Here, the pressure and velocity components are defined by:

$$\begin{aligned} p &= p(r,z,t) , \\ u_z &= u_z(r,z,t) , \\ u_r &= u_r(r,z,t) . \end{aligned} \qquad \text{(A.3)}$$

The following theorem is also used in the derivation. For a continuous function $f=f(x_1,x_2,x_3)$ on a domain V with boundary ∂V, the following applies:

$$\frac{\partial}{\partial x_i} \int_V f dV = \int_V \frac{\partial f}{\partial x_i} + \int_{\partial V} f \vec{u}_{\partial V} \cdot \vec{n} d\sigma , \qquad \text{(A.4)}$$

where $\vec{u}_{\partial V}$ and $\vec{n}$ are the velocity and unit normal of the boundary respectively. In this derivation, since the flow is predominantly axial and a no-slip condition is applied on the wall, Equation (A.4) reduces to:

$$\frac{\partial}{\partial x_i}\int_V f dV = \int_V \frac{\partial f}{\partial x_i}\,. \tag{A.5}$$

Finally, the area-averaged volumetric flow, $\overline{Q}(z)$ and the domain-averaged volumetric flow and pressure, $\hat{Q}$ and $\hat{p}$ respectively are defined as follows:

$$\overline{Q}(z) = 2\pi\int_0^{R(z)} u_z r dr\,, \tag{A.6}$$

$$\hat{Q} = \frac{1}{l}\int_0^1 \overline{Q}(z) dz\,, \tag{A.7}$$

$$\hat{p} = \frac{1}{l}\int_0^1 \overline{p}(z) dz\,. \tag{A.8}$$

Continuity:

The continuity equation, in cylindrical coordinates, simplified based on the assumptions presented above, is given by:

$$\frac{\partial u_z}{\partial z} + \frac{1}{r}\frac{\partial}{\partial r}(r u_r) = 0\,. \tag{A.9}$$

Equation (A.9) is integrated with respect to θ. Then, using Equation (A.5) the expression is integrated with respect to r and substituted in Equation (A.6) to obtain the area-averaged mass conservation:

$$\begin{aligned}
&\int_0^{R(z)}\int_0^{2\pi}\frac{\partial u_z}{\partial z} d\theta dr + \int_0^{R(z)}\int_0^{2\pi}\frac{1}{r}\frac{\partial}{\partial r}(r u_r) d\theta dr = 0\,,\\
&2\pi\int_0^{R(z)}\frac{\partial r u_z}{\partial z} dr + 2\pi\int_0^{R(z) u_r|_{R(z)}} d(r u_r) = 0\,,\\
&2\pi\frac{\partial}{\partial z}\int_0^{R(z)} r u_z dr + 2\pi R(z) u_r\big|_R = 0\,,\\
&\frac{\partial \overline{Q}(z)}{\partial z} + 2\pi R(z) u_r\big|_R = 0\,.
\end{aligned} \tag{A.10}$$

Due to the no-slip condition, the radial velocity at the vessel wall, $u_r|_R$ is equal to the speed of the vessel wall such that:

$$u_r|_R = \frac{\partial R(z)}{\partial t} . \tag{A.11}$$

By substituting Equation (A.11) into Equation (A.10), the resulting expression is:

$$\frac{\partial \overline{Q}(z)}{\partial z} + 2\pi R(z)\frac{\partial R(z)}{\partial t} = 0 . \tag{A.12}$$

Here, a constitutive equation for the vessel wall is required in order to express the rate of change of the radius with the rate of change of the pressure. Assuming a linear elastic, isotropic and incompressible material and considering the vessel to be a thin-walled cylinder ($h/R << 1$ for wall thickness h), the circumferential stress in the vessel wall is given by:

$$\sigma_\theta = \overline{p}(z)\frac{R_0(z)}{h} , \tag{A.13}$$

where $R_0(z)$ is the equilibrium vessel radius. Using Hooke's law and the principle of superposition, the circumferential stress can be equivalently derived through the following steps (where ε is the strain, ν the Poisson's ratio, and E the Young's modulus and the subscript L corresponds to the longitudinal component). The circumferential and longitudinal strains are:

$$\varepsilon_\theta = \frac{1}{E}(\sigma_\theta - \nu\sigma_L) , \tag{A.14}$$

$$\varepsilon_L = \frac{1}{E}(\sigma_L - \nu\sigma_\theta) . \tag{A.15}$$

By combining Equation (A.14) with Equation (A.15), the circumferential strain reduces to:

$$\varepsilon_\theta = \frac{1}{E}\left[\sigma_\theta - \nu(E\varepsilon_L + \nu\sigma_\theta)\right]. \tag{A.16}$$

With the vessel assumed longitudinally tethered ($\varepsilon_L = 0$) and the circumferential strain defined by:

$$\varepsilon_\theta = \frac{R(z) - R_0(z)}{R_0(z)}, \tag{A.17}$$

and the circumferential stress is given by:

$$\sigma_\theta = \frac{E}{1-\nu^2}\frac{R(z) - R_0(z)}{R_0(z)}. \tag{A.18}$$

By equating Equation (A.13) with Equation (A.18), and differentiating the result with respect to time, an expression for the radial rate of change with respect to the rate of change of pressure is obtained:

$$\begin{aligned}
&\bar{p}(z)\frac{R_0(z)}{h} = \frac{E}{1-\nu^2}\frac{R(z) - R_0(z)}{R_0(z)}, \\
&\bar{p}(z) = \frac{Eh}{R_0^2(z)(1-\nu^2)}\left[R(z) - R_0(z)\right], \\
&\frac{\partial \bar{p}(z)}{\partial t} = \frac{Eh}{R_0^2(z)(1-\nu^2)}\frac{\partial R(z)}{\partial t}, \\
&\frac{\partial R(z)}{\partial t} = \frac{R_0^2(z)(1-\nu^2)}{Eh}\frac{\partial \bar{p}(z)}{\partial t}.
\end{aligned} \tag{A.19}$$

By substituting the final expression in Equation (A.19) into Equation (A.12), the 1D mass conservation is obtained:

$$\frac{\partial \hat{Q}(z)}{\partial z} + \frac{2\pi(R(z))^3(1-\nu^2)}{EH}\frac{\partial \bar{p}(z)}{\partial t} = 0. \tag{A.20}$$

Finally, to obtain the continuity equation for the LPM, Equation (A.20) is integrated with respect to the axial component, z, over the length of the vessel, l. By recalling Equation (A.16) and assuming that vessel tapering is minimal:

$$\begin{aligned}
&\int_{\hat{Q}(z_1)}^{\hat{Q}(z_2)} d\bar{Q}(z) + \int_1^l \frac{2\pi(R(z))^3(1-\nu^2)}{Eh}\frac{\partial \bar{p}(z)}{\partial t}dz = 0, \\
&Q_2 - Q_1 + \frac{2\pi l R^3(1-\nu^2)}{Eh}\frac{d\hat{p}}{dt} = 0.
\end{aligned} \tag{A.21}$$

Equation (A.21) is simplified to the following expression, to identify the compliance, C:

$$C\frac{d\hat{p}}{dt} = Q_1 - Q_2 \ , \tag{A.22}$$

Finally, by taking $\nu = 0.5$ for an incompressible, isotropic vessel, the compliance is

$$C = \frac{3\pi d R^3}{2Eh} \ . \tag{A.23}$$

Conservation of momentum:

Due to assumptions 1 and 2, the axial component (z) of the momentum equation is the governing equation:

$$\rho\frac{\partial u_z}{\partial t} + \frac{\partial p}{\partial z} - \mu\left[\frac{1}{r}\frac{\partial}{\partial r}\left(\frac{\partial u_z}{\partial r}\right)\right] = 0 \ . \tag{A.24}$$

Equation (A.24) is integrated with respect to r and θ to obtain the area-averaged (cross-sectional) expression. Equation (A.5) is used for integration of the first term of Equation (A.24):

$$\begin{aligned} &\rho\int_0^{R(z)}\int_0^{2\pi} r\frac{\partial u_z}{\partial t}\,d\theta dr + \int_0^{R(z)}\int_0^{2\pi} r\frac{\partial p}{\partial z}\,d\theta dr - \mu\int_0^{R(z)}\int_0^{2\pi}\frac{\partial}{\partial r}\left(r\frac{\partial u_z}{\partial r}\right)d\theta dr = 0 \ , \\ &2\pi\rho\int_0^{R(z)} r\frac{\partial u_z}{\partial t}dr + 2\pi\int_0^{R(z)} r\frac{\partial p}{\partial z}dr - 2\pi\mu\int_0^{R(z)}\frac{\partial}{\partial r}\left(r\frac{\partial u_z}{\partial r}\right)dr = 0 \ . \end{aligned} \tag{A.25}$$

Recalling Equation (A.6), the above integration yields (where $\bar{p}(z)$ is the area-averaged pressure on section z):

$$\rho\frac{\partial \bar{Q}(z)}{\partial t} + \pi(R(z))^2\frac{\partial \bar{p}(z)}{\partial z} - 2\pi\mu R(z)\frac{\partial u_z}{\partial r}\bigg|_{r=R(z)} = 0 \ . \tag{A.26}$$

Assuming that the tapering of the vessel is minimal, the radius (and area, A) is taken to be constant ($R(z)=R$):

$$\rho\frac{\partial \bar{Q}(z)}{\partial t} + A\frac{\partial \bar{p}(z)}{\partial z} - 2\pi\mu R(z)\frac{\partial u_z}{\partial r}\bigg|_{r=R} = 0 \ . \tag{A.27}$$

In order to simplify the last term of the above equation, the velocity profile ($u_z(r,z)$) must be known. Here, a fully-developed parabolic profile is assumed such that:

$$u_z(r,z) = \frac{R^2}{4\mu}\frac{d\bar{p}(z)}{dz}\left(1-\frac{r^2}{R^2}\right), \tag{A.28}$$

$$u_z(r,z) = u_{\max}(z)\left(1-\frac{r^2}{R^2}\right). \tag{A.29}$$

The maximum velocity can be written with respect to the average velocity, given as a function of flow rate and area:

$$u_{\max}(z) = 2\bar{u}_z(z), \tag{A.30}$$

$$u_{\max}(z) = 2\frac{\bar{Q}(z)}{A}. \tag{A.31}$$

Therefore,

$$u_z(r,z) = 2\frac{\bar{Q}(z)}{A}\left(1-\frac{r^2}{R^2}\right), \tag{A.32}$$

and

$$\left.\frac{\partial u_z}{\partial r}\right|_{r=R} = -\frac{4\bar{Q}(z)}{RA}. \tag{A.33}$$

Substituting Equation (A.33) into Equation (A.27), we obtain the linearized (1D) momentum equation:

$$\frac{\rho}{A}\frac{\partial\bar{Q}(z)}{\partial t}+\frac{\partial\bar{p}(z)}{\partial z}+\frac{8\pi\mu}{A^2}\bar{Q}(z)=0. \tag{A.34}$$

Similarly to the continuity equation, the governing equation for the LPM is obtained by integrating Equation (A.34) over the length, *l*, of the vessel:

$$\frac{\rho}{A}\int_0^l\frac{\partial\bar{Q}(z)}{\partial t}dz+\int_{\bar{p}(z_1)}^{\bar{p}(z_2)}d\bar{p}(z)+\frac{8\pi\mu}{A^2}\int_0^l\bar{Q}(z)dz=0,$$

$$\frac{\rho l}{A}\frac{d\hat{Q}}{dt} + \bar{p}(z_2) - \bar{p}(z_1) + \frac{8\pi\mu l}{A^2}\hat{Q} = 0\,. \tag{A.35}$$

By denoting $\bar{p}(z_2)$ as $\bar{p}_2$ and $\bar{p}(z_1)$ as $\bar{p}_1$, the above equation simplifies to:

$$L\frac{d\hat{Q}}{dt} = -R\hat{Q} + \bar{p}_1 - \bar{p}_2\,, \tag{A.36}$$

with

$$L = \frac{4\rho l}{\pi D^2}\,, \tag{A.37}$$

$$R = \frac{128\mu l}{\pi D^4}\,. \tag{A.38}$$

Appendix B : Derivation of ODE system for LPM model

The full LPM with the corresponding state variables (pressures and flows), which are to be computed, are provided in Figure B.1. The derivation of the system of 38 ODEs is provided below.

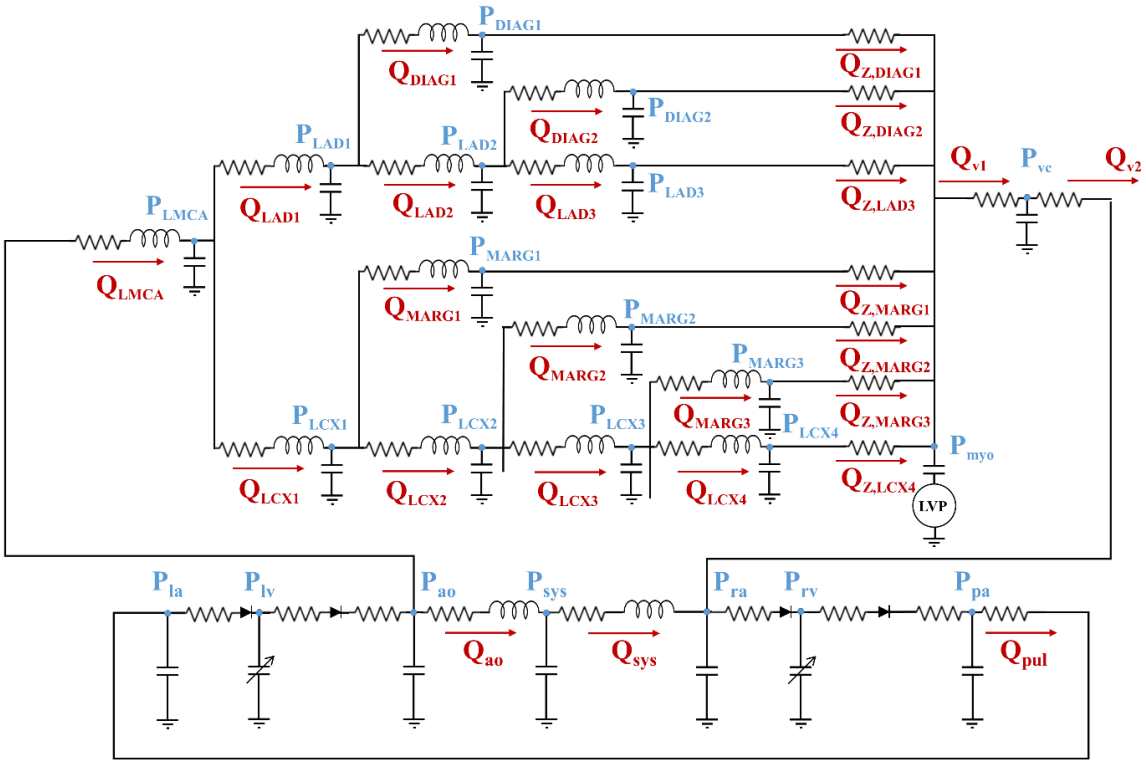

Figure B.1: Full LPM denoting the flows and pressures to be calculated. All variables corresponding to the electrical analogue components are presented in Figure 4.2.

Heart, systemic and pulmonary models:

The atrial and ventricular pressures are expressed as a function of their elastances and volumes, as follows:

$$\begin{aligned} P_{la} &= E_{la}(V_{la} - V_{0,la}) \\ P_{ra} &= E_{ra}(V_{ra} - V_{0,ra}) \\ P_{lv} &= E_{lv}(t)(V_{lv} - V_{0,lv}) \\ P_{rv} &= E_{rv}(t)(V_{rv} - V_{0,rv}) \end{aligned} \tag{B.1}$$

Furthermore, the flow through each of the valves can be expressed with respect to the valve states and their corresponding resistances:

$$
\begin{aligned}
Q_{Sv,mit} &= \frac{S_{v,mit}(P_{la} - P_{lv})}{R_{v,mit}} \\
Q_{Sv,ao} &= \frac{S_{v,ao}(P_{lv} - P_{ao})}{R_{v,ao} + Z_{as}} \\
Q_{Sv,tri} &= \frac{S_{v,tri}(P_{ra} - P_{rv})}{R_{v,tri}} \\
Q_{Sv,pul} &= \frac{S_{v,pul}(P_{rv} - P_{pa})}{R_{v,pul} + Z_{pa}}
\end{aligned}
\tag{B.2}
$$

Consequently, based on Equations (B.1), (B.2), and (4.9)-(4.13), the system of ODEs for the heart, systemic and pulmonary models is derived as follows:

$$
\begin{aligned}
\frac{dV_{la}}{dt} &= Q_{pul} - \frac{S_{v,mit}\left[E_{la}(V_{la} - V_{0,la}) - E_{lv}(t)(V_{lv} - V_{0,lv})\right]}{R_{v,mit}} \\
\frac{dV_{lv}}{dt} &= \frac{S_{v,mit}\left[E_{la}(V_{la} - V_{0,la}) - E_{lv}(t)(V_{lv} - V_{0,lv})\right]}{R_{v,mit}} - \frac{S_{v,ao}\left[E_{lv}(t)(V_{lv} - V_{0,lv}) - P_{ao}\right]}{R_{v,ao} + Z_{as}} \\
\frac{dP_{ao}}{dt} &= \frac{1}{C_{as}}\left[\frac{S_{v,ao}\left[E_{lv}(t)(V_{lv} - V_{0,lv}) - P_{ao}\right]}{R_{v,ao} + Z_{as}} - Q_{ao} - Q_{LMCA}\right] \\
\frac{dQ_{ao}}{dt} &= \frac{1}{L_{ao}}\left[P_{ao} - Z_{ao}Q_{ao} - P_{sys}\right] \\
\frac{dP_{sys}}{dt} &= \frac{1}{C_{sys}}\left[Q_{ao} - Q_{sys}\right] \\
\frac{dQ_{sys}}{dt} &= \frac{1}{L_{sys}}\left[P_{sys} - R_{sys}Q_{sys} - E_{ra}(V_{ra} - V_{0,ra})\right] \\
\frac{dV_{ra}}{dt} &= Q_{sys} + Q_{v2} - \frac{S_{v,tri}\left[E_{ra}(V_{ra} - V_{0,ra}) - E_{lr}(t)(V_{rv} - V_{0,lr})\right]}{R_{v,tri}} \\
\frac{dV_{rv}}{dt} &= \frac{S_{v,tri}\left[E_{ra}(V_{ra} - V_{0,ra}) - E_{lr}(t)(V_{rv} - V_{0,lr})\right]}{R_{v,tri}} - \frac{S_{v,pul}\left[E_{rv}(t)(V_{rv} - V_{0,rv}) - P_{pul}\right]}{R_{v,pul} + Z_{pa}}
\end{aligned}
$$

$$\frac{dP_{pa}}{dt} = \frac{1}{C_{pul}}\left[\frac{S_{v,pul}\left[E_{rv}(t)(V_{rv} - V_{0,rv}) - P_{pul}\right]}{R_{v,pul} + Z_{pa}} - Q_{pul}\right]$$

$$\frac{dQ_{pul}}{dt} = \frac{1}{R_{sys}}\left[\frac{dP_{pa}}{dt} - E_{la}\frac{dV_{la}}{dt}\right]$$

The system of ODEs corresponding to the dynamics of the epicardial coronary system are based on the conservation of mass and momentum for the basic, LPM compartmental unit (Figure 4.1), provided in Equation (4.1).

$$\frac{dQ_{LMCA}}{dt} = \frac{1}{L_{LMCA}}\left[P_{ao} - R_{LMCA}Q_{LMCA} - P_{LMCA}\right]$$

$$\frac{dP_{LMCA}}{dt} = \frac{1}{C_{LMCA}}\left[Q_{LMCA} - Q_{LAD1} - Q_{LCX1}\right]$$

$$\frac{dQ_{LAD1}}{dt} = \frac{1}{L_{LAD1}}\left[P_{LMCA} - R_{LAD1}Q_{LAD1} - P_{LAD1}\right]$$

$$\frac{dP_{LAD1}}{dt} = \frac{1}{C_{LAD1}}\left[Q_{LAD1} - Q_{LAD2} - Q_{DIAG1}\right]$$

$$\frac{dQ_{LAD2}}{dt} = \frac{1}{L_{LAD2}}\left[P_{LAD1} - R_{LAD2}Q_{LAD2} - P_{LAD2}\right]$$

$$\frac{dP_{LAD2}}{dt} = \frac{1}{C_{LAD2}}\left[Q_{LAD2} - Q_{LAD3} - Q_{DIAG2}\right]$$

$$\frac{dQ_{LAD3}}{dt} = \frac{1}{L_{LAD3}}\left[P_{LAD2} - R_{LAD3}Q_{LAD3} - P_{LAD3}\right]$$

$$\frac{dP_{LAD3}}{dt} = \frac{1}{C_{LAD3}}\left[Q_{LAD3} - Q_{Z,LAD3}\right]$$

$$\frac{dQ_{DIAG1}}{dt} = \frac{1}{L_{DIAG1}}\left[P_{LAD1} - R_{DIAG1}Q_{DIAG1} - P_{DIAG1}\right]$$

$$\frac{dP_{DIAG1}}{dt} = \frac{1}{C_{DIAG1}}\left[Q_{DIAG1} - Q_{Z,DIAG1}\right]$$

$$\frac{dQ_{DIAG2}}{dt} = \frac{1}{L_{DIAG2}}\left[P_{LAD2} - R_{DIAG2}Q_{DIAG2} - P_{DIAG2}\right]$$

$$\frac{dP_{DIAG2}}{dt} = \frac{1}{C_{DIAG1}}\left[Q_{DIAG2} - Q_{Z,DIAG2}\right]$$
$$\frac{dQ_{LCX1}}{dt} = \frac{1}{L_{LCX1}}\left[P_{LMCA} - R_{LCX1}Q_{LCX1} - P_{LCX1}\right]$$
$$\frac{dP_{LCX1}}{dt} = \frac{1}{C_{LCX1}}\left[Q_{LCX1} - Q_{LCX2} - Q_{MARG1}\right]$$
$$\frac{dQ_{LCX2}}{dt} = \frac{1}{L_{LCX2}}\left[P_{LCX1} - R_{LCX2}Q_{LCX2} - P_{LCX2}\right]$$
$$\frac{dP_{LCX2}}{dt} = \frac{1}{C_{LCX2}}\left[Q_{LCX2} - Q_{LCX3} - Q_{MARG2}\right]$$
$$\frac{dQ_{LCX3}}{dt} = \frac{1}{L_{LCX3}}\left[P_{LCX2} - R_{LCX3}Q_{LCX3} - P_{LCX3}\right]$$
$$\frac{dP_{LCX3}}{dt} = \frac{1}{C_{LCX3}}\left[Q_{LCX3} - Q_{LCX4} - Q_{MARG3}\right]$$
$$\frac{dQ_{LCX4}}{dt} = \frac{1}{L_{LCX4}}\left[P_{LCX3} - R_{LCX4}Q_{LCX4} - P_{LCX4}\right]$$
$$\frac{dP_{LCX4}}{dt} = \frac{1}{C_{LCX4}}\left[Q_{LCX4} - Q_{Z,LCX4}\right]$$
$$\frac{dQ_{MARG1}}{dt} = \frac{1}{L_{MARG1}}\left[P_{LCX1} - R_{MARG1}Q_{MARG1} - P_{MARG1}\right]$$
$$\frac{dP_{MARG1}}{dt} = \frac{1}{C_{MARG1}}\left[Q_{MARG1} - Q_{Z,MARG1}\right]$$
$$\frac{dQ_{MARG2}}{dt} = \frac{1}{L_{MARG2}}\left[P_{LCX2} - R_{MARG2}Q_{MARG2} - P_{MARG2}\right]$$
$$\frac{dP_{MARG2}}{dt} = \frac{1}{C_{MARG2}}\left[Q_{MARG2} - Q_{Z,MARG2}\right]$$
$$\frac{dQ_{MARG3}}{dt} = \frac{1}{L_{MARG3}}\left[P_{LCX3} - R_{MARG3}Q_{MARG3} - P_{MARG3}\right]$$
$$\frac{dP_{MARG3}}{dt} = \frac{1}{C_{MARG3}}\left[Q_{MARG3} - Q_{Z,MARG3}\right]$$

where, for terminal resistance i,

$$Q_{Z,i} = \frac{P_i - P_{myo} - E_{lv}(t)\left[V_{lv} - V_{0,lv}\right]}{Z_i}$$

such that $i =$ *DIAG1, DIAG2, LAD3, MARG1, MARG2, MARG3, LCX4.*

To close the system of ODEs, the coronary myocardial and venous dynamics are described by:

$$\frac{dP_{myo}}{dt} = \frac{1}{C_{myo}}\left[\sum Q_{Z,i} - Q_{v1}\right]$$

$$\frac{dP_{vc}}{dt} = \frac{1}{C_v}\left[Q_{v1} - Q_{v2}\right]$$

where

$$Q_{v1} = \frac{P_{myo} + E_{lv}(t)\left[V_{lv} - V_{0,lv}\right] - P_{vc}}{R_{v1}}$$

$$Q_{v2} = \frac{P_{vc} - E_{la}\left[V_{la} - V_{0,la}\right]}{R_{v2}}$$

Appendix C : Runge-Kutta method

An explicit fourth-order Runge-Kutta method was used for the numerical integration of the system of ODEs describing the dynamics of the full LPM of the cardiovascular system. The details pertaining to this method are described below.

For a first-order ODE of the form:

$$\frac{dy}{dx} = f(x, y) \tag{C.1}$$

with initial conditions

$$y(x = 0) = y_0 \tag{C.2}$$

the value of y at $x = x_{n+1}$, denoted as y_{n+1}, for integration step n, can be determined by

$$y_{n+1} = y_n + \frac{h}{6}(k_1 + 2k_2 + 2k_3 + k_4) \tag{C.3}$$

where $h = x_{n+1} - x_n$, $y_n = y(x_n)$ as determined from the previous step and k_i for $i = 1,2,3,4$ given by

$$\begin{aligned} k_1 &= f(x_n, y_n) \\ k_2 &= f(x_n + 0.5h, y_n + 0.5k_1h) \\ k_3 &= f(x_n + 0.5h, y_n + 0.5k_2h) \\ k_4 &= f(x_n + h, y_n + k_3h) \end{aligned} \tag{C.4}$$

The integration of the system of ODEs using the fourth-order Runge-Kutta method was implemented through an in-house C++ code with a timestep of 1.0×10^{-4}s. A set of initial conditions for each state variable, based on *a priori* knowledge of the system dynamics and expected physiological parameter values, were set. The code was executed for several cardiac cycles until a cyclic solution was obtained, such that the initial values (at time $t = t_0$) and the final values (at time $t = T$, where T is the length of the cardiac cycle),

displayed a maximum 0.1 percent difference. For cycle i, the initial conditions were taken to be the values computed at time $t = T$ for cycle $i-1$.

Appendix D : Finite Volume Method

The following appendix provides an overview of the Finite Volume Method (FVM) employed within ANSYS Fluent for the numerical simulation of the flow within the 3D domain of the LMCA bifurcation. The governing equations are also provided.

Let the velocity in the 3D domain be defined as:

$$\vec{u} = (u_x, u_y, u_z)$$
$$\vec{u} = (u, v, w) \tag{D.1}$$

Therefore, the continuity equation is given by:

$$\frac{D\rho}{Dt} + \nabla \cdot (\rho \vec{u}) = 0$$
$$\frac{\partial \rho}{\partial t} + u\frac{\partial \rho}{\partial x} + v\frac{\partial \rho}{\partial y} + w\frac{\partial \rho}{\partial z} + \frac{\partial \rho u}{\partial x} + \frac{\partial \rho v}{\partial y} + \frac{\partial \rho w}{\partial z} = 0 \tag{D.2}$$

By considering the fluid as incompressible, where the density, ρ, does not change in space or time, Equation (D.2) simplifies to

$$\rho(\nabla \cdot \vec{u}) = 0 \tag{D.3}$$

Furthermore, the general equation for the conservation of momentum is given by:

$$\rho \frac{D\vec{u}}{Dt} = -\nabla p + \sum \vec{F}_b + \nabla \cdot \vec{\tau} \tag{D.4}$$

where $\vec{F}_b$ are the body forces and source terms, p is the pressure and $\vec{\tau}$ is the stress tensor associated with viscous dissipation. For a Newtonian and incompressible fluid, the stress tensor, is given by:

$$\vec{\tau} = \mu \nabla \cdot \vec{u} \tag{D.5}$$

where μ is the viscosity. Therefore, for an incompressible, Newtonian fluid, where the effect of gravitational forces is considered negligible, the general momentum conservation equation (Equation (D.4)) simplifies to:

$$\rho \frac{D\vec{u}}{Dt} = -\nabla p + \mu \nabla^2 \vec{u} \tag{D.6}$$

The material derivative in Equation (D.6) can be expanded, such that the momentum conservation is expressed as:

$$\rho \frac{\partial \vec{u}}{\partial t} + \rho(\vec{u} \cdot \nabla \vec{u}) + \nabla p - \mu \nabla^2 \vec{u} = 0 \tag{D.7}$$

Therefore, Equation (D.3) and Equation (D.7) constitute the governing equations for the dynamics of an incompressible, Newtonian and isothermal fluid; these equations were provided in Section 5.2 (Equation (5.2)) in the description of the 3D model of the LMCA bifurcation.

In the FVM, Equation (D.3) and Equation (D.7) are integrated over a control volume. A two-dimensional case of a control volume V_0 with center C_0, surrounded by control volumes V_1, V_2 and V_3, with centers C_1, C_2 and C_3 respectively is provided in Figure D.1.

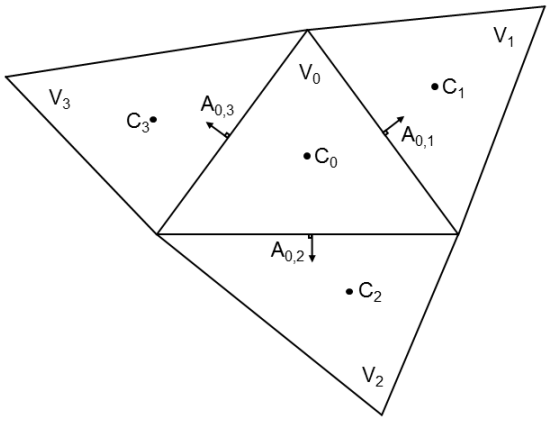

Figure D.1: Two-dimensional control volume V_0 with cell center C_0, surrounded by control volumes V_1, V_2 and V_3 with cell centers C_1, C_2, and C_3 respectively and area vectors $A_{0,1}$, $A_{0,2}$ and $A_{0,3}$ respectively

For the continuity constraint, Equation (D.3) is integrated over control volume V_0:

$$\int_{V_0} \rho(\nabla \cdot \vec{u}) dV_0 = 0 \tag{D.8}$$

By applying the divergence theorem:

$$\int_{V} (\nabla \cdot \vec{v}) dV = \oint_{A} \vec{v} \cdot d\vec{A} \tag{D.9}$$

for a vector $\vec{v}$ in a control volume V with surface area A, the volume integral in Equation (D.8) is converted to a surface integral, as follows:

$$\oint_{A_0} \rho \vec{u} \cdot d\vec{A}_0 = 0 \tag{D.10}$$

where $\vec{A}_0$ is the area vector of the surface enclosing control volume V_0. When considering a control volume enclosed by N_f faces (in the 2D case provided in Figure D.1, $N_f = 3$), Equation (D.10) reduces to the algebraic equation:

$$\sum_{i=1}^{N_f} \rho \vec{u} \cdot \vec{A}_{0,i} = 0 \tag{D.11}$$

The same procedure can be applied to the conservation of momentum (Equation (D.7)). The integral over control volume V_0 is taken:

$$\int_{V_0} \rho \frac{\partial \vec{u}}{\partial t} dV_0 + \int_{V_0} \rho(\vec{u} \cdot \nabla \vec{u}) dV_0 + \int_{V_0} \nabla p dV_0 - \int_{V_0} \mu \nabla^2 \vec{u} dV_0 = 0 \tag{D.12}$$

Subsequently, the divergence theorem is applied such that Equation (D.12) reduces to:

$$\rho \frac{\partial \vec{u}}{\partial t} V_0 + \oint_{A} \rho(\vec{u} \cdot \vec{u}) \cdot d\vec{A} + \oint_{A} p \cdot \vec{I} \cdot d\vec{A} - \oint_{A} \mu \nabla \cdot \vec{u} \cdot d\vec{A} = 0 \tag{D.13}$$

where I is the identity matrix. Again, by considering a control volume with N_f faces, Equation (D.13) can be expressed by:

$$\rho \frac{\partial \vec{u}}{\partial t} V_0 + \sum_{i=1}^{N_f} \rho(\vec{u} \cdot \vec{u}) \cdot \vec{A}_i + \sum_{i=1}^{N_f} p \cdot \vec{I} \cdot \vec{A}_i - \sum_{i=1}^{N_f} \mu \nabla \cdot \vec{u} \cdot \vec{A}_i = 0 \tag{D.14}$$

In transient simulations, as one can observe through Equation (D.14), discretization in time must occur in conjunction to discretization in space. For example, by considering a first-order, backwards implicit time discretization, Equation (D.14) is expressed as:

$$\rho \left[\frac{\vec{u}^{n+1} - \vec{u}^{n}}{\Delta t} \right] V_0 + \sum_{i=1}^{N_f} \rho(\vec{u}^{n+1} \cdot \vec{u}^{n+1}) \cdot \vec{A}_i + \sum_{i=1}^{N_f} p^{n+1} \cdot \vec{I} \cdot \vec{A}_i - \sum_{i=1}^{N_f} \mu \nabla \cdot \vec{u}^{n+1} \cdot \vec{A}_i = 0 \tag{D.15}$$

where Δt is the time step, defined as

$$\Delta t = t^{n+1} - t^{n}$$

where n is the current timestep. In the cell-centered method applied in ANSYS Fluent, the unknown pressure and velocities are computed and stored at the cell centers of each control volume. However, for the convective, diffusive and pressure terms of Equation (D.15), the values of the pressure and velocities are required at the cell faces and therefore must be interpolated based on the respective cell-centered values of the control volume of interest as well as those of the neighbouring cells. Various interpolation schemes can be implemented for the pressure and the velocity components in the convective and diffusive terms of Equation (D.15). Similarly to the momentum conservation, interpolation of the face values of the velocity must also be employed in the discretized continuity equation presented in Equation (D.11). Details regarding the different interpolation schemes as well as the computation of the velocity gradients in the diffusive term have been extensively outlined in [246].

Equation (D.15) can be written for each velocity component, which results in three discretized, scalar, nonlinear (due to the convective term of the momentum equation) algebraic equations, for each control volume. The resulting equations can be rearranged

to be expressed in terms of the scalar values, both at the center of the control volume of interest and the corresponding values in the neighbouring cells (from the interpolation schemes). For example, by considering the momentum conservation in the x-direction, the rearranged equation can be given in the general algebraic form as:

$$a_V u_V = \sum_{nb} a_{nb} u_{nb} + \sum p_f A_x \cdot \hat{i} \tag{D.16}$$

where the subscript V denotes the control volume of interest, the subscript nb denotes the neighbouring cells, $\hat{i}$ is the normal vector in the x-direction, and a_V and a_{nb} are the coefficients of the scalar values in the control volume of interest and in the neighbouring cells respectively. By employing this method for each unknown scalar variable in each control volume of the discretized domain, a system of algebraic equations is derived. The coefficients within Equation (D.16) are linearized implicitly, which signifies that they are expressed in terms of both known and unknown values of the variable in the neighbouring cells, so as to implement linear techniques. When combining the equations for the different control volumes so as to form a system of algebraic equations, the unknown variables appear in multiple equations such that the system must be solved simultaneously in an iterative manner. The linearized systems of algebraic equations are solved using a point-implicit Gauss-Seidel approach coupled with an algebraic multigrid method. For incompressible flows, ANSYS Fluent utilizes a pressure-based solver wherein the pressure field is computed based on a pressure-correction equation. Specifically, in the iterative segregated approach, each component of the momentum equation is decoupled from the other components such that its corresponding field is solved for independently and in a sequential manner. The resulting velocity field is subsequently corrected using a pressure-correction equation so that it satisfies the constraint of continuity. The aforementioned pressure equation inherently takes into account the velocity field as it is derived based on both the continuity and momentum; the exact form of the equation depends on the pressure-velocity coupling scheme for which there are various approaches, as outlined in [246]. The procedure is advanced iteratively until it has converged and is implemented within each timestep for transient simulations [246].